MULTISCALE THERMOVISCOELASTIC MODELING OF COMPOSITE MATERIALS

by

Orzuri Rique Garaizar

A Dissertation

Submitted to the Faculty of Purdue University

In Partial Fulfillment of the Requirements for the degree of

Doctor of Philosophy

School of Aeronautics and Astronautics

West Lafayette, Indiana

May 2021

THE PURDUE UNIVERSITY GRADUATE SCHOOL
STATEMENT OF COMMITTEE APPROVAL

Dr. Wenbin Yu, Chair

School of Aeronautics and Astronautics

Dr. R. Byron Pipes

School of Aeronautics and Astronautics, Materials, and Chemical Engineering

Dr. Weinong Chen

School of Aeronautics and Astronautics, and Materials Engineering

Dr. Johnathan E. Goodsell

School of Aeronautics and Astronautics

Approved by:

Dr. Gregory A. Blaisdell

Ainara, maite zaitugu laztana.

ACKNOWLEDGMENTS

First of all, I would like to thank my advisor Dr. Wenbin Yu and my co-advisor Dr. R. Byron Pipes for giving me this wonderful opportunity. The work presented in this dissertation would not be possible without their continuous guidance and insightful advice. I would also like to thank my committee members Dr. Weinong Chen and Dr. Johnathan Goodsell, who took their valuable time from their busy schedules to provide a lot of constructive suggestions to improve my work and challenge my knowledge.

I would like to acknowledge the Composites Manufacturing and Simulation Center, Purdue College of Engineering and NASA Langley Research Center (LaRC) for their financial support. My special appreciation goes to Dr. Juan M. Fernandez and Dr. Andrew C. Bergan who helped me in understanding the simulation tool needs by the thin-ply high strain composites community. My research efforts and publications greatly benefited from our monthly discussions during this last year. NASA LaRC also provided some of the experimental data under a Space Act Agreement (SAA) between NASA LaRC and Purdue University.

I would also like to thank my past and current members of the Multiscale Structural Mechanics group (Dr. Liang Zhang, Dr. Fang Jiang, Dr. Bo Peng, Dr. Hamsasew M. Sertse, Dr. Ernesto Camarena, Dr. Ning Liu, Dr. Zhenyuan Gao, Dr. Xin Liu, Yufei Long, Su Tian, Rong Chiu, Ankit Deo, Fei Tao, Banghua Zhao and Haodong Du) and of the Composites Manufacturing and Simulation Center (Dr. Eduardo Barocio, Dr. Sergey Kravchenko, Dr. Drew Sommerd, Dr. Michael Knauf, Dr. Benjamin Denos, Dr. Garam Kim, Dr. Anthony Favaloro, Dr. Rebecca Cutting, Sushrut Karkamar, Miguel Ramirez, Jorge Ramirez, Joseph Kirchhoff, Chris Cowden, Eric Smoldt and many more) for all their contributions and collaboration. I have been fortunate to have very supportive research colleagues, who helped me every step of the way.

Finally, I would like to acknowledge the understanding of my parents, sister, grandma, entire family, and friends for the missed moments and sacrifices. An especial thank also goes to Fermina, as she will always be in my memories. To conclude, I would also like to recognize my soulmate, friend, and husband Arnau for his unwavering support, encouragement, love,

and patience. We both walked together in this intellectual endeavor of becoming Doctor of Philosophy in Aeronautics and Astronautics at Purdue University.

TABLE OF CONTENTS

LIST OF TABLES

LIST OF FIGURES

LIST OF SYMBOLS

ABD	Plate/shell stiffness matrix
C^b	Beam stiffness matrix
C_{ijkl}	Stiffness tensor
c_v	Specific heat per unit volume at constant volume
E_i	Young's modulus, engineering constant
E_a	Activation energy
F_1, M_1, M_2, M_3	1D Euler-Bernoulli beam stress resultants
G_i	Shear modulus, engineering constant
N, M	Plate/shell force and moment resultants
N_T, M_T	Plate/shell thermal force and moment resultants
Q	Plane-stress reduced stiffness matrix
R	Gas constant
S_{ijkl}	Compliance tensor
t	Time
T	Temperature
u_i	Displacement
U	Strain energy
X	Degree of cure/crystallinity
α_{ij}	Coefficients of thermal expansion
β_{ij}	Thermal stress tensor
γ_{11}, κ_{11}, κ_{12}, κ_{13}	1D Euler-Bernoulli beam strains
Γ_h	Operator matrix dependent on the SG dimension
Γ_ε	Operator matrix dependent on the macroscopic structural model
ε_{ij}	Strain tensor
$\epsilon_{\alpha\beta}$	Plate/shell in-plane strains
$\kappa_{\alpha\beta}$	Plate/shell curvatures
λ	Discrete stress relaxation times
ν_{ij}	Poisson's ratio, engineering constant

Φ_1	Beam section rotation or twist angle
ξ	Reduced time
θ	Temperature change from stress free starting temperature
σ_{ij}	Stress tensor
χ_i	Fluctuating function

Subscripts

g	Glass-transition
0	Reference

Superscripts

$*$	Effective, homogenized value

ABBREVIATIONS

1D	One-dimensional
2D	Two-dimensional
3D	Three-dimensional
aPBC	Aperiodic boundary condition
ASC	American Society for Composites
CBT	Column bending test
cdmHUB	Composites Design & Manufacturing HUB
CFRP	Carbon fiber reinforced polymer
CHILE	Cure hardening instantaneous linear elastic
CLPT	Classical laminated plate theory
CPU	Central processing unit
CTE	Coefficient of thermal expansion
CTM	Collapsible tubular mast
DI	Direct integration
DNS	Direct numerical simulation
DOC	Degree of cure/crystallinity
FEA	Finite element analysis
FEM	Finite element method
GUI	Graphic user interface
HRM	Hybrid rules of mixtures
IACMI	Institute of Advanced Composites Manufacturing Innovation
LaRC	Langley Research Center
MSG	Mechanics of structure genome
MUBC	Mixed uniform boundary conditions
PBC	Periodic boundary condition
PEEK	Polyetheretherketone
PMIL	Principle of minimum information loss
PW	Plain weave

QE	Quasi-elastic
RVE	Representative volume element
SG	Structure gene
SI	International system of units
SLS	Standard linear solid
TP-HSC	Thin-ply high strain composites
TRAC	Triangular rollable and collapsible
TTSP	Time-temperature superposition principle
TVHRM	Thermoviscoelastic hybrid rules of mixtures
UD	Unidirectional
UDFRC	Unidirectional fiber reinforced composite
UEL	User-defined elements subroutine for Abaqus
UEXPAN	User-defined thermal expansion subroutine for Abaqus
UGENS	User-defined shell general section subroutine for Abaqus
UMAT	User-defined material subroutine for Abaqus
UMATHT	User-defined thermal material subroutine for Abaqus
VAM	Variational asymptotic method
WLF	Williams-Landel-Ferry

ABSTRACT

Polymer matrices present in composite materials are prone to have time-dependent behavior very sensitive to changes in temperature. The modeling of thermoviscoelasticity is fundamental for capturing the performance of anisotropic viscoelastic materials subjected to both mechanical and thermal loads, or for manufacturing simulation of composites. In addition, improved plate/shell and beam models are required to efficiently design and simulate large anisotropic composite structures. Numerical models have been extensively used to capture the linear viscoelasticity in composites, which can be generalized in integral or differential forms. The hereditary integral constitutive form has been adopted by many researchers to be implemented into finite element codes, but its formulation is complex and time consuming as it is function of the time history. The differential formulation provides faster computation times, but its applicability has been limited to capture the behavior of three-dimensional thermoviscoelastic orthotropic materials.

This work extends mechanics of structure genome (MSG) to construct linear thermoviscoelastic solid, plate/shell and beam models for multiscale constitutive modeling of three-dimensional heterogeneous materials made of time and temperature dependent constituents. The formulation derives the transient strain energy based on integral formulation for thermorheologically simple materials subject to finite temperature changes. The reduced time parameter is introduced to relate the time-temperature dependency of the anisotropic material by means of master curves at reference conditions. The thermal expansion creep is treated as inherent material behavior. Exact three-dimensional thermoviscoelastic homogenization solutions are also formulated for laminates modeled as an equivalent, homogeneous, anisotropic solid. The new model is implemented in SwiftComp$^{\text{TM}}$, a general-purpose multiscale constitutive modeling code based on MSG, to handle real heterogeneous materials with arbitrary microstructures, mesostructures or cross-sectional shapes.

Three-dimensional representative volume element (RVE) analyses and direct numerical simulations using a commercial finite element software are conducted to verify the accuracy of the MSG-based constitutive modeling. Additionally, MSG-based plate/shell results are validated against thin-ply high-strain composites experimental data showing good agreement.

Numerical cases with uniform and nonuniform cross-sectional temperature distributions are studied. The results showed that unlike MSG, the RVE method exhibits limitations to properly capture the long-term behavior of effective coefficients of thermal expansion (CTEs) when time-dependent constituent CTEs are considered. The analyses of the homogenized properties also revealed that despite the heterogeneous nature of the composite material, from a multiscale analysis perspective, the temperature dependencies of the effective stiffness and thermal stress properties are governed by the same shift factor as the polymer matrix. This conclusion remains the same for MSG-based solid, plate/shell and beam models with uniform temperature distributions.

1. INTRODUCTION

1.1 Background and Motivation

Fiber reinforced composites are increasingly being used in high-performance structures and aerospace applications such as light weight components, additively manufactured composite tools ([1], [2]) such as the one shown in Figure 1.1, deployable booms, solar sails or space antennas [3]. These structures need to withstand certain mechanical loads under wide temperature variations and operate for long periods of time. Polymer matrices present in composite materials are prone to have time-dependent behavior very sensitive to changes in temperature. Creep happens when a viscoelastic material is exposed to quasi-static persistent stresses and stress changes which may lead to a reduction of the load bearing capacity of the material and energy dissipation [4]. In case strains are applied instead of stresses, the phenomenon is called relaxation. This time-dependent behavior is significantly influenced by the environmental conditions such as temperature, mechanical loads, or a combination of both [3].

Figure 1.1. An additively manufactured composite tool (also presented in Ref. [1]).

During the thermal cure cycle of a composite, two types of shrinkage appear, including thermal shrinkage and chemical shrinkage. The thermal shrinkage is due to the thermal deformation during heating and cooling of the composite and it is represented by means of the coefficients of thermal expansion (CTEs). The chemical shrinkage is caused by the reduction in the resin volume. In case of thermoset resins, the chemical shrinkage depends on the progression of the degree of cure (DOC). For thermoplastic resin, it is function of the crystallization and it can be expressed as a function of the degree of crystallinity (DOC).

Since the deformation is restrained in composite materials, residual stresses appear due to the process-induced chemical shrinkage and thermal shrinkage. The thermomechanical anisotropy leads to the manifestation of residual stresses at both macroscopic and microscopic levels. At microscopic level, the residual stresses may provoke matrix cracking as well as fiber-matrix debonding; at macroscopic level, they are detrimental for the dimensional stability of the product, fatigue life of the part and yield strength [5]. Once the composite part is removed from the tool, the presence of residual stresses in the part generates undesired distortions that provoke geometrical deviations with respect to manufacturing tolerances. These distortions are mitigated following a mold compensation strategy that often relies on numerical models based on the finite element method.

In general, the higher the shrinkage strain of the resin, the higher is the residual stress [6]. Although the residual stresses can be beneficial under certain circumstances, they are in general detrimental and undesired on-dominated transverse loading, depending on the magnitude of the residual stress and the material strength. However, for pure shear loading and compression-dominated transverse loading, the residual stress is always detrimental [6].

If thermoelastic analysis is used instead of thermoviscoelastic analysis (see Figure 1.2), the former will give a reasonable prediction of the dimensional stability of the final shape of the de-tooled part. However, the absolute deformation and the residual stress levels will be inaccurate ([7], [8]). The thermoelastic type of analysis does not account for the time-dependence of the material properties and thus, no effect of the cooling rate on the dimensional stability will be predicted. A thermoelastic approach can be used to obtain initial estimation of internal stresses, but it will tend to provide over-estimations since it ignores relaxation [9]. In other words, the thermoelastic model accounts for the generation of the strains but the relaxation of the stresses will not be considered. Once the composite processing is completed, the residual stress tends to relax to a constant value [7]. It is noted that the proper prediction of the internal stress state is essential for accurate initial failure and fatigue analyses of composite materials. Albeit the stress state obtained from a thermoelastic analysis could be more conservative as it neglects relaxation, it could lead to the design of heavier composite materials due to not predicting properly the initial stress states for the performance analysis.

One of the main challenges of thermoviscoelastic analysis compared to thermoelastic analysis is that the number of variables required to characterize the material can be high and thus, increase the experimental work. Thermoviscoelastic analysis can also require significant amount of storage space and computation time if conventional analysis is considered. For instance, if the material is orthotropic, nine independent stiffness matrix components need to be defined, which in turn also requires the expensive characterization of nine independent master curves at the lab [10]. Stiffness components could also have significantly different temperature dependencies and require their independent characterization. This is even more time-consuming if some material behavior simplifications such as thermorheologically simple materials are not assumed. Furthermore, it is not trivial to experimentally characterize several components like off-axis stiffness components in relaxation experiments [11]. These facts lead to adoption of accurate and efficient multiscale approaches to generate the required equivalent microscale, mesoscale, and macroscale thermoviscoelastic properties. Indeed, the necessity to improve the homogenization process of highly filled composite materials has been identified by other researches ([10], [12]).

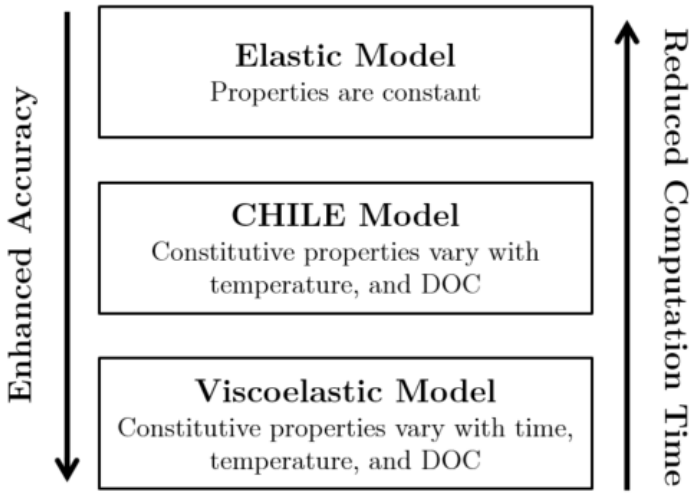

Figure 1.2. Different fidelity levels of constitutive modeling (adapted from Ref. [13]).

In case of thin-ply high-strain composites (TP-HSC) technology, it is more widely being adopted for high-performance aerospace applications such as flexible composites for morphing wings and deployable space structures like solar sails, deployable booms or space antennas [3] (see Figure 1.3). TP-HSC are made of thin laminae, which are approximately 0.02 to 0.1 mm

thick, and are thermally more stable than traditional space-rated metals [14]. In addition, some of their main advantages are that they offer excellent packaging properties, low-cost, lightweight, higher resistance to material failure by delamination, resistance to microcracking, improved aging and fatigue resistance, and improved damage tolerance to manufacturing imperfections ([15], [16]). These space structures can be stored after launch for years before deployment and thus, are designed to operate for long periods of time and withstand certain mechanical loads under wide range of temperature variations and sometimes under extreme conditions. However, the changes in temperature for long periods of time can affect the material properties of the polymer matrices present in composite materials. The relaxation of the polymer matrix can indeed lead to an unsuccessful deployment, and their short-term and long-term durability, thermal stability as well as structural integrity are a source of great concern ([14], [17]). The success of a mission can be compromised by the reduction of the bending stiffness and an incomplete recovery of the structural shape caused by the relaxation of the matrix ([18], [19]). In case of thermal effects, three types of thermally induced motions namely thermal snap, thermally induced vibrations, and thermally induced flutter, which provoke thermal-mechanical iterations and attitude disturbances have been observed in flown spacecrafts [20]. Thermal snap consists of a bending deformation caused by rapidly changing temperature gradients that does not result in vibration. For this kind of applications, composite materials offer a significant advantage over metals as they are lightweight and thermally more stable [14]. Engineering of the coefficients of thermal expansion (CTEs) has been a key feature to increase the thermal stability of composite structures and avoid these undesired deformations [3]. The effective CTEs of these structures are controlled by selecting the adequate constituent material for the mesostructures [21]. The control over the CTEs should be more pronounced over the orientations in which the polymer matrix dominates [4] as the fiber has almost negligible coefficients of thermal expansion. This can be achieved by engineering either the microstructure (i.e. arrangement of the fibers and matrix) or the mesostructure (i.e. layup angles or lattice configurations) [22]. Therefore, improved multiscale models that also account for thermoviscoelastic behavior are fundamental for proper design and deployment planning of these structures.

Many TP-HSC structures such as deployed composite booms can be modeled using plate/shell models or beam models, thus leading to much simpler governing equations and convenient interpretation of the results. Traditional plate/shell models, however, cannot satisfactorily handle TP-HSC structures having small thicknesses because these models rely on different ad hoc assumptions such as the Kirchhoff–Love assumptions and the plane stress assumption. Plates are degenerated shells with zero initial curvatures. As far as the constitutive modeling is concerned, a MSG-based plate model can also be used for shells as long as the initial curvature is not too large [23]. In case of beam models, one has to capture the behavior associated with the eliminated two dimensions, named the cross-sectional coordinates [24], to take advantage of this geometric feature without loss of accuracy. Bearing in mind its efficiency and simplicity, beam models are often interesting to be used in system level analyses or preliminary designs. Traditional beam models, nonetheless, cannot accurately handle slender structures consisting of highly anisotropic, and heterogeneous materials such as TP-HSC because these models rely on different ad hoc assumptions such as the uniaxial stress assumption. The fully populated matrix of cross-sectional stiffness properties that capture the couplings among all forms of deformation modes are not considered with traditional methods [25], and there is a gap between existing linear thermoviscoelastic constitutive solid models and existing beam models.

(a) Lenticular boom (source [25]) (b) Hinge (source [26])

Figure 1.3. Self-deployable structures made of composite materials.

The technology developed for self-deployable space structures has encountered other commercial applications such as expeditionary structures or shelters for disaster relief scenarios, temporary infrastructure, or consumer goods such as golf shafts. In all these applications the aforementioned relaxation behavior is of great concern. Therefore, the accurate modeling of thermoviscoelasticity is fundamental for capturing the performance of anisotropic viscoelastic materials subjected to both mechanical and thermal loads that are present during the manufacturing and operations of the composite parts.

1.2 Literature Review

Earlier linear thermoviscoelastic analyses of composite materials were proposed by Hashin ([27]–[30]), Schapery ([31]–[33]), and Christensen [34]. These homogenization approaches relied on the correspondence principle ([32], [34]–[36]) and analytical models such as the self-consistent [37], Mori and Tanaka [38], and dilute solution models. Later, Park and Schapery [39] derived an efficient numerical method to convert the compliance and modulus functions among the Laplace, time, and frequency domains. Noh and Whitcomb [40] derived an analytical solution to study the behavior of symmetric and balanced laminates considering orthotropic lamina properties. Levin et al. [41] derived an analytical approach for computing the effective viscoelastic properties based on the fraction-exponential operator. Liu and Shi [42] proposed an analytical solution based on trigonometric series to capture the residual stress and deformation in flat composite laminates considering thermoviscoelastic effects.

Several authors have proposed numerical approaches to compute the effective viscoelastic stiffness of composite materials without considering the temperature effects. For instance, the homogenization of viscoelastic matrices reinforced with spherical particles was studied by several authors ([43]–[48]). The effective mechanical properties of three-phase viscoelastic composites featuring viscoelastic interphases between the matrix and spherical inclusions were predicted by Brinson et al. ([43], [44]).

Nonlinear viscoelastic composites reinforced with randomly generated spherical inclusions were studied by Lévesque et al.[45]. Muliana and Kim [46] developed a micromechanics model based on representative volume element analysis (RVE) for composites made of non-

linear viscoelastic matrix and linearly elastic spherical solids. Gusev [49] studied short fiber reinforced composites predicting their viscoelastic stiffness. Zobeiry [13] proposed a differential approach to numerically study the thermoviscoelastic behavior of composite materials, and implemented it to homogenize isotropic and transversely isotropic thermoviscoelastic media [50]. Pathan et al. [51] used numerical approaches to get the effective properties of unidirectional fiber reinforced composites (UDFRC). Tang and Felicelli [52] followed the variational asymptotic method for unit cell homogenization (VAMUCH) [53] to compute the effective viscoelastic properties of a UDFRC. Textile composites were analyzed by El Mourid et al. [54], who consider linearly viscoelastic resin with a constant Poisson's ratio and elastic yarns. Courtois et al. ([12], [55]) proposed a numerical thermoviscoelastic model to homogenize textile composites following a thermodynamics framework ([56], [57]) assuming orthotropic behavior. The epoxy resin was experimentally characterized according to the model proposed in Ref. [58], integrated in an Abaqus framework [59], and used to analyze the distortion of plates ([60], [61]).

Few authors studied the temperature-dependent viscoelastic behavior ([62], [63]) and analyzed the role of the CTEs for viscoelastic media undergoing thermal or mechanical deformations. Cai and Sun [64] simulated the thermoviscoelastic behavior of 3D braided composites and a priori assumed without mathematically proving the same time-temperature superposition principle (TTSP) relationship for the composite and for the resin. Zobeiry et al. ([13], [50]) implemented a temperature-dependent viscoelastic model into a FE software to model isotropic and transversely isotropic behaviors. Spencer and Boyer [65] experimentally observed the thermal relaxation behavior in polymer materials. Mukherjee et al. [66] experimentally found the same behavior for thin polymer films as a function of the glass-transition temperature, T_g. The thinner the polymer film, the more evident are the counter-intuitive effects of the thermal relaxation [67] and negative thermal expansivity [68]. Schapery formulated relaxation type effects occurring for the thermal expansion behavior and applied them to describe the behavior of composite materials considering the quasi-elastic approach ([33], [69]). Zocher et al. [70] derived a numerical algorithm to solve the uncoupled initial boundary value problem involving orthotropic viscoelastic media that considered the contribution of the stiffness matrix and CTEs. The relaxation of the thermal expansion behavior was also

formulated by Lakes [71]. Khan and Muliana [72] performed parametric studies of the effective time-temperature-stress-dependent CTEs for particulate composites considering that the particle and matrix constituents are temperature dependent. Cai and Sun [64] assumed a Prony series expression of the effective CTEs of braided composites to simulate the thermal expansion deformation with time. Pettermann and DeSimone followed the thermal strain approach to express CTEs in terms of Prony series and analyze the thermal expansion creep [73]. The formulation was implemented into an implicit finite element method (FEM) code under plane stress assumption.

Different cure-dependent viscoelastic models for epoxy resins have been proposed in the literature. Kim and White [74] captured the cure dependency of the composite material through the time shift factor a_T which also had temperature dependent behavior. This model has been extensively adopted in subsequent work of Kim and White ([75]–[77]) and by several other authors that modeled thermoviscoelasticity ([50], [78]–[81]). Simon et al. [82] considered the DiBenedetto equation [83] to relate the degree of cure with the glass-transition temperature T_g and to do so, they proposed to adopt the cure-dependent T_g as the reference temperature. O'Brien et al. [84] suggested to use a cure dependency stiffness of a linearly viscoelastic model. Courtois et al. ([12], [55], [58], [59]) linked the resin behavior to the thermodynamic principles and introduced the cure dependency of the resin using single convoluted integrals. In case of thermoplastic composite materials, Chapman et al. [85] introduced the Standard Linear Solid (SLS) viscoelastic constitutive model to describe the behavior of polyetheretherketone (PEEK). The model accounted for the effects of crystallinity assuming that the PEEK behaved as an isotropic material. Lawrence et al. [86] implemented the SLS model to predict the residual stress generation in a laminate.

Experimental results have also been used to validate homogenization results. A numerical time-dependent model for plain weave composites was proposed by Xuet al. [87], who later compared their predictions against uniaxial tension relaxation tests at room temperature. Nonlinear viscoelastic composites were studied by means of a numerical finite element (FE) approach by Haj-Ali and Muliana [88]. This FE approach relied on the RVE analysis. They used creep and stress relaxation data to validate their simulation results. The same finite element approach was extended to capture the behavior of thermorheologically complex

materials with time-temperature variations. The homogenized predictions were compared against experimental creep results on orthotropic laminates [63] and multi-layered composites [62]. 3D interlock woven composite structures were numerically and experimentally studied by Courtois et al. [12]. The homogenization approach assumed that the matrices were orthotropic. Temperature dependence for the mesoscale was assumed to be the same as that of the neat resin because the Arrhenius parameters of the tows were already the same as that of the neat resin [12]. To represent 3D interlock woven, they used conventional RVE analysis on a voxel mesh and applied mixed uniform boundary conditions (MUBC). It is noted that whereas MUBC and periodic boundary conditions (PBCs) led to the same elastic properties if orthotropic materials are considered ([89], [90]), MUBC provided non-trivial differences for randomly oriented fibers under macroscopic uniaxial tensile stress and using strong matrix hardening. Their 3D interlock woven voxel model also exhibited some convergence issues [12].

In the area of micromechanics of TP-HSC, little work has been published. Polymer beams and tape springs were first computationally analyzed under stowage conditions by Kwok and Pellegrino ([91]–[93]). This work was extended to composite tape springs by considering a viscoelastic model for plain weave structures ([94], [95]). Gomez-Delrio and Kwok [96] analyzed the bending of a TP-HSC plate with a simplified analytical model and a finite element simulation. They found that the results from the two models match well when a uniform distribution of curvature is assumed. Most of the research in the linear thermoviscoelastic modeling with beam elements has been focused on the experimental characterization of the bending stiffness ([97], [98]), using Euler-Bernoulli viscoelastic beam models in draping simulation of textile composites [99], or Timoshenko beam models in the frequency domain [100]. Limited work has been done in modeling TP-HSC by means of beam models.

Among commercially available simulation software, Digimat-AM© [101] supports the homogenization of temperature dependent elastic material properties and temperature dependent shrinkage behavior. It also computes homogenized thermoviscoelastic properties based on the mean-field homogenization approach, which is a semi-analytical homogenization approach [102]. To capture the warpage behavior of the material, it uses the inherent strain approach that required an experimental preprocessing to account for the material behavior

under different processing conditions. If the processing conditions and utilized material does not change, these values can be utilized in future simulations. However, if one of the parameters is changed, a new calibration is required. Moldex3D has also recently incorporated a viscoelasticity module as part of its add-on [103], but this module is limited to calculate the viscous and elastic properties of plastic materials in flow simulations. Abaqus [104] has been used to perform numerical analysis by means of representative volume elements of fiber reinforced polymer matrix composites considering the stress relaxation response ([81], [105]) or creep response [106]. For these analyses, PBCs need to be applied and only isotropic materials with time-temperature dependency can be defined using the default libraries of Abaqus [104]. The current Micromechanics Plugin for Abaqus [107] also allows to use RVE to compute homogenized properties, but the model should be manually modified to perform thermoviscoelastic analysis.

1.3 Objectives and Outline

Conventional linear thermoviscoelastic constitutive models are built upon ad hoc assumptions that limit their generalities, accuracy, and efficiency. The focus of the present work is to investigate the following three challenges related with constitutive modeling of linear thermoviscoelastic behavior.

1. Derive a thermodynamically consistent constitutive model for composite materials exhibiting linear thermoviscoelastic behavior. The constitutive model should be able to accurately capture different dependencies such as time, and temperature.

2. Predict time and temperature dependent behavior of composite solids, plates/shells, and beams.

3. Investigate the multiscale relationship of the shift function to establish links between properties and to reduce the required characterization data.

The novelty of this work relies on extending the recently discovered mechanics of structure genome (MSG) [108] to provide a complete thermoviscoelastic behavior of composites as a function of the time and temperature regardless of the heterogeneity and periodicity of

the microstructure. MSG proved to be a valid approach to capture the long-time mechanical behavior of textile composites following the quasi-elastic method for linear thermoviscoelasticity at reference temperature ([40], [95]). MSG showed the capability to overcome the limitations of the traditional approaches to model viscoelasticity in textile composites. First, MSG allowed to model a broader weave pattern spectrum as it removed the assumptions used to describe the geometry. Second, ad hoc assumptions, such as plane strain or plane stress, used in the description of the local strain and stress state that affect the accuracy of the predictions were avoided. In addition, compared to RVE analysis, MSG also allowed to handle aperiodic microstructures [109]. It is noted that RVE analysis can accurately model general microstructures as far as it is possible to apply PBCs, which implies periodicity in the three directions (i.e. $x-$, $y-$ and $z-$ directions). Nonetheless, thin textile composites are aperiodic in the thickness direction [110] and thus, their behavior is not well represented with RVE analysis. Furthermore, when analyzing some structures with complex cross sections such as triangular rollable and collapsible (TRAC) or lenticular booms [14], MSG allows to obtain effective properties from cross-sectional analysis avoiding the finite element modeling of the entire structure. In addition, anisotropic viscoelastic materials with time- and temperature-dependency are not available in most commercial finite element analysis (FEA) packages, and further efforts are required to define the properties through user-defined functions, such as the combination of Abaqus user-defined thermal material behavior (UMATHT) or user-defined material subroutine (UMAT) with user-defined thermal expansion subroutine (UEXPAN) ([73], [104], [111]).

This dissertation is arranged as follows.

Chapter 1 introduces the background and motivation of this study, a comprehensive literature review, and the objectives and outline of this study.

Chapter 2 provides a brief introduction to linear thermoviscoelasticity and presents the numerical formulations used to solve the problem. In the present study, the quasi-elastic method and the direct integration method were considered.

Chapter 3 extends the MSG theory to compute the effective properties of thermoviscoelastic media following the quasi-elastic approach. It also presents the MSG-based direct integration approach to model the global behavior of thermoviscoelastic composites by means

of solid, plate/shell, and beam elements. The formulation presented captures the effects of pointwise temperature distribution in the composite for steady-state thermoviscoelastic problems, and uniform temperature distribution for transient thermoviscoelastic problems. Exact solutions for the case of symmetric and balanced laminates were also derived.

Chapter 4 presents numerical case studies with MSG-based solid model and quasi-elastic approach. Three different composite SGs were considered to homogenize and compute the equivalent thermoviscoelastic properties. These case studies were a UDFRC, a balanced and symmetric laminate, and a textile composite. The effective engineering constants and CTEs were directly obtained from the MSG analysis and compared with 3D direct numerical simulations (DNS) for the first and third case, and with an analytical solution for the second case, respectively.

Chapter 5 describes several numerical case studies with the MSG-based shell/plate model. The first subsection explains how MSG was used to engineer the mesostructure and match the effective experimental properties of the M30S/PMT-F7 plain weave composite. In this case, a MSG-based plate/shell model with quasi-elastic approach was considered to compute the effective plate/shell properties of a $[\pm 45_{PW}]_4$ laminate and compare them against the experimental bending stiffness data provided by NASA Langley Research Center (LaRC). The second subsection presents the validation of MSG-based plate/shell model with direct integration approach. To do so, the formulation was implemented into a user-defined shell general section (UGENS) subroutine for Abaqus and compared against column bending test (CBT) data provided by NASA LaRC.

Chapter 6 presents numerical case studies with MSG-based beam model. The first subsection uses the MSG-based quasi-elastic approach to compute the effective beam stiffness properties. To demonstrate the accuracy of the MSG-based beam model, three different numerical examples were selected to homogenize and compute the equivalent beam properties. The first and the second cases consisted of both lenticular and TRAC booms with uniform temperature distributions. The third case considered both lenticular and TRAC booms with steady-state pointwise nonuniform temperature distribution. Finally, the second subsection describes the implementation of the MSG-based direct integration approach to compute the global beam behavior for lenticular and TRAC booms with uniform tempera-

ture distribution, and a lenticular boom with steady-state pointwise nonuniform temperature distribution. These latter cases were verified against 3D DNS and MSG-based plate/shell model with direct numerical approach showing excellent agreement.

Chapter 7 outlines the main conclusions and contributions of this research work, as well as areas of future work to improve upon the current research.

Appendix A first briefly presents the formulation required to describe the behavior of thermoset and thermoplastic composites. It also summarizes the material data used for the numerical cases of this dissertation. Most of these data were found in the literature. However, experimental data of the PMT-F7 toughened epoxy resin were provided by NASA LaRC and compared in this appendix against the one available in the literature.

Appendix B complements the formulation of the direct integration approach presented in Chapter 3 by providing more detailed steps for its derivation.

Appendix C briefly explains the software development carried out as part of this dissertation. Since the viscoelastic and thermoviscoelastic homogenization capabilities developed in this dissertation were added to SwiftComp$^{\text{TM}}$ [112], the Abaqus SwiftComp GUI [113] was accordingly updated to accommodate these new capabilities.

2. THERMOVISCOELASTICITY

This chapter introduces the linear thermoviscoelastic theory. It also describes the solution methods used to solve the problem which in the present study are the quasi-elastic (QE) method and direct integration (DI) method.

2.1 Introduction

Following the Boltzmann superposition principle and assuming that there is no previous strain history prior to $t = 0$, a thermodynamically valid expression to describe the three-dimensional constitutive equation for a general anisotropic linear thermoviscoelastic non-aging material reads as ([32], [69]–[71])

$$\sigma_{ij}(t) = \int_0^t \left[C_{ijkl}(T, t-\tau)\dot{\varepsilon}_{kl}(\tau) + \beta_{ij}(T, t-\tau)\dot{\theta}(\tau) \right] d\tau \tag{2.1}$$

where $\sigma_{ij}(t)$ are the instantaneous stress components, T is the temperature, t is time, $C_{ijkl}(T,t)$ is the stress relaxation stiffness tensor which is function of temperature and time, $\dot{\varepsilon}_{kl}$ is the strain rate tensor, $\dot{\theta}(\tau)$ is the temperature change rate from a stress free starting temperature, and $\beta_{ij}(T,t)$ is the instantaneous thermal stress tensor. The term C_{ijkl} represents the fourth-order tensor of relaxation moduli relating stress to strain, and β_{ij} stands for the second-order tensor of relaxation moduli relating stress to temperature change [70]. It is noted that for solid elements the CTEs can be calculated as $\alpha_{ij}(T,t) = -\Big(C_{ijkl}(T,t)\Big)^{-1}\beta_{kl}(T,t)$.

If we assume that the material is thermorheologically simple, the effects on the material properties caused by temperature changes are equivalent to the effects caused by changes in the time scale [114]. In general viscoelastic materials each molecular transition is associated with a relaxation mechanism, but thermorheologically simple materials only show one dominant molecular transition [115], which in turn implies that the same sequence of molecular processes is always present in similar deformations at different temperatures [116]. For thermorheologically simple materials, the time-temperature superposition principle (TTSP) [117] applies as the material tested at a higher temperature shows the same mechanical be-

havior as if it was tested over a significant longer period of time. Most amorphous polymers with only one major molecular transition around the glass transition temperature T_g behave as thermorheologically simple materials [115]. Based on the thermorheologically simple material assumption, we can define a reduced time parameter ξ for all the components of C_{ijkl} as [70]

$$\xi(t) = \int_0^t \frac{ds}{a_T(T)} \tag{2.2}$$

where a_T is the shift factor depending on the temperature. The corresponding value of real time t can be found for each value of reduced time ξ and vice versa [118]. The shift factor represents a property that embodies the material temperature dependencies and can be expressed either in terms of an Arrhenius or Williams-Landel-Ferry (WLF) equation as ([10], [70])

$$\begin{cases} \log a_T = \frac{E_a}{\ln 10 R}\left(\frac{1}{T} - \frac{1}{T_0}\right) & T < T_g(X) \\ \log a_T = \frac{-C_1(T-T_0)}{C_2+(T-T_0)} & T \geq T_g(X) \end{cases} \tag{2.3}$$

where E_a represents the activation energy expressed with unit J/mol, R stands for the universal gas constant equal to 8.314 J/K/mol, C_1 and C_2 are material constants adjusted from experimental data, and T_0 stands for reference temperature at which the master curve was defined. More details of the shift function for both thermoset and thermoplastic composites are presented in Appendix A.1. In general, albeit the composite material is viscoelastic in nature, the viscoelastic behavior of the matrix has proved to determine the shift factor that expresses the temperature dependencies of effective Young's moduli, shear moduli, and Poisson's ratios of the composites for one-step homogenization [119].

The stress, strain, and temperature change values of the real time can be used to replace their corresponding values of the reduced time domain as ([31], [118], [120])

$$\begin{aligned} \sigma_{ij}(\xi) &\equiv \sigma_{ij}(\xi(t)) \equiv \sigma_{ij}(t) \\ \varepsilon_{ij}(\xi) &\equiv \varepsilon_{ij}(\xi(t)) \equiv \varepsilon_{ij}(t) \\ \dot{\theta}(\xi) &\equiv \dot{\theta}(\xi(t)) \equiv \dot{\theta}(t) \end{aligned} \tag{2.4}$$

and similarly [71]

$$C_{ijkl}(T_0,\xi) \equiv C_{ijkl}(T,t) \qquad \beta_{ij}(T_0,\xi) \equiv \beta_{ij}(T,t) \tag{2.5}$$

Hence, using Eqs. (2.2)-(2.5), Eq. (2.1) can be simplified to be a thermodynamically valid expression for a thermorheologically simple material as [32]

$$\sigma_{ij}(t) = \int_0^t \Big[C_{ijkl}\left(T_0, \xi(t) - \xi(\tau)\right) \dot{\varepsilon}_{kl}(\tau) + \beta_{ij}\left(T_0, \xi(t) - \xi(\tau)\right) \dot{\theta}(\tau) \Big] d\tau \tag{2.6}$$

2.2 Solution Methods

The complete set of homogenized thermoviscoelastic properties can be computed following the quasi-elastic method, correspondence principle, and direct time integration of the incremental viscoelastic equations [40]. Schapery ([31], [32], [121]) proposed the quasi-elastic (QE) method to use the elastic approach to homogenize a viscoelastic composite by considering the time-dependent relaxation moduli as the replacement of the elastic constants. It is the simplest approach to determine the effective relaxation moduli ([95], [110]) but it does not assure the accuracy of the local stress field for a general strain input [40]. The correspondence principle is a classical method to solve the boundary value problem in the linear theory of viscoelasticity. An integral transform is applied to the field equations and boundary conditions, transforming them from time domain to Laplace domain [35]. Then, the solution of the original problem is reduced to transform inversion if an elastic solution compatible with the transformed boundary conditions exists. This methodology guarantees the accuracy of the results only if the inversion to the time domain is successful [40]. It is not a valid approach when the boundaries are time-dependent as the boundary conditions cannot be transformed [31]. The direct time integration (DI) with the incremental stress form considers time marching procedure. The constitutive relation can be represented by a recursive form in which the stresses and strains in the current state are affected by the stress history of the previous steps ([120], [122]). The three methods agree well in terms of computing homogenized values [40], but in this work only the QE and DI approaches will be used. The correspondence principle is not considered because the computational efficiency of

this method is limited and the applications are constrained as it required to first transform to the Laplace domain, solve the problem in the this domain and then, and carry out the inverse transform to the real time domain. The forward and backward transformation must exist for this method to work.

2.2.1 Quasi-Elastic Method

Schapery ([31], [32], [121]) derived the QE method applying the direct method of inversion to the correspondence principle. The detailed derivation to prove validity and guarantee the thermodynamic consistency of the QE formulation to describe time- and temperature-dependent media can be found in Schapery's work ([31], [32]). In the formulation, the derivation was focused on the mechanical behavior without temperature effects and then, the results found were applied to study some viscoelastic problems with temperature changes. This section complements the derivation presented by Schapery [32] extending the derivation of the QE method to thermoviscoelastic thermorheologically simple media withstanding temperature changes. The thermal expansion creep is treated as inherent material behavior. However, when the formulation includes the thermal effects through CTEs and temperature dependent stiffness properties, Schapery's derivation [31] should be considered. The formulation here developed is later linked with the transient strain energy $U(t)$ required to formulate MSG-based QE method presented in section 3.2.

If we assume that the thermoset composite material has a fixed degree of cure value or analogously that the thermoplastic composite material has a fixed degree of crystallinity, the relaxation functions of $C_{ijkl}(T_0,\xi)$ and $\beta_{ijkl}(T_0,\xi)$ from Eq.(2.6) can be expressed in an exponential series form as [32]

$$\begin{aligned} C_{ijkl}(T_0,\xi) &= C_{ijkl,\infty} + \sum_{s=1}^{n} C_{ijkl,s} \exp\left(-\frac{\xi}{\lambda_s}\right) \\ \beta_{ij}(T_0,\xi) &= \beta_{ij,\infty} + \sum_{s=1}^{n} \beta_{ij,s} \exp\left(-\frac{\xi}{\lambda_s}\right) \end{aligned} \tag{2.7}$$

where $C_{ijkl,\infty}$ and $\beta_{ij,\infty}$ are the long-term properties, $C_{ijkl,s}$ and $\beta_{ij,s}$ stand for the Prony series coefficients, and λ_s are the discrete stress relaxation times.

Following the correspondence principle, the constitutive equation expression given by Eq. (2.6) is very similar to the ones of the elastic media when they are Laplace transformed. For thermorheologically simple materials with transient temperature, it is advantageous to take the Laplace transform of Eq. (2.6) with respect to the reduced time ξ [32]. The Laplace transform with respect to the reduced time is given by

$$\hat{f} = \hat{f}(p) \equiv \int_0^\infty f(\xi) \exp(-p\xi) d\xi \tag{2.8}$$

which is used to Laplace transform Eq. (2.6) into [32]

$$\hat{\sigma}_{ij} = \tilde{C}_{ijkl}\hat{\varepsilon}_{kl} + \tilde{\beta}_{ij}\hat{\theta} \tag{2.9}$$

where the operational moduli $\tilde{C}_{ijkl}$ and $\tilde{\beta}_{ij}$ read as

$$\begin{aligned} \tilde{C}_{ijkl} \equiv p\hat{C}_{ijkl} = C_{ijkl,\infty} + \sum_s \frac{pC_{ijkl,s}}{p + 1/\lambda_s} \\ \tilde{\beta}_{ij} \equiv p\hat{\beta}_{ij} = \beta_{ij,\infty} + \sum_s \frac{p\beta_{ij,s}}{p + 1/\lambda_s} \end{aligned} \tag{2.10}$$

Therefore, the transformed constitutive Eq. (2.9) is formally equivalent to the constitutive equation for an anisotropic elastic media with $\tilde{C}_{ijkl}$ and $\tilde{\beta}_{ij}$ as the material properties. When temperature is transient but changes slowly enough that it is spacewise constant, an expression in the Laplace domain equivalent to the Helmholtz free energy in a thermoelastic body [29] can be found as well [32]. For that, all the variables should be transformed with respect to the reduced time given by Eq. (2.8).

Once the associated elastic solution is solved in the Laplace domain, the Laplace transform inversion should be applied to the elastic results to find the solution in the time domain. In the derivation of the QE method, Schapery proposed to use the direct method to compute the inverse [31]. The direct method is an approximate inversion technique that enables a direct relationship between the transformed solutions and the time-dependent domain. It provides an accurate approach when the surface tractions and displacements are step function applied at $t = 0$, and realistic relaxation moduli are used. It is noted that the step

function inputs are used for the RVE analysis of linear viscoelastic composite materials to compute the effective properties ([52], [110]).

If $f(\xi)$ has small curvature when plotted against $\log \xi$, then [123]

$$p\hat{f} \simeq [f(\xi)]_{\xi=\frac{1}{2p}} \tag{2.11}$$

which is an exact solution if $f(\xi)$ is proportional to $\log \xi$. To apply the direct inversion method, the equivalent form of Eq. (2.11) reads as

$$f(\xi) \simeq \left[p\hat{f}\right]_{p=\frac{1}{2\xi}} \tag{2.12}$$

If the variation of the operational moduli $\tilde{C}_{ijkl}$ and $\tilde{\beta}_{ijkl}$ are spread smoothly over several decades of p, the small curvature condition is met ([123], [32]). Then, it is possible to relate $p\hat{f}$ with the operational moduli $\tilde{C}_{ijkl}$ and $\tilde{\beta}_{ijkl}$ to obtain the transformed solution as [32]

$$p\hat{f} = C_{\mathrm{e}1} f_{\mathrm{e}1}\left(\tilde{C}_{ijkl}\right) + C_{\mathrm{e}2} f_{\mathrm{e}2}\left(\tilde{\beta}_{ij}\right) \tag{2.13}$$

where $C_{\mathrm{e}1}$ and $C_{\mathrm{e}2}$ are timewise constants, and the right side represent the response of an thermoelastic body with elasticity tensor and thermal stress tensor equal to $\tilde{C}_{ijkl}$ and $\tilde{\beta}_{ij}$, respectively. Since $\tilde{C}_{ijkl}$ and $\tilde{\beta}_{ij}$ represent the p-transforms of relaxation moduli, substituting Eq. (2.10) into Eq. (2.11)

$$\begin{aligned} \tilde{C}_{ijkl} \equiv p\hat{C}_{ijkl} &\simeq [C_{ijkl}(T_0,\xi)]_{\xi=\frac{1}{2p}} \\ \tilde{\beta}_{ij} \equiv p\hat{\beta}_{ij} &\simeq [\beta_{ij}(T_0,\xi)]_{\xi=\frac{1}{2p}} \end{aligned} \tag{2.14}$$

Then, Eq. (2.12) is applied to the transformed solution in Eq. (2.13) and the result of Eq. (2.14) is substituted, it reads as

$$\begin{aligned} f(\xi) &\simeq \left[C_{\mathrm{e}1} f_{\mathrm{e}1}\left(\tilde{C}_{ijkl}\right) + C_{\mathrm{e}2} f_{\mathrm{e}2}\left(\tilde{\beta}_{ij}\right)\right]_{p=\frac{1}{2\xi}} \\ &\simeq C_{\mathrm{e}1} f_{\mathrm{e}1}\left(C_{ijkl}(T_0,\xi)\right) + C_{\mathrm{e}2} f_{\mathrm{e}2}\left(\beta_{ijkl}(T_0,\xi)\right) \end{aligned} \tag{2.15}$$

where rather than the convolution type expressions of Eq. (2.6), Eq.(2.15) represents the solution of a thermoelastic body whose constitutive equation reads as

$$\sigma_{ij} = C_{ijkl}(T_0, \xi)\varepsilon_{ij} + \beta_{ij}(T_0, \xi)\theta \tag{2.16}$$

In summary, the QE method allows the approximation of a viscoelastic solution by an elastic solution replacing the elastic constants with time-dependent viscoelastic properties [32]. For thermorheologically simple media with time- and temperature-dependent properties, thermoviscoelastic properties in the reduced time domain should be used to replace the thermoelastic properties. For MSG formulation, the thermoviscoelastic solution of $U(t)$ is approximated by a thermoelastic solution replacing the thermoelastic constants with time-dependent thermoviscoelastic properties.

To complete the basic three-dimensional equations needed for the linear thermoviscoelastic problem, the kinematics contains three displacements u_1, u_2, u_3 and six strains ε_{11}, ε_{22}, ε_{33}, ε_{23}, ε_{13}, ε_{12}, which are all functions of the three coordinates x_1, x_2, x_3, and time t. The strain-displacement relationships are given as [32]

$$\varepsilon_{ij} = \frac{1}{2}\left(\frac{\partial u_i}{\partial x_j} + \frac{\partial u_j}{\partial x_i}\right) \tag{2.17}$$

For the kinetics, the stresses are governed by the following equilibrium equations [32]

$$\frac{\partial \sigma_{ij}}{\partial x_j} + F_i = 0 \tag{2.18}$$

where F_i are the components of a prescribed body force vector. It is noted that the six stresses are also functions of x_1, x_2, x_3, and t [32].

The constitutive equations have been written in terms of both the real time t (see Eq. (2.1)) and the reduced time ξ (see Eq. (2.6)). The constitutive equations are better suited for some applications when ξ is used and hence, it may be interesting to rewrite the strain-displacement and equilibrium equations in terms of x_i and ξ. Let us define f to represent

either u_i or σ_i in Eqs. (2.17) and (2.18), respectively. The original variables x_i and t are transformed to the new variables $\hat{x}_i$ and ξ as

$$\hat{x}_i = x_i \quad \xi = \xi(x_i, t) = \int_0^t \frac{ds}{a_T[T(x_i, s)]} \tag{2.19}$$

where it is assumed that the temperature is also function of x_i. Then, if f is derived

$$\frac{\partial f}{\partial x_i} = \frac{\partial f}{\partial \hat{x}_i}\frac{\partial \hat{x}_i}{\partial x_i} + \frac{\partial f}{\partial \xi}\frac{\partial \xi}{\partial x_i} = \frac{\partial f}{\partial x_i} + \frac{\partial f}{\partial \xi}\frac{\partial \xi}{\partial x_i} \tag{2.20}$$

Consequently, if Eqs. (2.17) and (2.18) are used together with Eq. (2.6), all the spatial derivatives should be changed to [32]

$$\frac{\partial}{\partial x_i} \rightarrow \frac{\partial}{\partial x_i} + \frac{\partial \xi}{\partial x_i}\frac{\partial}{\partial \xi} \tag{2.21}$$

However, if the temperature is spacewise constant or has a steady-state distribution, the second-term on the right-hand side of Eq. (2.21) vanishes and hence, the original form of the strain-displacement and equilibrium equations are recovered.

2.2.2 Direct Integration Method

In the recursive method, due to the nonlinear dependency between the stresses and strains of the composite material, the analysis is presented as incremental [40]. Therefore, the current stress state is affected by the previous stress state [120]. Using Eq. (2.6), the stress increment due to a time increment Δt reads as

$$\begin{aligned}
\Delta\sigma_{ij}(t) = \sigma_{ij}(t+\Delta t) - \sigma_{ij}(t) = \int_t^{t+\Delta t} \Big[& C_{ijkl}(T_0, \xi(t+\Delta t) - \xi(\tau))\dot{\varepsilon}_{kl}(\tau) \\
& + \beta_{ij}(T_0, \xi(t+\Delta t) - \xi(\tau))\dot{\theta}(\tau) \Big] d\tau \\
+ \int_0^t \Big[& C_{ijkl}(T_0, \xi(t+\Delta t) - \xi(\tau))\dot{\varepsilon}_{kl}(\tau) + \beta_{ij}(T_0, \xi(t+\Delta t) - \xi(\tau))\dot{\theta}(\tau) \Big] d\tau \\
- \int_0^t \Big[& C_{ijkl}(T_0, \xi(t) - \xi(\tau))\dot{\varepsilon}_{kl}(\tau) + \beta_{ij}(T_0, \xi(t) - \xi(\tau))\dot{\theta}(\tau) \Big] d\tau
\end{aligned} \tag{2.22}$$

If small time increments are considered, we can assume that the strain rate $\dot{\varepsilon}_{kl}(\tau)$ and temperature change rate $\dot{\theta}(\tau)$ are kept constant during each time increment Δt ([120], [122]). Then Eq. (2.22) reads as

$$\Delta\sigma_{ij}(t) = M_{ijkl}(T_0,\xi)\Delta\varepsilon_{kl}(t) + \eta_{ij}(T_0,\xi)\Delta\theta(t) + \Omega_{ij}(T_0,\xi) \tag{2.23}$$

where

$$M_{ijkl}(T_0,\xi) = \frac{1}{\Delta t}\int_t^{t+\Delta t} C_{ijkl}(T_0,\xi(t+\Delta t)-\xi(\tau))d\tau \tag{2.24}$$

$$\eta_{ij}(T_0,\xi) = \frac{1}{\Delta t}\int_t^{t+\Delta t} \beta_{ij}(T_0,\xi(t+\Delta t)-\xi(\tau))d\tau \tag{2.25}$$

$$\begin{aligned}\Omega_{ij}(T_0,\xi) = \int_0^t \Big[& C_{ijkl}(T_0,\xi(t+\Delta t)-\xi(\tau))\dot{\varepsilon}_{kl}(\tau) \\ & +\beta_{ij}(T_0,\xi(t+\Delta t)-\xi(\tau))\dot{\theta}(\tau)\Big]d\tau \\ -\int_0^t \Big[& C_{ijkl}(T_0,\xi(t)-\xi(\tau))\dot{\varepsilon}_{kl}(\tau) + \beta_{ij}(T_0,\xi(t)-\xi(\tau))\dot{\theta}(\tau)\Big]d\tau\end{aligned} \tag{2.26}$$

where $M_{ijkl}(T_0,\xi)$, and $\eta_{ij}(T_0,\xi)$ given in Eqs. (2.24)-(2.25) represent the instantaneous effective tangent stiffness matrices of the properties represented by $C_{ijkl}(T_0,\xi)$ and $\beta_{ij}(T_0,\xi)$ [124]. The viscoelastic problem is completed by six strain-displacement relations of Eq. (2.17) and the three equilibrium equations given by Eq. (2.18).

3. MSG THERMOVISCOELASTIC FORMULATION

This chapter extends the MSG theory to compute the effective properties of thermoviscoelastic media and model its global behavior by means of solid, Kirchhoff-Love plate/shell and Euler-Bernoulli beam models. The QE approach was implemented in SwiftComp^{TM} to compute the effective thermoviscoelastic properties as it is the most efficient approach. However, the QE approach does not properly capture the residual stresses and strains for a general loading case [125]. Therefore, to solve the global linear thermoviscoelastic problem and accurately predict the residual stresses and strains, MSG-based solid, Kirchhoff-Love plate/shell and Euler- Bernoulli beam models using DI method were formulated. The effects of pointwise temperature distributions in the composite for steady-state thermoviscoelastic problems and uniform temperature distribution for transient thermoviscoelastic problems are captured with the present formulation. Exact solutions were also derived for the simple case of symmetric and balanced laminates.

3.1 The Concept of Structure Gene

Mechanics of structure genome (MSG) has been developed to provide a unified theory for multiscale and multiphysics constitutive modeling for all types of composite structures including 3D structures, plates/shells, and beams by Yu ([108], [126]). MSG provides a general-purpose micromechanics theory when it is specialized to constitutive modeling of 3D structures [127].

Structural properties in terms of microstructures can be predicted with different MSG models. Homogenized beam, plate/ shell, and 3D properties can be computed from the analysis domain of MSG, known as structure gene (SG). SG is defined as the *smallest mathematical* building block of the structure and the word *gene* is used to accentuate the fact that it contains all the constitutive information needed for a structure in the same fashion as the gene contains all the intrinsic information for an organism's growth and development. For 3D bodies, SG has a similar role as RVE or unit cell (UC) concept in micromechanics (Figure 3.1). However, they are significantly different. For example, if we assume that a composite laminate is made of homogeneous layers, it features 1D heterogeneity (see Fig-

ure 3.1a) and hence, the SG will be the transverse normal line with segments denoting the corresponding layers. One can mathematically repeat this straight line in-plane to build the composite laminate. The constitutive modeling over the 1D SG can compute the complete set of 3D properties and local fields. Such applications of SG are not equivalent to RVE. For a structure made of composites featuring 2D heterogeneity (e.g. continuous unidirectional fiber reinforced composites, Figure 3.1b), the SG will be a 2D domain. Although 2D RVEs are also used in micromechanics, only in-plane properties and in-plane local fields can be obtained from a common RVE analysis. In this case, if the complete set of properties are needed for a 3D structural analysis, a 3D RVE is usually required ([128], [129]), while a 2D domain is sufficient if it is modeled using MSG (Figure 3.1b). For a structure made of composites featuring 3D heterogeneity (e.g. particle reinforced composites, Figure 3.1c), the SG will be a 3D volume. Although 3D SG for 3D structures represents the most similar case to RVE, boundary conditions in terms of displacements and tractions indispensable in the RVE analysis are not needed for micromechanics models constructed using MSG.

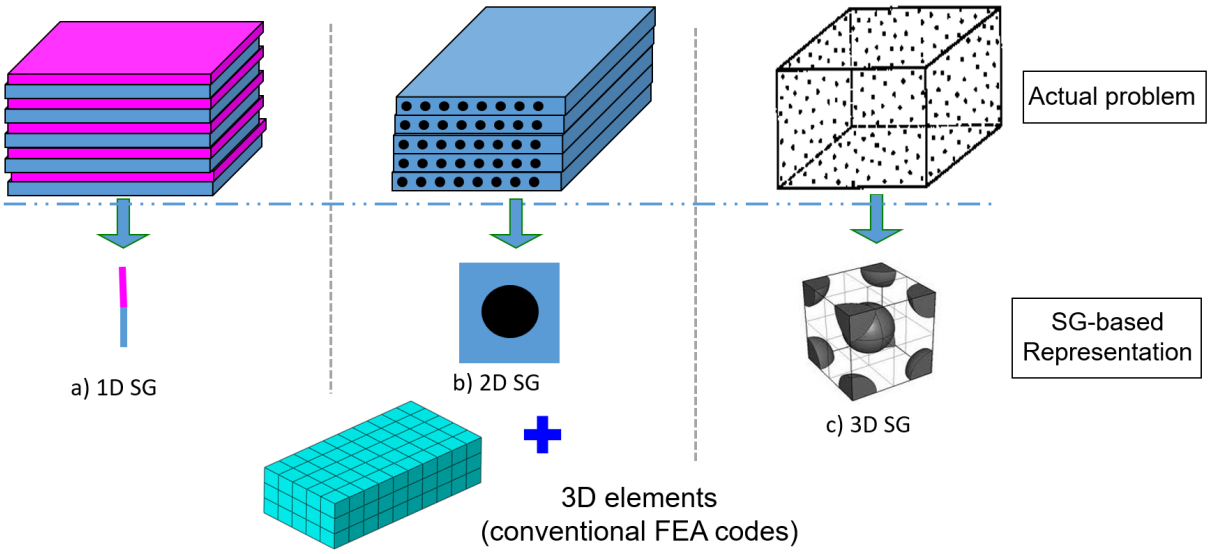

Figure 3.1. SG for 3D structures.

For plate/shell analysis, take as an example the different internal constructions shown in Figure 3.2. Their SGs can be identified based on their internal constructions. Regardless of the dimension of an SG, the constitutive modeling over the SG can always give the effective

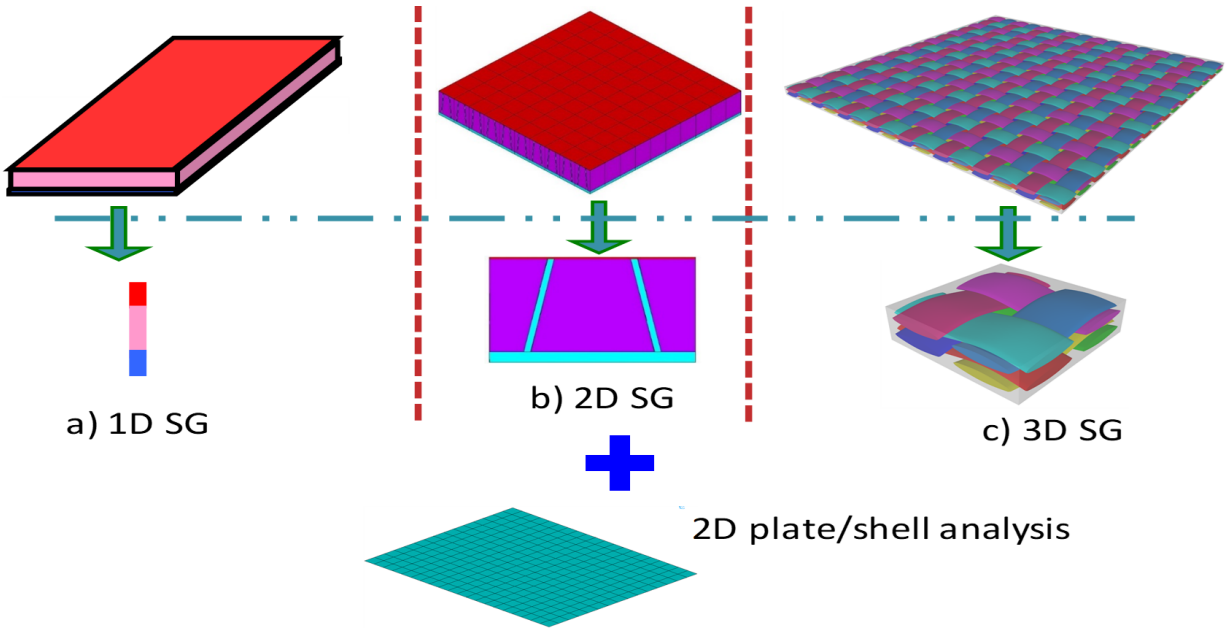

Figure 3.2. SG for 2D structures.

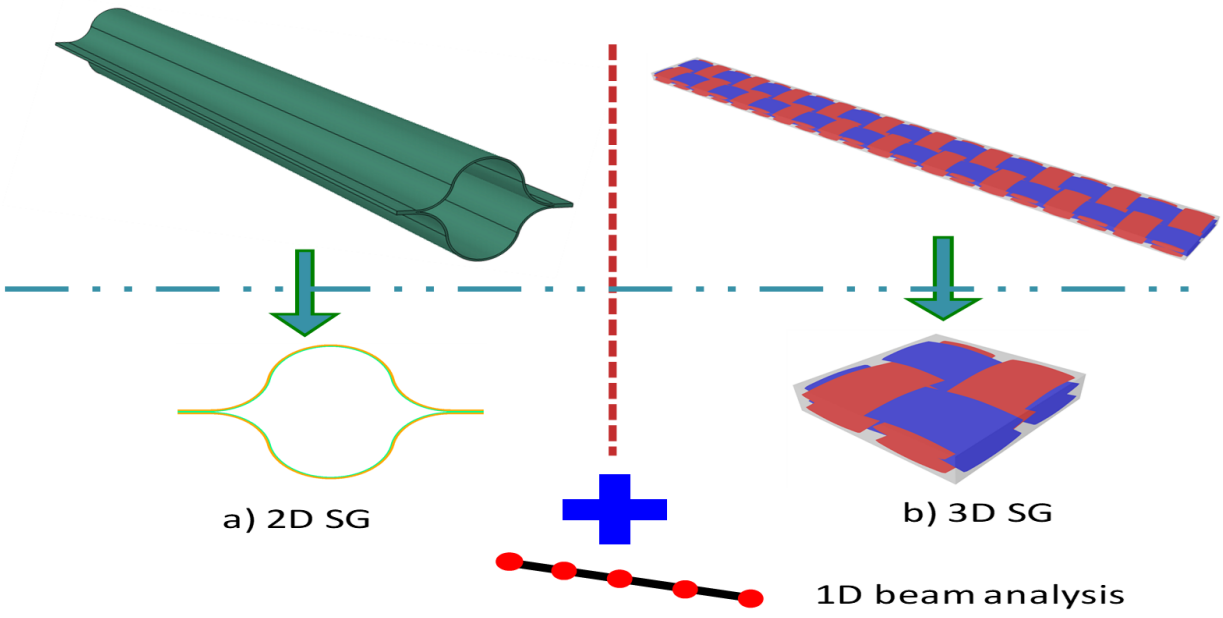

Figure 3.3. SG for 1D structures.

plate/shell properties needed by two-dimensional (2D) plate/shell analysis and the local fields in the original 3D structure. In case of beam models, such as a deployed composite boom with uniform cross sections (see Figure 3.3), its SG can simply be the cross section. The constitutive modeling over the cross section can give the effective beam properties needed by the one-dimensional (1D) beam analysis and the local fields in the original 3D structure. All in all, 1D, 2D and 3D SGs have been successfully used to provide an accurate and efficient approach to analyze many engineering structures with complex geometry made of anisotropic and/or heterogeneous materials ([130], [131]). Once the structural analysis is complete, the global structural responses can be used to recover local stress, strain, and displacement fields within the SG.

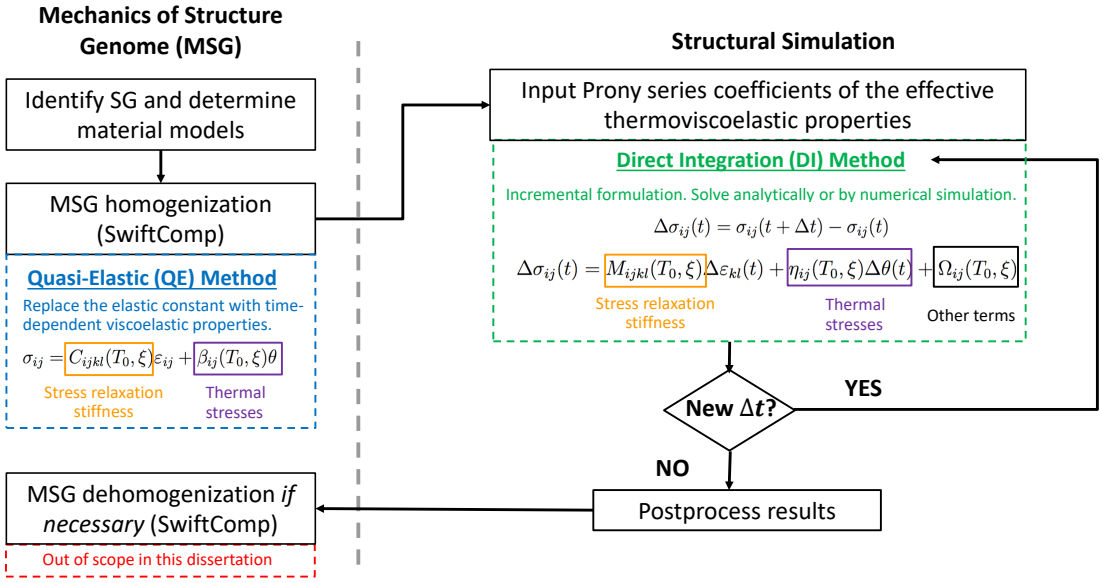

Figure 3.4. Workflow of the MSG-based thermoviscoelastic simulation framework.

The principle of minimum information loss (PMIL) is one of the kernels of MSG. It states that the homogenized model can be constructed through minimizing the information loss between the homogenized body and the original heterogeneous body. In case of a linear thermoviscoelastic material, the transient strain energy density represents this information [110] and it is valid regardless quasi-elastic (QE) method or direct integration (DI) method

are used. Figure 3.4 shows the workflow of the MSG-based simulation framework. Once the type of SG and degree of heterogeneity of the thermoviscoelastic material model are identified, the effective thermoviscoelastic properties are computed. To solve the homogenization problem, the QE method is applied within the MSG framework as it is more efficient than the DI method for computing homogenized values [40]. Subsequently, the DI method is used to solve the global composites structural problem by means of solid, plate/shells or beam models, as it accounts for residual stresses and strains for any arbitrary loading or displacement conditions [125]. The DI method requires the effective thermoviscoelastic properties computed from the homogenization step expressed by means of Prony series coefficients. Once the global problem is analytically or numerically solved, MSG can be used for dehomogenization. It is noted that the MSG-based dehomogenization for linear thermoviscoelastic materials has not been pursued in this dissertation.

3.2 Quasi-Elastic Method

The QE method allows the approximation of a viscoelastic solution by an elastic solution replacing the elastic constants with time-dependent viscoelastic properties [31]. Next, this procedure is used to construct the transient strain energy $U(t)$ of a thermoviscoelastic media with time- and temperature-dependent behavior. It is noted that for thermorheologically simple media with time- and temperature-dependent properties, the reduced time domain thermoviscoelastic properties should be used to replace the thermoelastic properties.

3.2.1 3D Solid Model

The homogenized body can be described by the global coordinate system denoted as x_i. As the size of the macroscopic structure is much larger than the size of SG, micro coordinates $y_i = x_i/\delta$ are introduced to describe the domain occupied by SG, with δ being a small parameter. The displacement field of the original heterogeneous body can be expressed in terms of that of the homogeneous body at the time t for the MSG-based solid model as

$$u_i(x_1, x_2, x_3, y_1, y_2, y_3, t) = \bar{u}_i(x_1, x_2, x_3, t) + \delta\chi_i(x_1, x_2, x_3, y_1, y_2, y_3, t) \tag{3.1}$$

with u_i standing for the displacement field of the heterogeneous body, $\bar{u}_i$ denoting the displacement of the homogenized body, and χ_i representing the difference between these two fields, which is commonly called the fluctuating function in micromechanics or warping functions in structural mechanics literature [126]. It is noted that the Latin indices used here and throughout this document assume 1, 2, and 3, and repeated indices are summed over their range except where explicitly indicated.

Then, we can express the instantaneous strain field of the linear viscoelastic body as

$$\varepsilon_{ij}(t) = \frac{1}{2}\left(\frac{\partial u_i(t)}{\partial x_j} + \frac{\partial u_j(t)}{\partial x_i}\right) \tag{3.2}$$

Dropping higher-order terms following the variational asymptotic method (VAM) [132], the instantaneous strain field of the heterogeneous body reads as

$$\varepsilon_{ij}(x, y, t) = \bar{\varepsilon}_{ij}(x, t) + \chi_{(i|j)}(t) \tag{3.3}$$

Here ε_{ij} represents the instantaneous strain field in the original heterogeneous body and $\bar{\varepsilon}_{ij} = \bar{u}_{(i,j)}$ represents the instantaneous strain field of the homogenized body. The parenthesis in subscript indicates a symmetric operation and the vertical bar indicates differentiation with respect to the micro coordinates, $\chi_{(i|j)} = \frac{1}{2}\left(\frac{\partial \chi_i(t)}{\partial y_j} + \frac{\partial \chi_j(t)}{\partial y_i}\right)$.

To construct the homogenized model out of the original heterogeneous model, the instantaneous kinematic variables of the homogenized model must be defined in terms of those of the original model. A reasonable election is to define

$$\bar{u}_i(t) \equiv \langle u_i(t) \rangle \qquad \bar{\varepsilon}_{ij}(t) \equiv \langle \varepsilon_{ij}(t) \rangle \tag{3.4}$$

where the angle brackets indicate the integration over the SG. The following constraints on the instantaneous fluctuating functions are implied from Eq. (3.4)

$$\langle \chi_i(t) \rangle = 0 \qquad \left\langle \chi_{(i|j)}(t) \right\rangle = 0 \tag{3.5}$$

where the first expression means that the averaged displacements of the homogenized and original structures over the SG are the same according to the first equation in Eq. (3.4), and the second expression represents that the averaged strains of the homogenized and original structures over the SG are the same according to the second equation in Eq. (3.4). It is noted that for MSG, the first Eq. (3.5) should be applied regardless PBCs or aPBCs are considered [109]. In the former case, PBCs can be applied to the fluctuating functions by enforcing the equality of χ_i on the corresponding periodic boundaries and the second equation of Eq. (3.5) will be automatically satisfied. In the latter case, the second expression of Eq. (3.5) should be applied for taking care of everything that it is not periodic.

Let us denote $\bar{\epsilon}(t) = [\bar{\varepsilon}_{11}(t) \;\; \bar{\varepsilon}_{22}(t) \;\; \bar{\varepsilon}_{33}(t) \;\; 2\bar{\varepsilon}_{23}(t) \;\; 2\bar{\varepsilon}_{13}(t) \;\; 2\bar{\varepsilon}_{12}(t)]$ and $\omega(t) = [\chi_1(t) \;\; \chi_2(t) \;\; \chi_3(t)]$. Then the 3D strain field of the MSG solid model can be written as

$$\Gamma(t) = \Gamma_\epsilon \bar{\epsilon}(t) + \Gamma_h \omega(t) \tag{3.6}$$

where $\Gamma(t) = [\Gamma_{11} \;\; \Gamma_{22} \;\; \Gamma_{33} \;\; 2\Gamma_{23} \;\; 2\Gamma_{13} \;\; 2\Gamma_{12}]^T$ is the strain field of the original structure, and $\omega(t)$ is the fluctuating function. Γ_ϵ is an operator matrix depending on the macroscopic structural model. If the macroscopic structural model is the 3D Cauchy continuum model, Γ_ϵ is the 6×6 identity matrix. Finally, Γ_h is an operator matrix that depends on the dimension of the SG. For 3D SG it is given as

$$\Gamma_h = \begin{bmatrix} \frac{\partial}{\partial y_1} & 0 & 0 & 0 & \frac{\partial}{\partial y_3} & \frac{\partial}{\partial y_2} \\ 0 & \frac{\partial}{\partial y_2} & 0 & \frac{\partial}{\partial y_3} & 0 & \frac{\partial}{\partial y_1} \\ 0 & 0 & \frac{\partial}{\partial y_3} & \frac{\partial}{\partial y_2} & \frac{\partial}{\partial y_1} & 0 \end{bmatrix}^T \tag{3.7}$$

In case of 2D SGs, the derivatives with respect to y_1 should be vanished in Γ_h. It is noted that the infinitesimal strain field is used to derive the operator matrix and the asymptotically smaller terms have been dropped based on VAM ([126],[132]).

3.2.2 2D Kirchhoff-Love Plate/Shell Model

The kinematics of the MSG-based Kirchhoff-Love plate/shell model accounts for the time-dependent displacement field expressed as

$$\begin{aligned} u_1(x_1, x_2, y_1, y_2, y_3, t) &= \bar{u}_1(x_1, x_2, t) - \delta y_3 \bar{u}_{3,1}(x_1, x_2, t) + \delta\chi_1(x_1, x_2, y_1, y_2, y_3, t) \\ u_2(x_1, x_2, y_1, y_2, y_3, t) &= \bar{u}_2(x_1, x_2, t) - \delta y_3 \bar{u}_{3,2}(x_1, x_2, t) + \delta\chi_2(x_1, x_2, y_1, y_2, y_3, t) \\ u_3(x_1, x_2, y_1, y_2, y_3, t) &= \bar{u}_3(x_1, x_2, t) + \delta\chi_3(x_1, x_2, y_1, y_2, y_3, t) \end{aligned} \tag{3.8}$$

where $\bar{u}_i$ are the displacements of the homogenized plate structure. The comma in the subscript express differentiation with respect to macro-coordinates x_i.

The plate/shell strain measures can be defined as

$$\begin{aligned} \epsilon_{\alpha\beta}(x_1, x_2, t) &= \frac{1}{2}\left(\bar{u}_{\alpha,\beta}(t) + \bar{u}_{\beta,\alpha}(t)\right) \\ \kappa_{\alpha\beta}(x_1, x_2, t) &= -\bar{u}_{3,\alpha\beta}(t) \end{aligned} \tag{3.9}$$

where $\epsilon_{\alpha\beta}(x_1, x_2, t)$ stand for the instantaneous in-plane strains, and $\kappa_{\alpha\beta}(x_1, x_2, t)$ denote the instantaneous curvature strains. where the double digits after the comma in the subscript indicate the second derivatives with respect to the macro-coordinates.

In case of the fluctuating functions, the MSG-based plate model only needs to satisfy the following constraints on the instantaneous fluctuating functions $\chi_i(t)$ as

$$\langle \chi_i(t) \rangle = 0 \tag{3.10}$$

It should be pointed out that in-plane periodicity is also enforced for $\chi_i(t)$. Additional constraints can be added as needed depending on the periodicity of the SG.

The asymptotically smaller terms can be dropped based on VAM. Then the 3D strain field of the MSG plate/shell model can be written as

$$\Gamma(t) = \Gamma_\epsilon \bar{\epsilon}(t) + \Gamma_h \omega(t) \tag{3.11}$$

where $\bar{\epsilon}$ is the generalized plate/shell strain measures defined as $\bar{\epsilon}(t) = [\epsilon_{11}\ \epsilon_{22}\ 2\epsilon_{12}\ \kappa_{11}\ \kappa_{22}\ 2\kappa_{12}]^T$ if the macroscopic structure is modeled using a classical (also called Kirchhoff-Love) plate/shell model. Γ_ϵ is an operator matrix depending on the macroscopic structural model. For the classical plate/shell model it is given as

$$\Gamma_\epsilon = \begin{bmatrix} 1 & 0 & 0 & \delta y_3 & 0 & 0 \\ 0 & 1 & 0 & 0 & \delta y_3 & 0 \\ 0 & 0 & 0 & 0 & 0 & 0 \\ 0 & 0 & 0 & 0 & 0 & 0 \\ 0 & 0 & 0 & 0 & 0 & 0 \\ 0 & 0 & 1 & 0 & 0\delta y_3 & \end{bmatrix} \tag{3.12}$$

3.2.3 1D Euler-Bernoulli Beam Model

The 1D Euler-Bernoulli contains four beam strains named $\gamma_{11}(x_1,t)$, $\kappa_{11}(x_1,t)$, $\kappa_{12}(x_1,t)$ and $\kappa_{13}(x_1,t)$. $\gamma_{11}(x_1,t)$ denotes the instantaneous axial strain, and $\kappa_{11}(x_1,t)$ denotes the instantaneous twist rate, and $\kappa_{12}(x_1,t)$ and $\kappa_{13}(x_1,t)$ represent the instantaneous curvatures around x_2 and x_3, respectively. It is noted that x_1 represents the beam reference axis, and x_2 and x_3 represent the cross-sectional axes. Following MSG to construct a thermoviscoelastic beam model, the displacement field of the original 3D linear thermoviscoelastic model, u_i is described in terms of the desired beam model. For a general 1D Euler-Bernoulli beam model, four displacement variables including a rotation Φ_1 also known as the beam sectional rotation or twist angle, and three displacements $\bar{u}_i$ are required ([108], [126], [133]). These four time-dependent beam displacement variables can be used to describe the displacement field of the original 3D body as

$$\begin{aligned} u_1(x_1,y_1,y_2,y_3,t) &= \bar{u}_1(x_1,t) - \delta y_2 \bar{u}_{2,1}(x_1,t) - \delta y_3 \bar{u}_{3,1}(x_1,t) + \delta\chi_1(x_1,y_1,y_2,y_3,t) \\ u_2(x_1,y_1,y_2,y_3,t) &= \bar{u}_2(x_1,t) - \delta y_3 \Phi_1(x_1,t) + \delta\chi_2(x_1,y_1,y_2,y_3,t) \\ u_3(x_1,y_1,y_2,y_3,t) &= \bar{u}_3(x_1,t) + \delta y_2 \Phi_1(x_1,t) + \delta\chi_3(x_1,y_1,y_2,y_3,t) \end{aligned} \tag{3.13}$$

It is noted that $\delta y_\alpha = x_\alpha$ with $\alpha = 2,3$.

Since the beam model is constructed out of the original 3D model, the time-dependent kinematic field of the beam model needs to be defined in terms of those of the original model such that

$$\begin{aligned}
\Phi_1(x_1,t) &= \frac{1}{2}\langle u_{3,2} - u_{2,3}\rangle \\
\bar{u}_2(x_1,t) &= \langle u_2\rangle + \delta\langle y_3\rangle\Phi_1(x_1,t) \\
\bar{u}_3(x_1,t) &= \langle u_3\rangle - \delta\langle y_2\rangle\Phi_1(x_1,t) \\
\bar{u}_1(x_1,t) &= \langle u_1\rangle + \delta\langle y_3\rangle\bar{u}_{3,1}(x_1,t) + \delta\langle y_2\rangle\bar{u}_{2,1}(x_1,t)
\end{aligned} \tag{3.14}$$

where the angle brackets denote the average over the SG. The physical meaning of the first term is that the true instantaneous 3D twist average over the SG is the same as the instantaneous 1D rotation. The other three terms define the true instantaneous 3D displacements over the SG offset by the corresponding rotations as the instantaneous 1D displacements. If the origin of y_2 and y_3 is located at the geometric center of the SG, $\langle y_2\rangle = \langle y_3\rangle = 0$ and thus, the instantaneous 1D displacements are the average of the corresponding 3D displacements. From the definitions of Eq. (3.14), we effectively introduce the following four constraints on the fluctuating functions [134]

$$\langle\chi_i(t)\rangle = 0 \quad \langle\chi_{3|2}(t) - \chi_{2|3}(t)\rangle = 0 \tag{3.15}$$

where the vertical bar in the subscript indicates differentiation with respect to the micro-coordinates, y_i. Note that additional constraints can be added as needed depending on the periodicity of the SG [109].

The four beam strains of the 1D Euler-Bernoulli beam model are defined as ([108], [126], [133])

$$\begin{aligned}
\gamma_{11}(x_1,t) &= \bar{u}_{1,1}(x_1,t) & \kappa_{11}(x_1,t) &= \Phi_{1,1}(x_1,t) \\
\kappa_{12}(x_1,t) &= -\bar{u}_{3,11}(x_1,t) & \kappa_{13}(x_1,t) &= \bar{u}_{2,11}(x_1,t)
\end{aligned} \tag{3.16}$$

The corresponding 3D strain field can be written as

$$\Gamma(t) = \Gamma_\epsilon \bar{\epsilon}(t) + \Gamma_h \omega(t) \tag{3.17}$$

where $\bar{\epsilon}$ is the generalized beam strain measures defined as $\bar{\epsilon}(t) = \lfloor \gamma_{11} \ \kappa_{11} \ \kappa_{12} \ \ \kappa_{13} \rfloor^T$ if the macroscopic structure is modeled using the 1D Euler-Bernoulli beam model and Γ_ϵ is an operator matrix depending on the macroscopic structural model. For the Euler-Bernoulli beam model it is defined as

$$\Gamma_\epsilon = \begin{bmatrix} 1 & 0 & \delta y_3 & -\delta y_2 \\ 0 & 0 & 0 & 0 \\ 0 & 0 & 0 & 0 \\ 0 & 0 & 0 & 0 \\ 0 & \delta y_2 & 0 & 0 \\ 0 & -\delta y_3 & 1 & 0 \end{bmatrix} \tag{3.18}$$

3.2.4 Finite Element Implementation with Uniform Temperature Distribution

The temperature dependency of the material with a logarithmic time shift can be related through the TTSP and thus, after applying this time shift the material behavior is assumed as instantaneously temperature independent. Based on the QE method and Eq. (2.16), linear thermoelasticity is used to derive the transient Helmholtz free energy [135] and construct the transient strain energy of the original model as

$$U(t) = \left\langle \frac{1}{2} C_{ijkl}(T_0, \xi) \varepsilon_{ij}(t) \varepsilon_{kl}(t) + \beta_{ij}(T_0, \xi) \varepsilon_{ij}(t) \bar{\theta}(t) \right\rangle \tag{3.19}$$

The instantaneous temperature within a SG is approximated as uniform to enforce that the temperature change is spacewise constant and thus, the instantaneous temperature change is denoted by $\bar{\theta}(t)$. No a priori assumptions are invoked in terms of the reduced time ξ for the homogenized model.

The transient strain energy of Eq. (3.19) expressed in a matrix form reads as

$$U(t) = \left\langle \frac{1}{2}\Big(\Gamma_h\omega(t) + \Gamma_\epsilon\bar{\epsilon}(t)\Big)^T C(T_0,\xi)\Big(\Gamma_h\omega(t) + \Gamma_\epsilon\bar{\epsilon}(t)\Big) + \Big(\Gamma_h\omega(t) + \Gamma_\epsilon\bar{\epsilon}(t)\Big)^T \beta(T_0,\xi)\bar{\theta}(t)\right\rangle \tag{3.20}$$

with the operator matrix Γ_h defined in Eq. (3.7) and the operator matrix Γ_ϵ depending on the macroscopic structure as defined fro solid, plate/shell and beam models.

We can solve this problem using the finite element method (FEM). In general FEM, the displacement fields are approximated using shape functions. In case of MSG, shape functions are used to approximate the fluctuating functions [133]. The discretization of the instantaneous fluctuating functions χ over the SG reads as

$$\chi(x_k, y_j, t) = S(y_j)V(x_k, t) \tag{3.21}$$

where $S(y_j)$ represents the standard shape functions according to the type of element, and $V(x_k, t)$ is the instantaneous nodal value that we need to solve for. We can obtain the discretized version of the transient strain energy substituting Eq. (3.21) in Eq. (3.20) as

$$U(t) = \left(\frac{1}{2}V(t)^T E(T_0,\xi)V(t) + V(t)^T D_{h\epsilon}(T_0,\xi)\bar{\epsilon}(t) + \frac{1}{2}\bar{\epsilon}(t)^T D_{\epsilon\epsilon}(T_0,\xi)\bar{\epsilon}(t) + V(t)^T D_{h\theta}(T_0,\xi)\bar{\theta}(t) + \bar{\epsilon}(t)^T D_{\epsilon\theta}(T_0,\xi)\bar{\theta}(t)\right) \tag{3.22}$$

where

$$\begin{aligned} E(T_0,\xi) &= \langle(\Gamma_h S)^T C(T_0,\xi)(\Gamma_h S)\rangle & D_{h\epsilon}(T_0,\xi) &= \langle(\Gamma_h S)^T C(T_0,\xi)\Gamma_\epsilon\rangle \\ D_{\epsilon\epsilon}(T_0,\xi) &= \langle\Gamma_\epsilon^T C(T_0,\xi)\Gamma_\epsilon\rangle & D_{h\theta}(T_0,\xi) &= \langle(\Gamma_h S)^T\beta(T_0,\xi)\rangle \\ D_{\epsilon\theta}(T_0,\xi) &= \langle\beta(T_0,\xi)\rangle \end{aligned} \tag{3.23}$$

If we minimize Eq. (3.22) applying the constraints defined in Eq. (3.5) and adding additional constraints as needed, the following instantaneous linear system is found

$$E(T_0,\xi)V(t) = -D_{h\epsilon}(T_0,\xi)\bar{\epsilon}(t) - D_{h\theta}(T_0,\xi)\bar{\theta}(t) \tag{3.24}$$

From Eq. (3.24) we can determine that in each instant of time $V(t)$ linearly depends on $\bar{\theta}(t)$ and $\bar{\epsilon}(t)$. The symbolic writing of this relationship reads as

$$V(t) = V_0(T_0,\xi)\bar{\epsilon}(t) + V_\theta(T_0,\xi)\bar{\theta}(t) \tag{3.25}$$

The transient strain energy stored in the SG can be computed by substituting Eq. (3.25) into Eq. (3.22) obtaining

$$\begin{aligned} U(t) &= \frac{1}{2}\bar{\epsilon}(t)^T\Big(V_0^T(T_0,\xi)D_{h\epsilon}(T_0,\xi) + D_{\epsilon\epsilon}(T_0,\xi)\Big)\bar{\epsilon}(t) \\ &+ \bar{\epsilon}(t)^T\left[\frac{1}{2}\Big(D_{h\epsilon}^T(T_0,\xi)V_\theta(T_0,\xi) + V_0^T(T_0,\xi)D_{h\theta}(T_0,\xi)\Big) + D_{\epsilon\theta}(T_0,\xi)\right]\bar{\theta}(t) \\ &\equiv \frac{1}{2}\bar{\epsilon}(t)^T C^*(T,t)\bar{\epsilon}(t) + \bar{\epsilon}(t)^T\beta^*(T,t)\bar{\theta}(t) \end{aligned} \tag{3.26}$$

The identification of terms in Eq. (3.26) leads to

$$\begin{aligned} C^*(T,t) &= V_0^T(T_0,\xi)D_{h\epsilon}(T_0,\xi) + D_{\epsilon\epsilon}(T_0,\xi) = C^*(T_0,\xi) \\ \beta^*(T,t) &= \frac{1}{2}\Big(D_{h\epsilon}^T(T_0,\xi)V_\theta(T_0,\xi) + V_0^T(T_0,\xi)D_{h\theta}(T_0,\xi)\Big) + D_{\epsilon\theta}(T_0,\xi) = \beta^*(T_0,\xi) \end{aligned} \tag{3.27}$$

which implies that the effective properties in the time domain can be expressed in the reduced time domain. This is applicable if the composite is thermorheologically simple, which is automatic when one thermorheologically simple thermoviscoelastic phase exists. In a composite made of two or more distinct thermoviscoelastic phases, if each phase is thermorheologically simple and all have the same a_T, the effective properties of the composite will also be thermorheologically simple. However, if each phase has a distinct shift factor, for the composite to be thermorheologically simple all the phases except one need to be elastic over the temperature range studied [31].

It is noted that Eq. (3.27) provides the effective thermoviscoelastic properties of the macroscopic structural model. For the 3D solid model, $C^*(T,t)$ is the fully populated 6×6 stiffness matrix and the effective CTEs can be computed from

$$\alpha^*_{ij}(T,t) = -\Big(C^*_{ijkl}(T,t)\Big)^{-1}\beta^*_{kl}(T,t) \tag{3.28}$$

where according to Eq. (3.27), $\alpha^*_{ij}(T,t) = \alpha^*_{ij}(T_0,\xi)$ applies.

For the 2D plate/shell model, $C^*(T,t)$ is the fully populated 6×6 stiffness matrix, also know as ABD matrix. $\beta^*(T,t)$ represents the effetive thermal induced plate/shell stress resultants divided by $\bar{\theta}$, as uniform temperature distribution within the SG is assumed. Finally, for the 1D Euler-Bernoulli beam model, $C^*(T,t)$ is the fully populated 4×4 stiffness matrix (i.e. $C^*(T,t) = C^b(T,t)$) and $\beta^*(T,t)$ represents the effective thermal induced beam stress resultants divided by $\bar{\theta}$.

3.2.5 Quasi-Elastic Thermoviscoelastic Hybrid Rules of Mixture

For the particular case of homogenizing a composite laminate with uniform temperature distribution as an equivalent anisotropic solid, an analytical solution can be derived. To do so, first we write the transient strain energy difference between the original model and the 3D solid homogenized model as

$$\begin{aligned}\Pi(t) = &\left\langle \frac{1}{2}C_{ijkl}(T_0,\xi)\varepsilon_{ij}(t)\varepsilon_{kl}(t) + \beta_{ij}(T_0,\xi)\varepsilon_{ij}(t)\bar{\theta}(t)\right\rangle \\ &-\left\langle \frac{1}{2}C^*_{ijkl}(T,t)\bar{\varepsilon}_{ij}(t)\bar{\varepsilon}_{kl}(t) + \beta^*_{ij}(T,t)\bar{\varepsilon}_{ij}(t)\bar{\theta}(t)\right\rangle\end{aligned} \tag{3.29}$$

The free energy of the homogenized model is independent of the fluctuating functions. Therefore, the homogenized model is considered as given, which in turn implied that $C^*_{ijkl}(T,t)$, $\beta^*_{ij}(T,t)$, $\bar{\varepsilon}_{ij}(t)$ and $\bar{\theta}(t)$ cannot be varied. The variational statement to solve for χ_i reads as

$$\begin{aligned}\min_{\chi_i(t)\in \text{Eq. (3.5)}} \Bigg\langle &\frac{1}{2}C_{ijkl}(T_0,\xi)\Big(\bar{\varepsilon}_{ij}(t) + \chi_{(i|j)}(t)\Big)\Big(\bar{\varepsilon}_{kl}(t) + \chi_{(k|l)}(t)\Big) \\ &+\beta_{ij}(T_0,\xi)\Big(\bar{\varepsilon}_{ij}(t) + \chi_{(i|j)}(t)\Big)\bar{\theta}(t)\Bigg\rangle\end{aligned} \tag{3.30}$$

Additional constraints can be incorporated as needed along with the constraints given by Eq. (3.5). It is noted that for periodic materials, $\chi_i(t)$ must be periodic, and the second equation in Eq. (3.5) is automatically satisfied.

If we assume that the laminate is made of homogeneous anisotropic thermoviscoelastic layers, a through-the-thickness SG containing all segments needed to represent each layer can be used to model the laminate. In this analytical solution, we do not constrain the stacking sequence of the laminate or the anisotropy of the laminae. However, due to approximating the laminate as an anisotropic, homogeneous solid, the coupling between bending and extension deformations is not captured for asymmetric laminates.

Let us denote the in-plane coordinates as y_1 and y_2, and use y_3 to denote the thickness coordinate. Since the composite laminate is heterogeneous along y_3 direction and uniform in the $y_1 - y_2$ plane, $\chi_i(t)$ are instantaneous functions of y_3 only. This dependency implies that the partial derivatives of the fluctuating functions, $\chi_{i|j}(t)$, will vanish except $\chi_{i|3}(t)$. Then the simplified governing differential equations read as

$$\Big(C_{i3kl}(T_0,\xi)\left(\bar{\varepsilon}_{kl}(t)+\chi_{k|l}(t)\right)+\beta_{i3}(T_0,\xi)\bar{\theta}(t)\Big)_{|3}=0 \tag{3.31}$$

which can be integrated reading as

$$C_{i3kl}(T_0,\xi)\left(\bar{\varepsilon}_{kl}(t)+\chi_{k|l}(t)\right)+\beta_{i3}(T_0,\xi)\bar{\theta}(t)=c_i(t) \tag{3.32}$$

where $c_i(t)$ indicates that three constants per each time instance are considered. It is easy to conclude that

$$\sigma_{i3}(t)=C_{i3kl}(T_0,\xi)\left(\bar{\varepsilon}_{kl}(t)+\chi_{k|l}(t)\right)+\beta_{i3}(T_0,\xi)\bar{\theta}(t) \tag{3.33}$$

Thus we can conclude from Eqs. (3.32) and (3.33) that the through-the-thickness normal and transverse shear stresses are constant per each time instance according to the QE method. The chosen modeling technique leads to this conclusion as we want to model the laminate as an anisotropic, homogeneous solid. However, it is noteworthy to mention that in reality these

stress components are usually not constant through the thickness, such as when free-edge stress effects are matter of study [130].

We can solve for the fluctuating functions from Eq. (3.32) obtaining an equation for each constant c_i (t). The fluctuating functions for each layer are linear functions of y_3. For the local strain field, it is interesting to remark that

$$\varepsilon_{11}(t) = \bar{\varepsilon}_{11}(t) \quad \varepsilon_{22}(t) = \bar{\varepsilon}_{22}(t) \quad \varepsilon_{12}(t) = \bar{\varepsilon}_{12}(t)$$
$$\varepsilon_{33}(t) = \bar{\varepsilon}_{33}(t) + \chi_{3|3}(t) \quad \varepsilon_{13}(t) = \bar{\varepsilon}_{13}(t) + \chi_{1|3}(t) \quad \varepsilon_{23}(t) = \bar{\varepsilon}_{23}(t) + \chi_{2|3}(t)$$

which implies that the in-plane strains are constant and transverse strains are piecewise constant through the thickness per each instant of time. A simple thermoviscoelastic hybrid rule of mixtures (TVHRM) for composite laminates can be derived bearing in mind this evidence along with the fact that transverse stresses are constant, as concluded from Eq. (3.33).

Let $\sigma_{\parallel} = \lfloor \sigma_{11}(t) \;\; \sigma_{22}(t) \;\; \sigma_{12}(t) \rfloor^T$, $\sigma_{\perp} = \lfloor \sigma_{33}(t) \;\; \sigma_{23}(t) \;\; \sigma_{13}(t) \rfloor^T$, $\varepsilon_{\parallel} = \lfloor \varepsilon_{11}(t) \;\; \varepsilon_{22}(t) \;\; 2\varepsilon_{12}(t) \rfloor^T$, $\varepsilon_{\perp} = \lfloor \varepsilon_{33}(t) \;\; 2\varepsilon_{23}(t) \;\; 2\varepsilon_{13}(t) \rfloor^T$, $\alpha_{\perp} = \lfloor \alpha_{33}(T_0, \xi) \;\; 2\alpha_{23}(T_0, \xi) \; 2\alpha_{13}(T_0, \xi) \rfloor^T$, $\alpha_{\parallel} = \lfloor \alpha_{11}(T_0, \xi) \; \alpha_{22}(T_0, \xi) \;\; 2\alpha_{12}(T_0, \xi) \rfloor^T$ and $S_{ij}(T_0, \xi)$ be the components of the 6 $\times$ 6 instantaneous compliance matrix. It is noted that although material properties are function of T_0 and ξ and the stress, strain, and temperature change are function of time t, for clarity purposes these terms have been omitted in the formulation hereinafter presented. Then, the instantaneous constitutive relation of each layer reads as

$$\begin{Bmatrix} \varepsilon_{\parallel} \\ \varepsilon_{\perp} \end{Bmatrix} = \begin{bmatrix} S_{\parallel} & S_{\angle} \\ S_{\angle}^T & S_{\perp} \end{bmatrix} \begin{Bmatrix} \sigma_{\parallel} \\ \sigma_{\perp} \end{Bmatrix} + \begin{Bmatrix} \alpha_{\parallel} \\ \alpha_{\perp} \end{Bmatrix} \bar{\theta} \tag{3.34}$$

From Eq. (3.34), it follows that

$$\begin{aligned} \varepsilon_{\parallel} &= S_{\parallel}\sigma_{\parallel} + S_{\angle}\sigma_{\perp} + \alpha_{\parallel}\bar{\theta} \\ \varepsilon_{\perp} &= S_{\angle}^T\sigma_{\parallel} + S_{\perp}\sigma_{\perp} + \alpha_{\perp}\bar{\theta} \end{aligned} \tag{3.35}$$

From which $\sigma_{\parallel}$ and $\varepsilon_{\perp}$ can be solved leading to

$$\begin{aligned}\sigma_{\parallel} &= S_{\parallel}^{-1}(\varepsilon_{\parallel} - \alpha_{\parallel}\bar{\theta}) - S_{\parallel}^{-1}S_{\angle}\sigma_{\perp} \\ \varepsilon_{\perp} - \alpha_{\perp}\bar{\theta} &= \left(S_{\perp} - S_{\angle}^{T}S_{\parallel}^{-1}S_{\angle}\right)\sigma_{\perp} + S_{\angle}^{T}S_{\parallel}^{-1}(\varepsilon_{\parallel} - \alpha_{\parallel}\bar{\theta})\end{aligned} \tag{3.36}$$

Letting $Q = S_{\parallel}^{-1}$ and bearing in mind that both $\sigma_{\perp}$ and $\varepsilon_{\parallel}$ are constant through the thickness, for it to be homogenized to an equivalent homogeneous body with no a priori assumptions, the through-the-thickness average on both sides of the first equation in Eq. (3.36) can be computed as

$$\bar{\sigma}_{\parallel} = \langle Q \rangle \bar{\varepsilon}_{\parallel} - \left\langle Q\alpha_{\parallel} \right\rangle \bar{\theta} - \langle QS_{\angle} \rangle \bar{\sigma}_{\perp} = Q^{*}(\bar{\varepsilon}_{\parallel} - \alpha_{\parallel}^{*}\bar{\theta}) - Q^{*}S_{\angle}^{*}\bar{\sigma}_{\perp} \tag{3.37}$$

with

$$\begin{aligned}Q^{*} &= Q^{*}(T,t) = \langle Q \rangle = Q^{*}(T_0,\xi) \\ S_{\angle}^{*} &= S_{\angle}^{*}(T,t) = (Q^{*})^{-1}\langle QS_{\angle} \rangle = S_{\angle}^{*}(T_0,\xi) \\ \alpha_{\parallel}^{*} &= \alpha_{\parallel}^{*}(T,t) = (Q^{*})^{-1}\left\langle Q\alpha_{\parallel} \right\rangle = \alpha_{\parallel}^{*}(T_o,\xi)\end{aligned} \tag{3.38}$$

It is clearly concluded that since Q, $S_{\angle}$, and $\alpha_{\parallel}$ are functions of T_0 and ξ, the effective properties in the real time domain also have their equivalent properties in the reduced time domain.

The average of both sides of the second equation in Eq. (3.36) can also be computed as

$$\left\langle \varepsilon_{\perp} - \alpha_{\perp}\bar{\theta} \right\rangle = \left\langle S_{\angle}^{T}Q \right\rangle \bar{\varepsilon}_{\parallel} - \left\langle S_{\angle}^{T}Q\alpha_{\parallel} \right\rangle \bar{\theta} + \left\langle S_{\perp} - S_{\angle}^{T}QS_{\angle} \right\rangle \bar{\sigma}_{\perp} \tag{3.39}$$

This equation can be rewritten as

$$\bar{\varepsilon}_{\perp} - \alpha_{\perp}^{*}\bar{\theta} = S_{\angle}^{*T}Q^{*}(\bar{\varepsilon}_{\parallel} - \alpha_{\parallel}^{*}\bar{\theta}) + \left(S_{\perp}^{*} - S_{\angle}^{*T}Q^{*}S_{\angle}^{*}\right)\bar{\sigma}_{\perp} \tag{3.40}$$

with

$$
\begin{aligned}
S^*_{\perp} &= S^*_{\perp}(T,t) = \left\langle S_{\perp} - S^T_{\angle} Q S_{\angle} \right\rangle + S^{*T}_{\angle} Q^* S^*_{\angle} \\
\alpha^*_{\perp} &= \alpha^*_{\perp}(T,t) = \left\langle \alpha_{\perp} - S^T_{\angle} Q \alpha_{\parallel} \right\rangle + S^{*T}_{\angle} Q^* \alpha^*_{\parallel}
\end{aligned}
\tag{3.41}
$$

From Eq. (3.38) we concluded that Q^*, $S^*_{\angle}$, and $\alpha^*_{\parallel}$ can be expressed in the reduced time domain, and $S_{\perp}$ and $\alpha_{\perp}$ are also function of T_0 and ξ. Therefore, we can determine that $S^*_{\perp}$ and $\alpha^*_{\perp}$ are also function of the reduced time domain, and thus, $S^*_{\perp} = S^*_{\perp}(T,t) = S^*_{\perp}(T_0,\xi)$ and $\alpha^*_{\perp} = \alpha^*_{\perp}(T,t) = \alpha^*_{\perp}(T_0,\xi)$. From Eqs. (3.38) and (3.41) we can also determine that the behavior of the equivalent homogeneous solid is thermorheologically simple.

Finally, the effective thermoviscoelastic constitutive relations for the equivalent anisotropic solid of the composite laminate read as

$$
\begin{Bmatrix} \bar{\varepsilon}_{\parallel}(t) \\ \bar{\varepsilon}_{\perp}(t) \end{Bmatrix} = \begin{bmatrix} S^*_{\parallel}(T,t) & S^*_{\angle}(T,t) \\ S^{*T}_{\angle}(T,t) & S^*_{\perp}(T,t) \end{bmatrix} \begin{Bmatrix} \bar{\sigma}_{\parallel}(t) \\ \bar{\sigma}_{\perp}(t) \end{Bmatrix} + \begin{Bmatrix} \alpha^*_{\parallel}(T,t) \\ \alpha^*_{\perp}(T,t) \end{Bmatrix} \bar{\theta}(t) \tag{3.42}
$$

with $S^*_{\parallel}(T,t) = \Big(Q^*(T,t)\Big)^{-1}$. It is noted that we can extract the effective engineering constants from the effective instantaneous compliance matrix in Eq. (3.42) for each instant of time.

3.2.6 Finite Element Implementation with Nonuniform Temperature Distribution

When nonuniform steady-state temperature distribution is considered withing the SG, the constitutive equation given by Eq. (2.1) is used to construct the transient strain energy of the original model as

$$
\begin{aligned}
U(t) = \Bigg\langle & \frac{1}{2}\Big(\Gamma_h \omega(t) + \Gamma_\epsilon \bar{\epsilon}(t)\Big)^T C(T,t) \Big(\Gamma_h \omega(t) + \Gamma_\epsilon \bar{\epsilon}(t)\Big) \\
& + \Big(\Gamma_h \omega(t) + \Gamma_\epsilon \bar{\epsilon}(t)\Big)^T \beta(T,t)\theta \Bigg\rangle
\end{aligned}
\tag{3.43}
$$

where θ could be pointwisely distributed within the SG. Therefore, following the QE method, the associated themoelastic problem has spatially dependent properties [32].

Substituting Eq. (3.21) into Eq. (3.43), the discretized version of the transient strain energy is obtained as

$$\begin{aligned} U(t) = \Bigg(& \frac{1}{2} V(t)^T E(t) V(t) + V(t)^T D_{h\epsilon}(t) \bar{\epsilon}(t) + \frac{1}{2} \bar{\epsilon}(t)^T D_{\epsilon\epsilon}(t) \bar{\epsilon}(t) \\ & + V(t)^T D_{h\theta}(t) + \bar{\epsilon}(t)^T D_{\epsilon\theta}(t) \Bigg) \end{aligned} \tag{3.44}$$

where

$$\begin{aligned} E(t) &= \langle (\Gamma_h S)^T C(T,t) (\Gamma_h S) \rangle \quad & D_{h\epsilon}(t) &= \langle (\Gamma_h S)^T C(T,t) \Gamma_\epsilon \rangle \\ D_{\epsilon\epsilon}(t) &= \langle \Gamma_\epsilon^T C(T,t) \Gamma_\epsilon \rangle & D_{h\theta}(t) &= \langle (\Gamma_h S)^T \beta(T,t) \theta \rangle \\ D_{\epsilon\theta}(t) &= \langle \beta(T,t) \Gamma_\epsilon \theta \rangle \end{aligned} \tag{3.45}$$

Minimizing Eq. (3.44) applying the constraints defined in Eq. (3.15) and adding additional constraints as needed, the following instantaneous linear system is found

$$E(t) V(t) = -D_{h\epsilon}(t) \bar{\epsilon}(t) - D_{h\theta}(t) \tag{3.46}$$

In each instant of time, $V(t)$ linearly depends on $\bar{\epsilon}(t)$ as determined from Eq. (3.46). The symbolic writing of this relationship reads as

$$V(t) = V_0(t) \bar{\epsilon}(t) + V_\theta(t) \tag{3.47}$$

To compute the transient strain energy stored in the SG, Eq. (3.47) is substituted into Eq. (3.44) obtaining

$$\begin{aligned} U(t) &= \frac{1}{2} \bar{\epsilon}(t)^T \Big(V_0^T(t) D_{h\epsilon}(t) + D_{\epsilon\epsilon}(t) \Big) \bar{\epsilon}(t) \\ &+ \bar{\epsilon}(t)^T \Big[\frac{1}{2} \Big(D_{h\epsilon}^T(t) V_\theta(t) + V_0^T(t) D_{h\theta}(t) \Big) + D_{\epsilon\theta}(t) \Big] \\ &\equiv \frac{1}{2} \bar{\epsilon}(t)^T C^*(t) \bar{\epsilon}(t) + \bar{\epsilon}(t)^T \beta^*(t) \end{aligned} \tag{3.48}$$

The identification of terms in Eq. (3.48) leads to

$$\begin{aligned} C^*(t) &= V_0^T(t) D_{h\epsilon}(t) + D_{\epsilon\epsilon}(t) \\ \beta^*(t) &= \frac{1}{2}\Big(D_{h\epsilon}^T(t) V_\theta(t) + V_0^T(t) D_{h\theta}(t) \Big) + D_{\epsilon\theta}(t) \end{aligned} \tag{3.49}$$

For the macroscopic 3D solid model, $C^*(t)$ is the time-dependent effective the 6×6 stiffness matrix; for the 2D plate/shell model, $C^*(t)$ is the 6×6 $ABD(t)$ matrix, and for the 1D Euler-Bernoulli beam model, is the 4×4 $C^b(t)$ matrix. However, Eq. (3.49), $\beta^*(t)$ represents the effective thermal induced stress resultants. For the 2D plate/shell model, these thermal induced stress resultants are

$$\beta^*(t) = [N_{T_{11}}(t)\ N_{T_{22}}(t)\ N_{T_{12}}(t)\ M_{T_{11}}(t)\ M_{T_{22}}(t)\ M_{T_{12}}(t)] \tag{3.50}$$

In case of the 1D Euler-Bernoulli beam model, these thermal induced stress resultants are

$$\beta^*(t) = [F_{T_1}(t)\ M_{T_1}(t)\ M_{T_2}(t)\ M_{T_3}(t)] \tag{3.51}$$

3.3 Direct Integration Method

3.3.1 3D Solid Model

The formulation next presented was adapted from Zocher et al. [70] to solve the linear thermoviscoelastic problem. This section presents the main steps of its derivation and intermediate steps are provided as complementary in Appendix B. The stress state at the current reduced time ξ_{n+1} should be expressed by means of an incremental stress form that uses a time marching procedure. Let us assume that the reduced time can be subdivided in discrete intervals as

$$\xi_{n+1} = \xi_n + \Delta\xi_{n+1} \tag{3.52}$$

where $\Delta\xi_{n+1}$ stands for the reduced time increment in the current step, and ξ_{n+1} and ξ_n represent the reduced time in the current and previous, respectively. We also assume that

the stress state at the previous reduced time ξ_n is known. Following Eq. (2.6) the stress state at the reduced time ξ_{n+1} reads as

$$\sigma_{ij}(\xi_{n+1}) = \int_0^{\xi_{n+1}} \Big[C_{ijkl}\left(T_0, \xi_{n+1}(t) - \xi(\tau)\right) \dot{\varepsilon}_{kl}(\tau) + \beta_{ij}\left(T_0, \xi_{n+1}(t) - \xi(\tau)\right) \dot{\theta}(\tau) \Big] d\tau \tag{3.53}$$

which can also be written as

$$\begin{aligned} &\sigma_{ij}(\xi_{n+1}) = \\ &\int_0^{\xi_n} C_{ijkl}\left(T_0, \xi_{n+1}(t) - \xi(\tau)\right) \dot{\varepsilon}_{kl}(\tau) d\tau + \int_{\xi_n}^{\xi_{n+1}} C_{ijkl}\left(T_0, \xi_{n+1}(t) - \xi(\tau)\right) \dot{\varepsilon}_{kl}(\tau) d\tau \\ &+ \int_0^{\xi_n} \beta_{ij}\left(T_0, \xi_{n+1}(t) - \xi(\tau)\right) \dot{\theta}(\tau) d\tau + \int_{\xi_n}^{\xi_{n+1}} \beta_{ij}\left(T_0, \xi_{n+1}(t) - \xi(\tau)\right) \dot{\theta}(\tau) d\tau \end{aligned} \tag{3.54}$$

We can define the incremental stress field $\Delta\sigma_{ij}$ as

$$\begin{aligned} \Delta\sigma_{ij}(\xi_{n+1}) &\equiv \sigma_{ij}(\xi_{n+1}) - \sigma_{ij}(\xi_n) \\ &= \int_{\xi_n}^{\xi_{n+1}} C_{ijkl}\left(T_0, \xi_{n+1}(t) - \xi(\tau)\right) \dot{\varepsilon}_{kl}(\tau) d\tau \\ &+ \int_{\xi_n}^{\xi_{n+1}} \beta_{ij}\left(T_0, \xi_{n+1}(t) - \xi(\tau)\right) \dot{\theta}(\tau) d\tau + \Omega_{ij} \end{aligned} \tag{3.55}$$

where Ω_{ij} is defined as

$$\Omega_{ij} = \int_0^{\xi_n} \Delta C_{ijkl} \dot{\varepsilon}_{kl}(\tau) d\tau + \int_0^{\xi_n} \Delta\beta_{ij} \dot{\theta}(\tau) d\tau \tag{3.56}$$

and ΔC_{ijkl} and $\Delta\beta_{ij}$ read as

$$\begin{aligned} \Delta C_{ijkl} &\equiv C_{ijkl}\left(T_0, \xi_{n+1}(t) - \xi(\tau)\right) - C_{ijkl}\left(T_0, \xi_n(t) - \xi(\tau)\right) \\ \Delta\beta_{ij} &\equiv \beta_{ij}\left(T_0, \xi_{n+1}(t) - \xi(\tau)\right) - \beta_{ij}\left(T_0, \xi_n(t) - \xi(\tau)\right) \end{aligned} \tag{3.57}$$

Let us assume that C_{ijkl} and β_{ij} are expressed with Prony series coefficients. Then, $C_{ijkl}\left(T_0, \xi_{n+1}(t) - \xi(\tau)\right)$ and $\beta_{ij}\left(T_0, \xi_{n+1}(t) - \xi(\tau)\right)$ can be written as

$$\begin{aligned} C_{ijkl}\left(T_0, \xi_{n+1}(t) - \xi(\tau)\right) &= C_{ijkl,\infty} + \sum_{s_1=1}^{m_1} C_{ijkl,s_1} \mathrm{e}^{\left(-\frac{\xi_{n+1}(t)-\xi(\tau)}{\lambda_{s_1}}\right)} \\ \beta_{ij}\left(T_0, \xi_{n+1}(t) - \xi(\tau)\right) &= \beta_{ij,\infty} + \sum_{s_2=1}^{m_2} \beta_{ij,s_2} \mathrm{e}^{\left(-\frac{\xi_{n+1}(t)-\xi(\tau)}{\lambda_{s_2}}\right)} \end{aligned} \tag{3.58}$$

where $C_{ijkl,\infty}$ is the long-term stiffness matrix, $\beta_{ij,\infty}$ is the long-term thermal stress tensor, λ_s are the discrete stress relaxation times, and $C_{ijkl,s}$ and $\beta_{ij,s}$ stand for the Prony series coefficients of the stiffness matrix and thermal stress tensor, respectively. For the sake of simplicity, the same discrete stress relaxation times are considered for all the components of the stress relaxation stiffness and thermal stress tensor. It is noted that when time- and temperature-dependent experimental or simulation data are reduced, it is possible to constrain λ_s in the algorithm to compute the corresponding Prony series coefficients.

Furthermore, we approximate the strain and temperature difference over the interval $\Delta\xi_{n+1}$ (i.e. $\xi_n \leq \xi \leq \xi_{n+1}$) as

$$\begin{aligned} \varepsilon_{ij}(\xi) &= \varepsilon_{ij_n} + R_{\varepsilon_{ij_{n+1}}}(\xi - \xi_n)H(\xi - \xi_n) \\ \theta(\xi) &= \theta_n + R_{\theta_{n+1}}(\xi - \xi_n)H(\xi - \xi_n) \end{aligned} \tag{3.59}$$

where ε_{ij_n} and θ_n stand for the strain and temperature change values at the beginning of the interval, $R_{\varepsilon ij_{n+1}}$ is a vector of constants representing the strain rate change over the interval, $R_{\theta_{n+1}}$ is a constant representing the temperature rate change over the interval, and $H(\xi - \xi_n)$ is the Heaviside step function. Substituting Eq. (3.59) into Eq. (3.57), it can be integrated in a closed form as

$$\Delta\sigma_{ij}(\xi_{n+1}) = M_{ijkl}\Delta\varepsilon_{kl}(\xi_{n+1}) + \eta_{ij}\Delta\theta(\xi_{n+1}) + \Omega_{ij} \tag{3.60}$$

where

$$
\begin{aligned}
&M_{ijkl} \equiv C_{ijkl,\infty} + \frac{1}{\Delta\xi_{n+1}} \sum_{s_1=1}^{m_1} \lambda_{s_1} C_{ijkl,s_1} \left(1 - \mathrm{e}^{\frac{-\Delta\xi_{n+1}}{\lambda_{s_1}}}\right) \quad \text{(No sum on } i,j,k,l\text{)} \\
&\eta_{ij} \equiv \beta_{ij,\infty} + \frac{1}{\Delta\xi_{n+1}} \sum_{s_2=1}^{m_2} \lambda_{s_2} \beta_{ij,s_2} \left(1 - \mathrm{e}^{\frac{-\Delta\xi_{n+1}}{\lambda_{s_2}}}\right) \quad \text{(No sum on } i,j\text{)} \\
&\Delta\varepsilon_{ij}(\xi_{n+1}) \equiv R_{\varepsilon_{ij}{}_{n+1}} \Delta\xi_{n+1} \\
&\Delta\theta(\xi_{n+1}) \equiv R_{\theta_{n+1}} \Delta\xi_{n+1} \\
&\Omega_{ij} \equiv -\sum_{s_1=1}^{m_1} \left(1 - \mathrm{e}^{\frac{-\Delta\xi_{n+1}}{\lambda_{s_1}}}\right) D_{ij,s_1}(\xi_n) - \sum_{s_2=1}^{m_2} \left(1 - \mathrm{e}^{\frac{-\Delta\xi_{n+1}}{\lambda_{s_2}}}\right) B_{ij,s_2}(\xi_n) \quad \text{(No sum on } i,j\text{)}
\end{aligned}
\tag{3.61}
$$

where $R_{\varepsilon_{ij}{}_{n+1}}$ is a second-order tensor evaluated in the current time increment, $R_{\theta_{n+1}}$ is a constant evaluated in the current time increment, and

$$
\begin{aligned}
&D_{ij,s_1}(\xi_n) = \mathrm{e}^{\frac{-\Delta\xi_n}{\lambda_{s_1}}} D_{ij,s_1}(\xi_{n-1}) + \lambda_{s_1} C_{ijkl,s_1} R_{\varepsilon_{kl}{}_n} \left(1 - \mathrm{e}^{\frac{-\Delta\xi_n}{\lambda_{s_1}}}\right) \quad \text{(No sum on } i,j\text{)} \\
&B_{ij,s_2}(\xi_n) = \mathrm{e}^{\frac{-\Delta\xi_n}{\lambda_{s_2}}} B_{ij,s_2}(\xi_{n-1}) + \lambda_{s_2} \beta_{ij,s_2} R_{\theta_n} \left(1 - \mathrm{e}^{\frac{-\Delta\xi_n}{\lambda_{s_2}}}\right) \quad \text{(No sum on } i,j\text{)}
\end{aligned}
\tag{3.62}
$$

Finally, for a given strain field $\varepsilon_{kl}(t)$, it is possible to compute $\Delta\sigma_{ij}(\xi_{n+1})$ with the formulation here presented. Then, $\sigma_{ij}(\xi_{n+1})$ is computed as

$$
\sigma_{ij}(\xi_{n+1}) = \sigma_{ij}(\xi_n) + \Delta\sigma_{ij}(\xi_{n+1}) \tag{3.63}
$$

3.3.2 2D Kirchhoff-Love Plate/Shell Model

For the MSG-based plate/shell model with the DI method let us define the shell strains, curvatures, forces, moments, thermal force and moment resultants as $\epsilon(t) = \lfloor \epsilon_{11}(t) \;\; \epsilon_{22}(t) \;\; 2\epsilon_{12}(t) \rfloor^T$, $\kappa(t) = \lfloor \kappa_{11}(t) \;\; \kappa_{22}(t) \;\; 2\kappa_{12}(t) \rfloor^T$, $N(t) = \lfloor N_{11}(t) \;\; N_{22}(t) \;\; N_{12}(t) \rfloor^T$, $M(t) = \lfloor M_{11}(t) \;\; M_{22}(t) \;\; M_{12}(t) \rfloor^T$, $N_T(t) = \lfloor N_{T_{11}}(t) \;\; N_{T_{22}}(t) \;\; N_{T_{12}}(t) \rfloor^T$, $M_T(t) = \lfloor M_{T_{11}}(t) \;\; M_{T_{22}}(t) \;\; M_{T_{12}}(t) \rfloor^T$. Then, we also define the time- and temperature-dependent shell stiffness ma-

trix by means of extension relaxation stiffness matrix $A(T,t)$, extension-bending coupling relaxation stiffness matrix $B(T,t)$, and bending relaxation stiffness matrix $D(T,t)$ as

$$A(T,t) = \begin{bmatrix} A_{11}(T,t) & A_{12}(T,t) & A_{16}(T,t) \\ A_{12}(T,t) & A_{22}(T,t) & A_{26}(T,t) \\ A_{16}(T,t) & A_{26}(T,t) & A_{66}(T,t) \end{bmatrix}$$

$$B(T,t) = \begin{bmatrix} B_{11}(T,t) & B_{12}(T,t) & B_{16}(T,t) \\ B_{12}(T,t) & B_{22}(T,t) & B_{26}(T,t) \\ B_{16}(T,t) & B_{26}(T,t) & B_{66}(T,t) \end{bmatrix}$$

$$D(T,t) = \begin{bmatrix} D_{11}(T,t) & D_{12}(T,t) & D_{16}(T,t) \\ D_{12}(T,t) & D_{22}(T,t) & D_{26}(T,t) \\ D_{16}(T,t) & D_{26}(T,t) & D_{66}(T,t) \end{bmatrix}$$

Then, Eq. (2.1) can be rewritten in terms of the 2D Kirchhoff-Love plate/shell model as

$$\begin{aligned} N(t) &= \int_0^t A(T,t-\tau)\dot{\epsilon}(\tau)d\tau + \int_0^t B(T,t-\tau)\dot{\kappa}(\tau)d\tau + N_T(t) \\ M(t) &= \int_0^t B(T,t-\tau)\dot{\epsilon}(\tau)d\tau + \int_0^t D(T,t-\tau)\dot{\kappa}(\tau)d\tau + M_T(t) \end{aligned} \tag{3.64}$$

where the terms $N_T(t)$ and $M_T(t)$ are given as

$$\begin{aligned} N_T(t) &= \int_0^t \beta^{N_T}(T,t-\tau)\dot{\theta}(\tau)d\tau \\ M_T(t) &= \int_0^t \beta^{M_T}(T,t-\tau)\dot{\theta}(\tau)d\tau \end{aligned} \tag{3.65}$$

where β_{N_T} and β_{M_T} represent 3×1 column matrices of relaxation moduli relating the force and moment resultants to temperature change in 2D Kirchhoff-Love plate/shell model, respectively. Likewise, Eq. (2.6) can be rewritten as

$$\begin{aligned} N(t) &= \int_0^t A(T_0,\xi(t)-\xi(\tau))\dot{\epsilon}(\tau)d\tau + \int_0^t B(T_0,\xi(t)-\xi(\tau))\dot{\kappa}(\tau)d\tau + N_T(t) \\ M(t) &= \int_0^t B(T_0,\xi(t)-\xi(\tau))\dot{\epsilon}(\tau)d\tau + \int_0^t D(T_0,\xi(t)-\xi(\tau))\dot{\kappa}(\tau)d\tau + M_T(t) \end{aligned} \tag{3.66}$$

where the terms $N^T(t)$ and $M^T(t)$ for Eq. (3.66) are given as

$$\begin{aligned} N_T(t) &= \int_0^t \beta^{N_T}(T_0, \xi(t) - \xi(\tau))\dot{\theta}(\tau)d\tau \\ M_T(t) &= \int_0^t \beta^{M_T}(T_0, \xi(t) - \xi(\tau))\dot{\theta}(\tau)d\tau \end{aligned} \tag{3.67}$$

The DI method follows the incremental approach to solve Eq. (3.64) and hence, we want to compute the incremental force $\Delta N(\xi_{n+1})$ and moment $\Delta M(\xi_{n+1})$ resultants as

$$\begin{aligned} \Delta N(\xi_{n+1}) &\equiv N(\xi_{n+1}) - N(\xi_n) \\ \Delta M(\xi_{n+1}) &\equiv M(\xi_{n+1}) - M(\xi_n) \end{aligned} \tag{3.68}$$

where the reduced time increments are computed as given by Eq. (3.52). To solve Eq. (3.68), we apply two assumptions. The first assumption is that the terms $A(T,t)$, $B(T,t)$, $D(T,t)$, $\beta^{N_T}(T,t)$ and $\beta^{M_T}(T,t)$ are expressed in terms of Prony series coefficients as

$$\begin{aligned} A\left(T_0,\xi\right) &= A_\infty + \sum_{s=1}^{m} A_s \mathrm{e}^{\left(-\frac{\xi}{\lambda_s}\right)} \\ B\left(T_0,\xi\right) &= B_\infty + \sum_{s=1}^{m} B_s \mathrm{e}^{\left(-\frac{\xi}{\lambda_s}\right)} \\ D\left(T_0,\xi\right) &= D_\infty + \sum_{s=1}^{m} D_s \mathrm{e}^{\left(-\frac{\xi}{\lambda_s}\right)} \\ \beta^{N_T}\left(T_0,\xi\right) &= \beta_\infty^{N_T} + \sum_{s=1}^{m} \beta_s^{N_T} \mathrm{e}^{\left(-\frac{\xi}{\lambda_s}\right)} \\ \beta^{M_T}\left(T_0,\xi\right) &= \beta_\infty^{M_T} + \sum_{s=1}^{m} \beta_s^{M_T} \mathrm{e}^{\left(-\frac{\xi}{\lambda_s}\right)} \end{aligned} \tag{3.69}$$

where A_∞, B_∞ and D_∞ are the long-term shell stiffness matrices, $\beta_\infty^{N_T}$ and $\beta_\infty^{M_T}$ are the long-term values of the 3×1 column matrices of relaxation moduli relating the force and moment resultants to temperature change, and A_s, B_s, D_s, $\beta_s^{N_T}$ and $\beta_s^{M_T}$ are the Prony series coefficients. For the sake of simplicity, the same discrete stress relaxation times are considered for all the components of the thermoviscoelastic stiffness and thermal stress resultant matrices. The QE method implemented in SwiftComp$^{\text{TM}}$ and uniform temperature distribution within the plate/shell model were used to compute all these thermoviscoelastic

matrices and hence, all these terms correspond to the effective thermoviscoelastic plate/shell properties computed according to Eq. (3.27).

The second assumption is that we approximate the plate strains and curvatures over the time interval $\Delta\xi_{n+1}$ (i.e. $\xi_n \leq \xi \leq \xi_{n+1}$) as

$$\begin{aligned}
\dot{\epsilon}(\tau) &= \frac{\partial \epsilon}{\partial \tau} \approx R_{\epsilon_{n+1}} \equiv \frac{\Delta\epsilon(\xi_{n+1})}{\Delta\xi_{n+1}} \\
\dot{\kappa}(\tau) &= \frac{\partial \kappa}{\partial \tau} \approx R_{\kappa_{n+1}} \equiv \frac{\Delta\kappa(\xi_{n+1})}{\Delta\xi_{n+1}} \\
\dot{\theta}(\tau) &= \frac{\partial \theta}{\partial \tau} \approx R_{\theta_{n+1}} \equiv \frac{\Delta\theta(\xi_{n+1})}{\Delta\xi_{n+1}}
\end{aligned} \tag{3.70}$$

where $\Delta\epsilon(t_{n+1})$, $\Delta\kappa(t_{n+1})$ and $\Delta\theta(t_{n+1})$ stand for the plate strain, curvature, and temperature change increments, $R_{\epsilon_{n+1}}$ and $R_{\kappa_{n+1}}$ are constant column matrices containing the plate strain and curvature changes over the interval, and $R_{\theta_{n+1}}$ is defined as in Eq. (3.59).

Substituting the approximations given by Eqs. (3.69) and (3.70), Eq. (3.66) can be integrated in a closed form leading to

$$\begin{aligned}
\Delta N(\xi_{n+1}) &= A_{\text{eq}}\Delta\epsilon(\xi_{n+1}) + B_{\text{eq}}\Delta\kappa(\xi_{n+1}) + \beta_{\text{eq}}^{N_T}\Delta\theta(\xi_{n+1}) + \Omega_N \\
\Delta M(\xi_{n+1}) &= B_{\text{eq}}\Delta\epsilon(\xi_{n+1}) + D_{\text{eq}}\Delta\kappa(\xi_{n+1}) + \beta_{\text{eq}}^{M_T}\Delta\theta(\xi_{n+1}) + \Omega_M
\end{aligned} \tag{3.71}$$

where

$$
\begin{aligned}
A_{\text{eq}} &\equiv A_\infty + \frac{1}{\Delta\xi_{n+1}} \sum_{s=1}^{m} \lambda_s A_s \left(1 - \mathrm{e}^{\frac{-\Delta\xi_{n+1}}{\lambda_s}}\right) \\
B_{\text{eq}} &\equiv B_\infty + \frac{1}{\Delta\xi_{n+1}} \sum_{s=1}^{m} \lambda_s B_s \left(1 - \mathrm{e}^{\frac{-\Delta\xi_{n+1}}{\lambda_s}}\right) \\
D_{\text{eq}} &\equiv D_\infty + \frac{1}{\Delta\xi_{n+1}} \sum_{s=1}^{m} \lambda_s D_s \left(1 - \mathrm{e}^{\frac{-\Delta\xi_{n+1}}{\lambda_s}}\right) \\
\beta_{\text{eq}}^{N_T} &\equiv \beta_\infty^{N_T} + \frac{1}{\Delta\xi_{n+1}} \sum_{s=1}^{m} \lambda_s \beta_s^{N_T} \left(1 - \mathrm{e}^{\frac{-\Delta\xi_{n+1}}{\lambda_s}}\right) \\
\beta_{\text{eq}}^{M_T} &\equiv \beta_\infty^{M_T} + \frac{1}{\Delta\xi_{n+1}} \sum_{s=1}^{m} \lambda_s \beta_s^{M_T} \left(1 - \mathrm{e}^{\frac{-\Delta\xi_{n+1}}{\lambda_s}}\right) \\
\Delta\epsilon(\xi_{n+1}) &\equiv R_{\epsilon_{n+1}} \Delta\xi_{n+1} \\
\Delta\kappa(\xi_{n+1}) &\equiv R_{\kappa_{n+1}} \Delta\xi_{n+1} \\
\Delta\theta(\theta_{n+1}) &\equiv R_{\theta_{n+1}} \Delta\xi_{n+1} \\
\Omega_N &\equiv -\sum_{s=1}^{m} \left(1 - \mathrm{e}^{\frac{-\Delta\xi_{n+1}}{\lambda_s}}\right) \left(a_{N,s}(\xi_n) + b_{N,s}(\xi_n) + f_{N,s}(\xi_n)\right) \\
\Omega_M &\equiv -\sum_{s=1}^{m} \left(1 - \mathrm{e}^{\frac{-\Delta\xi_{n+1}}{\lambda_s}}\right) \left(b_{M,s}(\xi_n) + d_{M,s}(\xi_n) + f_{M,s}(\xi_n)\right)
\end{aligned}
\tag{3.72}
$$

where $R_{\epsilon_{n+1}}$ and $R_{\kappa_{n+1}}$ are column matrices evaluated in the current time increment, $R_{\theta_{n+1}}$ is a constant evaluated in the current time increment, and $a_{N,s}$, $b_{N,s}$, $f_{N,s}$, $b_{M,s}$, $d_{M,s}$ and $f_{M,s}$ are 3×1 column matrices defined as

$$
\begin{aligned}
a_{N,s}(\xi_n) &= \mathrm{e}^{\frac{-\Delta\xi_n}{\lambda_s}} a_{N,s}(\xi_{n-1}) + \lambda_s A_s R_{\epsilon_n} \left(1 - \mathrm{e}^{\frac{-\Delta\xi_n}{\lambda_s}}\right) \\
b_{N,s}(\xi_n) &= \mathrm{e}^{\frac{-\Delta\xi_n}{\lambda_s}} b_{N,s}(\xi_{n-1}) + \lambda_s B_s R_{\kappa_n} \left(1 - \mathrm{e}^{\frac{-\Delta\xi_n}{\lambda_s}}\right) \\
f_{N,s}(\xi_n) &= \mathrm{e}^{\frac{-\Delta\xi_n}{\lambda_s}} f_{N,s}(\xi_{n-1}) + \lambda_s \beta_s^{N_T} R_{\theta_n} \left(1 - \mathrm{e}^{\frac{-\Delta\xi_n}{\lambda_s}}\right) \\
b_{M,s}(\xi_n) &= \mathrm{e}^{\frac{-\Delta\xi_n}{\lambda_s}} b_{M,s}(\xi_{n-1}) + \lambda_s B_s R_{\epsilon_n} \left(1 - \mathrm{e}^{\frac{-\Delta\xi_n}{\lambda_s}}\right) \\
d_{M,s}(\xi_n) &= \mathrm{e}^{\frac{-\Delta\xi_n}{\lambda_s}} d_{M,s}(\xi_{n-1}) + \lambda_s D_s R_{\kappa_n} \left(1 - \mathrm{e}^{\frac{-\Delta\xi_n}{\lambda_s}}\right) \\
f_{M,s}(\xi_n) &= \mathrm{e}^{\frac{-\Delta\xi_n}{\lambda_s}} f_{M,s}(\xi_{n-1}) + \lambda_s \beta_s^{M_T} R_{\theta_n} \left(1 - \mathrm{e}^{\frac{-\Delta\xi_n}{\lambda_s}}\right)
\end{aligned}
\tag{3.73}
$$

It is noted that $a_{N,s}$, $b_{N,s}$, $b_{M,s}$ and $d_{M,s}$ store the change of in-plane forces and moments history for each of the discrete stress relaxation times, λ_s, used to define the Prony series coefficients. For instance, if 10 discrete stress relaxation times are used to define the Prony series coefficients of the ABD matrices, there will be 10 different matrices for $a_{N,s}$, $b_{N,s}$, $b_{M,s}$ and $d_{M,s}$ as $s = 1, 2, ..., 10$ (i.e. 40 matrices total). The units of $a_{N,s}$, $b_{N,s}$ and $f_{N,s}$ are plate/shell force, and the ones of $b_{M,s}$, $d_{M,s}$ and $b_{M,s}$ are plate/shell moment. In addition, at the first step of the computation (i.e. $n = 1$), the values of Eq. (3.73) are equal to

$$\begin{aligned}
a_{N,s}(\xi_1) &= \lambda_s A_s R_{\epsilon_1}\left(1 - \mathrm{e}^{\frac{-\Delta\xi_1}{\lambda_s}}\right) \\
b_{N,s}(\xi_1) &= \lambda_s B_s R_{\kappa_1}\left(1 - \mathrm{e}^{\frac{-\Delta\xi_1}{\lambda_s}}\right) \\
f_{N,s}(\xi_1) &= \lambda_s \beta_s^{N_T} R_{\theta_1}\left(1 - \mathrm{e}^{\frac{-\Delta\xi_1}{\lambda_s}}\right) \\
b_{M,s}(\xi_1) &= \lambda_s B_s R_{\epsilon_1}\left(1 - \mathrm{e}^{\frac{-\Delta\xi_1}{\lambda_s}}\right) \\
d_{M,s}(\xi_1) &= \lambda_s D_s R_{\kappa_1}\left(1 - \mathrm{e}^{\frac{-\Delta\xi_1}{\lambda_s}}\right) \\
f_{M,s}(\xi_1) &= \lambda_s \beta_s^{M_T} R_{\theta_1}\left(1 - \mathrm{e}^{\frac{-\Delta\xi_1}{\lambda_s}}\right)
\end{aligned} \tag{3.74}$$

as the first terms on the right hand side of Eq. (3.73) vanish. Finally, for a given plate strain ϵ, curvature κ and temperature change θ fields, it is possible to compute $\Delta N(\xi_{n+1})$ and $\Delta M(\xi_{n+1})$ with the formulation here presented. Then, $N(\xi_{n+1})$ and $M(\xi_{n+1})$ are given as

$$\begin{aligned}
N(\xi_{n+1}) &= N(\xi_n) + \Delta N(\xi_{n+1}) \\
M(\xi_{n+1}) &= M(\xi_n) + \Delta M(\xi_{n+1})
\end{aligned} \tag{3.75}$$

The present formulation differs from the formulation presented by Gomez-Delrio and Kwok [96] in the way Ω_N and Ω_M are computed for the particular case of $a_T = 1$ and $\theta = 0$ in Eqs. (3.71) and (3.72). The present formulation allows to use different time increments from step to step and hence, both formulations are only equal if $\Delta t_n = \Delta t_{n+1}$. This discrepancy in the formulation may not lead to a significant difference when real time increment, Δt is

used to solve the problem but it can be noteworthy when reduced time increment ξ_n is used instead.

3.3.3 1D Euler-Bernoulli Beam Model

The kinetics of the 1D Euler-Bernoulli beam model contains four time-dependent stress resultants $F_1(x_1,t)$, $M_1(x_1,t)$, $M_2(x_1,t)$, $M_3(x_1,t)$ with $F_1(x_1,t)$ denoting the time-dependent axial force, $M_1(t)$ denoting the torque, and $M_2(x_1,t)$, $M_3(x_1,t)$ denoting the time-dependent bending moments around x_2, and x_3 respectively. Let us define ς as $\varsigma(t) = \lfloor F_1\ M_1\ M_2\ M_3 \rfloor^T$, and the 4×4 beam stiffness matrix $C^b(T,t)$ capturing extension, torsion, and bending in two directions as

$$C^b(T,t) = \begin{bmatrix} C^b_{11}(T,t) & C^b_{12}(T,t) & C^b_{13}(T,t) & C^b_{14}(T,t) \\ C^b_{12}(T,t) & C^b_{22}(T,t) & C^b_{23}(T,t) & C^b_{24}(T,t) \\ C^b_{13}(T,t) & C^b_{23}(T,t) & C^b_{33}(T,t) & C^b_{34}(T,t) \\ C^b_{14}(T,t) & C^b_{24}(T,t) & C^b_{34}(T,t) & C^b_{44}(T,t) \end{bmatrix} \tag{3.76}$$

Then, Eq. (2.1) can be rewritten in terms of the 1D Euler-Bernoulli beam model as

$$\varsigma(t) = \int_0^t \Big[C^b(T, t-\tau)\dot{\bar{\epsilon}} + \beta^b\,(T, t-\tau)\,\dot{\theta}(\tau) \Big] d\tau \tag{3.77}$$

where β^b represents a 4×1 column matrix of relaxation moduli relating the stress resultants to temperature change in the 1D Euler-Bernoulli beam model. Similarly, Eq. (2.6) can be rewritten as

$$\varsigma(t) = \int_0^t \Big[C^b(T_0, \xi(t) - \xi(\tau))\dot{\bar{\epsilon}} + \beta^b\,(T_0, \xi(t) - \xi(\tau))\,\dot{\theta}(\tau) \Big] d\tau \tag{3.78}$$

Following the DI method, the incremental beam stress resultants are solved as

$$\Delta\varsigma(\xi_{n+1}) \equiv \varsigma(\xi_{n+1}) - \varsigma(\xi_n) + \tag{3.79}$$

where the reduced time increments are computed as given by Eq. (3.52). Then, let us assume that the terms of $C^b(T,t)$ are expressed with Prony series as

$$\begin{aligned} C^b\left(T_0,\xi\right) &= C^b_\infty + \sum_{s=1}^{m} C^b_s \mathrm{e}^{\left(-\frac{\xi}{\lambda_s}\right)} \\ \beta^b\left(T_0,\xi\right) &= \beta^b_\infty + \sum_{s=1}^{m} \beta^b_s \mathrm{e}^{\left(-\frac{\xi}{\lambda_s}\right)} \end{aligned} \tag{3.80}$$

where C^b_∞ is the long-term beam stiffness matrix, β^b_∞ is the long-term relaxation moduli relating the stress resultants to temperature change, and C^b_s and β^b_s denote the Prony series coefficients. To simplify the formulation, the same discrete stress relaxation times are considered for all the components of the 4×4 beam stiffness and thermal stress resultant matrices. We first compute the time- and temperature-dependent beam thermoviscoelastic stiffness and thermal stress resultant matrix using SwiftComp$^{\mathrm{TM}}$ [112] assuming that the beam cross-section has uniform temperature distribution (see Eq. (3.27) for beam models). Afterwards, all the terms can be fit into Prony series coefficients.

Furthermore, we approximate the beam strains over the interval $\Delta\xi_{n+1}$ (i.e. $\xi_n \leq \xi \leq \xi_{n+1}$) as

$$\begin{aligned} \dot{\bar{\epsilon}}(\tau) &= \begin{bmatrix} \dot{\gamma}_{11}(\tau) \\ \dot{\kappa}_{11}(\tau) \\ \dot{\kappa}_{12}(\tau) \\ \dot{\kappa}_{13}(\tau) \end{bmatrix} = \begin{bmatrix} \frac{\partial \gamma_{11}}{\partial \tau} \\ \frac{\partial \kappa_{11}}{\partial \tau} \\ \frac{\partial \kappa_{12}}{\partial \tau} \\ \frac{\partial \kappa_{13}}{\partial \tau} \end{bmatrix} \approx \begin{bmatrix} R_{\gamma_{11}{}_{n+1}} \\ R_{\kappa_{11}{}_{n+1}} \\ R_{\kappa_{12}{}_{n+1}} \\ R_{\kappa_{13}{}_{n+1}} \end{bmatrix} \equiv \begin{bmatrix} \frac{\Delta\gamma_{11}}{\Delta\xi} \\ \frac{\Delta\kappa_{11}}{\Delta\xi} \\ \frac{\Delta\kappa_{12}}{\Delta\xi} \\ \frac{\Delta\kappa_{13}}{\Delta\xi} \end{bmatrix} \equiv R_{\bar{\epsilon}_{n+1}} \\ \dot{\theta}(\tau) &= \frac{\partial\theta}{\partial\tau} \approx R_{\theta_{n+1}} \equiv \frac{\Delta\theta(\xi_{n+1})}{\Delta\xi_{n+1}} \end{aligned} \tag{3.81}$$

where $R_{\gamma_{11}}$, $R_{\kappa_{11}}$, $R_{\kappa_{12}}$ and $R_{\kappa_{13}}$ are constants representing beam strain changes over the interval, and $R_{\bar{\epsilon}}$ is a column matrix containing these constants.

Substituting the approximations given by Eqs. (3.80) and (3.81), and bearing in mind Eq. (2.4), Eq. (3.78) can be integrated in a closed form leading to

$$\Delta\varsigma(\xi_{n+1}) = C^b_{eq}\Delta\bar{\epsilon}(\xi_{n+1}) + \beta^b_{eq}\Delta\theta(\xi_{n+1}) + \Omega^b \tag{3.82}$$

with

$$
\begin{aligned}
C^b_{eq} &\equiv C^b_\infty + \frac{1}{\Delta\xi_{n+1}} \sum_{s=1}^{m} \lambda_s C^b_s \left(1 - \mathrm{e}^{\frac{-\Delta\xi_{n+1}}{\lambda_s}}\right) \\
\beta^b_{eq} &\equiv \beta^b_\infty + \frac{1}{\Delta\xi_{n+1}} \sum_{s=1}^{m} \lambda_s \beta^b_s \left(1 - \mathrm{e}^{\frac{-\Delta\xi_{n+1}}{\lambda_s}}\right) \\
\Delta\bar{\epsilon}(\xi_{n+1}) &\equiv R_{\bar{\epsilon}_{n+1}} \Delta\xi_{n+1} \\
\Delta\theta(\xi_{n+1}) &\equiv R_{\theta_{n+1}} \Delta\xi_{n+1} \\
\Omega^b &\equiv -\sum_{s=1}^{m} \left(1 - \mathrm{e}^{\frac{-\Delta\xi_{n+1}}{\lambda_s}}\right) \left(a_s(\xi_n) + f_s(\xi_n)\right)
\end{aligned}
\tag{3.83}
$$

where $R_{\bar{\epsilon}_{n+1}}$ and $R_{\theta_{n+1}}$ are evaluated for the current time increment, and a_s and f_s are a 4×1 column matrices defined as

$$
\begin{aligned}
a_s(\xi_n) &= \mathrm{e}^{\frac{-\Delta\xi_n}{\lambda_s}} a_s(\xi_{n-1}) + \lambda_s C^b_s R_{\bar{\epsilon}_n} \left(1 - \mathrm{e}^{\frac{-\Delta\xi_n}{\lambda_s}}\right) \\
f_s(\xi_n) &= \mathrm{e}^{\frac{-\Delta\xi_n}{\lambda_s}} f_s(\xi_{n-1}) + \lambda_s \beta^b_s R_{\theta_n} \left(1 - \mathrm{e}^{\frac{-\Delta\xi_n}{\lambda_s}}\right)
\end{aligned}
\tag{3.84}
$$

It is noted that a_s stores the change of beam forces and moments for each of the discrete relaxation times, λ_s, used to define the Prony series coefficients. As an example, if five discrete relaxation times are used to define the Prony series coefficients of $C^b(T,t)$, there will be five different matrices for a_s as $s = 1, 2, ..., 5$. For a given beam strain $\bar{\epsilon}$ and temperature change θ fields, it is possible to compute $\Delta\varsigma(\xi_{n+1})$ with the formulation here presented. Then, following Eq. (3.79), $\varsigma(\xi_{n+1})$ is given as

$$
\varsigma(\xi_{n+1}) = \varsigma(\xi_n) + \Delta\varsigma(\xi_{n+1}) \tag{3.85}
$$

It is noted that if all the computations are performed at reference temperature T_0, $a_T = 1$ and hence, $t = \xi$. The DI method can be implemented analytically to compute the global behavior of thermoviscoelastic beams or, alternatively, using a user-defined element (UEL) subroutine in Abaqus. In the present work, the DI method was implemented analytically.

3.3.4 Direct Integration Thermoviscoelastic Hybrid Rules of Mixture

An analytical solution is derived next for the particular case of computing the structural behavior of a composite laminate with uniform temperature distribution as an equivalent anisotropic solid. We assume that the laminate is made of homogeneous anisotropic thermo-viscoelastic layers whose three-dimensional strain-stress relationship is given by Eqs. (3.60) - (3.63). Then, a 1D SG through the thickness containing all segments needed to represent each layer is used to model the laminate. This analytical solution does not constrain the anisotropy of the laminae or the stacking sequence of the laminate. However, similarly to the analytical case presented in Subsection 3.2.5, the coupling between bending and extension deformations is not captured for asymmetric laminates as we approximated the laminate as an anisotropic, homogeneous solid.

Let $\Delta\sigma_{\parallel} = \lfloor \Delta\sigma_{11} \ \Delta\sigma_{22} \ \Delta\sigma_{12} \rfloor^T$, $\Delta\sigma_{\perp} = \lfloor \Delta\sigma_{33} \ \Delta\sigma_{23} \ \Delta\sigma_{13} \rfloor^T$, $\Delta\varepsilon_{\parallel} = \lfloor \Delta\varepsilon_{11} \ \Delta\varepsilon_{22} \ 2\Delta\varepsilon_{12} \rfloor^T$, $\Delta\varepsilon_{\perp} = \lfloor \Delta\varepsilon_{33} \ \ 2\Delta\varepsilon_{23} \ \ 2\Delta\varepsilon_{13} \rfloor^T$, $\eta_{\parallel} = \lfloor \eta_{11} \ \ \eta_{22} \ \ \eta_{12} \rfloor^T$, $\eta_{\perp} = \lfloor \eta_{33} \ \ \eta_{23} \ \ \eta_{13} \rfloor^T$, $\Omega_{\parallel} = \lfloor \Omega_{11} \ \ \Omega_{22} \ \ \Omega_{12} \rfloor^T$, $\Omega_{\perp} = \lfloor \Omega_{33} \ \ \Omega_{23} \ \ \Omega_{13} \rfloor^T$ and M_{ij} be the components of the 6×6 tangent stiffness matrix given as

$$\begin{Bmatrix} \Delta\sigma_{\parallel} \\ \Delta\sigma_{\perp} \end{Bmatrix} = \begin{bmatrix} M_{\parallel} & M_{\angle} \\ M_{\angle}^T & M_{\perp} \end{bmatrix} \begin{Bmatrix} \Delta\varepsilon_{\parallel} \\ \Delta\varepsilon_{\perp} \end{Bmatrix} + \begin{Bmatrix} \eta_{\parallel} \\ \eta_{\perp} \end{Bmatrix} \Delta\bar{\theta} + \begin{Bmatrix} \Omega_{\parallel} \\ \Omega_{\perp} \end{Bmatrix} \tag{3.86}$$

with

$$M_{\parallel} = \begin{bmatrix} M_{11} & M_{12} & M_{16} \\ M_{12} & M_{22} & M_{26} \\ M_{16} & M_{26} & M_{66} \end{bmatrix}$$
$$M_{\angle} = \begin{bmatrix} M_{13} & M_{14} & M_{15} \\ M_{23} & M_{24} & M_{25} \\ M_{36} & M_{46} & M_{56} \end{bmatrix}$$
$$M_{\perp} = \begin{bmatrix} M_{33} & M_{34} & M_{35} \\ M_{34} & M_{44} & M_{45} \\ M_{35} & M_{45} & M_{55} \end{bmatrix}$$

From Eq. (3.86) we have that

$$\begin{aligned} \Delta\sigma_{\parallel} &= M_{\parallel}\Delta\varepsilon_{\parallel} + M_{\angle}\Delta\varepsilon_{\perp} + \eta_{\parallel}\Delta\bar{\theta} + \Omega_{\parallel} \\ \Delta\sigma_{\perp} &= M_{\angle}^{T}\Delta\varepsilon_{\parallel} + M_{\perp}\Delta\varepsilon_{\perp} + \eta_{\perp}\Delta\bar{\theta} + \Omega_{\perp} \end{aligned} \tag{3.87}$$

From which $\Delta\sigma_{\parallel}$ and $\Delta\varepsilon_{\perp}$ can be solved leading to

$$\begin{aligned} \Delta\sigma_{\parallel} =& \left(M_{\parallel} - M_{\angle}M_{\perp}^{-1}M_{\angle}^{T}\right)\Delta\varepsilon_{\parallel} + M_{\angle}M_{\perp}^{-1}\Delta\sigma_{\perp} - M_{\angle}M_{\perp}^{-1}\eta_{\perp}\Delta\bar{\theta} \\ & - M_{\angle}M_{\perp}^{-1}\Omega_{\perp} + \eta_{\parallel}\Delta\bar{\theta} + \Omega_{\parallel} \\ \Delta\varepsilon_{\perp} =& M_{\perp}^{-1}\Delta\sigma_{\perp} - M_{\perp}^{-1}M_{\angle}^{T}\Delta\varepsilon_{\parallel} - M_{\perp}^{-1}\eta_{\perp}\Delta\bar{\theta} - M_{\perp}^{-1}\Omega_{\perp} \end{aligned} \tag{3.88}$$

Bearing in mind that both $\Delta\sigma_{\perp}$ and $\Delta\varepsilon_{\parallel}$ are constant through the thickness, for it to be homogenized to an equivalent homogeneous body with no a priori assumptions, the through-the-thickness average on both sides of Eq. (3.88) can be computed as

$$\begin{aligned} \Delta\bar{\sigma}_{\parallel} =& \left\langle M_{\parallel} - M_{\angle}M_{\perp}^{-1}M_{\angle}^{T}\right\rangle \Delta\bar{\varepsilon}_{\parallel} + \left\langle M_{\angle}M_{\perp}^{-1}\right\rangle \Delta\bar{\sigma}_{\perp} + \left\langle \eta_{\parallel} - M_{\angle}M_{\perp}^{-1}\eta_{\perp}\right\rangle \Delta\bar{\theta} \\ & + \left\langle \Omega_{\parallel} - M_{\angle}M_{\perp}^{-1}\Omega_{\perp}\right\rangle \\ \Delta\bar{\varepsilon}_{\perp} =& \left\langle M_{\perp}^{-1}\right\rangle \Delta\bar{\sigma}_{\perp} - \left\langle M_{\perp}^{-1}M_{\angle}^{T}\right\rangle \Delta\varepsilon_{\parallel} - \left\langle M_{\perp}^{-1}\eta_{\perp}\right\rangle \Delta\bar{\theta} - \left\langle M_{\perp}^{-1}\Omega_{\perp}\right\rangle \end{aligned} \tag{3.89}$$

It can be concluded that

$$
\begin{aligned}
M_{\perp}^{*} &= \left\langle M_{\perp}^{-1} \right\rangle^{-1} \\
M_{\angle}^{*} &= \left\langle M_{\angle} M_{\perp}^{-1} \right\rangle M_{\perp}^{*} \\
M_{\parallel}^{*} &= \left\langle M_{\parallel} - M_{\angle} M_{\perp}^{-1} M_{\angle}^{T} \right\rangle + M_{\angle}^{*} M_{\perp}^{*-1} M_{\angle}^{*T} \\
\eta_{\perp}^{*} &= M_{\perp}^{*} \left\langle M_{\perp}^{-1} \eta_{\perp} \right\rangle \\
\eta_{\parallel}^{*} &= \left\langle \eta_{\parallel} - M_{\angle} M_{\perp}^{-1} \eta_{\perp} \right\rangle + M_{\angle}^{*} M_{\perp}^{*-1} \eta_{\perp}^{*} \\
\Omega_{\perp}^{*} &= M_{\perp}^{*} \left\langle M_{\perp}^{-1} \Omega_{\perp} \right\rangle \\
\Omega_{\parallel}^{*} &= \left\langle \Omega_{\parallel} - M_{\angle} M_{\perp}^{-1} \Omega_{\perp} \right\rangle + M_{\angle}^{*} M_{\perp}^{*-1} \Omega_{\perp}
\end{aligned}
\tag{3.90}
$$

Finally, the effective thermoviscoelastic constitutive relations for the equivalent anisotropic solid of the composite laminate read as

$$
\begin{Bmatrix} \Delta\bar{\sigma}_{\parallel} \\ \Delta\bar{\sigma}_{\perp} \end{Bmatrix} = \begin{bmatrix} M_{\parallel}^{*} & M_{\angle}^{*} \\ M_{\angle}^{*T} & M_{\perp}^{*} \end{bmatrix} \begin{Bmatrix} \Delta\bar{\varepsilon}_{\parallel} \\ \Delta\bar{\varepsilon}_{\perp} \end{Bmatrix} + \begin{Bmatrix} \eta_{\parallel}^{*} \\ \eta_{\perp}^{*} \end{Bmatrix} \Delta\bar{\theta} + \begin{Bmatrix} \Omega_{\parallel}^{*} \\ \Omega_{\perp}^{*} \end{Bmatrix} \tag{3.91}
$$

Then, the stress state of the homogenized laminate in each time increment is computed substituting Eq. (3.91) into Eq. (3.63).

4. CASE STUDIES WITH THERMOVISCOELASTIC THREE-DIMENSIONAL SOLIDS

This chapter presents numerical case studies with MSG-based solid model and the QE method to compute the effective thermoviscoelastic properties of three different composite SGs. Analytical solutions and 3D numerical simulations were used to verify the MSG-based solid model. As part of this research work, these results were published in a journal article [136]. In regard to MSG-based solid model and the DI method presented in Section 3.3.1, numerical results of the lenticular and TRAC booms using this approach are presented in Chapter 6.

4.1 Effective Thermoviscoelastic Solid Properties

To illustrate the accuracy of the MSG-based QE solid model presented in Section 3.2, three different composites were considered to homogenize and compute the equivalent thermoviscoelastic properties. For these numerical studies, it was assumed that the composite material was completely cured and thus, there were no shrinkage effects. The first case study was a unidirectional fiber reinforced composite (UDFRC). The second case consisted of a balanced and symmetric composite laminate and was used to prove validity of the analytical solution presented by means of the TVHRM. The last case considered a plain weave textile composite created using TexGen [137]. For this mesostructure the influences of periodic and aperiodic boundary conditions on the homogenized properties were studied. All the formulation was implemented in SwiftComp$^{\text{TM}}$ and verified accordingly using RVE analysis and direct numerical simulation (DNS) in Abaqus 6.14 [104]. ABAQUS-SwiftComp GUI [113] and TexGen4SC [138] were also used to create the microstructures for different composites. For all the three cases the validity of the time shift given by Eq. (2.2) to represent the homogenized composite properties at different temperatures was also analyzed.

4.1.1 Unidirectional Fiber Reinforced Composite

A square-pack microstructure with fiber volume fraction equal to $V_f = 0.64$ was used to model the UDFRC. This is represented by the 2D SG shown in Figure 4.1(a) in which MSG was used to compute the equivalent solid properties. T300/PMT-F4 thermoset composite material properties were adapted for this study [95] and summarized in Appendix A.2.

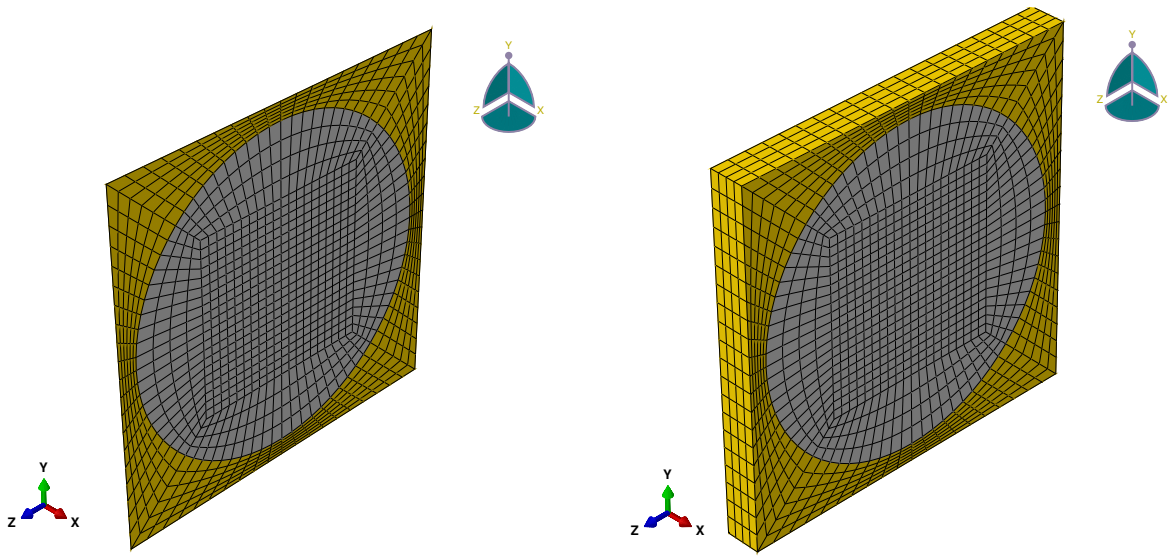

(a) 2D SG model

(b) RVE model

Figure 4.1. Modeling of the UDFRC by means of SG and RVE.

To confirm the results of the MSG solid model with 2D SG, a 3D RVE model shown in Figure 4.1(b) was built in Abaqus 6.14 [104]. Periodic boundary conditions were applied to the RVE in $x-$, $y-$, and $z-$ directions. A total of 4,800 linear hexahedral elements of type C3D8 were used to discretize the 3D RVE. The planar direction mesh size was kept the same for the 2D SG with 1,200 linear four-noded quadrilateral elements used to mesh it. In the RVE model, both materials, the fiber and the matrix were directly defined using material libraries available in Abaqus 6.14 [104]. Five different separate analyses were used to determine C^*_{11}, C^*_{12}, C^*_{22}, C^*_{23}, C^*_{44}, C^*_{55}, α^*_{11}, and α^*_{22} for each temperature of interest. A two-step simulation was defined with the viscoelastic option to capture the effective time-dependent material behavior. In case of the homogenized stiffness components at different isothermal conditions, in the first step a unit strain was applied over a short period (i.e. 0.1

s) to the RVE, and then in the second step, the strain was kept constant for a long period of time (i.e. 10^{10} s). For computing the homogenized time-dependent CTEs, a temperature increment step function [31] and periodic boundary conditions with macroscopic strains equal to zero were applied [139]. The initial temperature was assigned to be the reference temperature. In the first step a temperature increase was applied for a short period of time (i.e. 0.1 s). In the second step, the material relaxed for a long period of time keeping the new temperature constant (i.e. 10^{10} s). Then, the effective CTEs were computed as [139]

$$\alpha^*_{ij}(T,t) = -\frac{1}{\bar{\theta}}\Big(C^*_{ijkl}(T,t)\Big)^{-1}\langle\sigma_{kl}(T,t)\rangle \tag{4.1}$$

where $C^*_{ijkl}(T,t)$ is the effective stress relaxation stiffness tensor, $\bar{\theta}$ is the applied temperature change, and the macroscopic stresses are computed from averaging the microscopic stresses over the volume of the RVE as $\langle\sigma_{kl}(T,t)\rangle$. The values of the effective thermoviscoelastic stiffness components for different temperature conditions are shown in Figure 4.2 and effective CTEs in Figure 4.3. The instantaneous creep compliance matrix can also be directly calculated from the inverse of the relaxation matrix at each time step and from it, the instantaneous equivalent engineering constants. For the reference temperature of $T_0 = 40°$C, the Prony series coefficients were computed using Levenberg-Marquardt algorithm in Matlab 2018b. The corresponding coefficients are given in Table 4.1 and the fitting curves are plotted with white round markers in Figures 4.2-4.3. The fit values showed a good agreement with the original effective property data.

The effective properties computed using the MSG solid model and 3D RVE analysis are shown with different markers and solid lines in Figures 4.2-4.3, respectively. It is noted that 3D RVE analyses were performed for every temperature case and all of the results are represented with the solid line in the legend. All the values of the effective stiffness components and CTEs based on the MSG solid model agreed well with the ones obtained using the 3D RVE analysis.

In regards to the efficiency for each temperature of interest, RVE analyses required different simulations to compute the effective properties taking on average 194 s, while MSG was done in a single analysis and took 1.07 s. The results revealed that in the directions

Table 4.1. Effective properties for the UDFRC at $T_0 = 40°$C. Note that $C^*_{22} = C^*_{33}$, $C^*_{12} = C^*_{13}$, $C^*_{55} = C^*_{66}$, and $\alpha^*_{22} = \alpha^*_{33}$.

s	∞	1	2	3	4	5	6	7
λ_s (s)	-	10^3	10^5	10^6	10^7	10^8	10^9	10^{10}
$C^*_{11,s}$(MPa)	150030.0	129.3	248.9	274.6	189.4	600.8	39.8	1244.2
$C^*_{12,s}$(MPa)	1475.8	94.3	165.3	257.3	84.6	626.1	-82.8	1453.7
$C^*_{22,s}$(MPa)	4836.0	257.7	431.7	743.6	162.7	1831.0	-361.8	4308.0
$C^*_{23,s}$(MPa)	1389.0	116.4	214.4	305.5	141.9	745.2	-30.0	1729.5
$C^*_{44,s}$(MPa)	1046.8	91.2	171.2	225.1	120.4	531.9	-5.1	1187.9
$C^*_{55,s}$(MPa)	1581.7	114.9	207.6	301.8	124.5	728.4	-59.0	1673.1
$\alpha^*_{11,s}(\mu/°\text{C})$	-0.371	0.036	0.071	0.066	0.062	0.132	0.031	0.246
$\alpha^*_{22,s}(\mu/°\text{C})$	29.974	0.120	0.232	0.258	0.183	0.573	0.049	1.198

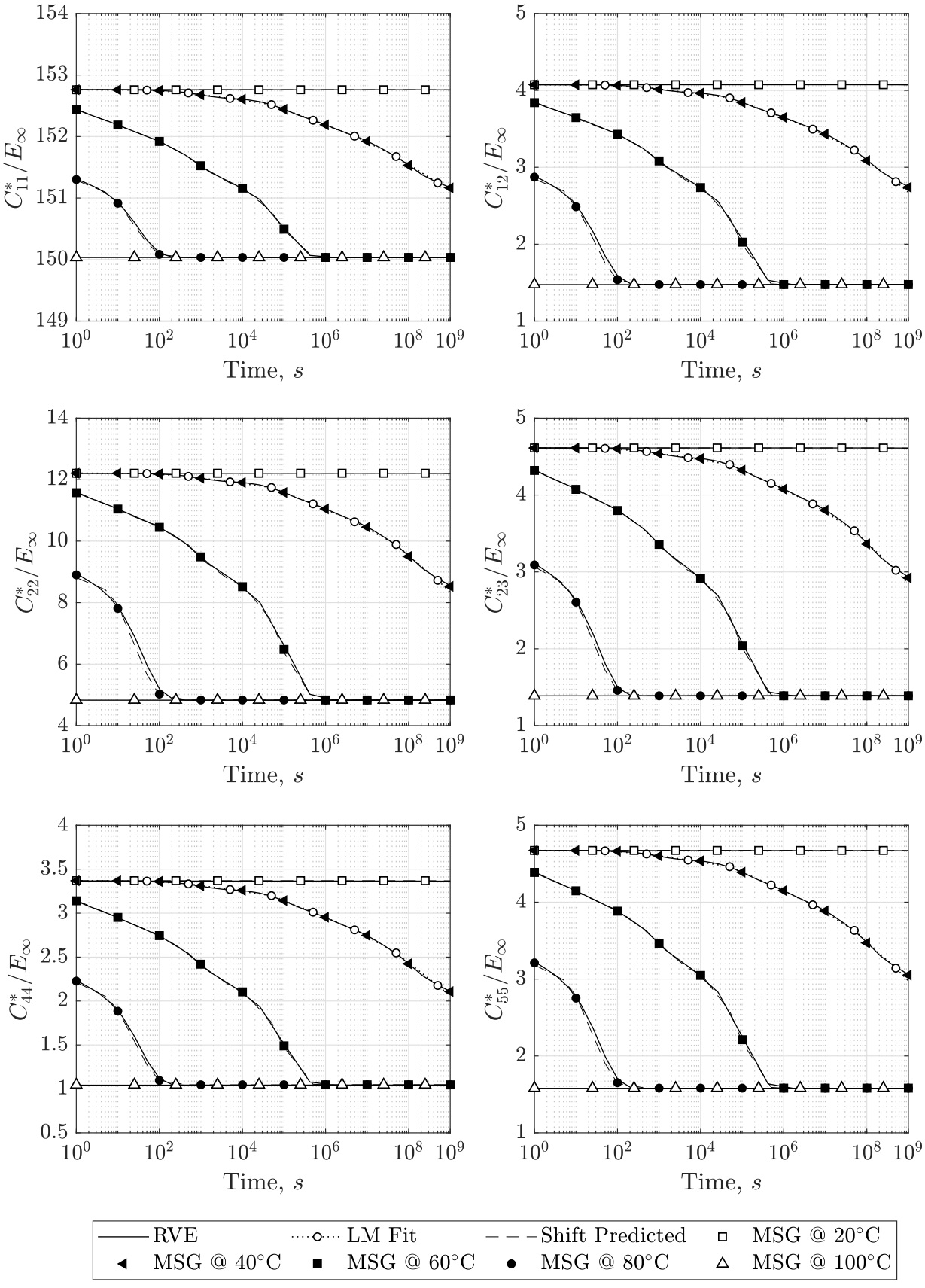

Figure 4.2. Evolution of normalized effective stiffness components of the UDFRC at different temperatures. 80

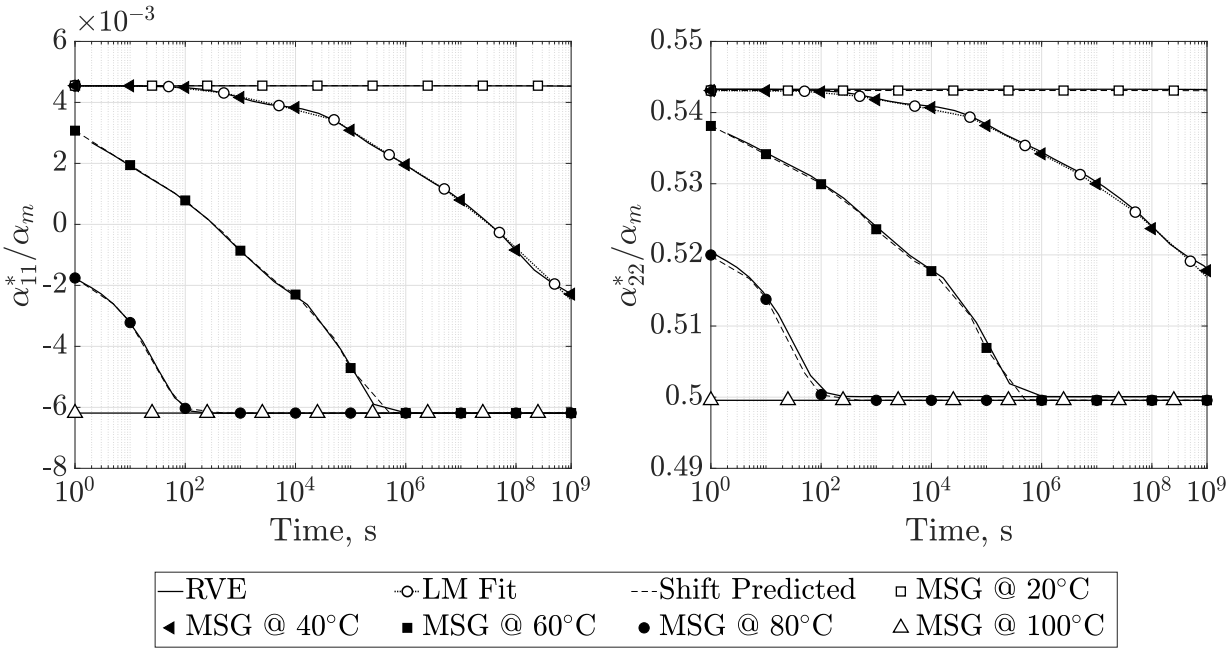

Figure 4.3. Evolution of normalized effective CTEs of the UDFRC at different temperatures.

dominated by the fiber behavior, such as in the case of C^*_{11}, the effect of the time-relaxation is negligible. However, for the directions dominated by the matrix, such as C^*_{22}, the effective material properties exhibited time- and temperature-dependent behavior as the values decreased with the increase of time and temperature. At $T = 20°\text{C}$ the material time-dependent behavior was not as evident as at $T = 40°\text{C}$, as the resin modulus slowly decreased over time. When the temperature is significantly above the reference temperature such as $T = 100°\text{C}$, the effective properties reached the long-term value.

One of the key findings of this numerical study was that although the CTEs of the constituent material were constant with time and temperature, the effective CTEs exhibited relaxation behavior with time and temperature. The nature of the effective CTEs was driven by the thermoviscoelastic behavior of the stiffness matrix of the resin and showed a good agreement with the conclusions of Khan and Muliana [72]. It was observed that α^*_{11} in Figure 4.3 (left) evolved from being positive at room temperature to negative as the temperature increased. In case of α^*_{22} shown in Figure 4.3 (right), although the relative difference between completely relaxed and unrelaxed values was smaller than for α^*_{11}, it was

higher in terms of absolute values as the CTEs in matrix dominated directions were more than one order of magnitude bigger than the CTEs in the fiber dominated one.

Dashed lines in Figures 4.2-4.3 represent the effective thermoviscoelastic properties at different temperatures computed applying the shift factor given by Eq. (2.2) to the effective properties at reference temperature of $T = 40°C$, as summarized in Table 4.1. Shifted values at $T = 20°C$, $60°C$, $80°C$ and $100°C$ were computed following this approach. We observed that the shifted homogenized values agreed well with the ones computed using MSG solid model with 2D SG and RVE analysis and thus, despite the heterogeneous thermoviscoelastic nature of the composite material, the temperature dependencies of the effective properties represented by the shift factor exhibited the same characteristics as those of the polymer matrix. This finding not only validated the conclusions of Martynenko and Lvov [119] for the effective thermoviscoelastic stiffness components but also extended their work accounting for the behavior of the effective CTEs. It also proved that the a priori assumption of Cai and Sun [64] is valid. Therefore, when computing the effective properties with one thermoviscoelastic constituent material, it is possible to calculate the effective properties at different temperatures by applying directly the shift factor to the thermoviscoelastic material and then homogenizing the properties, or by doing the homogenization at reference temperature first and then applying the shift factor directly to the effective properties. Clearly, the latter approach was much more efficient.

4.1.2 Composite Laminate

The complete set of homogenized three-dimensional thermoviscoelastic properties of a $[45/-45]_s$ balanced and symmetric laminate were computed using TVHRM, SwiftComp^{TM} with 1D SG (see Figure 4.4(a)), and 3D RVE analysis (see Figure 4.4(b)). The effective thermoviscoelastic properties of the UDFRC presented in Table 4.1 at $T_0 = 40°C$ were used as lamina properties. To assess the loss of accuracy of approximating as constant the time-dependent CTEs of the constituent materials, time-dependent CTEs given in Table 4.1 and constant CTEs obtained from the thermoelastic analysis (i.e. $\alpha^*_{e,11} = 0.2720\ \mu/°C$, $\alpha^*_{e,22} = \alpha^*_{e,33} = 33.07\ \mu/°C$) were considered as effective lamina CTEs.

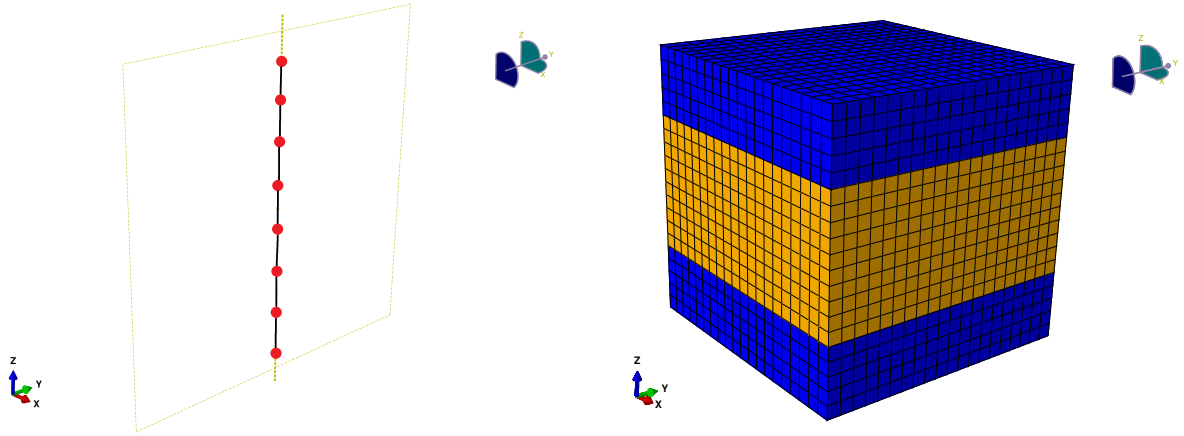

(a) 1D SG model

(b) 3D RVE model

Figure 4.4. Modeling of the $[45/-45]_s$ laminate by means of SG and RVE.

A total of 16 linear elements were used to mesh the 1D SG for MSG analysis. In case of 1D SG, periodic boundary conditions can be proved to be the same as the volume constraint in the second equation in Eq. (3.5). The 3D RVE model built in Abaqus 6.14 [104] was discretized using a total of 8,000 linear hexahedral elements of type C3D8, and periodic boundary conditions were applied in $x-$, $y-$, and $z-$ directions. For the 3D RVE analysis, the lamina properties were input through a UMAT, and CTEs were defined with a UEXPAN. Five analyses were required to determine all the effective stiffness and CTEs. The steps of the analyses were defined as previously explained for the UDFRC case. In the case of MSG analysis, the material properties were easily defined in the input file and only one analysis was needed. For each time step, the instantaneous creep compliance of the laminate was computed from the inverse of the relaxation matrix.

The engineering constants are shown in Figure 4.5. Since TVHRM and SwiftComp™ are both based on MSG, they provide the same effective properties and both are represented as MSG in the figures. Solid line is used to represent the effective properties at different temperatures of the 3D RVE analysis. The effective engineering constants and CTEs computed using MSG matched well the results of the 3D RVE analysis, except for when time-dependent lamina CTEs were considered as input (see Figure 4.6 bottom). In this latter case, the RVE analysis was able to properly capture the time-dependent behavior of the CTEs when $T = 20°\text{C}$ and $T = 100°\text{C}$. However, for $T = 40°\text{C}$, $T = 60°\text{C}$, and $T = 80°\text{C}$, the

Table 4.2. Effective properties for $[45/-45]_s$ laminate at $T_0 = 40°C$. It is noted that $E_1^* = E_2^*$, $\nu_{13}^* = \nu_{23}^*$, $G_{13}^* = G_{23}^*$, and $\alpha_{11}^* = \alpha_{22}^*$. Subscript c stands for the CTEs computed from the constant lamina CTEs, and t for the ones computed from the time-dependent lamina CTEs.

s	∞	1	2	3	4	5	6	7
λ_s (s)	-	10^3	10^5	10^6	10^7	10^8	10^9	10^{10}
$E_{1,s}^*$(MPa)	6152.4	363.4	771.8	772.4	806.9	1918.2	335.2	5703.4
$E_{3,s}^*$(MPa)	4802.8	226.5	471.9	505.3	464.9	1274.4	83.6	3946.6
$\nu_{12,s}^*$	0.921	-0.004	-0.008	-0.009	-0.009	-0.022	-0.004	-0.067
$\nu_{13,s}^*$	0.024	0.002	0.004	0.003	0.004	0.008	0.002	0.025
$G_{12,s}^*$(MPa)	38021.9	44.6	96.5	106.5	76.1	250.5	0.1	639.6
$G_{13,s}^*$(MPa)	1260.1	106.5	201.0	210.5	213.5	487.1	103.2	1337.8
$\alpha_{11c,s}^*(\mu/°C)$	1.383	0.052	0.046	0.192	-0.051	0.410	-0.157	0.953
$\alpha_{33c,s}^*(\mu/°C)$	42.161	0.005	-0.003	0.186	-0.098	0.401	-0.007	0.991
$\alpha_{11t,s}^*(\mu/°C)$	0.596	0.100	0.086	0.366	-0.124	0.726	-0.289	1.328
$\alpha_{33t,s}^*(\mu/°C)$	38.383	0.156	0.250	0.570	0.035	1.190	-0.014	2.429

effective CTEs matched MSG values at $t = 1$ s but did not converge to a single long-term value eventually leading to unrealistic results. This discrepancy was due to the fact that the RVE analysis requires applying a temperature difference to compute the effective CTEs. The applied temperature difference was only $\bar{\theta} \neq 0$ during the first step of the analysis and thus, the RVE analysis computed the effective properties for the second step (i.e. relaxation step) considering the lamina CTE values at the end of the first step. In the second step of the analysis the temperature was kept constant (i.e. $\bar{\theta} = 0$), although the lamina CTE values continued to evolve. Therefore, this evolution was not captured when computing the effective properties of the laminate as $\bar{\theta} = 0$ was used to compute the thermal strains. This limitation of the RVE analysis did not appear when constant lamina CTEs were used. Since MSG does not require the application of a priori thermal loads to compute effective CTEs, it was able to properly capture the convergence of the effective properties at $T = 40°C$, $T = 60°C$, and $T = 80°C$ towards the long-term value represented by $T = 100°C$ for both time-dependent and constant lamina CTEs.

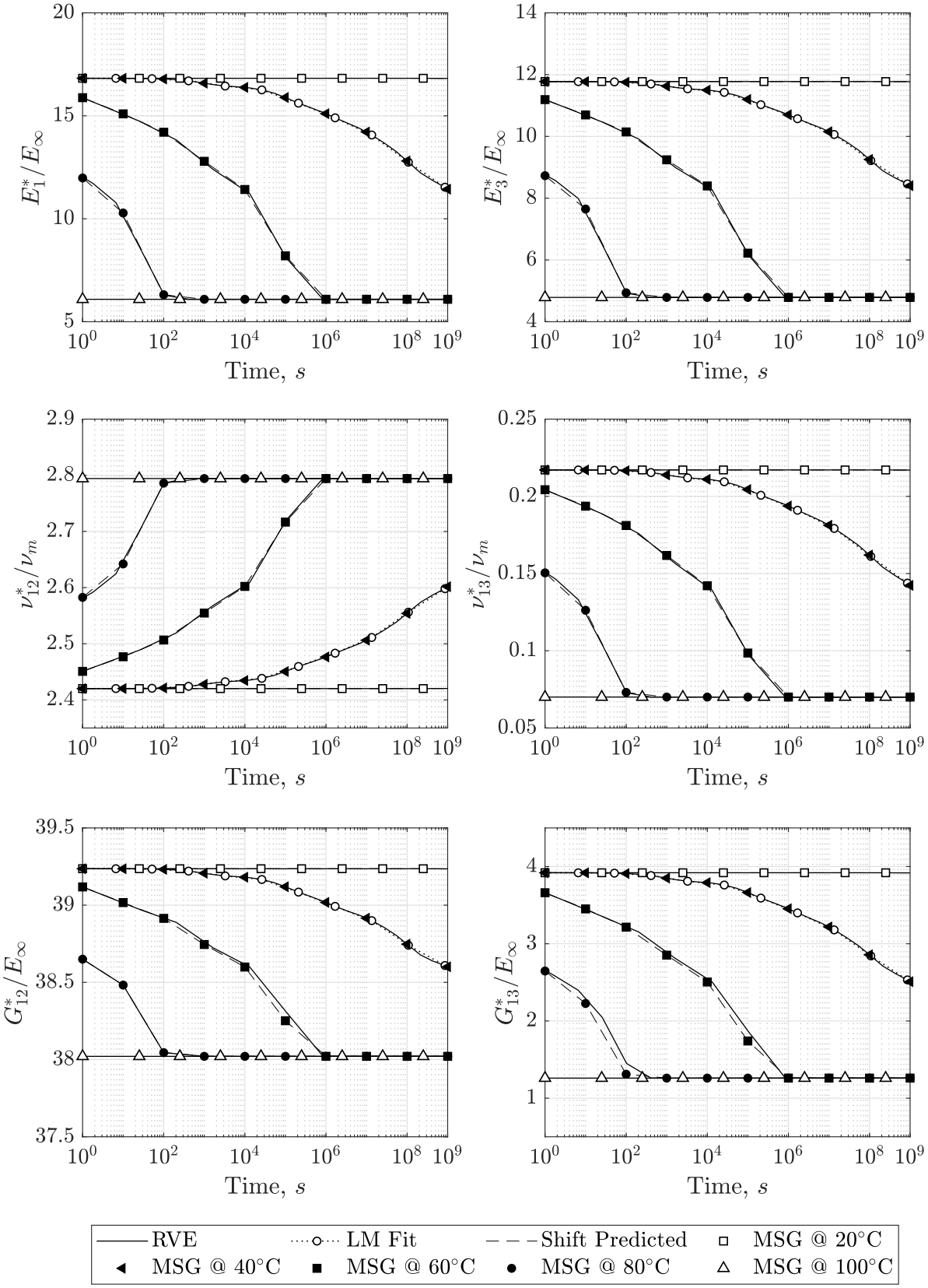

Figure 4.5. Evolution of normalized effective thermoviscoelastic engineering constants of $[45/-45]_s$ laminate. TVHRM and SwiftComp$^{\text{TM}}$ are both named as MSG.

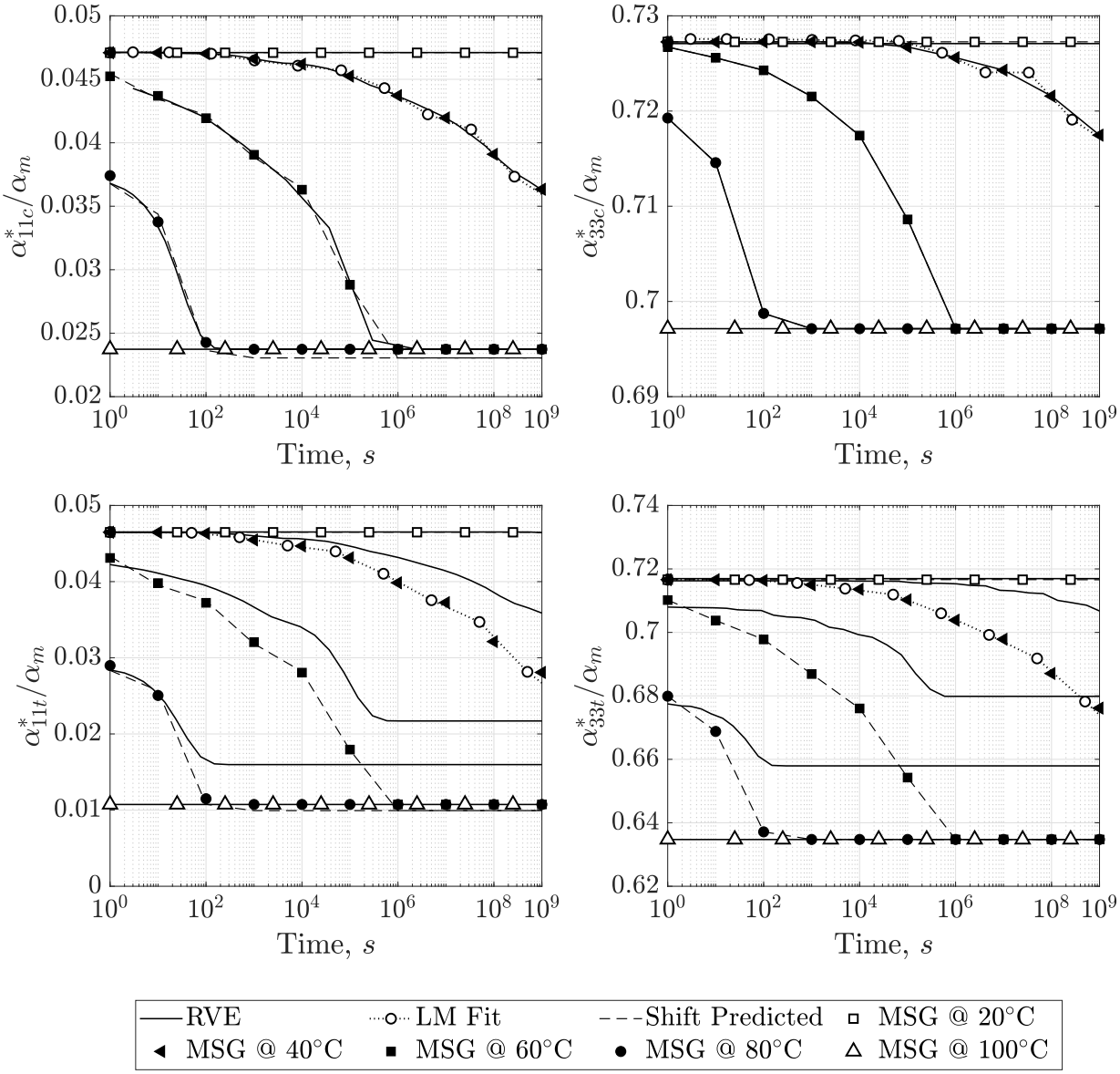

Figure 4.6. Evolution of normalized effective CTEs of $[45/-45]_s$ laminate for constant (top), and time-dependent (bottom) lamina CTEs, respectively. TVHRM and SwiftComp$^{\text{TM}}$ are both named as MSG.

Prony series coefficients of the laminate effective engineering constants at reference temperature of $T = 40°C$ are summarized in Table 4.2. The Prony series coefficients of the effective laminate Young's and shear moduli, and CTEs were computed using the Levenberg-Marquardt algorithm in Matlab 2018b. For the effective Poisson's ratios (i.e. ν_{12}^* and ν_{13}^*) the trust region reflective algorithm in Matlab 2018b was used instead, which provided a smoother approach to capture their time-dependent behavior. Fittings are shown with white round markers in Figures 4.5-4.6, which agree well with the original data.

All the effective engineering constants, including the Poisson's ratios, exhibited time- and temperature-dependent behavior. They all decreased with increased time and temperature, except for ν_{12}^* which grew for increased time and temperatures. Similarly to the UDFRC case, the effective CTEs exhibited time- and temperature-dependent behavior regardless of considering constant or time-dependent lamina CTEs (see Figure 4.6). Although the in-plane CTEs showed higher relative relaxation as the time passed and temperature increased, in terms of absolute values the through-the-thickness relaxation was more significant as α_{33}^* was considerably bigger than α_{11}^*.

The effective engineering constants and CTEs computed applying the shift defined by Eq. (2.2) to the effective properties at reference temperature are shown with dashed lines in Figures 4.5-4.6. The shift was applied to the effective stiffness at reference temperature (i.e. $T_0 = 40°C$) and afterwards, the effective engineering constants were extracted from the stiffness matrix for each time step. The shifted effective engineering constants showed a good agreement with the ones computed using MSG solid model with 1D SG, TVHRM, and 3D RVE analysis. The difference between the shifted and directly calculated results was less than 1%, and as depicted in Figure 4.6, it was valid for both constant and time-dependent CTE results. For comparison purposes of the latter case, the 3D RVE results with time-dependent lamina CTEs were disregarded due to the limitations shown by the 3D RVE analysis. Therefore, it can be concluded that when computing the effective properties departing from the reference temperature, it is possible to calculate the effective properties at different temperatures by applying directly the shift factor to the lamina properties and then homogenizing them, or by doing the homogenization at reference temperature first and then applying the shift factor to the effective properties. The latter approach appeared to

be more efficient. Furthermore, the shift factor of the lamina and laminate was the same as the one of the thermoviscoelastic resin.

4.1.3 Textile Composite

A plain weave composite material was analyzed using periodic (PBCs) and aperiodic (aPBCs) boundary conditions with MSG solid model and two-step homogenization approach [140]. Whereas the PBCs case properly modeled a textile composite with many layers and showed good agreement with the traditional 3D RVE analysis, through-the-thickness aPBCs should be used to capture the effective properties of textile composites made of few layers. TexGen [137] and TexGen4SC [138] were used to create the 3D SG model shown in Figure 4.7(a), which contained yarn and matrix material with thermovoviscoelastic behavior. The yarn had a width and thickness of 0.90 mm and 0.06 mm, respectively. The fabric was 0.12 mm thick with a yarn spacing of 1.75 mm. The effective thermoviscoelastic properties of the yarn were determined from the micro-homogenization step. For this numerical study, yarns were modeled with the square-pack microstructure presented on the first example. The effective properties summarized in Table 4.1 were used as yarn material properties for the macro-homogenization step. To assess the loss of accuracy of approximating as constant the time-dependent CTEs of the constituent materials with different boundary conditions, time-dependent CTEs given in Table 4.1 and constant CTEs obtained given in the previous case study were considered as effective yarn CTEs. The matrix consisted of PMT-F4 resin also presented in the first numerical study and hence, the yarn and the matrix can be described with the same shift factor given by Eq. (A.11). The anisotropic behavior of the constituent materials was easily defined in the MSG model without requiring any user-defined functions. A MSG solid model with 125,000 elements was used to describe the mesostructure. The current mesh size was in the order of magnitude of the mesh sizes used in previous studies that proved to have good agreements with experimental data ([95], [110]).

The effective engineering constants and CTEs were directly obtained from the MSG analysis. All the Prony series coefficients for the aPBCs case at reference temperature of $T = 40°C$ are summarized in Table 4.3. The corresponding fittings are shown with white

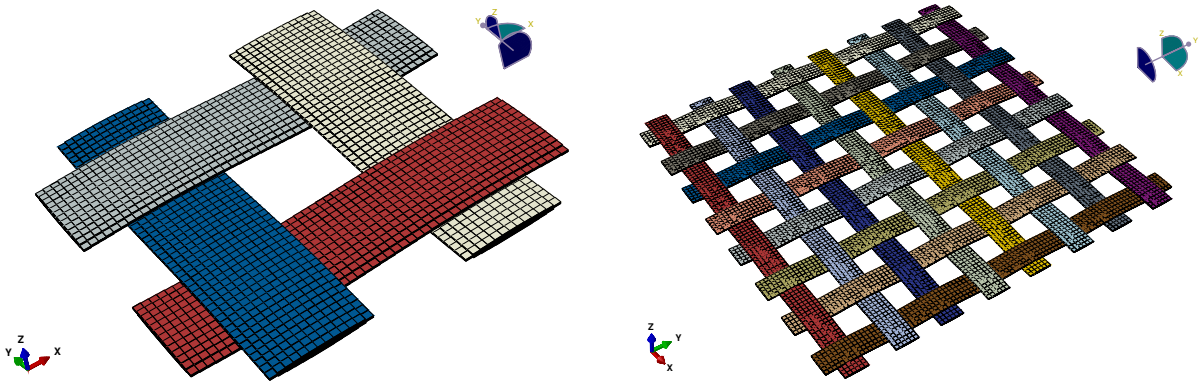

(a) 3D SG model

(b) 3D DNS model

Figure 4.7. Fabric models used in the mesostructural analysis with MSG, and direct numerical simulation. The matrix is hidden to facilitate the visualization of the yarns.

round markers in Figures 4.8-4.10 capturing well the results obtained from MSG analysis. All the effective engineering constants shown in Figures 4.8-4.9, including the Poisson's ratios, exhibited time- and temperature-dependent behavior. Similarly to the case of the laminate, all of them decreased with increased time and temperature, except for ν_{12}^*. The latter effective property for aPBCs increased with time and temperature while for PBCs was two orders of magnitude smaller ($\nu_{12,\ PBCs}^* \approx 0.07$). The magnitudes of the rest of the effective properties (i.e. E_1^*, E_3^*, ν_{13}^*, G_{13}^*, α_{11c}^* and α_{11t}^*) were slightly different for PBCs and aPBCs except the in-plane shear modulus G_{12}^*, which was the same for both cases. In case of α_{33}^*, aPBCs played a significant role. For the time-dependent CTE constituent properties, whereas $\alpha_{33t,\ PBCs}^*$ decreased with time and temperature (see the left figure of Figure 4.10), $\alpha_{33t,\ aPBCs}^*$ increases (see the right figure of Figure 4.10). Therefore, the long-term $\alpha_{33t,\ aPBCs}^*$ was bigger than the long-term $\alpha_{33t,\ PBCs}^*$. In case of constant CTE constituent properties, $\alpha_{33c,\ aPBCs}^*$ followed the same trend as $\alpha_{33t,\ aPBCs}^*$ (see Figure 4.11).

To prove the latter finding, a 3D DNS of a single layer plain weave composite was carried out in Abaqus 6.14 [104]. A total of 2,000,000 linear hexahedral elements of type C3D8 were used to discretize the 3D DNS model shown in Figure 4.7(b). UMAT subroutine was used to define the thermoviscoelastic material properties for the yarns. The PMT-F4 matrix

Table 4.3. Effective properties for the textile composite with aperiodic boundary conditions (aPBCs) in y_3 and $T_0 = 40°C$. Note that $E^*_{1,\ aPBCs} = E^*_{2,\ aPBCs}$, $\nu^*_{13,\ aPBCs} = \nu^*_{23,\ aPBCs}$, $G^*_{13,\ aPBCs} = G^*_{23,\ aPBCs}$, and $\alpha^*_{11,\ aPBCs} = \alpha^*_{22,\ aPBCs}$.

s, aPBCs	∞	1	2	3	4	5	6	7
λ_s (s)	-	10^3	10^5	10^6	10^7	10^8	10^9	10^{10}
$E^*_{1,s}$(MPa)	19584.0	326.0	603.0	771.0	399.0	1805.0	-170.0	4416.0
$E^*_{3,s}$(MPa)	2071.5	282.0	577.2	553.6	532.0	1197.3	285.2	2549.3
$\nu^*_{12,s}$	0.380	-0.003	-0.004	-0.011	0.002	-0.030	-0.014	-0.085
$\nu^*_{13,s}$	0.269	0.001	0.004	0.000	0.009	0.004	-0.006	0.046
$G^*_{12,s}$(MPa)	712.1	98.0	200.6	187.5	185.7	402.8	92.7	882.1
$G^*_{13,s}$(MPa)	538.1	96.6	192.9	180.4	175.6	373.3	93.6	743.4
$\alpha^*_{11t,s}(\mu/°C)$	2.258	0.350	0.606	0.848	0.370	1.766	0.030	3.449
$\alpha^*_{33t,s}(\mu/°C)$	83.585	-0.195	-0.401	-0.296	-0.439	-0.603	-0.304	-1.295

properties were directly defined using the available material libraries. Due to the difficulty of handling time dependent CTEs in Abaqus [104] when a thermal load is applied, constant CTEs were considered for both the yarn and the matrix, and the effective properties of the DNS simulation were compared against $\alpha^*_{11c,\ aPBCs}$ and $\alpha^*_{33c,\ aPBCs}$. Similarly to the case of 3D RVE analysis, two viscoelastic steps were defined and the initial temperature was assigned to be equal to the reference temperature. In the first step a temperature increase was applied for a short period of time and then, in the second step the material was relaxed for a long period of time keeping the new temperature constant.

The displacements of a region of interest (ROI) that mimics the 3D SG shown in Figure 4.7(a) and located just in the middle of the textile composite were considered for the effective CTEs calculations. The evolution of normalized effective CTEs of the DNS were shown in dashed lines Figure 4.11. Markers are used to plot the results for $\alpha^*_{11c,\ aPBCs}$ and $\alpha^*_{33c,\ aPBCs}$ computed using SwiftComp^{TM}. The MSG results exhibited good agreement with DNS results with the difference being less than 0.5%. Furthermore, whereas in-plane CTEs decreased with time and temperature, the through-the-thickness CTE increased corroborating the results found with MSG aPBCs analysis.

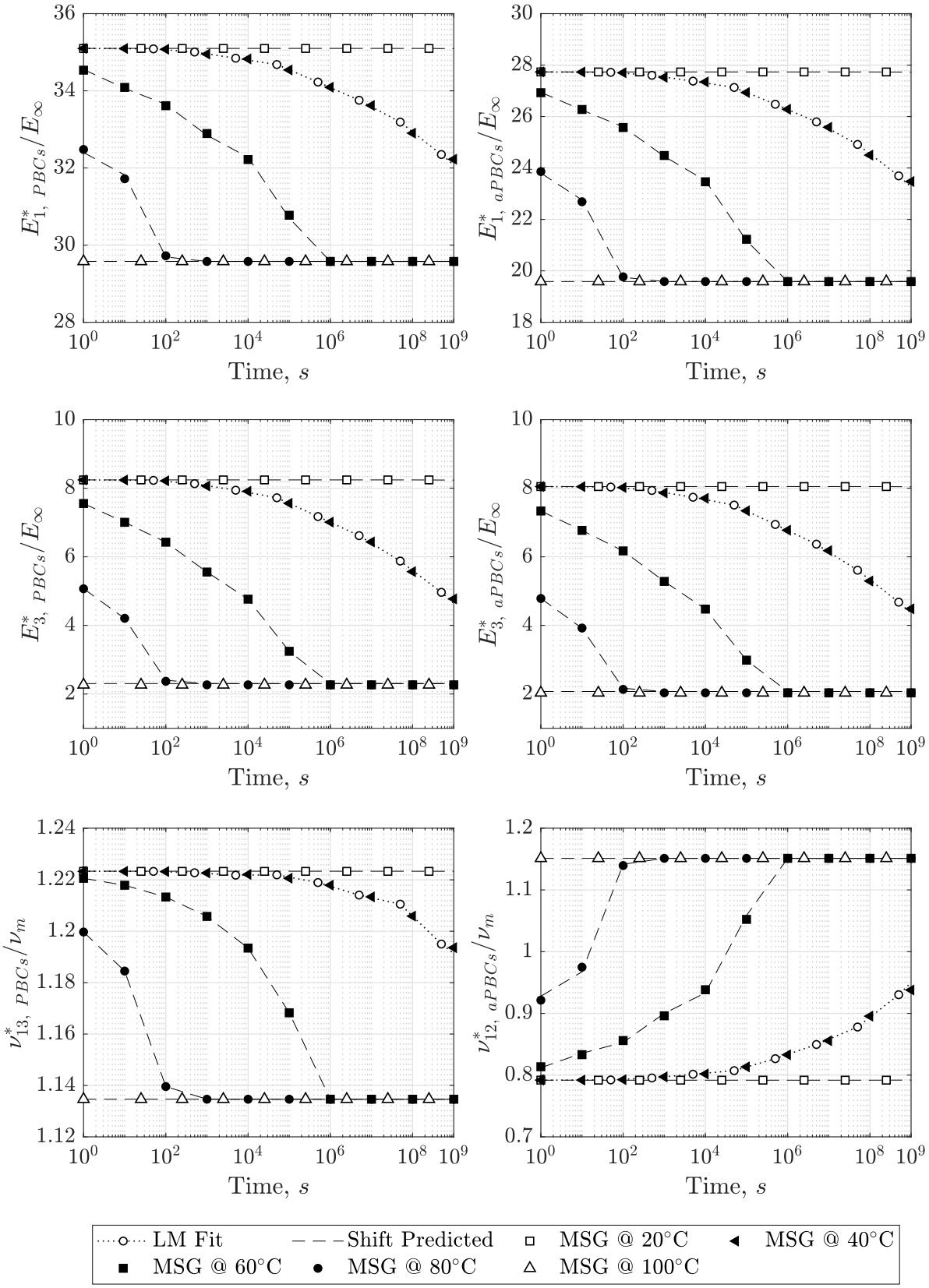

Figure 4.8. Evolution of normalized effective properties for the textile composite with PBCs (left) and aPBCs (right), respectively.

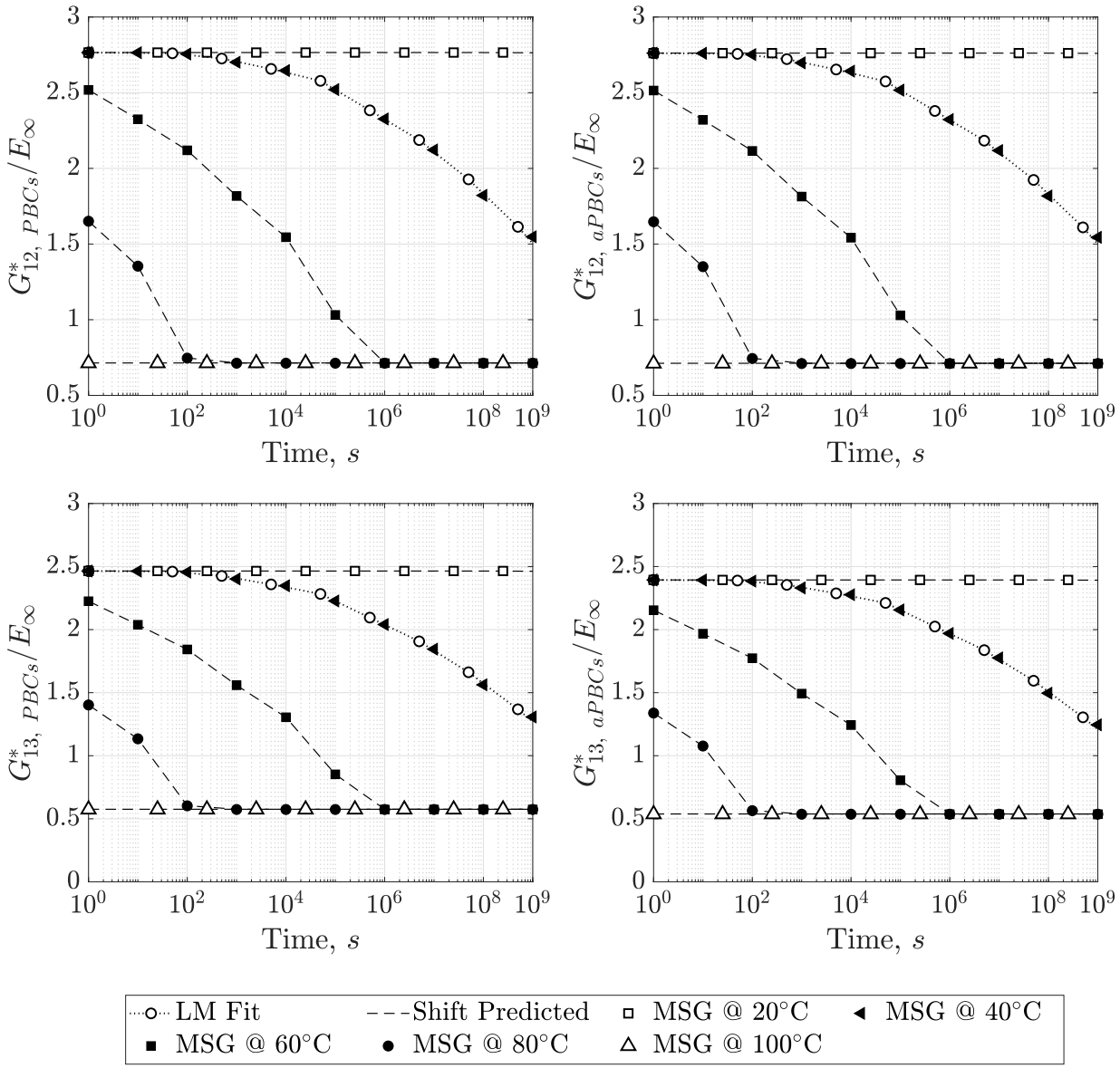

Figure 4.9. Evolution of normalized effective shear moduli for the textile composite with PBCs (left) and aPBCs (right), respectively.

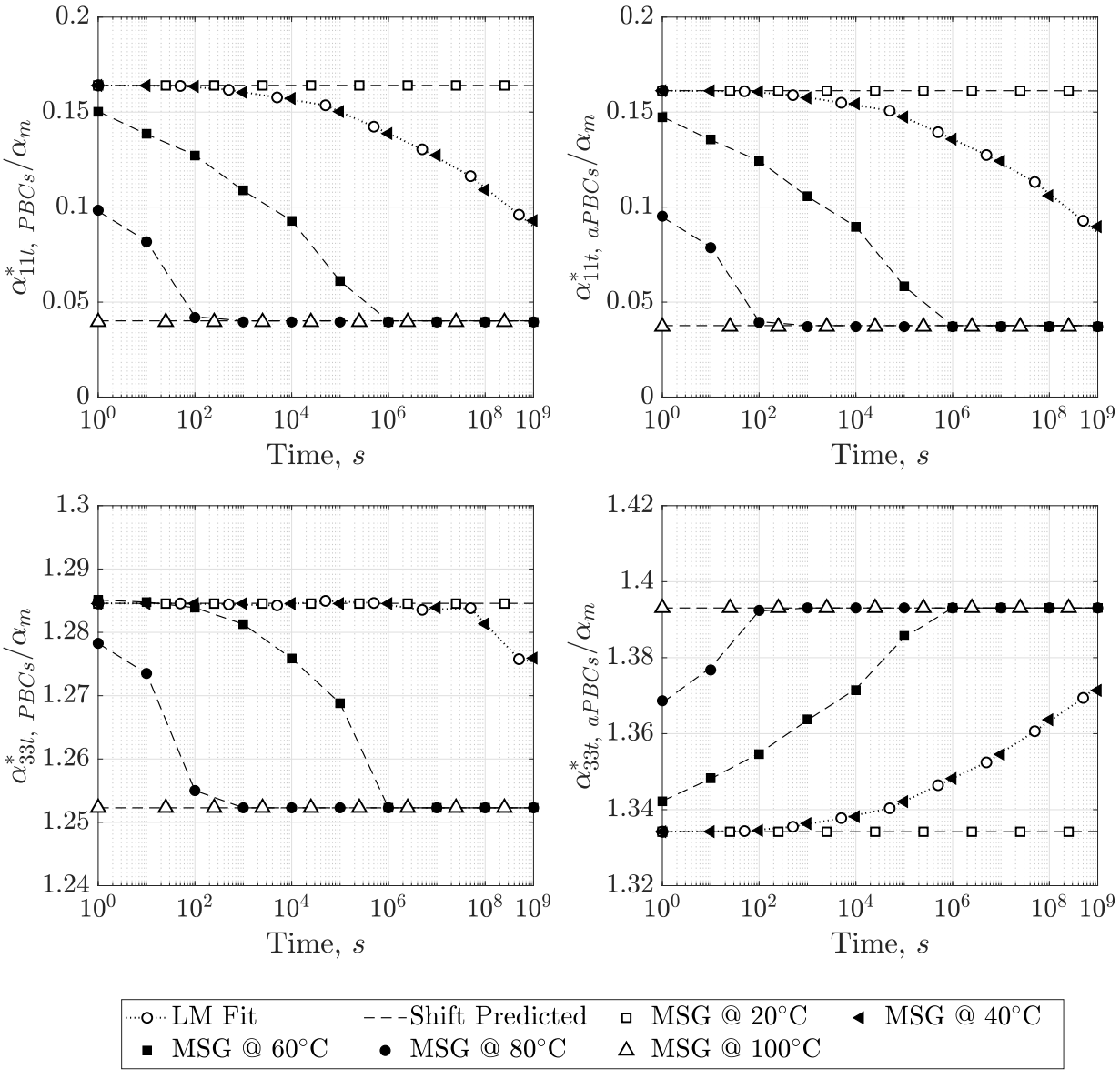

Figure 4.10. Evolution of normalized effective CTEs for the textile composite with PBCs (left) and aPBCs (right), respectively.

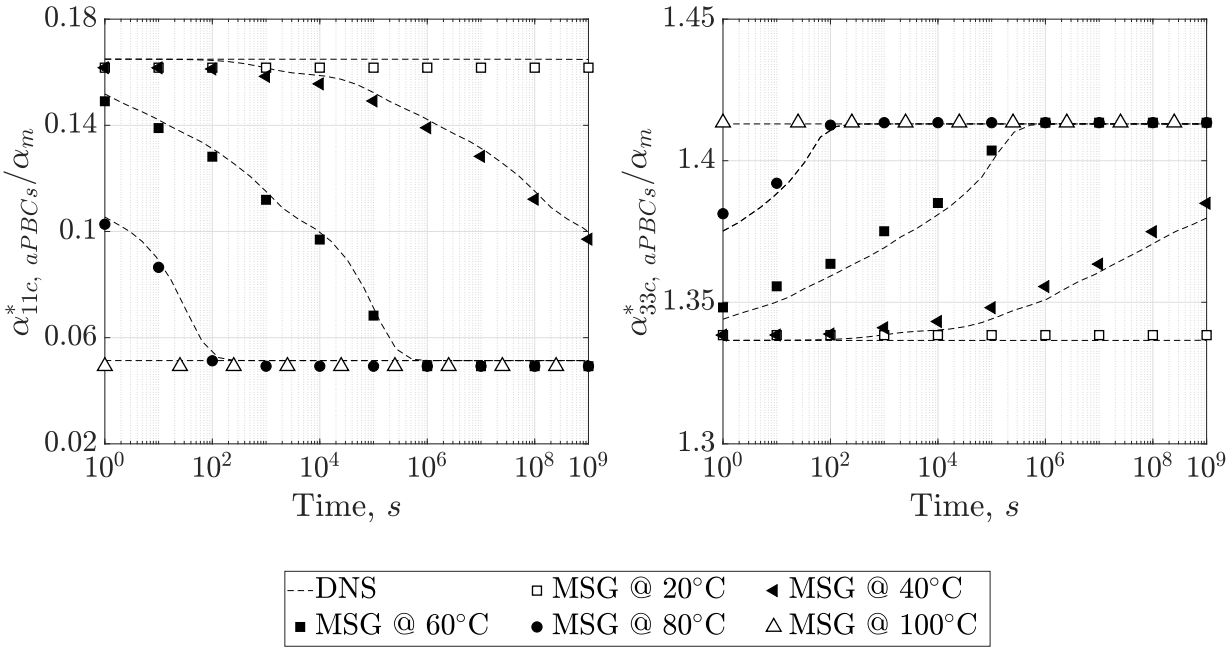

Figure 4.11. Normalized direct numerical simulation results of the textile composite and MSG with aPBCs.

Finally, the dashed lines of Figures 4.8-4.10 represent the effective engineering constants and CTEs computed applying the shift factor to the effective properties of the textile composite at reference temperature (i.e. $T = 40°C$). Similarly to the previous case, the shift was applied to the components of the stiffness matrix and then, the effective engineering constants were computed. As the difference between the shifted and directly calculated results was less than 1%, we can conclude that the shifted effective thermoviscoelastic properties agree well with the ones computed using the MSG solid model. In this way, when computing the effective properties departing from the reference temperature, both resin and yarn with thermoviscoelastic behavior, it is possible to calculate the effective properties at different temperatures by applying directly the shift factor to the constituents and then performing the homogenization, or by doing the homogenization at reference temperature first and then applying the shift factor directly to the effective properties. As it occurred in the previous two cases, the latter approach clearly appeared to be more efficient. The shift factor of the homogenized textile composite was the same as the one of the resin.

4.2 Summary

This chapter provided the numerical case studies to analyze the efficiency of the MSG-based QE model. Three numerical case studies comprising UDFRC, a balanced and symmetric laminate, and a textile composite were analyzed using MSG. The results were compared against 3D RVE analysis showing good agreement, except when time-dependent CTE properties were considered at constituent level. In these cases, 3D RVE analysis was not able to properly capture the convergence towards the long-term effective CTEs for $T = 40°C$, $T = 60°C$ and $T = 80°C$, as a priori assumptions of thermal loads are required for the computations. MSG accurately captured these long-term behaviors for both constant and time-dependent constituent CTEs, and also increased the computation efficiency. In addition, these simulation efforts allowed to conclude that the effective CTEs of a composite material that has thermoviscoelastic behavior show time and temperature dependency regardless of whether constant or time-dependent CTEs are considered at constituent level. When considering constant CTEs at constituent level, the thermoviscoelastic nature of the

stiffness matrix drives the time- and temperature-dependent behavior of the effective CTEs. Furthermore, the validity of the time shift to compute the homogenized properties at different temperatures departing from the effective properties at reference temperature was analyzed. This analysis revealed that despite the heterogeneous thermoviscoelastic nature of the composite material, the temperature dependencies of the effective properties given by the shift factor have the same character as the ones of the polymer matrix. This aspect was proved valid for the two-step homogenization approach used in textile composites, computing the effective laminate properties from homogenized lamina properties, and computing UDFRC properties in terms of fiber and matrix properties. The analysis of the textile composite also elucidated that the use of aPBCs allows to distinctively capture the increase of the through-the-thickness CTE with increased time and temperature. Direct numerical simulations corroborated this trend of the through-the-thickness CTE. It is noted that this feature was not properly captured using PBCs, as a decrease of the through-the-thickness CTE was observed for increased time and temperature. Although the proposed approach does not guarantee the accuracy of the local stress field for a general strain input, it is the most efficient and accurate method for multiscale homogenization of linear thermoviscoelastic composite structures when the long-term thermoviscoelastic behavior and thermal stability are of a concern. For instance, for thermoviscoelastic structures that undergo large deformations that induce geometrical nonlinearity on structural scale, the effective properties computed with the present approach can be used in a FEA package such as Abaqus [104] to model the thermoviscoelastic behavior. However, when geometrical or material nonlinearities, or both nonlinearities at the SG scale are also present, the approach here presented is no longer valid.

5. CASE STUDIES WITH THERMOVISCOELASTIC PLATES/SHELLS

This chapter presents the numerical case studies with MSG-based shell/plate model. In the first subsection, MSG plate/shell model with the QE method implemented in SwiftComp^{TM} is used to compute the effective properties, engineer the mesostructure and match the experimental experimental bending stiffness data provided by NASA LaRC. $[\pm 45_{PW}]_4$ laminate made of M30S/PMT-F7 plain weave composite is considered. Once the elastic properties of the selected mesostructure are in good agreement with the experimental data, the thermoviscoelastic ABD matrix and the plate thermal stress resultants of the laminate are also computed. Part of this work was presented in American Society for Composites (ASC) 2020 conference [141]. In the second section, the implementation of the MSG-based plate/shell model with the DI method into Abaqus as a UGENS user-defined subroutine is presented. This subroutine was used within our research group by a colleague to simulate the column bending test (CBT) of the $[\pm 45_{PW}]_4$ laminate and compare against experimental data provided by NASA LaRC validating the subroutine. In this dissertation, the main outcomes of this validation are briefly outlined for completeness. However, a more detailed description was published at SciTech 2021 [125] and later extended into a journal paper currently under review by NASA LaRC. It is also noted that the global behavior of lenticular and TRAC booms are numerically simulated using MSG-based plate/shell model with the DI method in Chapter 6 to verify the MSG-based beam model.

5.1 Effective Thermoviscoelastic Plate/Shell Properties

5.1.1 Engineering the Mesostructure

For this numerical case, SwiftComp^{TM} [112] was used to engineer the mesostructure and match the effective experimental properties of the M30S/PMT-F7 plain weave (PW) composite. The MSG-based plate/shell model with the QE method was implemented in SwiftComp^{TM}. Both the in-plane elastic experimental data and the relaxation of the bending stiffness D_{11} over the time were found in the literature [142]. Therefore, the objectives were

first to match the in-plane elastic lamina properties and then, compute the corresponding viscoelastic behavior of D_{11} over time.

Table 5.1. Prony series coefficients of PMT-F7 toughened epoxy resin computed from NASA LaRC experimental data at $T_0 = 40°C$.

s	λ_s (s)	E_s (MPa)
∞	–	1546.0
1	37.0	324.7
2	1.0E+02	236.3
3	5.0E+02	7.1
4	1.0E+03	201.2
5	5.0E+03	81.5
6	1.0E+04	89.5
7	5.0E+04	223.9
8	1.0E+05	19.5
9	5.0E+05	109.3
10	1.0E+06	60.0
11	5.0E+06	0.8

The effective lamina properties of the M30S/PMT-F7 PW textile composite was computed using PMT-F7 toughened epoxy resin characterized by NASA LaRC and fit into Prony series coefficients shown in Table 5.1. These data were later made available to the general public [143]. A Poisson's ratio of 0.36, a coefficient of thermal expansion (CTE) of α_m = 60 μ/°C at a reference temperature of 40°C and viscoelastic behavior was assumed to be isotropic for the resin. The fiber constituent properties and microstructure characteristics for the computation were found in literature ([142], [144]). The M30S fiber was modeled as transversely isotropic elastic materials and $\alpha_{11f} = 0.100$ μ/°C and $\alpha_{22f} = \alpha_{33f}$= 10.080 μ/°C at the reference temperature of 40°C were assumed. A two-step homogenization approach was applied [110] to compute the effective properties. First, the effective solid properties of the microstructure (i.e. yarn) were computed which later were input as constituent properties for the computation of the effective properties of the mesostructure (i.e. laminate). The yarn was modeled as a 2D SG with hexagonal pack microstructure and a fiber volume fraction of 0.62 (see Figure 5.1 left). Periodic boundary conditions were applied and 18,124 linear four-noded quadrilateral elements were used to mesh it.

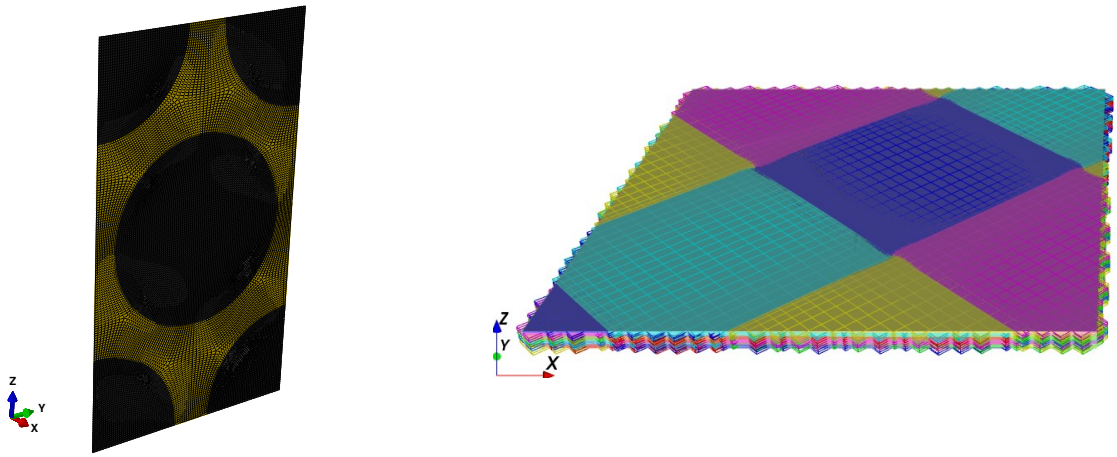

Figure 5.1. 2D SG for the yarn microstructure and 3D SG for the $[\pm 45_{PW}]_4$ mesostructure used to compute the effective properties (left and right).

Appendix A.3 provides a comparison about the yarn properties computed using PMT-F7 toughened epoxy data provided by NASA LaRC and the one found in the literature [145] using MSG-based solid model. From this comparison, it was concluded that the NASA LaRC resin relaxed faster than the one found in the literature. As for the composite laminate mesostructure, a 3D SG was created with TexGen4SC [138] to model $[0_{PW}]_4$ (i.e. 4-ply PW laminate oriented at 0/90 degrees). The geometry of the mesostructure was obtained from the literature [144]. PBCs were also considered and 256,000 elements were used to mesh it. For both the microstructure and mesostructure, the interphases between the fiber and the resin, and between the yarn and the resin were not modeled.

Then, the elastic lamina effective properties were computed using MSG-based solid model and compared against experimental in-plane lamina data available in the literature [142]. For that, the maximum Young's modulus of the experimental data was selected as the Young's modulus of the resin and the effective yarn properties for $t = 0$ s were considered as the elastic yarn properties. The mesh density was modified until the experimental properties for the M30S/PMT-F7 [142] were matched being the selected results the ones reported for the yarn and the laminate. As shown in Table 5.2, both Young's modulus values are within 1.2% of the experimental values and the highest difference comes from the shear modulus.

In addition, a $[\pm 45_{PW}]_4$ (i.e. 4-ply PW laminate oriented at 45/-45 degrees) 3D SG was created in TexGen [137] using the mesh density and geometrical properties of the $[0_{PW}]_4$ case

Table 5.2. Thin-ply lamina material properties for M30S/PMT-F7 PW composite at $T_0 = 40°$ C.

	Cured ply thickness	E_1	E_2	ν_{12}	G_{12}
Experimental M30S/PMT-F7 [142]	60±3 μm	94.2 GPa	94.2 GPa	0.026	3.9 GPa
MSG solid M30S/PMT-F7	57 μm	93.1 GPa	93.1 GPa	0.026	3.3 GPa
Difference M30S/PMT-F7, %	0-10%	1.2%	1.2%	0%	15%

(see Figure 5.1 right). Then, the MSG-based plate/shell model implemented in SwiftComp™ [112] was used to compute the effective viscoelastic plate/shell stiffness matrix. The MSG results are compared against the experimental results in Figure 5.2. A reference temperature of $T_0 = 40°$C was selected, as this is the maximum stowage temperature expected for the NASA solar sail application. The Prony series coefficients of the effective A, B, D relaxation matrices were computed using Levenberg-Marquardt algorithm in Matlab 2018b and are summarized in Table 5.3. It is noted that the effective A, B, D relaxation matrices were computed up to the maximum time available of the resin data, which is $t = 10^7$ s for NASA LaRC resin. The MSG NASA LaRC $D_{11,\infty} = D_{22,\infty}$ relaxed value at $t = 10^7$ s is within a 0.88% of the experimental relaxed value. In case of $t = 0$ s, this difference is 1.75%. Figure 5.2 also shows that MSG slightly underpredicts the experimental value of D_{11} but it provides closer results than the multiscale model presented in literature [142].

Table 5.3. Effective plate/shell viscoelastic stiffness properties of the M30S/PMT-F7 $[\pm 45_{PW}]_4$ laminate with hexagonal pack yarn and resin from NASA LaRC at $T_0 = 40°$C.

s	λ_s s	$A_{11,s} = A_{22,s}$ N/mm	$A_{12,s}$ N/mm	$A_{33,s}$ N/mm	$D_{11,s} = D_{22,s}$ N·mm	$D_{12,s}$ N·mm	$D_{33,s}$ N·mm
∞		1.093E+04	1.000E+04	1.011E+04	4.733E+01	4.334E+01	4.379E+01
1	3.70E+01	1.454E+02	2.383E+01	4.408E+01	6.304E-01	1.036E-01	1.912E-01
2	1.00E+02	1.285E+02	2.359E+01	4.200E+01	5.555E-01	1.013E-01	1.814E-01
3	1.00E+03	1.081E+02	1.969E+01	3.512E+01	4.654E-01	8.330E-02	1.508E-01
4	5.00E+03	4.632E+01	9.368E+00	1.614E+01	2.030E-01	4.220E-02	7.110E-02
5	1.00E+04	4.754E+01	8.497E+00	1.525E+01	2.039E-01	3.530E-02	6.490E-02
6	5.00E+04	1.318E+02	2.694E+01	4.624E+01	5.737E-01	1.190E-01	2.023E-01
7	1.00E+05	1.280E+01	2.895E+00	4.808E+00	5.190E-02	9.400E-03	1.800E-02
8	5.00E+05	6.690E+01	1.425E+01	2.413E+01	2.966E-01	6.790E-02	1.103E-01
9	1.00E+06	3.940E+01	9.122E+00	1.506E+01	1.631E-01	3.260E-02	5.880E-02
10	5.00E+06	4.446E-01	7.810E-02	1.414E-01	5.100E-03	3.300E-03	3.300E-03

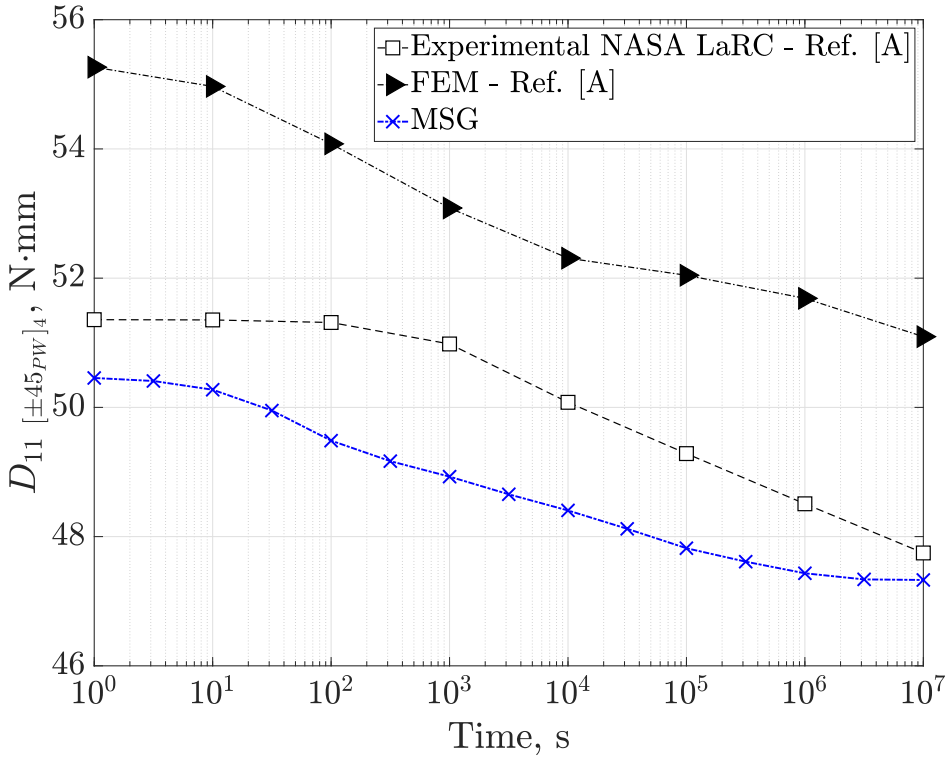

Figure 5.2. Comparison of the D_{11} term for a M30S/PMT-F7 $[\pm 45_{PW}]_4$ laminate. Note that Ref. [A] represents Ref. [142].

Finally, the parameters for the PMT-F7 toughened epoxy resin shift function were manually fit from experimental data provided by NASA LaRC for this study. The expression for WLF equation was found to be equal to

$$\log a_T = -\frac{3.6868(T - T_0)}{13.5513 + (T - T_0)} \tag{5.1}$$

where the temperature was expressed in °C and $T_0 = 40$ °C. Appendix A.3 provides further details for obtaining this expression.

5.1.2 Effective Thermoviscoelastic Plate/Shell Thermal Stress Resultants

Once the $[\pm 45_{PW}]_4$ 3D SG mesostructure presented in the previous subsection was validated, the plate/shell stiffness properties and thermal resultants at temperatures of 40°C, 60°C, 80°C, 100°C and 120°C were computed using SwiftComp™ [112]. To do so, first the effective yarn properties at different temperatures were computed using the MSG-based solid

model implemented SwiftComp^{TM}. To do so, the M30S fiber data, which was treated as elastic, and PMT-F7 toughened epoxy resin data, which was treated as thermoviscoelastic, at different temperatures were input as constituent material properties. Afterwards, the effective thermoviscoelastic properties of the yarn and the PMT-F7 toughened epoxy resin at different temperatures were used as constituent properties to run homogenization of the $[\pm 45_{PW}]_4$. As it was proved for the solid case, for this last computation the yarn and the resin were treated as thermoviscoelastic with the same time shift function. The effective plate/shell stiffness properties and thermal stress resultants divided by the temperature change (i.e. $N_{T_{11},\infty}/\bar{\theta}$) were normalized using the corresponding relaxed value as shown in Figures 5.3 - 5.4 (left). It is noted that all the relaxed values used to normalized the effective properties are listed in the first row of the Table 5.3 and $N_{T_{11},\infty}/\bar{\theta} = -0.035$ N/mm/$\circ$C. However, the thermal stress resultants were not normalized. For all the CTEs of the yarn and resin, $T_0 = 40°$C was considered as reference temperature and thus, the effective thermal stress resultants at these temperatures were equal to 0 N as depicted in Figure 5.4. FEM analysis was conducted to verify the results of the thermal stress resultants. As SwiftComp^{TM} and FEM analysis predicted the same thermal stress resultants, only the MSG results are shown in Figures 5.3-5.4. The results also revealed that the normalized values of $A_{11} = A_{22}$, $D_{11} = D_{22}$, and $N_{T_{11}}/\bar{\theta} = N_{T_{22}}/\bar{\theta}$ relaxed faster than A_{12}, A_{33}, D_{12}, and D_{33} as the former were more dominated by the thermoviscoelastic behavior of the resin.

In addition, to investigate the validity of the shift function of the resin to represent the effective beam properties, the shift factor of the resin given by Eq. (5.1) was applied to the effective beam properties at a reference temperature of $T_0 = 40°$C summarized in Table 5.3. Shifted values at $T = 60°$C, 80°C, 100°C and 120°C were computed following this approach and are represented with dashed lines in Figures 5.3 - 5.4 (left). We can observe that the shifted homogenized values agree well with the ones computed using the MSG-based plate/shell model. This conclusion is also valid for the thermal stress resultants divided by the temperature change (i.e. $N_{T_{11}}/\bar{\theta}$). Consequently, despite the heterogeneous thermoviscoelastic nature of the composite material, the temperature dependencies of the effective plate/shell stiffness properties represented by the shift factor have the same characteristics as those of the polymer matrix.

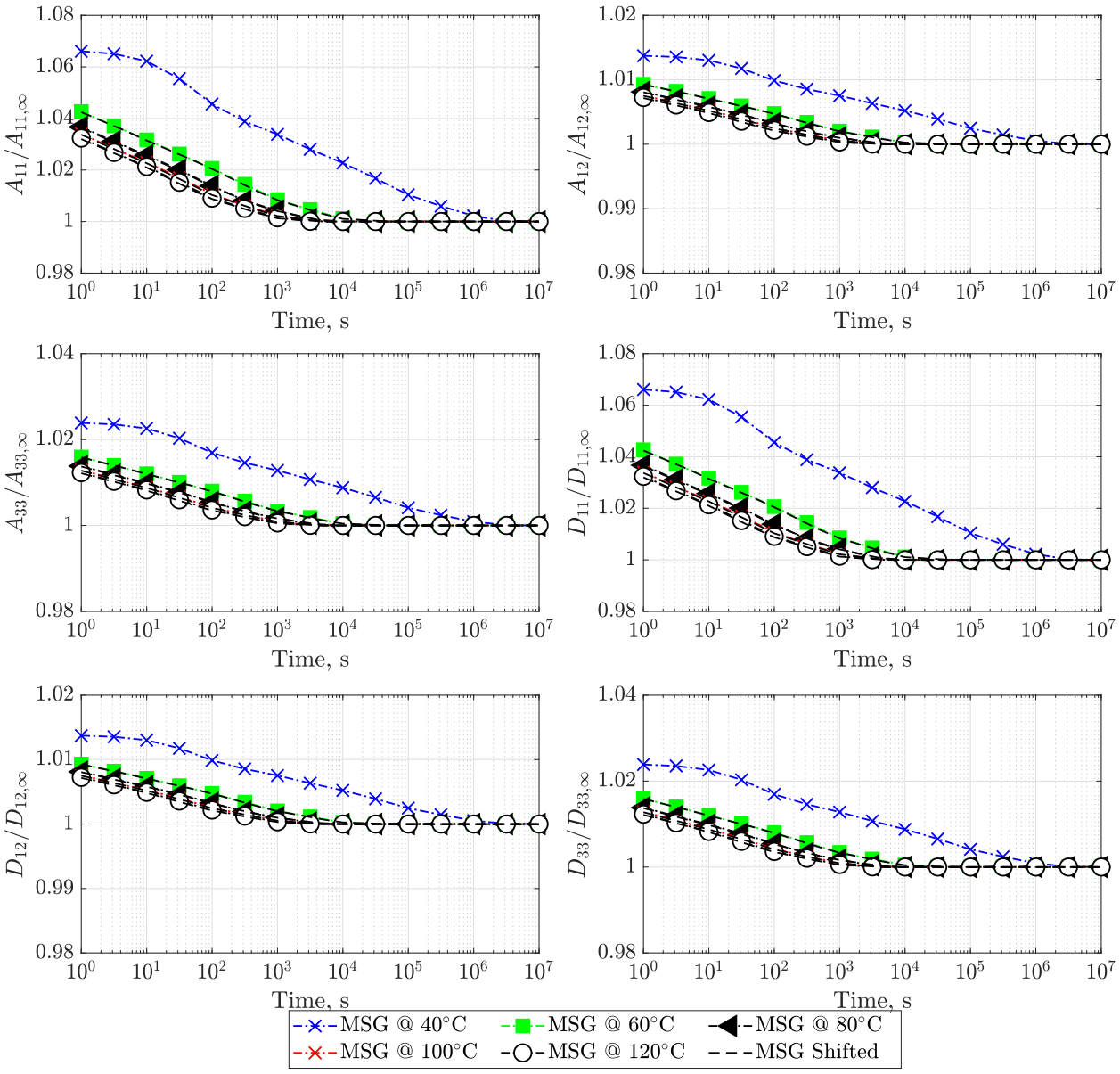

Figure 5.3. Evolution of the normalized plate/shell thermoviscoelastic stiffness properties of the M30S/PMT-F7 $[\pm 45_{PW}]_4$ laminate with hexagonal pack yarn and resin data from NASA LaRC. It is noted that $A_{11} = A_{22}$ and $D_{11} = D_{22}$.

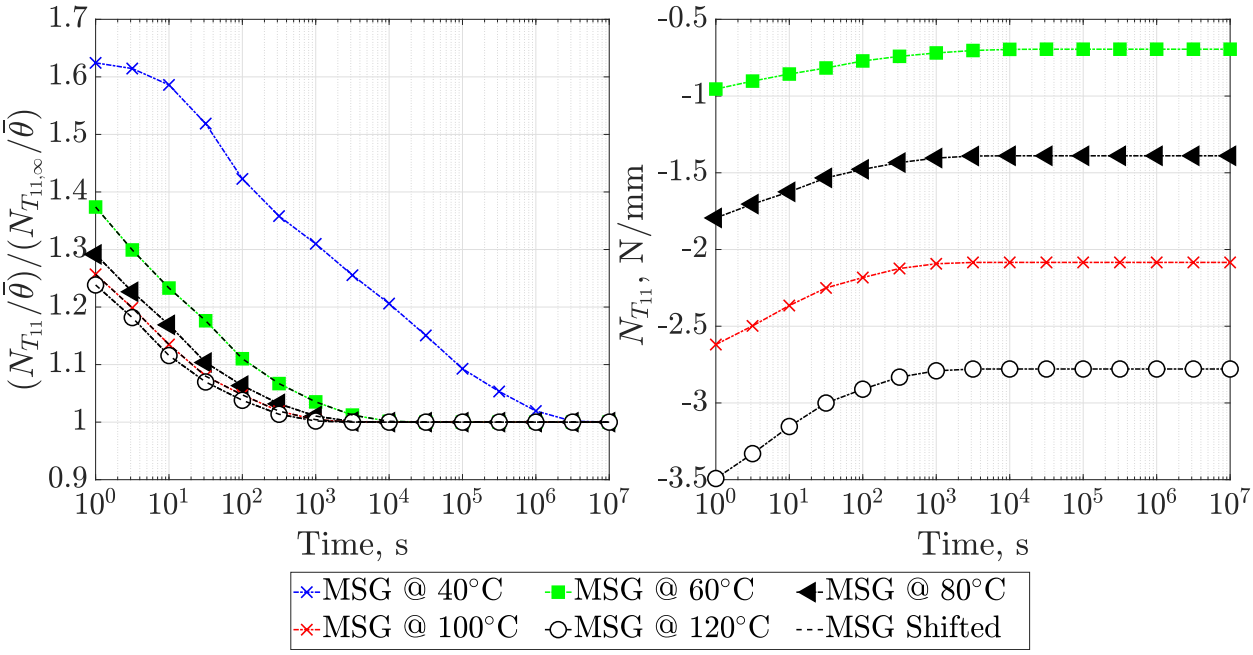

Figure 5.4. Evolution of the normalized plate/shell thermal stresses of the M30S/PMT-F7 $[\pm 45_{PW}]_4$ laminate with hexagonal pack yarn and resin data from NASA LaRC. It is noted that $N_{T_{11}}/\bar{\theta} = N_{T_{22}}/\bar{\theta}$.

5.2 Global Thermoviscoelastic Plate/Shell Model

5.2.1 Validation against Experimental Data

The MSG-based plate/shell model with the DI method was implemented into Abaqus as a UGENS user-defined subroutine. The analysis workflow followed to simulate the global behavior of large viscoelastic structures in Abaqus is shown in Figure 5.5. First, the material constituent behavior is homogenized using MSG and then fit each term of the ABD matrix in Prony series coefficients. For the sake of simplicity, the same discrete stress relaxation times are considered for all the terms. Then the structural simulation is carried out considering the viscoelastic shell section behavior that is directly input from the UGENS subroutine. The steps that the subroutine follows for each time increment are shown in green in Figure 5.5. Once the Abaqus structural simulation is finished, results are post-processed and MSG can be used for dehomogenization (not pursued herein). The focus of this section is on the structural simulation. In case large deformation is present, such as in TP-HSC used in deployable composite structures, geometric nonlinearity is considered in the structural FEA.

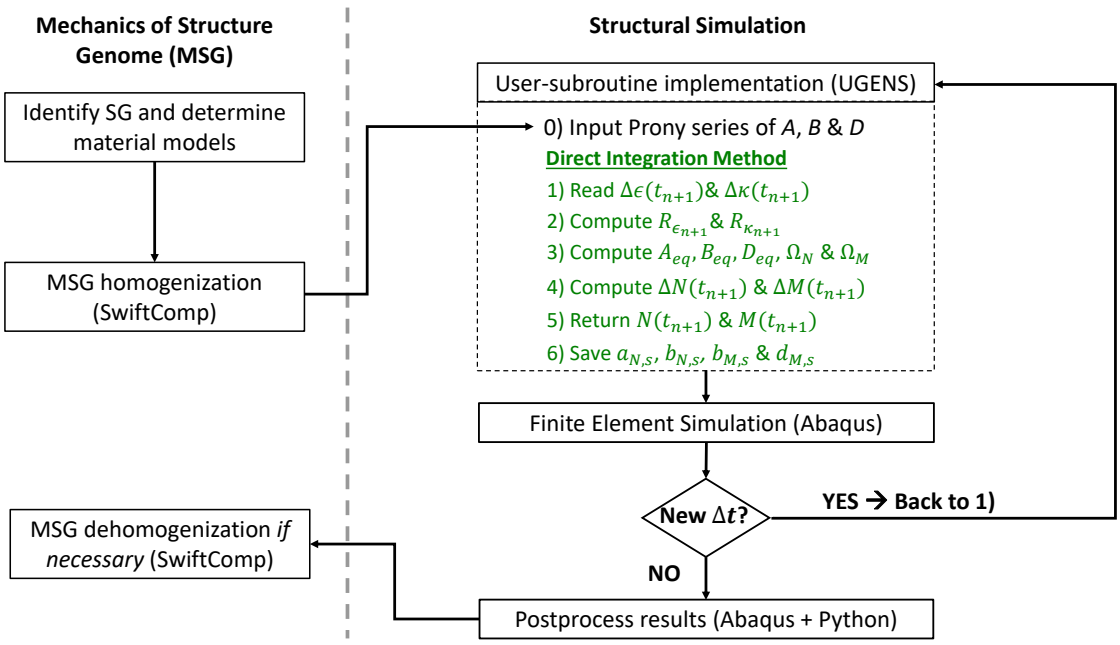

Figure 5.5. Workflow of the MSG-based simulation framework for UGENS subroutine in Abaqus.

As part of this work, a UGENS subroutine for the M30S/PMT-F7 $[\pm 45_{PW}]_4$ laminate was developed using the DI method and the Prony series coefficients of the ABD matrix presented in Table 5.3. Then, a colleague within our research group created the structural FEA of a column bending test for the M30S/PMT-F7 $[\pm 45_{PW}]_4$ laminate and run the simulations using this subroutine. Further details of the structural model of the CBT can be found in [125]. The simulated results were compared against the experimental data provided by NASA LaRC for the same CBT at $T = 40°C$. The experimental curvature during folding (see the left figure of Figure 5.6), moment during relaxation (see Figure 5.7), as well as residual curvature immediately after unfolding were in qualitative agreement with the simulation results computed using the DI method.

To evaluate the capability for predicting the residual deformation of the present model, the predicted and measured curvatures were also compared in the unfolding and recovery stages, as shown in the right figure of Figure 5.6. Table 5.4 also shows the curvature values during relaxation, after unfolding and after recovery. Approximate values of the experimental data were chosen for the curvature shown in the column "After unfolding" column of

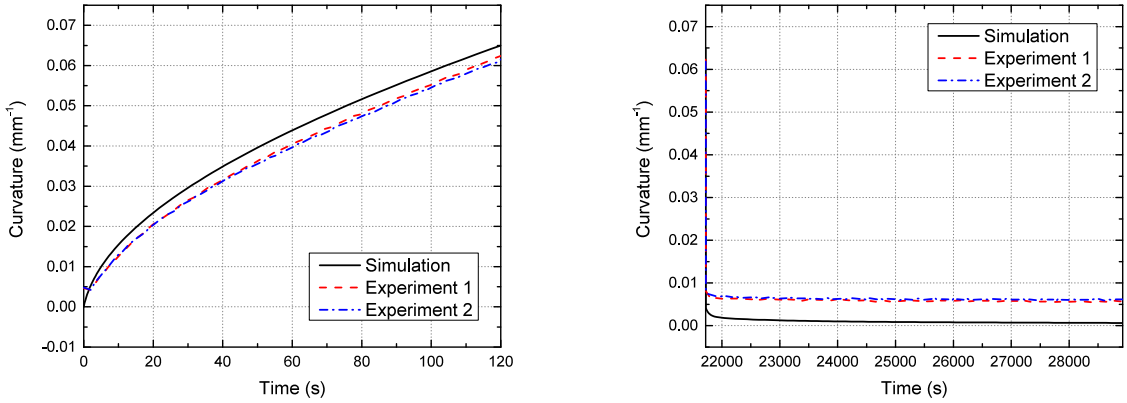

Figure 5.6. Curvature history during folding (left) and residual curvature after relaxation (right) [125].

Table 5.4, as it was cumbersome to clearly define the separation between the folding and relaxation steps. The analysis of residual deformation after relaxation revealed slight disagreement, especially in the final steady-state curvature. The presence of viscoplasticity was identified as the most likely reason for this discrepancy, as the difference between the computed and experimental results remained relatively constant through the recovery period [125]. Indeed, the large surface strains imposed on the specimens during the CBT experimental test likely caused some degree of plastic deformation. This allowed to validate the UGENS subroutine and identify the necessity to develop a viscoplastic material model and a nonlinear shell model as future work.

Table 5.4. Residual curvature after relaxation [125].

Curvature, mm^{-1}	Relaxation	After unfolding (Approx.)	After recovery
Simulation	0.06500	0.004130	0.0006444
Experiment 1	0.06239	0.007749	0.005936
Experiment 2	0.06153	0.008352	0.006154

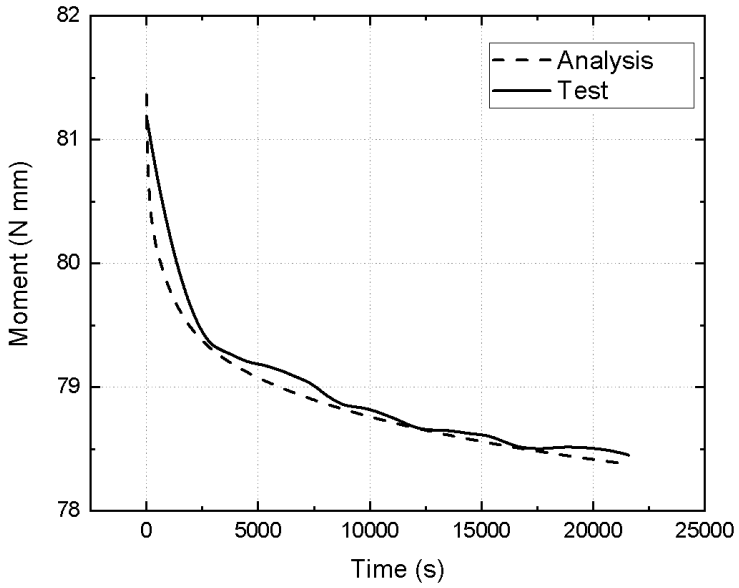

Figure 5.7. Moment relaxation history at $T_0 = 40°C$.

5.2.2 Temperature Shift

To validate the temperature shift capability of the thermoviscoelastic plate/shell model, CBT simulations were performed with the shift factor implemented within the UGENS subroutine in Abaqus. This capability enabled the simulation under different temperature using the reduced time. This is a common approach in experiments to achieve large creeping and relaxation without spending a long time. For this study, materials were considered thermorheologically simple and the shift function was represented with Eq. (5.1). The analysis of the effective plate/shell stiffness properties proved the temperature dependencies of the effective plate/shell stiffness properties are governed by the same shift factor as the polymer matrix. Using the reduced time given by Eq. (5.1), CBT under 40°C, 60°C and 80°C were simulated.

The results revealed that the simulation can capture the shifting of the curves and provides a good agreement with the experiment. Residual curvature and strain were not compared because of the strong noise in the experimental data.

5.3 Summary

This chapter presented numerical cases to validate the MSG-based plate/shell model. First, the MSG-based plate/shell model with the QE method was used to compute the viscoelastic properties of the $[\pm 45_{PW}]_4$ laminate made of M30S/PMT-F7 PW composite. Experimental PMT-F7 toughened epoxy resin data received from NASA LaRC was used as constituent property for both the yarn and the laminate in the two-step homogenization approach. To compute the effective yarn properties, MSG-based solid model was used. Then, effective viscoelastic properties were compared against the experimental bending stiffness data provided by NASA LaRC showing good agreement. The difference between the MSG and experimental results for both the initial (i.e. $t = 0$ S) and the relaxed values (i.e. $t = 10^7$ S) were smaller than the ones provided by the FEM models of the literature. Consequently, the viscoelastic analysis based on the MSG models can be safely used in the microscale (i.e. fiber and matrix level) and mesoscale (i.e. yarn and matrix level) modeling.

As a second step, the validated 3D SG of the $[\pm 45_{PW}]_4$ laminate was used to compute the effective plate/shell properties and thermal stress resultants at different temperatures. From a multiscale analysis perspective, it was concluded that despite the heterogeneous thermoviscoelastic nature of the composite material, the temperature dependencies of the effective plate/shell properties are driven by the same shift factor as the polymer matrix except for nonuniform temperature distribution. This is also valid for the thermal stresses divided by the temperature change $\bar{\theta}$ (i.e. $N_{T_{11}}/\bar{\theta}$) and corroborates the results found in the previous chapter for the MSG-based solid model.

The second section presented the validation of the MSG-based plate/shell model with the DI method. The model was implemented into Abaqus as a UGENS user-defined subroutine. Then, the subroutine was used within our research group to run CBT simulations [125]. These simulations were compared against experimental results provided by NASA LaRC. The comparison confirmed that whereas the QE method is convenient for computing thermoviscoelastic effective properties, it cannot capture the residual stresses and strains as it losses the stress history. Furthermore, the experimental curvature during folding, moment during relaxation, as well as residual curvature immediately after unfolding were in qualita-

tive agreement with the simulation results computed using the DI method. This comparison allowed to validate the MSG-based plate/shell model with the DI method and its subroutine that later was used for the simulation of thin-ply high strain composite booms.

6. CASE STUDIES WITH THERMOVISCOELASTIC BEAMS

This chapter presents a few numerical examples to verify the MSG-based linear thermoviscoelastic beam model. The first section uses the MSG-based QE method presented in Section 3.2.3 to compute the effective beam stiffness properties. Numerical examples containing uniform and nonuniform temperature distribution are presented to verify the formulation. Part of this work was presented in American Society for Composites (ASC) 2020 conference [141] and later transformed into a journal paper currently under review by NASA LaRC. The second section describes the implementation of the MSG-based DI method presented in Section 3.3.3 to compute the global beam behavior. The latter case is verified using direct numerical simulations (DNS) implemented following the DI method for solid elements derived in Section 3.3.1 and MSG-based plate/shell model with the DI method formulated in Section 3.3.2. Part of this work has been published at the SciTech 2021 conference [146].

6.1 Effective Thermoviscoelastic Beam Stiffness Properties

To demonstrate the accuracy of the MSG-based beam model, three different numerical examples were selected to homogenize and compute the equivalent beam properties. The first case consists of a collapsible tubular mast (CTM), referred here as a lenticular boom with uniform temperature distribution. The second case studies a triangular rollable and collapsible (TRAC) boom with a uniform temperature distribution. The last case considers both the lenticular and TRAC booms with steady-state nonuniform temperature distribution. SwiftComp^{TM} [112] is used to perform the thermoviscoelastic cross-sectional analyses of the three cases, which are also verified using DNS and available analytical solutions.

6.1.1 Material Properties

For these numerical cases two different TP-HSC composites, a M30S/PMT-F7 plain weave (PW) textile composite and a MR60H/PMT-F7 unidirectional (UD) composite were considered. The effective lamina properties of both composite materials were computed using PMT-F7 toughened epoxy resin characterized by NASA LaRC [143] and fit into Prony series

coefficients shown in Table 5.1. Further comparison between the resin experimental data provided by NASA LaRC and the one available in the literature is summarized in Appendix A.3. A Poisson's ratio of 0.36, a coefficient of thermal expansion (CTE) of $\alpha_m = 60$ μ/°C at a reference temperature of 40°C and viscoelastic behavior were assumed to be isotropic for the resin. The fiber constituent properties and microstructure characteristics for the computation were found in literature (see Refs. [144] and [142] for M30S/PMT-F7 and Refs. [25] and [142] for MR60H/PMT-F7). Both M30S and MR60H fibers were modeled as transversely isotropic elastic materials. In addition, for both fibers $\alpha_{11f} = 0.100$ μ/°C and $\alpha_{22f} = \alpha_{33f}$= 10.080 μ/°C at the reference temperature of 40°C were assumed. For the M30S/PMT-F7 PW textile composite, a two-step homogenization approach was applied [110]. First, the effective solid properties of the microstructure (i.e. yarn) were computed which later were input as constituent properties for the computation of the effective properties of the mesostructure (i.e. laminate). The yarn was modeled as a 2D SG with hexagonal pack microstructure and a fiber volume fraction of 0.62 (see the left figure of Figure 6.1). Periodic boundary conditions were applied and 18,124 linear four-noded quadrilateral elements were used to mesh it. A 3D SG was created with TexGen4SC [138] to model $[0_{PW}]_4$ (i.e. 4-ply PW laminate oriented at 0/90 degrees) composite laminate mesostructure (see the right figure of Figure 6.1). PBCs were also considered and 256,000 elements were used to mesh it. The MR60H/PMT-F7 UD composite was modeled as a 2D SG with hexagonal pack microstructure with PBCs and a fiber volume fraction equal to 0.56. In this case, 18,088 elements were used to mesh the 2D SG.

Before calculating the thermoviscoelastic effective properties, the elastic effective properties were computed and compared against experimental in-plane lamina data available in the literature [142]. For that, the maximum Young's modulus of the experimental data was selected as the Young's modulus of the resin and the effective yarn properties for $t = 0$ s were considered as the elastic yarn properties. As shown in Table 6.1, both Young's modulus values are within 1.2% of the experimental values and the highest difference comes from the shear modulus. With these geometrical properties and mesh density, time-dependent effective yarn properties and the resin's Prony series coefficients of Table 5.1 were input in the MSG-based solid thermoviscoelastic model available in SwiftComp$^{\text{TM}}$ [141] to compute the

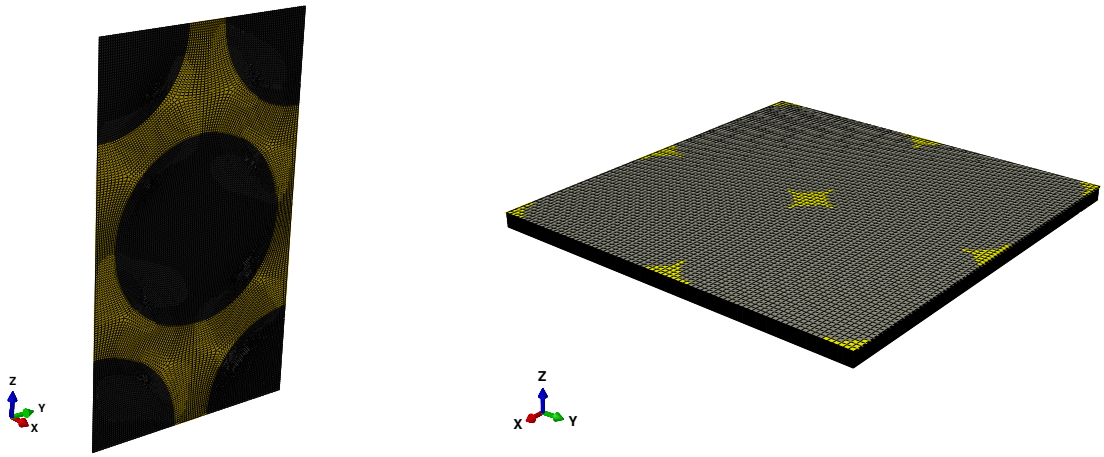

Figure 6.1. 2D SG for the yarn microstructure and 3D SG for the plain weave mesostructure used to compute the effective properties of the M30S/PMT-F7 PW textile composite at 0° orientation (left and right).

time-dependent effective lamina properties. The Prony series coefficients presented in Tables 6.2-6.3 were used to represent the effective viscoelastic properties of both TP-HSC materials at a reference temperature of $T_0 = 40°C$, as this is the maximum stowage temperature expected for the NASA solar sail application. The Prony series coefficients of the effective laminate stiffness, Young's and shear moduli were computed using Levenberg-Marquardt algorithm in Matlab 2018b. For the effective Poisson's ratios (i.e. ν_{12} and ν_{23}) the trust region reflective algorithm in Matlab 2018b was used instead, which provided a smoother approach to capture their time-dependent behavior.

Table 6.1. Thin-ply in-plane lamina material properties.

	Cured ply thickness	E_1	E_2	ν_{12}	G_{12}
Experimental M30S/PMT-F7 [142]	60±3 μm	94.2 GPa	94.2 GPa	0.026	3.9 GPa
MSG solid M30S/PMT-F7	57 μm	93.1 GPa	93.1 GPa	0.026	3.3 GPa
Difference M30S/PMT-F7, %	0-10%	1.2%	1.2%	0%	15%
Experimental MR60H/PMT-F7 [142]	40±3 μm	174.4 GPa	8.4 GPa	0.259	6.4 GPa
MSG solid MR60H/PMT-F7	-	174.4 GPa	8.3 GPa	0.259	2.9 GPa
Difference MR60H/PMT-F7, %	-	0 %	1.2%	0%	54.7%

Table 6.2. Effective viscoelastic lamina stiffness properties of the M30S/PMT-F7 PW textile composite at T_0 =40°C.

s	λ_s s	$C_{11,s} = C_{22,s}$ MPa	$C_{12,s}$ MPa	$C_{13,s} = C_{23,s}$ MPa	$C_{33,s}$ MPa	$C_{44,s} = C_{55,s}$ MPa	$C_{66,s}$ MPa	$\alpha_{11,s} = \alpha_{22,s}$ μ°/C	$\alpha_{33,s}$ μ°/C
∞		91,526.00	2,856.80	3,070.20	7,285.40	1,975.80	2,020.60	1.649	48.059
1	3.70E+01	765.69	379.04	447.69	993.64	254.12	266.56	0.193	0.016
2	1.00E+02	684.27	315.84	376.20	849.00	220.50	230.16	0.167	0.012
3	1.00E+03	575.65	267.59	318.51	716.91	185.74	194.00	0.140	0.010
4	5.00E+03	249.90	108.29	130.18	297.08	77.92	81.03	0.059	0.004
5	1.00E+04	252.27	118.50	140.78	316.55	81.94	85.61	0.061	0.005
6	5.00E+04	713.04	307.44	370.03	843.80	221.14	229.99	0.167	0.010
7	1.00E+05	70.53	28.36	34.57	79.42	20.94	21.72	0.016	0.003
8	5.00E+05	364.46	152.75	184.75	422.85	111.17	115.46	0.084	0.006
9	1.00E+06	218.08	85.97	105.20	242.39	64.08	66.40	0.049	0.000
10	5.00E+06	2.34	1.10	1.31	2.96	0.77	0.80	0.001	0.003

Table 6.3. Effective viscoelastic lamina stiffness properties of the MR60H/PMT-F7 unidirectional composite at $T_0 = 40$°C.

s	λ_s s	$E_{1,s}$ MPa	$E_{2,s} = E_{3,s}$ MPa	$G_{12,s} = G_{13,s}$ MPa	$G_{23,s}$ MPa	$\nu_{12,s} = \nu_{13,s}$	$\nu_{23,s}$	$\alpha_{11,s}$ μ/°C	$\alpha_{22,s} = \alpha_{33,s}$ μ/°C
∞		173,790.00	4,954.00	1,721.30	1,676.60	0.259	0.477	0.367	37.479
1	3.70E+01	144.97	722.78	240.38	240.66	0.000	0.000	0.055	0.051
2	1.00E+02	107.36	604.62	203.91	202.14	0.000	0.000	0.041	0.038
3	1.00E+03	93.42	512.56	172.42	171.25	0.000	0.000	0.036	0.033
4	5.00E+03	34.53	208.97	71.06	70.05	0.000	0.000	0.013	0.012
5	1.00E+04	41.53	226.57	76.16	75.68	0.000	0.000	0.016	0.015
6	5.00E+045	99.88	594.68	201.96	199.31	0.000	0.000	0.039	0.036
7	1.00E+05	9.09	55.59	18.95	18.66	0.000	0.000	0.002	0.002
8	5.00E+05	48.89	297.03	101.11	99.64	0.000	0.000	0.023	0.021
9	1.00E+06	27.00	169.06	57.78	56.80	0.000	0.000	0.005	0.005
10	5.00E+06	0.34	2.16	0.73	0.72	0.000	0.000	0.002	0.002

6.1.2 Lenticular Boom with Uniform Cross-sectional Temperature Distribution

A lenticular boom was used as a numerical example to verify the MSG-based linear thermoviscoelastic beam model. A schematic drawing with the boom cross-sectional design parameters is shown in the left figure of Figure 6.2 and the numerical values of the boom design parameters are summarized in Table 6.4. Although the geometry selected is representative of the lenticular boom presented in Refs. [15] and [16], for this study a M30S/PMT-F7 PW textile composite instead of the HTA40/PMT-F7 was considered. The design parameters from Table 6.4 were passed to the CAD preprocessor PreVABS to create a 2D SG for

the cross-section. A mesh size of 0.02 mm was used to create the input file for SwiftComp™ [112] (see the right figure of Figure 6.2). For both the left and right shells of the lenticular boom, $[0_{UD}/45_{PW}]$ lay-up was selected, where the PW lamina corresponds to the outer surface ply on both shells [15]. Perfect bonding between both shells was considered and the adhesive was not modeled. However, the viscoelastic properties for the adhesive have recently become available [143] and can be modeled for future implementation in this beam model.

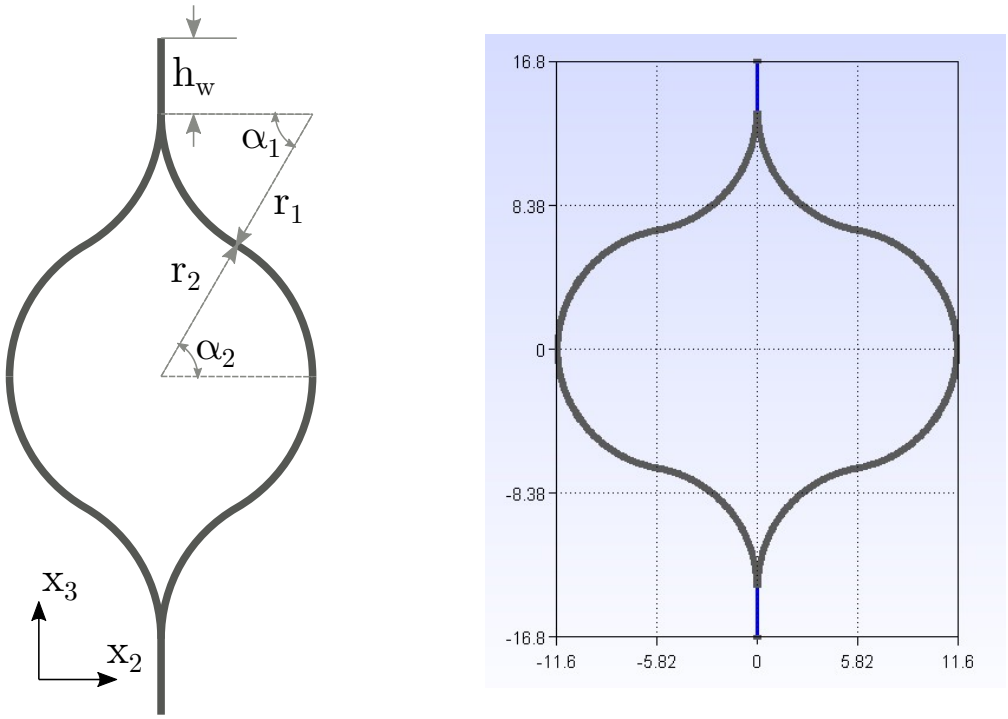

Figure 6.2. Cross-sectional parameters of the lenticular boom design (left) and mesh created for SwiftComp™ [112] input file (right). The sizes in the right figure are in mm.

Table 6.4. Geometric parameters of the lenticular boom design.

Name	Symbol	Fixed Value
Flattened height	h_f	45.00 mm
Web height	h_ω	3.00 mm
Shell section radius	$r_1 = r_2$	6.98 mm
Subtended angle	$\alpha_1 = \alpha_2$	80°

The effective 1D Euler-Bernoulli beam stiffness properties and thermal stress resultants at temperatures of 40°C, 60°C, 80°C, 100°C and 120°C were computed using SwiftComp^{TM} [112]. To do so, the effective laminae properties presented in Tables 6.2-6.3 at different temperatures were input as constituent materials and then, SwiftComp^{TM} [112] was run to calculate the effective properties. The ±45 degrees orientation of the PW laminate was handled by SwiftComp^{TM} [112]. For all the cases, uniform temperature distribution was assumed in the cross-section of the lenticular boom. The effective beam stiffness properties and thermal stress resultants divided by the temperature change (i.e. $F_{T_1,\infty}/\bar{\theta}$) were normalized using the corresponding relaxed value as shown in Figure 6.3. It is noted that $C^b_{11,\infty} = 6.73 \times 10^5$ N, $C^b_{22,\infty} = 1.39 \times 10^7$ N·mm^2, $C^b_{33,\infty} = 5.55 \times 10^7$ N·mm^2, $C^b_{44,\infty} = 2.95 \times 10^7$ N· mm^2 and $F_{T_1,\infty}/\bar{\theta} = 0.08$ N. However, the thermal stress resultants were not normalized since they also account for the temperature change distribution within the cross-section. For all the CTEs of the laminae, $T_0 = 40$°C was considered as reference temperature and thus, the effective thermal stress resultants at these temperatures were equal to 0 N as depicted in Figure 6.3. As SwiftComp^{TM} [112] and FEM analysis predicted the same effective stiffness properties, only the MSG results are shown in Figure 6.3. The normalized values of C^b_{11}, C^b_{22}, C^b_{33} and C^b_{44} exhibit the same behavior and relaxation rate for the increased time and temperature.

In addition, to investigate the validity of the shift function of the resin to represent the effective beam properties, the shift factor of the resin given by Eq. (5.1) was applied to the effective beam properties at a reference temperature of $T_0 = 40$°C summarized in Table 6.5. Shifted values at $T = 60$°C, 80°C, 100°C and 120°C were computed following this approach and are represented with dashed lines in Figure 6.3. We can observe that the shifted homogenized values agree well with the ones computed using MSG beam model with a 2D SG and constituent laminae properties at different temperatures. This conclusion is also valid for the thermal stress resultants divided by the temperature change (i.e. $F_{T_1}/\bar{\theta}$). Therefore, despite the heterogeneous thermoviscoelastic nature of the composite material, the temperature dependencies of the effective stiffness properties represented by the shift factor have the same characteristics as those of the polymer matrix.

To further verify the effective linear thermoviscoelastic properties, a DNS in Abaqus CAE 6.14 [104] and an analytical solution [147] were used. The torsional stiffness value given by

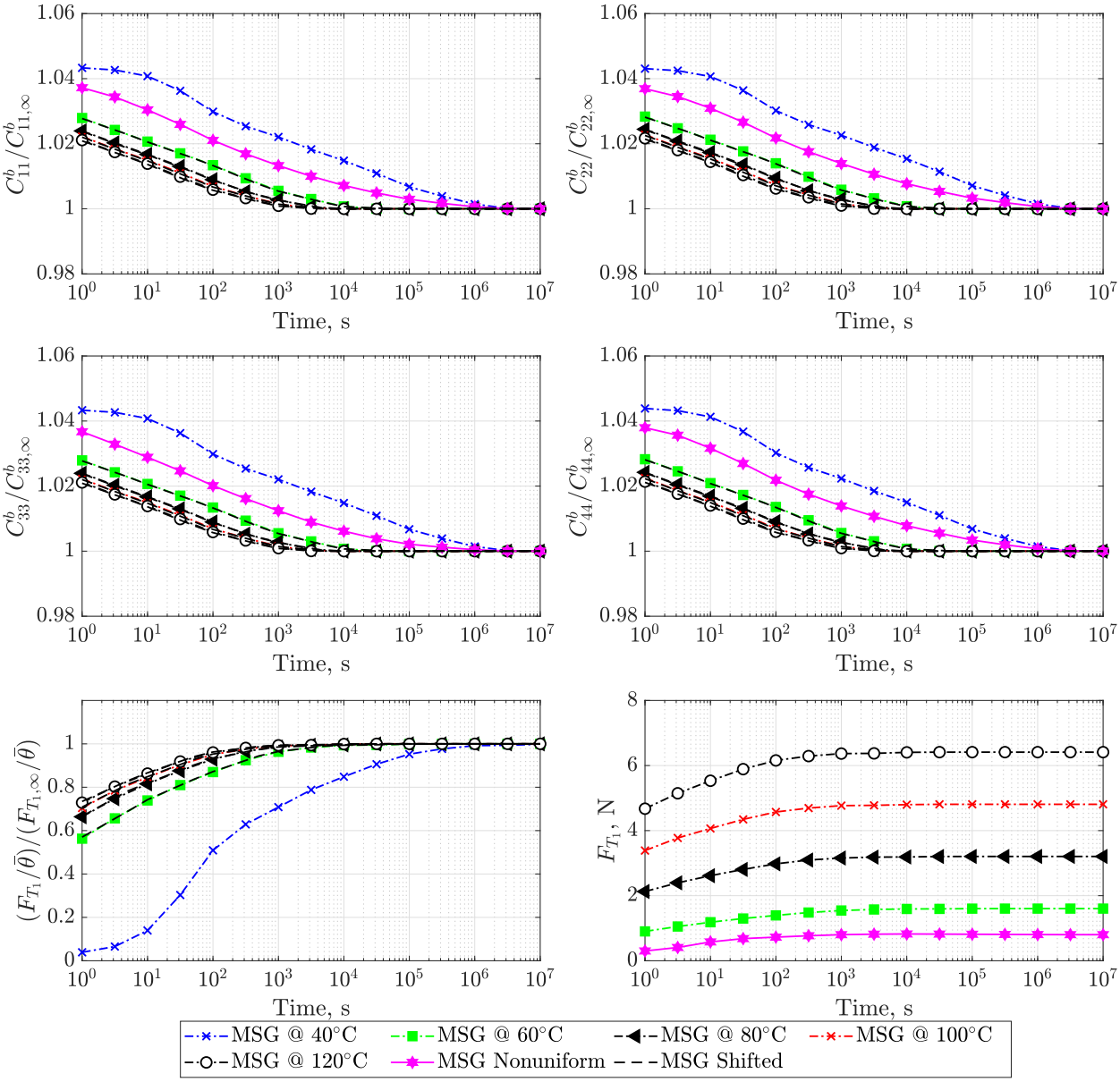

Figure 6.3. Evolution of the normalized effective beam stiffness properties for MSG-based 1D Euler-Bernoulli beam model of the lenticular boom ($C^b_{11,\infty} = 6.73 \times 10^5$ N, $C^b_{22,\infty} = 1.39 \times 10^7$ N·mm^2, $C^b_{33,\infty} = 5.55 \times 10^7$ N·mm^2, $C^b_{44,\infty} = 2.95 \times 10^7$ N·mm^2, $F_{T_1,\infty}/\bar{\theta} = 0.08$ N).

Table 6.5. Effective viscoelastic beam properties of the lenticular boom at $T_0 = 40°C$.

s	λ_s s	$C^b_{11,s}$ N	$C^b_{22,s}$ N·mm^2	$C^b_{33,s}$ N·mm^2	$C^b_{44,s}$ N·mm^2	$F_{T_1,s}/\bar{\theta}$ N/°C
∞		673,250	13,928,000	55,491,000	29,483,000	0.08
1	3.70E+01	5,898	114,890	486,260	261,410	-0.03
2	1.00E+02	5,221	105,530	430,340	231,460	-0.01
3	1.00E+03	4,385	88,520	361,430	194,380	-0.01
4	5.00E+03	1,870	39,370	154,120	82,920	-0.02
5	1.00E+04	1,931	38,660	159,190	85,610	-0.01
6	5.00E+04	5,304	112,470	437,150	235,180	-0.01
7	1.00E+05	507	11,350	41,790	22,490	-0.01
8	5.00E+05	2,678	57,990	220,730	118,760	-0.01
9	1.00E+06	1,557	35,300	128,320	69,060	0.00
10	5.00E+06	18	360	1,500	810	-0.01

$C^b_{22} \equiv GJ$ at a reference temperature (i.e. $T_0 = 40°C$) and $t = 0$ s was selected as reference parameter (see MSG Beam in Table 6.6) for comparison purposes. In case of the DNS model, a 1,000-mm-long lenticular boom was created in Abaqus CAE 6.14 [104]. All the plies were explicitly modeled as shown in Figure 6.4 by means of 588,800 linear hexahedral elements of type C3D8. The effective elastic lamina properties equivalent to thermoviscoelastic lamina properties at the reference temperature were used for the computation. These material properties were directly introduced using the material libraries available in Abaqus 6.14 [104]. The root of the boom was clamped and in the other end, a moment of $M_{x_1} = 1$ N·mm was applied. Then, the rotation around the axial direction x_1 was measured and from it, the twist rate κ_{11} and torsional stiffness were computed (see DNS in Table 6.6).

Table 6.6. Comparison of the torsional stiffness results at $t = 0$ s and $T_0 = 40°C$.

Case	Torsional Stiffness GJ N·mm^2	Difference w.r.t. MSG %
MSG Beam	1.453×10^7	Reference
Analytical	1.420×10^7	-2.27
DNS	1.459×10^7	0.41

As for the analytical solution, Catia V5 was used to compute the cross-sectional area and perimeter of the lenticular boom, which allows to estimate the equivalent torsional moment

of area J [147]. Then, three-dimensional homogenization of the $[0_{UD}/45_{PW}]$ was carried out using 1D SG in SwiftComp^{TM} [112]. Similarly to DNS, the effective elastic lamina properties equivalent to thermoviscoelastic lamina properties at the reference temperature of T_0 =40°C and $t = 0$ s were used for the computation. Multiplying the effective in-plane shear stiffness (i.e. G_{12}) of the laminate with the computed equivalent torsional moment of area, the torsional stiffness was estimated analytically (see Analytical in Table 6.6). Both the DNS and the analytical results exhibited good agreement with the torsional stiffness computed using the MSG-based linear thermoviscoelastic beam model as shown in Table 6.6.

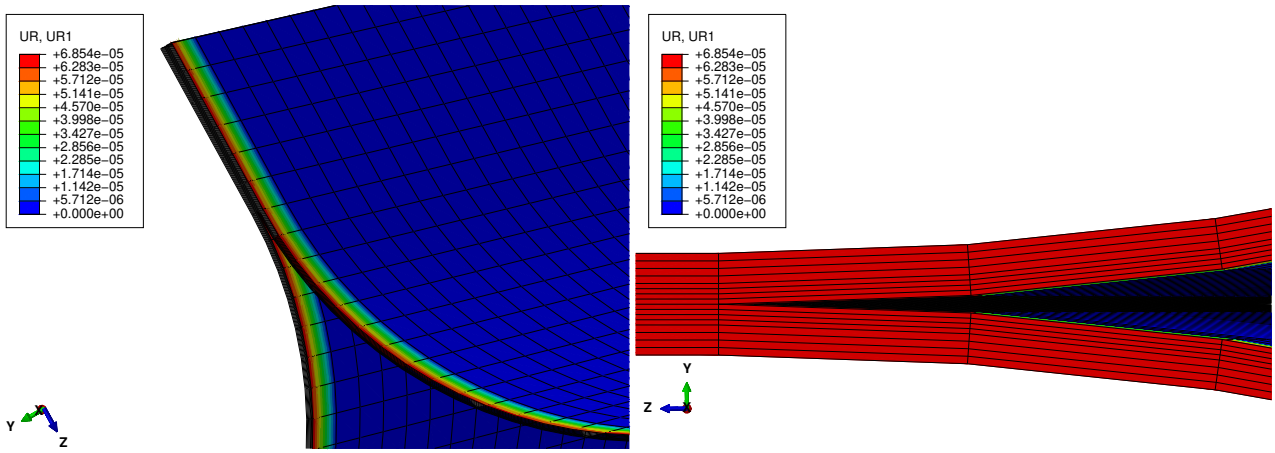

Figure 6.4. Direct numerical simulation model of the lenticular boom for the verification of the torsional stiffness.

6.1.3 TRAC Boom with Uniform Cross-sectional Temperature Distribution

A TRAC boom was also considered as a numerical example to verify the MSG-based linear thermoviscoelastic beam model. In contrast with the lenticular boom, the TRAC boom has more significant extension-bending coupling even at a reference temperature and hence, it is a relevant example to study the influence of these off-diagonal terms. A schematic drawing with the boom cross-sectional design parameters is shown in the left figure of Figure 6.5 and the numerical values of the boom design parameters are summarized in Table 6.7. Although the geometry selected is representative of the TRAC boom presented in Ref. [15], for this study a M30S/PMT-F7 plain weave composite instead of the HTA40/PMT-F7 was also considered. The design parameters from Table 6.7 were passed to the CAD preprocessor

PreVABS to create a 2D SG for the cross-section. A mesh size of 0.02 mm was used to create the input file for SwiftComp^{TM} [112] shown in the right figure of Figure 6.5. For both the left and right shells of the TRAC boom, $[45_{PW}/0_{UD}]$ lay-up was selected, where the 0_{UD} lamina corresponds to the outer surface ply on both shells [15]. Perfect bounding between both shells was considered and the adhesive was not modeled. However, the viscoelastic properties for the adhesive have recently become available [143] and can be modeled for future implementation in this beam model.

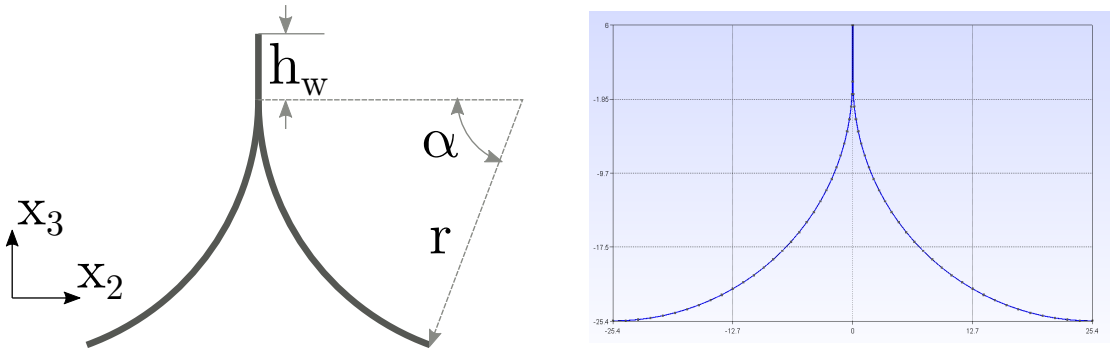

Figure 6.5. Cross-sectional parameters of the TRAC boom design (left) and mesh created for SwiftComp^{TM} [112] input file (right). The sizes in the right figure are in mm.

Table 6.7. Geometric parameters of the TRAC boom design.

Name	Symbol	Fixed Value
Flattened height	h_f	45.00 mm
Web height	h_ω	6.00 mm
Shell section radius	r	6.98 mm
Subtended angle	α	88°

A DNS in Abaqus CAE 6.14 [104] was carried out to verify the effective linear thermoviscoelastic behavior of the TRAC boom. A 1,000-mm-long TRAC boom was created in Abaqus CAE 6.14 [104] and all the plies were explicitly modeled by means of 576,000 linear hexahedral elements of type C3D8. Similarly to the lenticular boom, four elements through-the-thickness of each ply were considered. The origin of coordinates was located at the connection point of the web and the curved shells and hence, the center of gravity was located at $G_{x_2} = 0$ mm and $G_{x_3} = -13.40$ mm. The effective thermoviscoelastic lam-

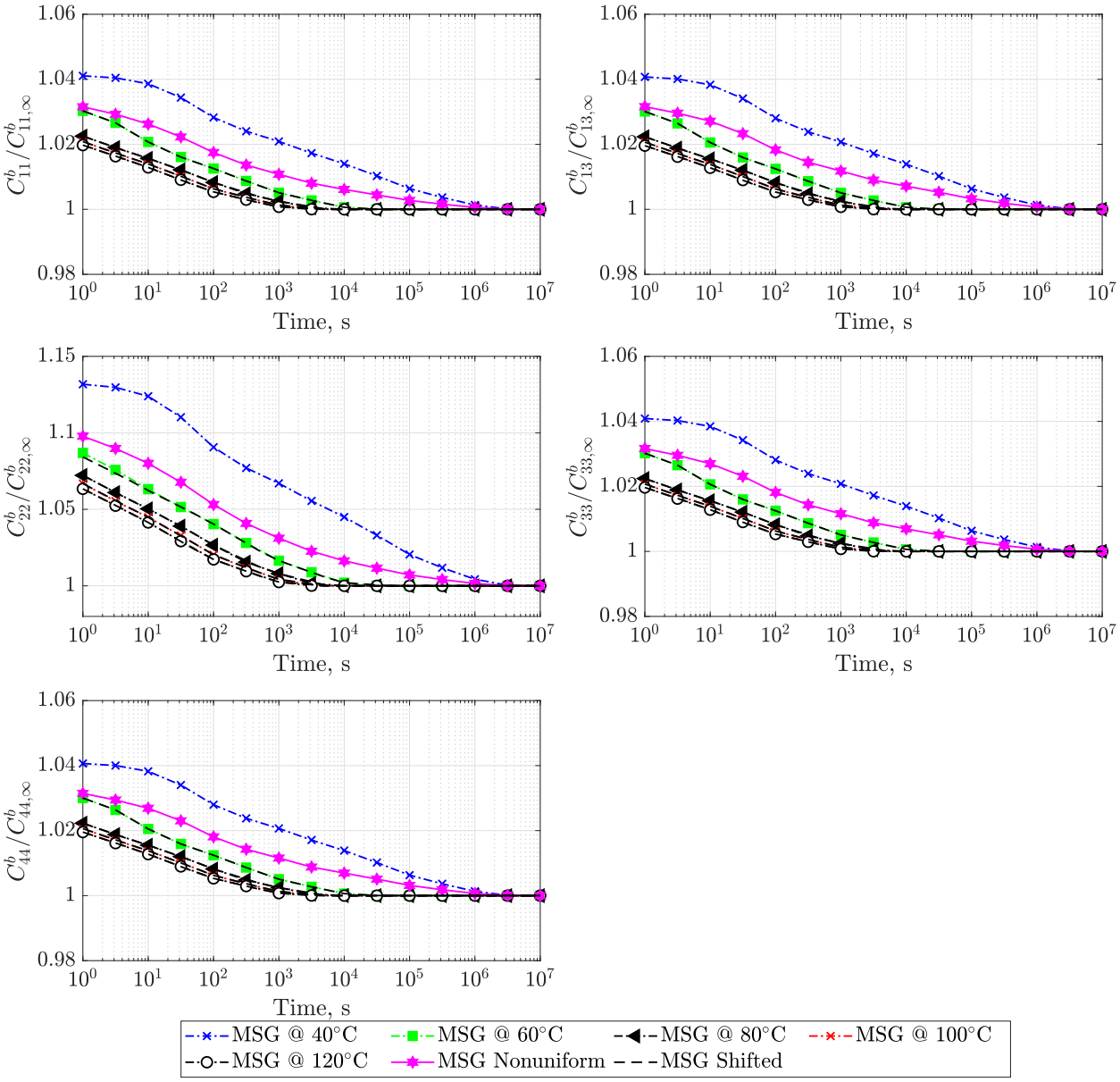

Figure 6.6. Evolution of the normalized effective beam stiffness properties for the MSG-based 1D Euler-Bernoulli beam model of the TRAC boom ($C^b_{11,\infty} = 6.83 \times 10^5$ N, $C^b_{13,\infty} = -9.28 \times 10^6$ N·mm, $C^b_{22,\infty} = 4.39 \times 10^2$ N·mm^2, $C^b_{33,\infty} = 1.91 \times 10^8$ N·mm^2, $C^b_{44,\infty} = 8.70 \times 10^7$ N·mm^2).

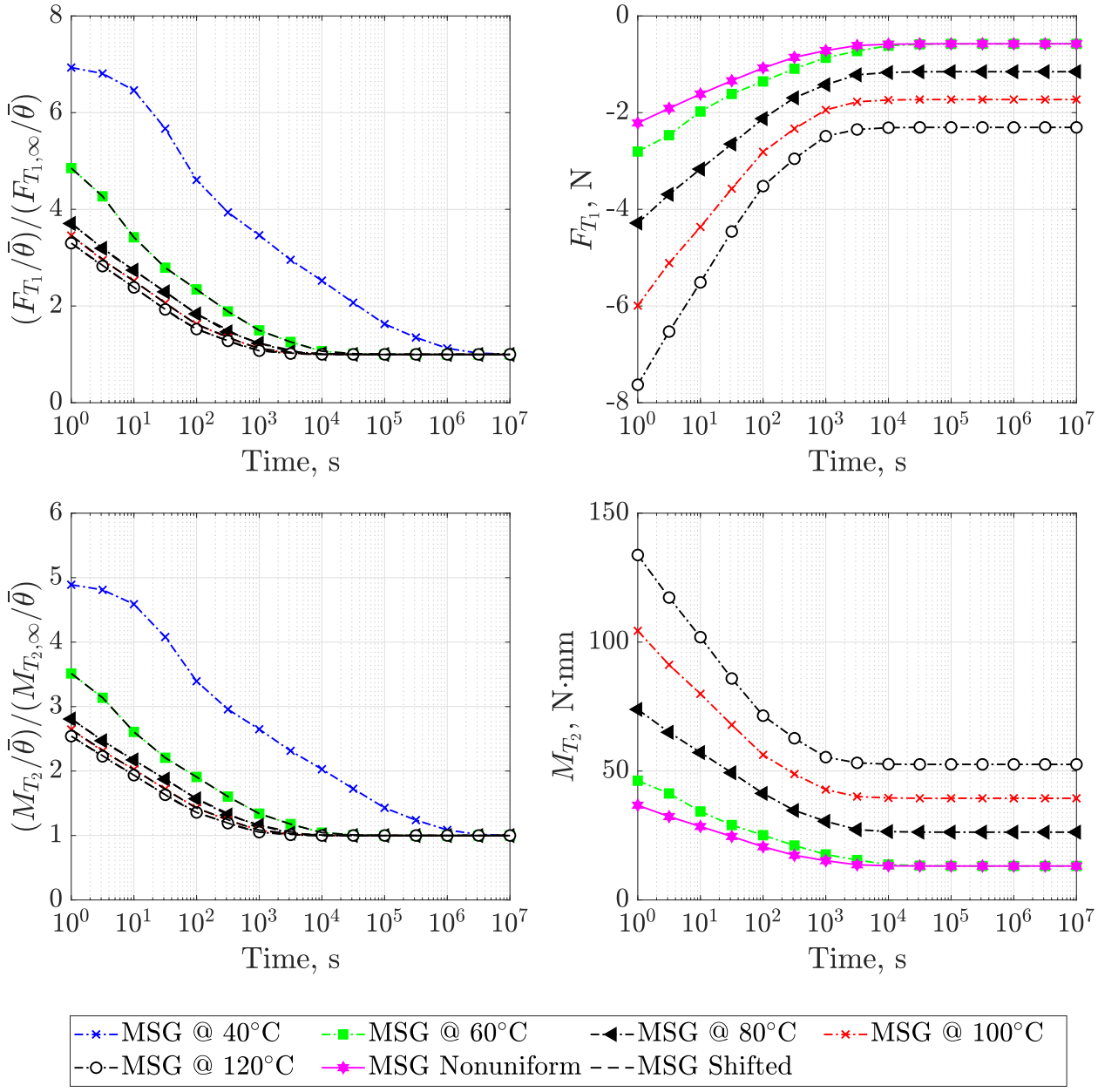

Figure 6.7. Evolution of the normalized effective thermal stress resultants for the MSG-based 1D Euler-Bernoulli beam model of the TRAC boom ($F_{T_1,\infty} = -0.03$ N, $M_{T_2,\infty} = 0.66$ N·mm).

ina properties of Tables 6.2-6.3 were input through user-defined subroutines. A two-step simulation is defined with the viscoelastic option to capture the effective time-dependent material behavior. The root of the boom was clamped and three different tip-loading cases were applied at the other end. A two-step simulation was defined with static option as the thermoviscoelasticity was handled by the user-defined subroutines. In the first step a unit load was applied over a short period (i.e. 1 s), and then in the second step, the load was kept constant for a long period of time (i.e. 10^7 s).

Table 6.8. Effective viscoelastic beam properties of the TRAC boom at T_0 =40°C.

s	λ_s s	$C^b_{11,s}$ N	$C^b_{13,s}$ N·mm	$C^b_{22,s}$ N·mm^2	$C^b_{33,s}$ N·mm^2	$C^b_{44,s}$ N·mm^2	$F_{T_1,s}/\bar{\theta}$ N/°C	$M_{T_2,s}/\bar{\theta}$ N·mm/°C
∞		682,520	-9,281,900	439	190,940,000	87,000,000	-0.03	0.66
1	3.70E+01	5,689	-76,775	12	1,584,900	718,190	-0.05	0.72
2	1.00E+02	5,016	-67,648	10	1,396,700	632,860	-0.03	0.46
3	1.00E+03	4,216	-56,867	9	1,174,100	532,000	-0.03	0.42
4	5.00E+03	1,794	-24,192	4	499,480	226,330	-0.01	0.13
5	1.00E+04	1,857	-25,045	4	517,130	234,300	-0.01	0.19
6	5.00E+04	5,092	-68,666	11	1,417,700	642,370	-0.03	0.38
7	1.00E+05	487	-6,568	1	135,710	61,465	0.00	0.02
8	5.00E+05	2,571	-34,674	5	715,880	3,243,607	-0.01	0.21
9	1.00E+06	1,495	-20,164	3	416,310	188,650	0.00	0.04
10	5.00E+06	18	-237	0	4,898	2,216	0.00	0.02

The effective 1D Euler-Bernoulli beam stiffness properties and thermal resultants at temperatures of 40°C, 60°C, 80°C, 100°C and 120°C were computed using SwiftComp™ [112]. Similarly to the previous case, the effective lamina properties at different temperatures were input as constituent materials and then, SwiftComp™ [112] was run to calculate the effective properties. For all the cases, uniform temperature distribution was assumed in the cross-section of the TRAC boom. The effective beam stiffness properties (see Figure 6.6) and thermal stress resultants divided by the temperature change (i.e. $F_{T_1,\infty}/\bar{\theta}$ and $M_{T_2,\infty}/\bar{\theta}$) were normalized using the corresponding relaxed value (see Figure 6.7). For all the CTEs of the lamina, T =40°C was considered as the reference temperature and thus, the effective thermal stress resultants at T =40°C were equal to F_{T_1} = 0 N and M_{T_2} = as depicted in Figure 6.7. As SwiftComp™ [112] and FEM analysis predicted the same effective stiffness

properties, only the MSG results are shown in Figures 6.6 and 6.7. The normalized values of C^b_{11}, C^b_{13}, $C^b_{33,}$ and C^b_{44} exhibit the same behavior and relaxation rate for increased time and temperature. In addition, compared to the lenticular boom, the TRAC boom has an increased extension-bending coupling as demonstrated by the nonzero values of C^b_{13} and M_{T_2}.

6.1.4 Nonuniform Cross-sectional Temperature Distribution

The previous numerical cases considered that the temperature distribution over the cross-section of the beam was uniform. However, there are circumstances in which the distribution of the temperature over the cross-section is not uniform accelerating even more the relaxation of the material and generating some undesired couplings. For instance, a nonuniform temperature distribution is a common phenomena of the booms in deployed configuration, as the side that faces the Sun has increased temperature compare to the one that is in the shadow [148]. In this subsection, the effective beam properties of both the lenticular boom and the TRAC boom with nonuniform temperature distribution are computed. The same geometry, laminate and lamina material properties are considered for this purpose. In regard to the temperature distribution of the lenticular boom, it was assumed that the web is at $T = 50°\text{C}$, the right shell (i.e. $x_2 > 0$) at $T_0 = 40°\text{C}$ and the left shell (i.e. $x_2 < 0$) at $T = 60°\text{C}$. For the TRAC boom, the web was assumed to be at $T = 60°\text{C}$, the left shell at $T_0 = 40°\text{C}$ and the right shell at $T = 80°\text{C}$. Therefore, in case of these analyses, $\theta \neq 0$ should be used in the MSG-based linear thermoviscoelastic beam model presented in the previous chapter.

The effective beam properties were computed using SwiftComp$^{\text{TM}}$ [112] and verified against DNS showing excellent agreement. The effective properties of the lenticular boom with a nonuniform temperature distribution are depicted as *MSG Nonuniform* in Figures 6.3 and 6.8. For the TRAC boom, *MSG Nonuniform* of Figures 6.6, 6.7 and 6.9 represent the effective beam properties for nonuniform temperature distribution. The effective properties corresponding to nonuniform temperature distribution also decrease with increased time. It can also be observed that while the effective beam thermal stresses for the lenticular boom are negligible, they do have more significant value, specially M_{T_2} in case of the TRAC boom.

Furthermore, the nonuniform temperature distribution yields the appearance of off-diagonal terms that lead to coupling such as C^b_{14} (see Figure 6.8) and C^b_{23} (see Figure 6.9).

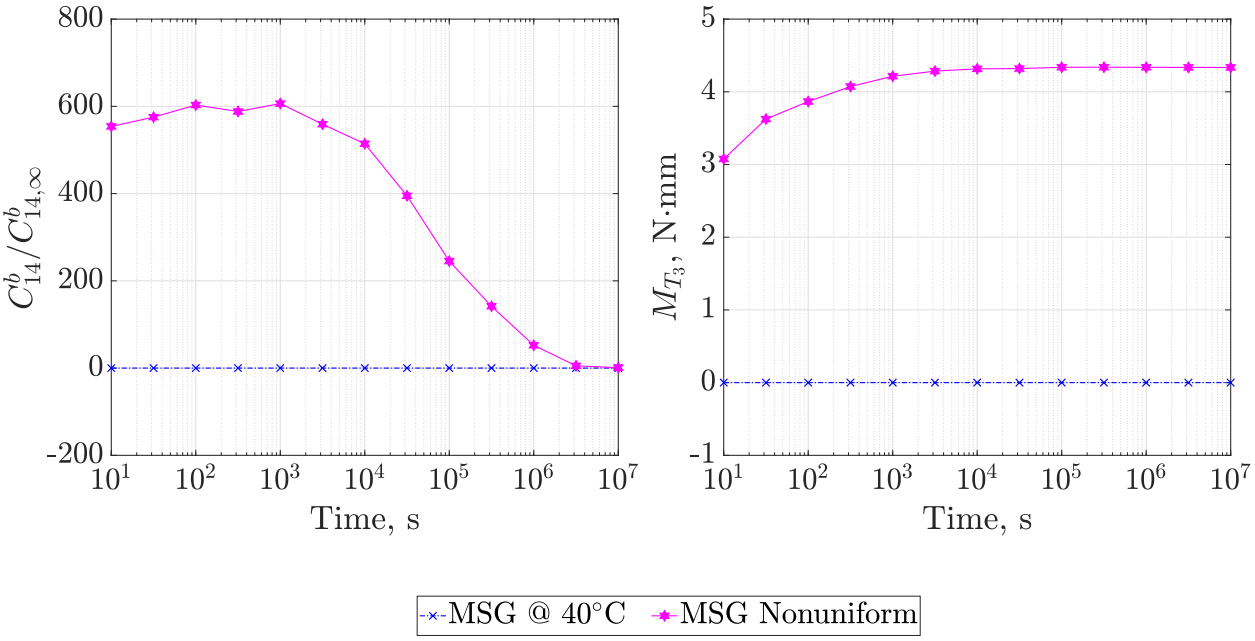

Figure 6.8. Evolution of the normalized effective properties for the lenticular boom with a nonuniform temperature distribution ($C^b_{14,\infty}$ = -46.94 N·mm).

Table 6.9. Effective viscoelastic beam properties of the lenticular boom with a nonuniform cross-sectional temperature distribution.

s	λ_s s	$C^b_{11,s}$ N	$C^b_{14,s}$ N·mm	$C^b_{22,s}$ N·mm^2	$C^b_{33,s}$ N·mm^2	$C^b_{44,s}$ N·mm^2
∞		673,220	-32.34	13,928,000	55,490,000	29,483,000
1	3.70E+01	10,903	11,278	208,660	886,040	483,290
2	1.00E+02	0	-7005	6,395	0.16	5,286
3	1.00E+03	6,121	2,934	128,580	491,120	271,550
4	5.00E+03	2	-4,547	0	22,917	15
5	1.00E+04	2,934	1,471	60,764	244,730	121,980
6	5.00E+04	1,864	-16,084	43694	166,240	93,503
7	1.00E+05	707	448	10725	11278	24,844
8	5.00E+05	789	-7,367	25,486	64,800	57,096
9	1.00E+06	899	-3,613	16,552	42,782	34,728
10	5.00E+06	23	-96.34	333	0.27	972

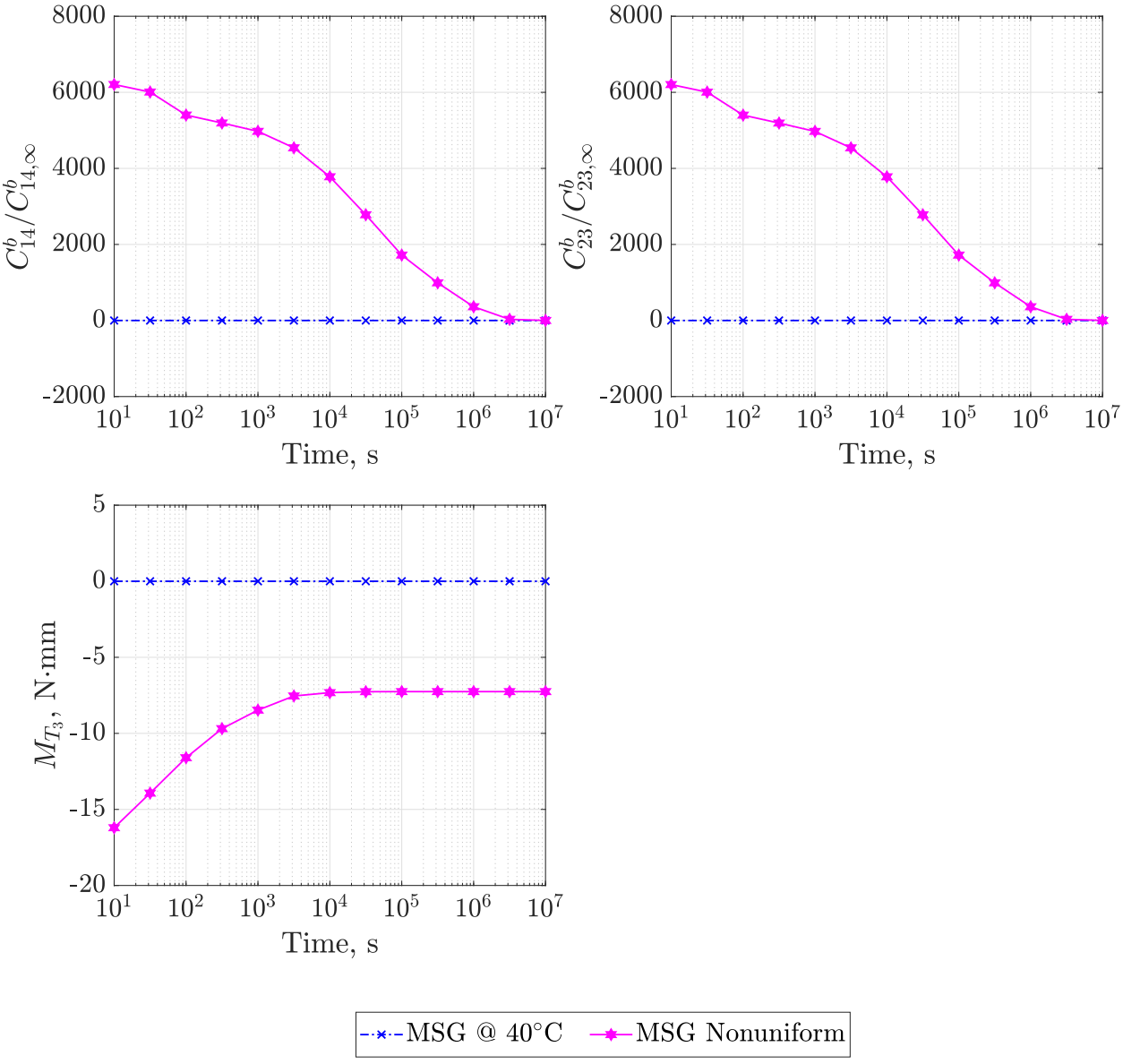

Figure 6.9. Evolution of the normalized effective properties for the TRAC boom with a nonuniform temperature distribution ($C^b_{14,\infty} = -10.06$ N·mm, $C^b_{23,\infty} = 223.24$ N·mm^2).

6.2 Global Thermoviscoelastic Beam Model

6.2.1 Lenticular Boom with Uniform Cross-sectional Temperature Distribution

The lenticular boom presented in Subsection 6.1.2 was selected as numerical case study to verify the MSG-based DI method. The MSG-based beam model was compared against a DNS simulation with 3D solid elements and a MSG-based plate/shell model to verify the formulation presented in Sections 3.3.1 and 3.3.2. For the three cases, the 1,000-mm-long lenticular boom in a deployed configuration was considered with clamped root in one end and subjected to three different tip-loading cases at the other end: axial compression force of F_{x_1} = -1 N, and transverse forces of F_{x_2} = 1 N and F_{x_3} = 1 N, respectively. For all the computations, a constant temperature of $T = 40°\text{C}$ was considered and hence, $a_T = 1$ and $t = \xi$.

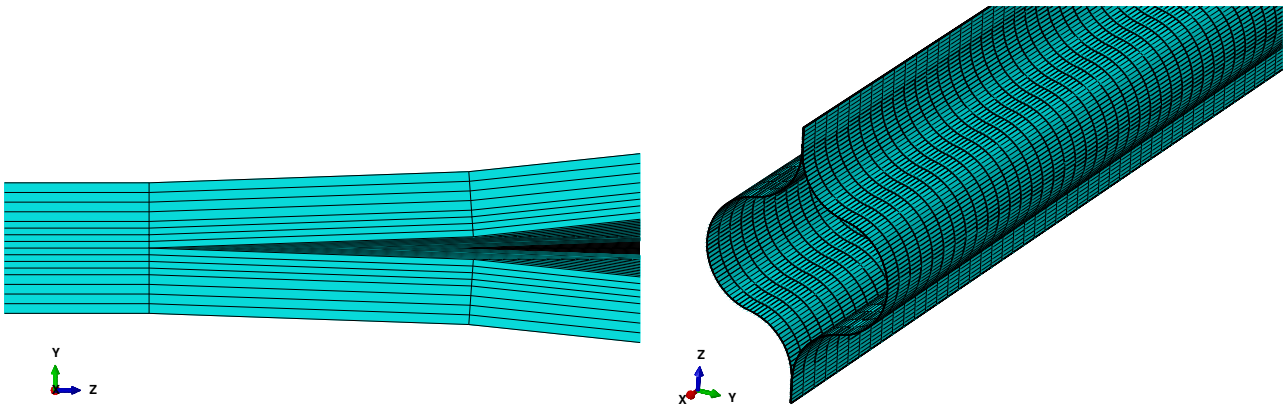

Figure 6.10. Direct numerical simulation model of the lenticular boom.

In the DNS model, all the plies were explicitly modeled as shown in Figure 6.10 by means of 588,800 linear hexahedral elements of type C3D8. The thermoviscoelastic lamina properties summarized in Tables 6.2 and 6.3 were introduced to the model through a user-defined mechanical material behavior (UMAT) subroutine in Abaqus 6.14 [104]. This UMAT subroutine also relied on the DI method to solve the hereditary integral but for 3D solid elements instead of beam elements. It is noted that this UMAT was verified for isotropic viscoelastic materials comparing it with default material libraries of Abaqus CAE [104], and showed good agreement. A static general analysis was selected in Abaqus 6.14 [104] as the

thermoviscoelasticity was handled by the UMAT. The root of the boom was clamped and three different tip-loading cases were applied at the other end. These loads were introduced in two steps. In the first step (i.e. concentrated load) the load was monotonically increased up to the desired value and then, in the second step (i.e. stress relaxation) the load was kept constant allowing relaxation until the desired time. Figures 6.11 (a), 6.12 (a), and 6.13 (a) show the evolution of the cross-sectional shape at several times of the analysis for the DNS case with different loading conditions. Due to the small relaxation of the selected laminate, once the deformed configuration is reached, the cross-sectional shape remains constant as the time increases. However, it should be noted that for any other layup with bigger relaxation behavior such as $[45_{UD}/45_{PW}]$, the cross-sectional shape keeps changing as the time passes, as can be observed in Figures 6.14 (a) and (b) and Figures 6.15.

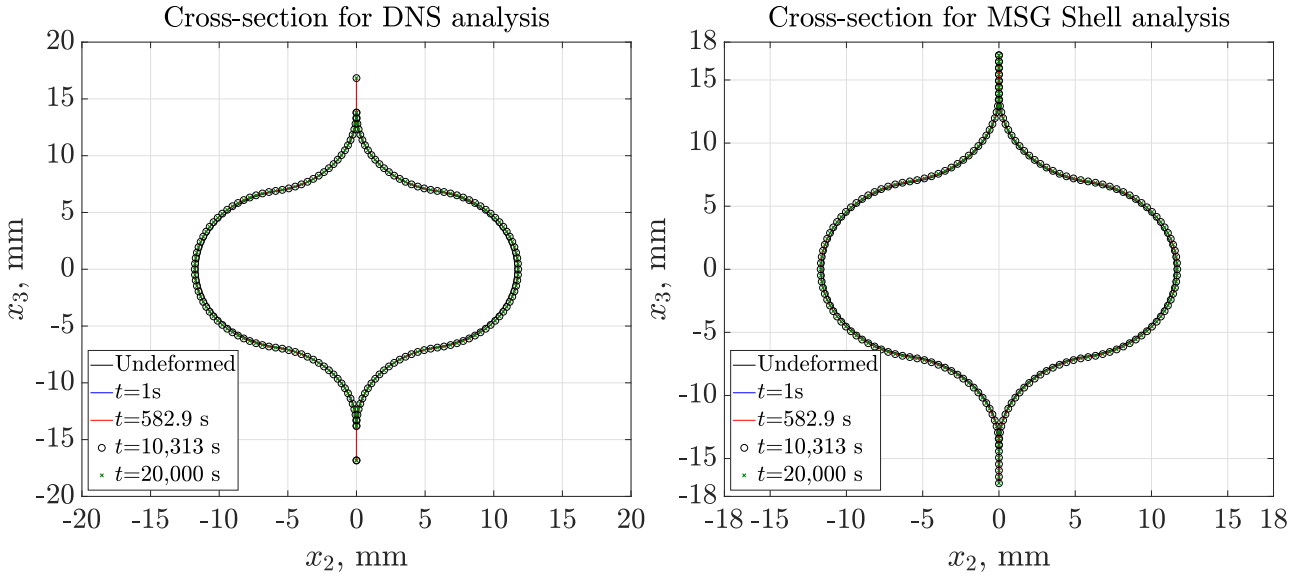

(a) DNS model (b) MSG-based plate/shell model

Figure 6.11. Evolution of the cross-sectional shape at midspan of the lenticular boom (i.e. $x_1 = 500$ mm) for the $F_{x_1} = -1$ N load case with a uniform temperature distribution of $T = 40°$C and $[0_{UD}/45_{PW}]$ lay-up. Displacements are scaled by a factor of 10^4.

The MSG-based plate/shell model was used to analyze the lenticular boom with plate/shell elements in Abaqus 6.14 [104]. In this case, two thermoviscoelastic plate/shell stiffness matrices, one for the web and one for the left and right shells of the boom were computed using

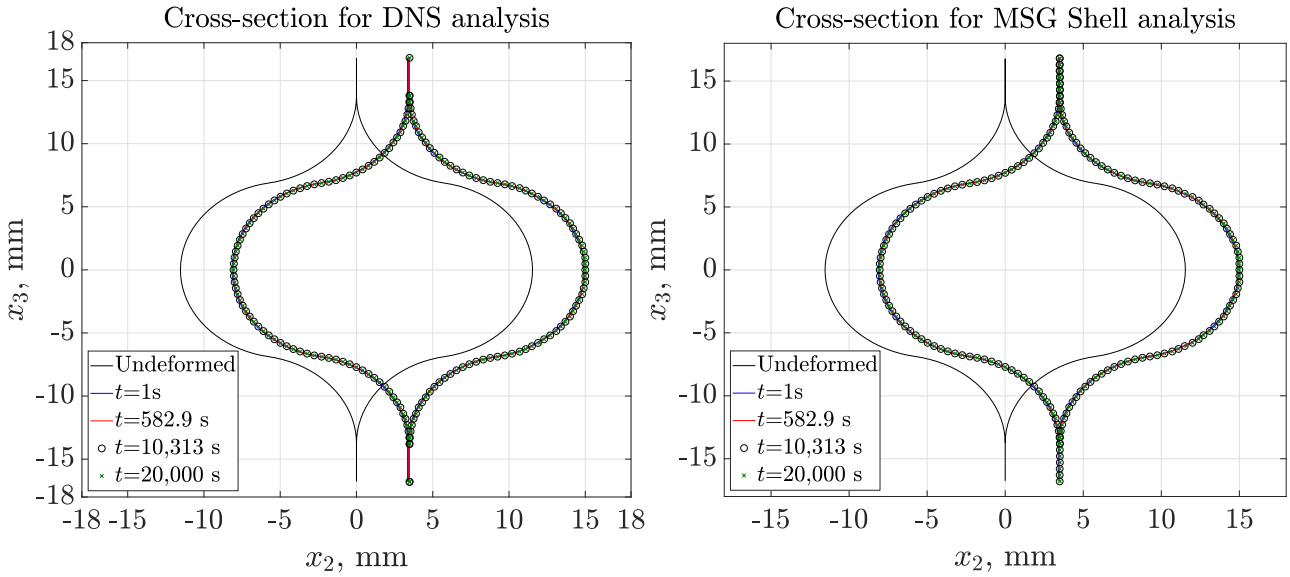

(a) DNS model (b) MSG-based plate/shell model

Figure 6.12. Evolution of the cross-sectional shape at midspan of the lenticular boom (i.e. $x_1 = 500$ mm) for the $F_{x_2} = 1$ N load case with a uniform temperature distribution of $T = 40°$C and $[0_{UD}/45_{PW}]$ lay-up.

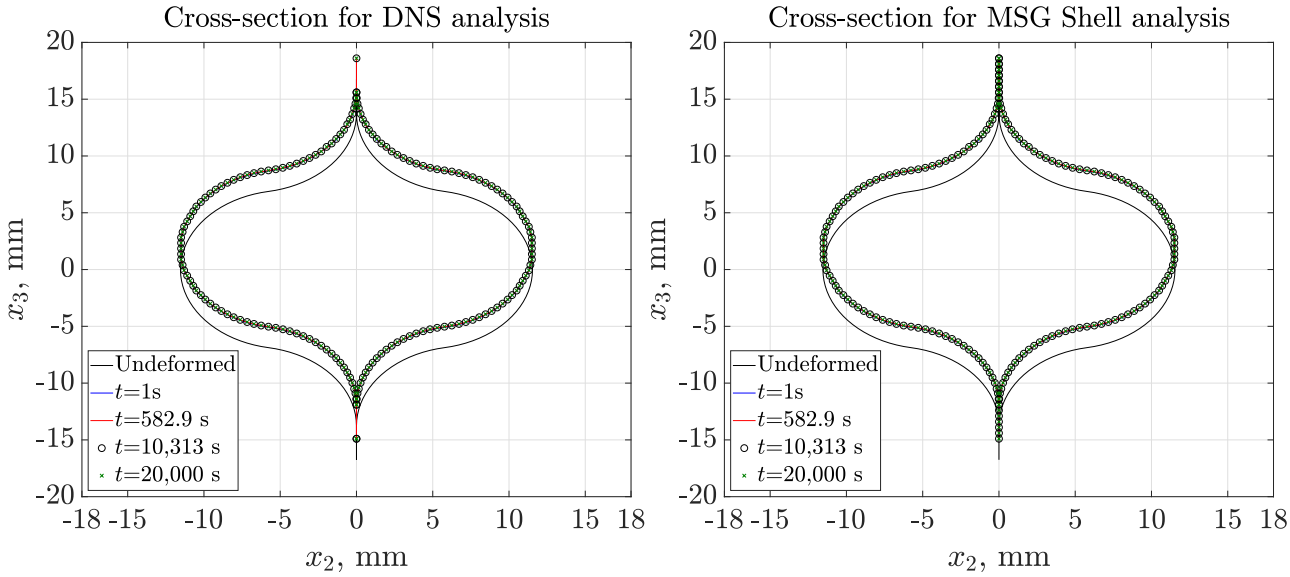

(a) DNS model (b) MSG-based plate/shell model

Figure 6.13. Evolution of the cross-sectional shape at midspan of the lenticular boom (i.e. $x_1 = 500$ mm) for the $F_{x_3} = 1$ N load case with a uniform temperature distribution of $T = 40°$C and $[0_{UD}/45_{PW}]$ lay-up.

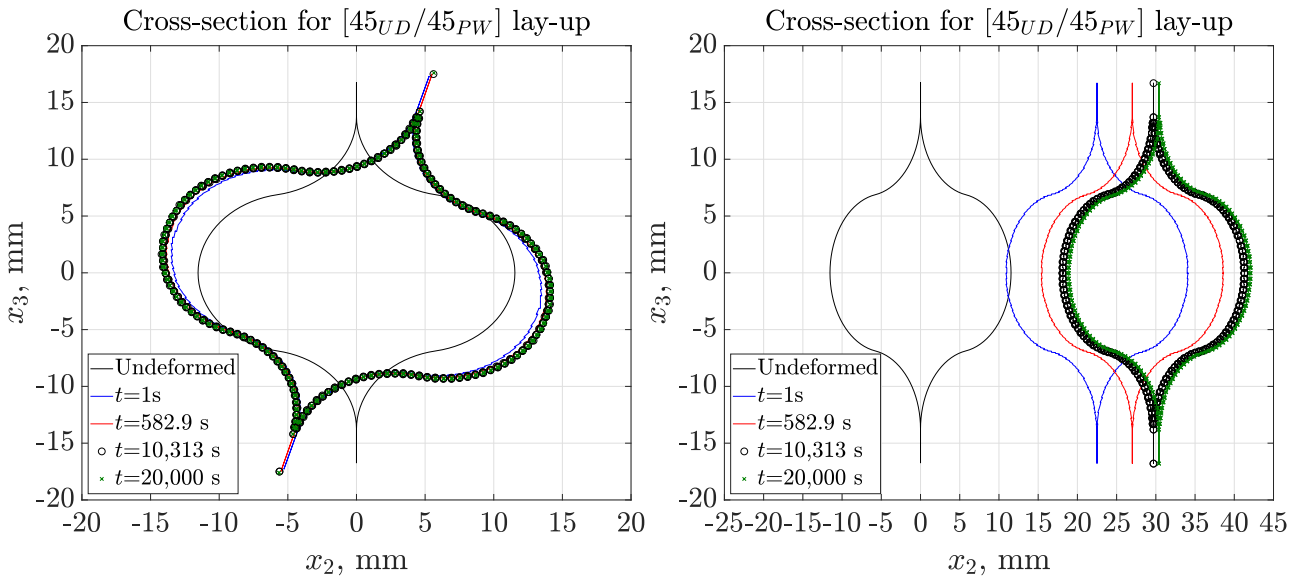

(a) F_{x_1} = -1 N load case

(b) F_{x_2} = 1 N load case

Figure 6.14. Evolution of the cross-sectional shape at midspan of the lenticular boom (i.e. $x_1 = 500$ mm) with a uniform temperature distribution of $T = 40°$C and $[45_{UD}/45_{PW}]$ lay-up. Displacement are scaled by a factor of 10^4 for the F_{x_1} = -1 N case (Figure (a)).

1D SG in SwiftComp^{TM} [112]. The thermoviscoelastic lamina properties of Tables 6.2 and 6.3 were input as constituent properties of the 1D SG. Since the web was made of four plies, the middle reference surface was used for the computation. However, the left and right shells of the boom were made of two plies and hence, the inner surface was used as a reference surface for the computation. The resulting ABD matrix had a nonzero extension-bending coupling matrix. Then, the effective thermoviscoelastic components for both the web and the shells were fit by means of Prony series coefficients (see Tables 6.10 and 6.11). These effective plate/shell properties were coded in a user-subroutine UGENS to be used as the sectional stiffness shell elements in Abaqus 6.14 [104]. This UGENS subroutine also relied on the DI method to solve the hereditary integral. The formulation was previously validated in column bending test (CBT) simulations performed for the $[\pm 45_{PW}]_4$ laminate showing excellent agreement [125]. The Abaqus 6.14 plate/shell global model was meshed with 68,800 general purpose shell element S4. Similarly to DNS, a static general analysis was used, as the thermoviscoelastic behavior was handled by the subroutine. In addition, the same boundary and loading conditions as those of the DNS model were assigned. Figures 6.11 (b), 6.12 (b), and 6.13 (b) show the evolution of the cross-sectional shape at several times in the analysis for the MSG-based plate/shell with different loading conditions. These results followed the same trend as the ones observed for the DNS cases.

Finally, the formulation presented in the MSG-based DI beam model was implemented analytically to solve the global beam model. For these analyses, the thermoviscoelastic beam stiffness properties that were fit into Prony series coefficients (see Table 6.5) were used as input. The displacements and cross-sectional shape evolution at the midspan of the boom (i.e. $x_1 = 500$ mm) were used as reference to compare the MSG-based beam model against DNS and MSG-based plate/shell model. For both the DNS and MSG-based plate/shell models, the required CPU time for the computations was recorded (see Tables 6.12, 6.13 and 6.14). This CPU time only accounted for the time required to solve the Abaqus computations, which were performed at Purdue University's Halstead Server using 2 nodes and 20 CPUs per node. Therefore, the computation of effective thermoviscoelastic properties, the recovery of the displacements, and the post-processing time was not accounted

Table 6.10. Effective viscoelastic plate/shell stiffness properties for the web area of the lenticular boom at $T_0 = 40°\text{C}$.

s	λ_s	$A_{11,s}$	$A_{12,s}$	$A_{22,s}$	$A_{33,s}$
	s	N/mm	N/mm	N/mm	N/mm
∞		19,488.00	5,192.30	5,955.60	5,280.50
1	3.70E+01	89.52	27.31	132.17	41.66
2	1.00E+02	77.27	24.64	114.02	37.68
3	1.00E+03	65.28	20.74	96.25	31.66
4	5.00E+03	27.46	9.12	40.35	13.90
5	1.00E+04	28.74	9.06	42.41	13.85
6	5.00E+04	78.25	26.11	114.85	39.68
7	1.00E+05	7.54	2.63	10.98	3.96
8	5.00E+05	39.55	13.44	57.89	20.37
9	1.00E+06	23.12	8.16	33.63	12.29
10	5.00E+06	0.26	0.08	0.39	0.13
s	λ_s	$D_{11,s}$	$D_{12,s}$	$D_{22,s}$	$D_{33,s}$
	s	N·mm	N·mm	N·mm	N·mm
∞		35.45	25.71	28.23	26.00
1	3.70E+01	0.38	0.07	0.40	0.12
2	1.00E+02	0.34	0.07	0.36	0.12
3	1.00E+03	0.28	0.06	0.30	0.10
4	5.00E+03	0.12	0.03	0.13	0.04
5	1.00E+04	0.12	0.02	0.13	0.04
6	5.00E+04	0.35	0.08	0.36	0.13
7	1.00E+05	0.03	0.01	0.03	0.01
8	5.00E+05	0.18	0.04	0.19	0.07
9	1.00E+06	0.09	0.02	0.10	0.04
10	5.00E+06	0.01	0.00	0.00	0.00

Table 6.11. Effective viscoelastic plate/shell stiffness properties for the left and right shells of the lenticular boom at $T_0 = 40°\text{C}$.

s	λ_s	$A_{11,s}$	$A_{12,s}$	$A_{22,s}$	$A_{33,s}$
	s	N/mm	N/mm	N/mm	N/mm
∞		9,744.10	2,596.20	2,977.80	2,640.30
1	3.70E+01	44.76	13.65	66.09	20.83
2	1.00E+02	38.64	12.32	57.01	18.84
3	1.00E+03	32.64	10.37	48.12	15.83
4	5.00E+03	13.73	4.56	20.18	6.95
5	1.00E+04	14.37	4.53	21.18	6.93
6	5.00E+04	39.14	13.05	57.42	19.84
7	1.00E+05	3.77	1.32	5.49	1.98
8	5.00E+05	19.78	6.72	28.95	10.18
9	1.00E+06	11.56	4.08	16.81	6.14
10	5.00E+06	0.13	0.04	0.20	0.06
s	λ_s	$B_{11,s}$	$B_{12,s}$	$B_{22,s}$	$B_{33,s}$
	s	N	N	N	N
∞		331.06	176.62	195.74	178.80
1	3.70E+01	2.71	0.57	3.13	0.97
2	1.00E+02	2.38	0.54	2.74	0.90
3	1.00E+03	2.00	0.45	2.31	0.75
4	5.00E+03	0.85	0.21	0.98	0.34
5	1.00E+04	0.88	0.20	1.02	0.32
6	5.00E+04	2.43	0.60	2.79	0.97
7	1.00E+05	0.23	0.06	0.27	0.10
8	5.00E+05	1.23	0.32	1.41	0.51
9	1.00E+06	0.72	0.19	0.83	0.30
10	5.00E+06	0.01	0.01	0.01	0.01
s	λ_s	$D_{11,s}$	$D_{12,s}$	$D_{22,s}$	$D_{33,s}$
	s	N·mm	N·mm	N·mm	N·mm
∞		17.73	12.86	14.12	13.00
1	3.70E+01	0.19	0.03	0.20	0.06
2	1.00E+02	0.17	0.03	0.18	0.06
3	1.00E+03	0.14	0.03	0.15	0.05
4	5.00E+03	0.06	0.01	0.06	0.02
5	1.00E+04	0.06	0.01	0.07	0.02
6	5.00E+04	0.17	0.04	0.18	0.06
7	1.00E+05	0.01	0.01	0.02	0.01
8	5.00E+05	0.09	0.02	0.09	0.03
9	1.00E+06	0.05	0.01	0.05	0.02
10	5.00E+06	0.00	0.00	0.00	0.00

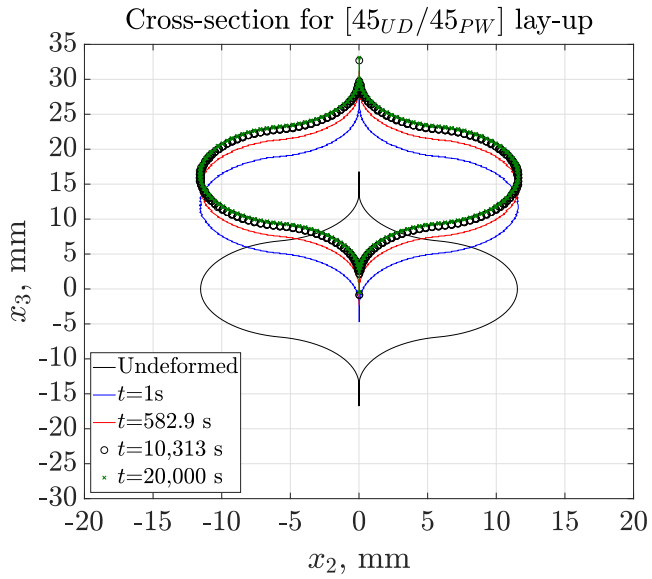

Figure 6.15. Evolution of the cross-sectional shape at midspan of the lenticular boom (i.e. $x_1 = 500$ mm) for $F_{x_3} = 1$ N load case with a uniform temperature distribution of $T = 40°$C and $[45_{UD}/45_{PW}]$ lay-up.

for in these values, but each of the SwiftComp™ [112] computations lasted less than one second.

As shown in Figures 6.17 and 6.16, and Tables 6.12-6.14, the MSG-based beam model exhibited excellent agreements with the DNS and MSG-based plate/shell model in both the predicted displacement field and the cross-sectional shape after 20,000 s of relaxation. Therefore, it is feasible to use the MSG-based beam model to analyze booms that are in a fully deployed configuration. This also applies when the entire boom has a uniform temperature distribution different from the reference one, such as $T = 60°$C. In this latter case, the value of a_T should be computed using Eq. (5.1), and accordingly used in the formulation presented in Section 3.1 to compute the reduced time. Finally, it is noted that higher compression and transverse loads would linearly scale up the displacements and deformations, as linear thermoviscoelastic behavior is analyzed and effective properties only depend on time and temperature. In reality, the stress and strain levels as well as the strain rate also have an effect in material properties and structural behavior.

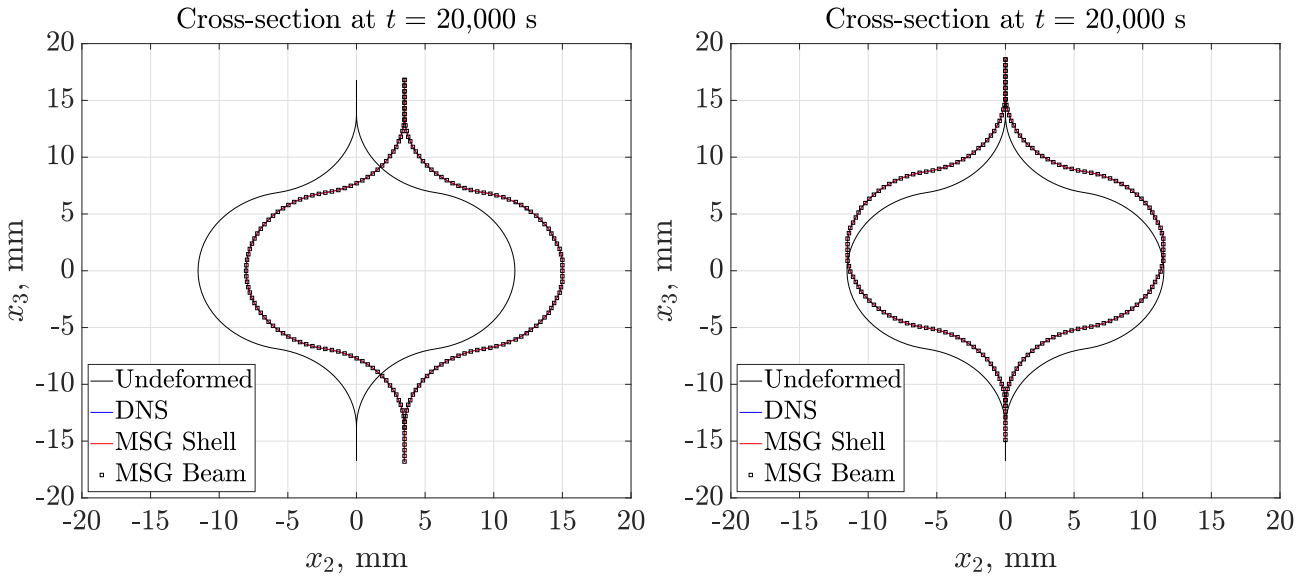

(a) Transverse force $F_{x_2} = 1$ N (b) Transverse force $F_{x_3} = 1$ N

Figure 6.16. Comparison of DNS, MSG-based plate/shell and MSG-based beam analysis for the lenticular boom at time $t = 20{,}000$ s with a uniform temperature distribution of $T = 40°\text{C}$ and $[0_{UD}/45_{PW}]$ lay-up.

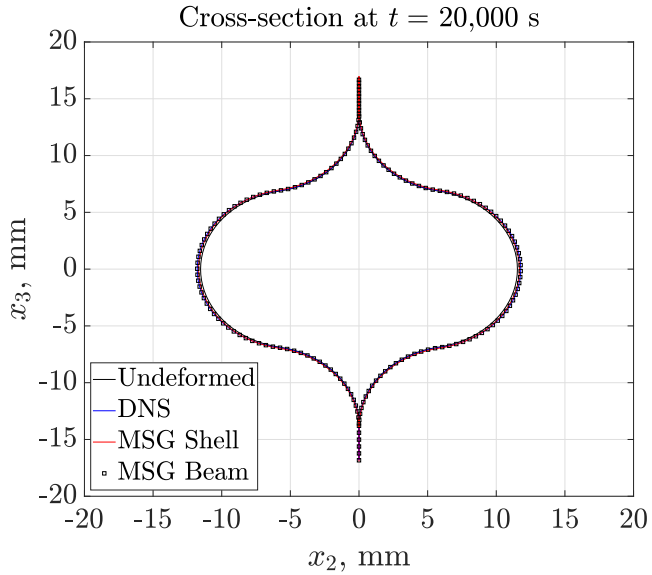

Figure 6.17. Comparison of DNS, MSG-based plate/shell and MSG-based beam analysis for the lenticular boom at time $t = 20{,}000$ s for the $F_{x_1} = -1$ N load case with a uniform temperature distribution of $T = 40°\text{C}$ and $[0_{UD}/45_{PW}]$ lay-up. Displacements are scaled by a factor of 10^4.

Table 6.12. Displacement at midspan of the lenticular boom (i.e. $x_1 = 500$ mm) and time $t = 20{,}000$ s for the $F_{x_1} = -1$ N load case with a uniform temperature distribution of $T = 40°C$ and $[0_{UD}/45_{PW}]$ lay-up.

Type	u_{x_1} mm	u_{x_2} mm	u_{x_3} mm	CPU time s
DNS	-7.3350e-04	2.4250e-05	7.8120e-06	20,591
MSG Shell	-7.3321e-04	1.4860e-05	2.0440e-05	1,218
MSG Beam	-7.3355e-04	0.0000	0.0000	Analytical

Table 6.13. Displacement at midspan of the lenticular boom (i.e. $x_1 = 500$ mm) and time $t = 20{,}000$ s for the $F_{x_2} = 1$ N load case with a uniform temperature distribution of $T = 40°C$ and $[0_{UD}/45_{PW}]$ lay-up.

Type	u_{x_1} mm	u_{x_2} mm	u_{x_3} mm	CPU time s
DNS	0.1460	3.4890	0.0007	27,104
MSG Shell	0.1454	3.5025	0.0007	1,160
MSG Beam	0.0000	3.4892	0.0000	Analytical

Table 6.14. Displacement at midspan of the lenticular boom (i.e. $x_1 = 500$ mm) and time $t = 20{,}000$ s for the $F_{x_3} = 1$ N load case with a uniform temperature distribution of $T = 40°C$ and $[0_{UD}/45_{PW}]$ lay-up.

Type	u_{x_1} mm	u_{x_2} mm	u_{x_3} mm	CPU time s
DNS	0.1116	0.0004	1.8550	27,665
MSG Shell	0.1116	0.0004	1.8554	1,164
MSG Beam	0.0000	0.0000	1.8542	Analytical

6.2.2 TRAC Boom with Uniform Cross-sectional Temperature Distribution

The TRAC boom presented in Subsection 6.1.3 was selected as numerical case study to verify the MSG-based DI method. The MSG-based beam model was compared against a DNS simulation with 3D solid elements and a MSG-based plate/shell model to verify the formulation presented in Sections 3.3.1 and 3.3.2. For the two cases, the 1,000-mm-long TRAC boom in a deployed configuration was considered with clamped root in one end and subjected to two different tip-loading conditions at the other end: axial compression force

of F_{x_1} = -1 N, and transverse force of F_{x_3} = 1 N. For all the computations, a constant temperature of $T = 40°\text{C}$ was considered and hence, $a_T = 1$ and $t = \xi$.

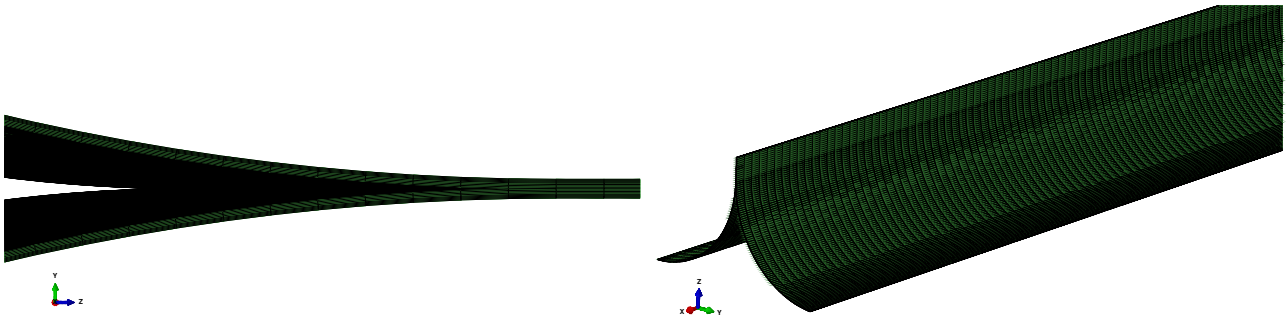

Figure 6.18. Direct numerical simulation model of the TRAC boom.

In the DNS model, all the plies were explicitly modeled as shown in Figure 6.18 by means of 576,000 linear hexahedral elements of type C3D8. The thermoviscoelastic lamina properties summarized in Tables 6.2 and 6.3 were introduced to the model through a user-defined mechanical material behavior (UMAT) subroutine in Abaqus 6.14 [104]. As in the previous case, the UMAT subroutine used the DI method to solve the hereditary integral for 3D solid elements instead of beam elements. A static general analysis was selected in Abaqus 6.14 [104] as the thermoviscoelasticity was handled by the UMAT. The root of the TRAC boom was clamped and two different tip-loading cases were applied at the other end. These loads were introduced in two steps. In the first step (i.e. concentrated load) the load was monotonically increased up to the desired value and then, in the second step (i.e. stress relaxation) the load was kept constant allowing relaxation until the desired time. Figures 6.19 (a) and 6.20 (a) show the evolution of the cross-sectional shape at several time instances of the analysis for the DNS case with different loading conditions. Although the selected laminate exhibits a small relaxation, the cross-sectional shape of the TRAC boom experiences a higher deformation over time than the lenticular boom case.

The MSG-based plate/shell model was used to analyze the TRAC boom with plate/shell elements in Abaqus 6.14 [104]. In this case, two thermoviscoelastic plate/shell stiffness matrices, one for the web and one for the left and right shells of the boom were computed using 1D SG in SwiftComp$^{\text{TM}}$ [112]. The thermoviscoelastic laminae properties of Tables 6.2

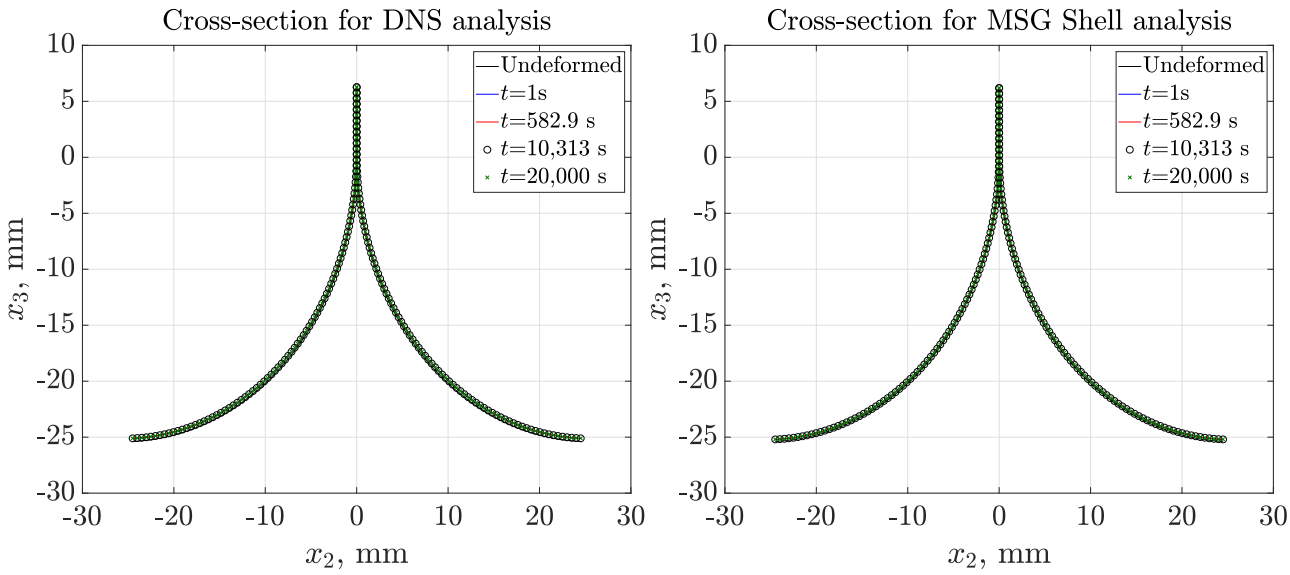

(a) DNS model (b) MSG-based plate/shell model

Figure 6.19. Evolution of the cross-sectional shape at midspan of the TRAC boom (i.e. $x_1 = 500$ mm) for the $F_{x_1} = -1$ N load case with a uniform temperature distribution of $T = 40°\text{C}$ and $[45_{PW}/0_{UD}]$ lay-up. Displacements are scaled by a factor of 10.

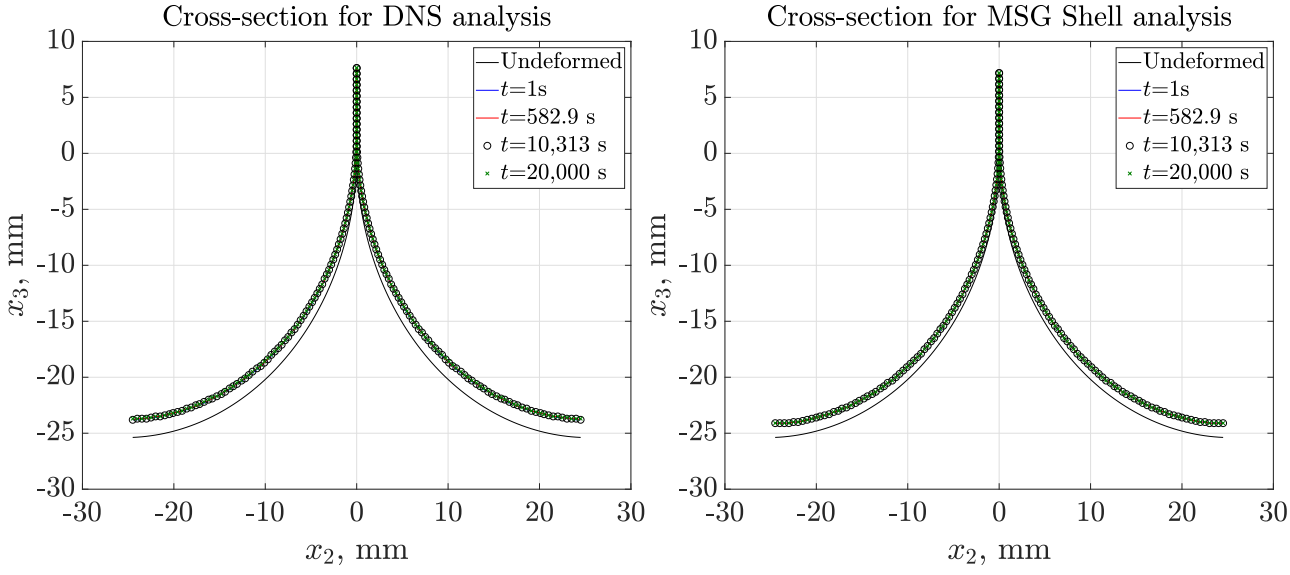

(a) DNS model (b) MSG-based plate/shell model

Figure 6.20. Evolution of the cross-sectional shape at midspan of the TRAC boom (i.e. $x_1 = 500$ mm) for the $F_{x_3} = 1$ N load case with a uniform temperature distribution of $T = 40°\text{C}$ and $[45_{PW}/0_{UD}]$ lay-up.

and 6.3 were input as constituent properties of the 1D SG. Since the web was made of four plies, the middle reference surface was used for the computation. However, the left and right shells of the boom were made of two plies and hence, the inner surface was used as a reference surface for the computation. The resulting ABD matrix had a nonzero extension-bending coupling matrix. Then, the effective thermoviscoelastic components for both the web and the shells were fit by means of Prony series coefficients (see Tables 6.15 and 6.16). These effective plate/shell properties were coded in a user-subroutine UGENS to be used as the sectional stiffness shell elements in Abaqus 6.14 [104]. The same UGENS subroutine as the lenticular boom was used with DI method to solve the hereditary integral. The Abaqus 6.14 plate/shell global model was meshed with 67,200 general purpose shell element S4. Similarly to DNS, a static general analysis was used, as the thermoviscoelastic behavior was handled by the subroutine. In addition, the same boundary and loading conditions as those of the DNS model were assigned. Figures 6.19 (b) and 6.20 (b) show the evolution of the cross-sectional shape at several times in the analysis for the MSG-based plate/shell with different loading conditions. These results followed the same trend as the ones observed for the DNS cases.

In addition, the formulation presented in the MSG-based DI beam model was implemented analytically to solve the global beam model. For these analyses, the thermoviscoelastic beam stiffness properties that were fit into Prony series coefficients (see Table 6.8) were used as input. The displacements and cross-sectional shape evolution at the midspan of the TRAC boom (i.e. $x_1 = 500$ mm) were used as reference to compare the MSG-based beam model against DNS and MSG-based plate/shell model. As shown in Figure 6.21, the MSG-based beam model exhibited excellent agreement with the DNS model in the cross-sectional shape after 20,000 s of relaxation. It should be noted that the difference for the MSG-based plate/shell and $F_{x_3} = 1$ N was slightly higher compared to the results of the lenticular case. However, it is feasible to use the MSG-based beam model to analyze booms with different cross-sectional shapes that are in a fully deployed configuration.

Table 6.15. Effective viscoelastic plate/shell stiffness properties for the web area of the TRAC boom at $T_0 = 40°\text{C}$.

s	λ_s	$A_{11,s}$	$A_{12,s}$	$A_{22,s}$	$A_{33,s}$
	s	N/mm	N/mm	N/mm	N/mm
∞		24031.00	3658.90	4409.20	3746.40
1	3.70E+01	73.57	30.37	135.41	43.35
2	1.00E+02	62.32	26.60	115.60	38.39
3	1.00E+03	52.83	22.45	97.72	32.32
4	5.00E+03	21.90	9.60	40.59	13.91
5	1.00E+04	23.29	9.86	43.11	14.19
6	5.00E+04	62.50	27.43	115.53	39.65
7	1.00E+05	5.98	2.70	10.97	3.89
8	5.00E+05	31.46	13.97	58.06	20.19
9	1.00E+06	18.29	8.31	33.52	11.99
10	5.00E+06	0.21	0.09	0.40	0.13
s	λ_s	$D_{11,s}$	$D_{12,s}$	$D_{22,s}$	$D_{33,s}$
	s	N·mm	N·mm	N·mm	N·mm
∞		103.87	2.62	4.95	2.90
1	3.70E+01	0.14	0.12	0.45	0.15
2	1.00E+02	0.11	0.10	0.38	0.13
3	1.00E+03	0.10	0.08	0.32	0.11
4	5.00E+03	0.04	0.03	0.13	0.05
5	1.00E+04	0.04	0.04	0.14	0.05
6	5.00E+04	0.11	0.10	0.38	0.13
7	1.00E+05	0.01	0.00	0.03	0.01
8	5.00E+05	0.06	0.06	0.19	0.07
9	1.00E+06	0.02	0.02	0.10	0.03
10	5.00E+06	0.00	0.00	0.00	0.00

Table 6.16. Effective viscoelastic plate/shell stiffness properties for the left and right shells of the TRAC boom at $T_0 = 40°C$.

s	λ_s	$A_{11,s}$	$A_{12,s}$	$A_{22,s}$	$A_{33,s}$
	s	N/mm	N/mm	N/mm	N/mm
∞		12016.00 1829.50		2204.60	1873.20
1	3.70E+01	36.79	15.19	67.70	21.67
2	1.00E+02	31.16	13.30	57.80	19.20
3	1.00E+03	26.41	11.23	48.86	16.16
4	5.00E+03	10.95	4.80	20.30	6.95
5	1.00E+04	11.64	4.93	21.30	7.09
6	5.00E+04	31.25	13.72	57.77	19.83
7	1.00E+05	2.99	1.35	5.48	1.94
8	5.00E+05	15.73	6.99	29.03	10.10
9	1.00E+06	9.14	4.15	16.76	6.00
10	5.00E+06	0.11	0.05	0.20	0.07
s	λ_s	$B_{11,s}$	$B_{12,s}$	$B_{22,s}$	$B_{33,s}$
	s	N	N	N	N
∞		735.17	40.23	58.20	42.36
1	3.70E+01	1.29	0.84	3.42	1.12
2	1.00E+02	1.04	0.71	2.88	0.96
3	1.00E+03	0.89	0.61	2.44	0.81
4	5.00E+03	0.36	0.25	1.00	0.34
5	1.00E+04	0.39	0.27	1.08	0.36
6	5.00E+04	1.02	0.72	2.85	0.97
7	1.00E+05	0.10	0.07	0.27	0.09
8	5.00E+05	0.51	0.36	1.43	0.50
9	1.00E+06	0.29	0.20	0.81	0.28
10	5.00E+06	0.00	0.00	0.01	0.01
s	λ_s	$D_{11,s}$	$D_{12,s}$	$D_{22,s}$	$D_{33,s}$
	s	N·mm	N·mm	N·mm	N·mm
∞		51.93	1.31	2.47	1.45
1	3.70E+01	0.07	0.06	0.23	0.07
2	1.00E+02	0.06	0.05	0.19	0.06
3	1.00E+03	0.05	0.04	0.16	0.05
4	5.00E+03	0.02	0.02	0.07	0.02
5	1.00E+04	0.02	0.02	0.07	0.02
6	5.00E+04	0.05	0.05	0.19	0.06
7	1.00E+05	0.00	0.00	0.02	0.01
8	5.00E+05	0.03	0.03	0.10	0.03
9	1.00E+06	0.01	0.01	0.05	0.02
10	5.00E+06	0.00	0.00	0.00	0.00

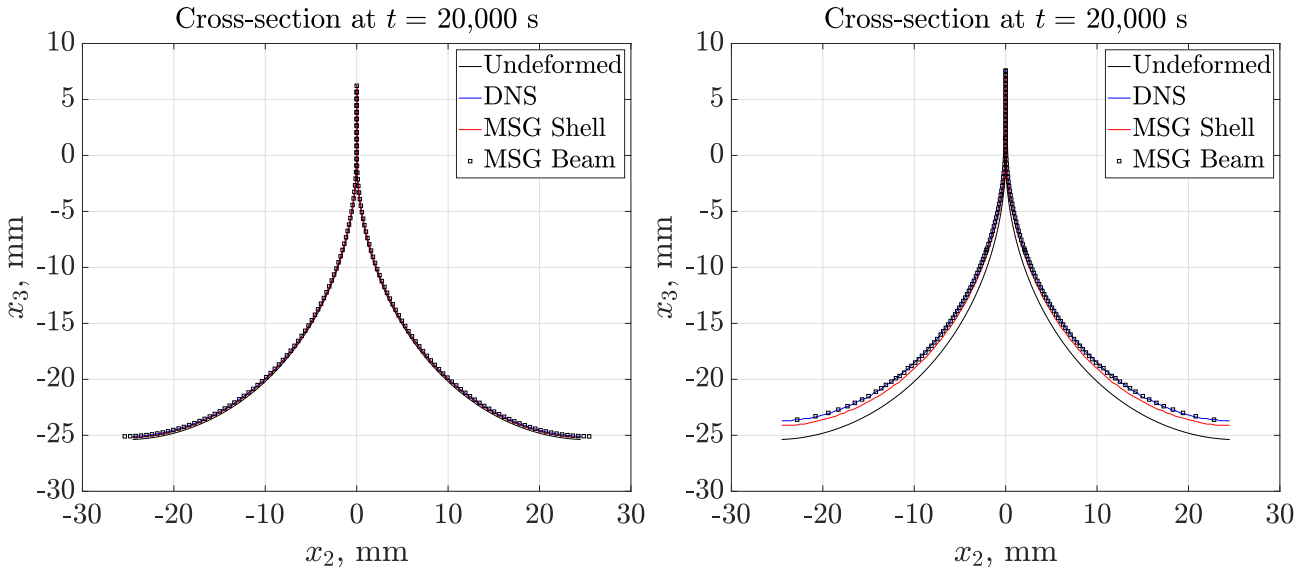

(a) $F_{x_1} = -1$ N (b) $F_{x_3} = 1$ N

Figure 6.21. Comparison of DNS, MSG-based plate/shell and MSG-based beam analysis for the TRAC boom at time $t = 20{,}000$ s with a uniform temperature distribution of $T = 40°\text{C}$ and $[45_{PW}/0_{UD}]$ lay-up. Displacements are scaled by a factor of 10 for the $F_{x_1} = -1$ N case.

6.2.3 Nonuniform Cross-sectional Temperature Distribution

The previous numerical cases considered that the thermal distribution along the cross-section of the beam was uniform. However, there are circumstances in which the distribution of the temperature through the cross-section is nonuniform, accelerating even more the relaxation of the material and generating some undesired couplings. For instance, a nonuniform temperature distribution is a common phenomenon for the booms in a deployed configuration in space, as the shell sections that face the Sun has increased temperature compared to the ones in the shadow [148]. This subsection studies the global behavior of the boom with steady-state nonuniform temperature distribution. The same geometry, lamina and laminate material properties were considered in this study. In regard to the temperature distribution of the lenticular boom, it was assumed that the web is at $T = 50°\text{C}$, the right shell (i.e. $x_2 > 0$) at $T = 40°\text{C}$ and the left shell (i.e. $x_2 < 0$) at $T = 60°\text{C}$. It is noted that this cross-sectional distribution was kept constant along the span of the boom. Therefore, the nonuniform cross-sectional temperature distribution is captured by the effective beam ther-

moviscoelastic properties, and in the MSG-based DI beam formulation presented in Chapter 6.2.1, $a_T = 1$ and hence, $\xi = t$ applies. The effective beam properties were computed using SwiftComp^{TM} [112] and following the approach and mesh size previously described. The fit Prony series coefficients are shown in Table 6.9. For verification purposes, the previously presented DNS and MSG-based plate/shell models were considered. The relationship between the reduced time and the real time is given by Eq. (5.1), which was implemented in the UMAT and UGENS subroutines, respectively.

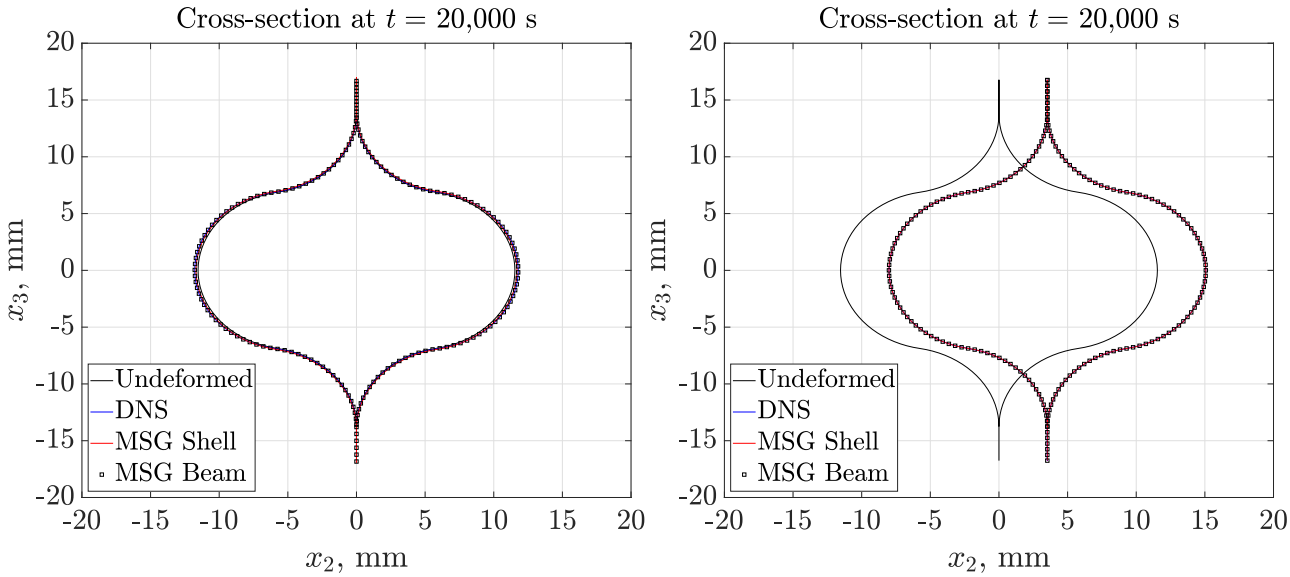

(a) F_{x_1} = -1 N load case (b) F_{x_2} = 1 N load case

Figure 6.22. Evolution of the cross-sectional shape at midspan of the lenticular boom (i.e. $x_1 = 500$ mm) with a nonuniform temperature distribution and $[0_{UD}/45_{PW}]$ lay-up. Displacement scaled by a factor of 10^4 for the F_{x_1} = -1 N case (Figure (a)).

Similarly to the uniform temperature distribution example, three loading conditions were studied: an axial compression force of F_{x_1} = -1 N, and transverse forces of $F_{x_2} = 1$ N and $F_{x_3} = 1$ N, respectively. Tables 6.17-6.19 show the displacement at the midspan of the boom for nonuniform temperature distribution at time of t = 20,000 s. The MSG-based beam model exhibits excellent agreement with the DNS and MSG-based plate/shell model while it is more computationally efficient. Furthermore, distinctively to the uniform temperature distribution, the nonuniform cross-sectional temperature yields extension-bending coupling,

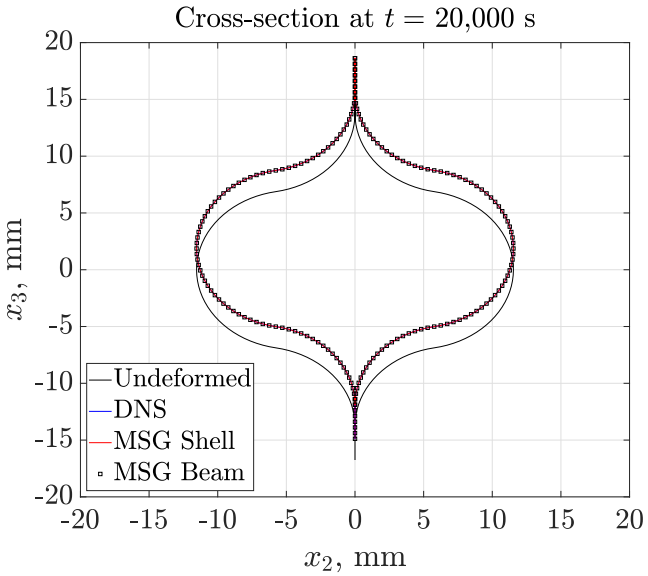

Figure 6.23. Evolution of the cross-sectional shape at midspan of the lenticular boom (i.e. $x_1 = 500$ mm) for $F_{x_3} = 1$ N load case with nonuniform temperature distribution of $T = 40°\text{C}$ and $[0_{UD}/45_{PW}]$ lay-up.

as can be observed in Table 6.17. Finally, as the $[0_{UD}/45_{PW}]$ laminate does not significantly relax with increased time and temperature, the evolution of the cross-section as well as the shape at time t = 20,000 s for the different loading conditions are similar to the ones presented for the uniform temperature distribution in Subsection 6.2.1 (see Figures 6.22-6.23). Therefore, it can be concluded that the $[0_{UD}/45_{PW}]$ laminate provides dimensional stability to the lenticular boom presented in this work.

Table 6.17. Displacement at midspan of the lenticular boom (i.e. x_1 = 500 mm) and time t = 20,000 s for the F_{x_1} = -1 N load case with nonuniform temperature distribution and $[0_{UD}/45_{PW}]$ lay-up.

Type	u_{x_1} mm	u_{x_2} mm	u_{x_3} mm	CPU time s
DNS	-7.3240e-04	-1.0650e-04	7.3800e-05	20,794
MSG Shell	-7.3220e-04	-1.1470e-04	1.9620e-05	1,252
MSG Beam	-7.3848e-04	-1.3101e-04	0.0000	Analytical

Table 6.18. Displacement at midspan of the lenticular boom (i.e. x_1 = 500 mm) and time t = 20,000 s for the F_{x_2} = 1 N load case with nonuniform temperature distribution and $[0_{UD}/45_{PW}]$ lay-up.

Type	u_{x_1} mm	u_{x_2} mm	u_{x_3} mm	CPU time s
DNS	0.1473	3.5120	0.0001	25,299
MSG Shell	0.1467	3.5280	0.0020	1,222
MSG Beam	0.0004	3.5109	0.0000	Analytical

Table 6.19. Displacement at midspan of the lenticular boom (i.e. x_1 = 500 mm) and time t = 20,000 s for the F_{x_3} = 1 N load case with nonuniform temperature distribution and $[0_{UD}/45_{PW}]$ lay-up.

Type	u_{x_1} mm	u_{x_2} mm	u_{x_3} mm	CPU time s
DNS	0.1125	0.0001	1.8700	24,161
MSG Shell	0.1125	0.0001	1.8700	1,130
MSG Beam	0.0000	0.0000	1.8685	Analytical

6.3 Summary

The MSG-based liner thermoviscoelastic beam model was developed to efficiently compute the effective thermoviscoelastic beam stiffness properties, thermal stress resultants and its global behavior of composite beams made of constituents with time- and temperature-dependent behavior. First, considering the 1D Euler-Bernoulli beam model, the QE method was used to the solve the hereditary integral describing the beam behavior and compute the effective themoviscoelastic beam stiffness properties. A lenticular boom and a TRAC boom with uniform and nonuniform temperature distributions were considered as numerical examples. Three-dimensional numerical simulations and analytical formulas were used to verify the accuracy of the results model showing excellent agreement with MSG results. In addition, the validity of the time shift to compute the effective beam stiffness properties at different temperatures departing from the effective beam stiffness properties at reference temperature was analyzed. PMT-F7 resin relaxation data characterized by NASA LaRC were used for this purpose. The study revealed that despite the heterogeneous thermoviscoelastic nature of the composite material, from a multiscale analysis perspective, the temperature dependencies of the effective beam stiffness properties are governed by the same shift factor as the polymer matrix except for nonuniform temperature distribution. Therefore, the most efficient approach is to compute the effective beam stiffness properties once at reference temperature and apply the shift function of the resin to these beam stiffness properties to compute the effective beam stiffness at other temperatures of interest. This conclusion remains the same for the MSG-based solid and plate/shell models. In addition, unlike traditional methods, the MSG-based model also allows to efficiently and accurately compute the extension-bending and torsion-bending terms of the stiffness matrix, which become more relevant when temperature distribution is not uniform over the cross-section. In addition, the analysis revealed that when steady-state nonuniform temperature distributions are considered within the SG, the effective thermoviscoelastic properties are required to be computed each time the temperature distribution changes.

In case of the global linear thermoviscoelastic beam problem, it was solved using the MSG-based DI method. This methodology assumed that the effective beam thermovis-

coelastic stiffness properties could be expressed by means of Prony series coefficients. 1D Euler-Bernoulli beam model was considered for this purpose. Then, the MSG-based DI beam model was analytically implemented to analyze a lenticular boom withstanding three different load conditions: compression, transverse force in x_2-direction and transverse force in x_3-direction. SwiftComp$^{\text{TM}}$ [112] was used to compute the effective thermoviscoelastic beam stiffness properties that then were fit into Prony series coefficients. Three-dimensional direct numerical simulations (DNS) and MSG-based thermoviscoelastic plate/shell model of a TRAC boom with uniform cross-sectional temperature distribution, and a lenticular boom with uniform and nonuniform cross-sectional temperature distribution were developed to verify the MSG-based thermoviscoelastic beam model. The latter showed excellent agreement for all the cases with both DNS and MSG-based plate/shell model in terms of global displacements and the recovered cross-sectional shape while significantly reducing the computational cost. The relaxation was practically nonexistent for the laminate of this study and hence, once the deformed shape was reached, the cross-sectional shape of the lenticular boom remained constant as the time increased time. The transverse load in the x_2-direction yielded the biggest displacement, followed by the transverse load in the x_3-direction and the compression load. However, the cross-sectional shape of the TRAC boom deformed more compared to the lenticular boom case and continued to evolve for increased time. Due to considering linear thermoviscoelastic behavior, the higher compression and transverse loads would scale up linearly the deformations as the effective properties only depended on time and temperature. Moreover, the MSG-based beam model of the lenticular boom was able to properly capture the behavior of the boom with a steady-state nonuniform cross-sectional temperature distribution. Distinctively to the uniform temperature distribution, the nonuniform cross-sectional temperature yielded extension-bending coupling. The fact that MSG-based thermoviscoelastic beam model provided accurate results with increased computational efficiency proves its feasibility to model booms that are in a fully deployed configuration. The MSG-based beam with nonuniform cross-sectional temperature distribution also brought new insights to predict the behavior of deployable booms.

7. SUMMARY

This work developed a unified thermodynamically consistent formulation to capture the behavior of linear thermoviscoelastic materials efficiently and accurately with time and temperature-dependency at different scales. To do so, mechanics of structure genome (MSG) was extended to capture the multiscale behavior of three-dimensional heterogeneous materials using solid, plate/shells or beam models subject to temperature changes. Thermorheologically simple materials were considered to derive MSG-based quasi-elastic (QE) and direct integration (DI) formulations from the integral form of the constitutive equation for a general anisotropic linear thermoviscoelastic non-aging material. The QE method was used for predicting thermoviscoelastic properties for composite solids, plate/shells and beams whereas the DI method was formulated to capture the global analysis of composite solids, plates/shells and beams. The computation of local fields by means of MSG-based dehomogenization step was not pursued in this work. The time-temperature superposition principle was used, and hence, the reduced time parameter related the time-temperature dependency of the anisotropic material by means of master curves at reference conditions. Uniform and nonuniform temperature distributions were considered. The derivation of exact three-dimensional thermoviscoelastic homogenization solutions for balanced and symmetric laminates was also presented. All the derived formulation based on QE method was implemented in SwiftComp$^{\text{TM}}$, for general-purpose constitutive modeling of time and temperature dependency for composites featuring arbitrary microstructure. The DI method was implemented in UMAT and UGENS subroutines in Abaqus for solids and plates/shells, respectively. The DI method required the Prony series coefficients of the effective thermoviscoelastic properties computed with SwiftComp$^{\text{TM}}$ as input.

The MSG-based solid model with the QE method was used to compute the effective thermoviscoelastic properties and analyze three numerical case studies comprising unidirectional fiber reinforced composite, a balanced and symmetric laminate, and a textile composite. The results were compared against 3D RVE analysis showing good agreement, except when time-dependent coefficients of thermal expansion (CTEs) were considered at constituent level. The 3D RVE analysis exhibited limitations to properly capture the long-term behavior of

effective CTEs when time-dependent constituent CTEs were considered. These limitations were not present for the case of MSG, as it accurately captured these long-term behaviors for both constant and time-dependent constituent CTEs, and also increased the computation efficiency. The analyses of the homogenized properties also revealed that the shift factor of the polymer matrix drives the temperature dependencies of the effective CTEs and engineering constants of the heterogeneous composite material across all the scales except for nonuniform temperature distribution. This finding was later proved to also hold for the equivalent thermoviscoelastic plate/shell and beam stiffness. Therefore, the most efficient approach is to compute the effective solid, plate/shell or beam stiffness properties once at reference temperature, and then apply the shift function of the resin to these stiffness properties to compute the effective solid, plate/shell or beam properties at other temperatures of interest. However, when steady-state nonuniform temperature distributions are considered within the SG, the effective thermoviscoelastic properties are required to be computed each time the temperature distribution changes.

The comparison of the simulated column bending test (CBT) results against the experimental data provided by NASA LaRC allowed to validate the MSG-based plate/shell models. The effective bending stiffness relaxation computed using MSG-based QE method showed excellent agreement against the experimental data provided by NASA LaRC. Then, this viscoelastic plate/shell stiffness matrix was fit into Prony series coefficients and used as input for the CBT simulated with the DI method. The results computed using MSG-based plate/shell model showed good qualitative agreement against the experimental data for the curvature during folding, moment during relaxation, as well as residual curvature immediately after unfolding, thereby validating the model and the UGENS subroutine [125].

The MSG-based 1D Euler-Bernoulli beam model was also used to model thin-ply high strain composite (TP-HSC) structures with uniform and nonuniform cross-sectional temperature distributions. A lenticular boom and a TRAC boom were selected for this study and 3D direct numerical simulations were conducted to verify the accuracy of SwiftComp$^{\text{TM}}$ results. It is noted that modeling TP-HSCs by means of beam models is a widely unexplored research area, and especially when different temperatures over the cross-section are present. Unlike traditional methods, the MSG-based model allowed to compute the extension-bending and

torsion-bending terms of the stiffness matrix efficiently and accurately, which became more relevant when nonuniform temperature distributions over the cross-section were present.

Finally, the MSG-based DI beam model was implemented analytically to analyze a lenticular boom withstanding three different load cases (i.e. compression force and transverse forces in x_2 and x_3 directions), and a TRAC boom withstanding two different load cases (i.e. compression and transverse force in x_3 direction). The thermoviscoelastic beam stiffness properties computed using MSG-based QE method were then fit into Prony series coefficients and used as input for the DI method. The DNS and MSG-based thermoviscoelastic plate/shell model of the lenticular and TRAC booms were developed to verify the MSG-based thermoviscoelastic beam model. The latter significantly reduced the computational cost while showing excellent agreement with both DNS and MSG-based plate/shell model. The consideration of linear thermoviscoelastic behavior implied that the higher compression and transverse loads would scale up linearly the deformations as the effective properties only depended on time and temperature. Moreover, the MSG-based beam model of the lenticular boom was able to properly capture the global behavior of the boom with a steady-state nonuniform cross-sectional temperature distribution. Distinctively to the uniform temperature distribution, the nonuniform cross-sectional temperature yielded extension-bending coupling. The fact that the MSG-based thermoviscoelastic beam model provided accurate results with increased computational efficiency proves its feasibility to model booms that are in a fully deployed configuration. This result is also applicable for the cases when the entire boom has a uniform temperature distribution different from the reference one. The MSG-based beam with nonuniform cross-sectional temperature distribution also demonstrated new capabilities to predict the behavior of large composite structures with uneven temperature distributions.

7.1 Recommendations

The current research work has identified several areas for further development building upon the formulation and methodology presented in this dissertation. A first step would consist of extending the MSG-based thermoviscoelastic method to handle dehomogenization

and recover the local fields within the SG. Although dehomogenization was not pursued in this work, some preliminary work to compute the local fields of step-type inputs at structural level has been carried out as QE and DI methods provide the same results for step-type inputs [125]. Nonetheless, a more general approach that considers arbitrary stress, displacement or strain inputs and computes local fields would be very convenient for failure and damage analysis, for instance.

It is also recommended to implement the MSG-based beam model in a user-defined element (UEL) subroutine in Abaqus to handle more general beam analyses. This subroutine would be very useful for early design stages of beam-like structures such as deployable composite booms and other large anisotropic composite structures.

Furthermore, a subsequent step to reinforce the use of the beam model would consist of extending the range of conditions to cover higher temperature differences and/or more extreme nonuniform temperature distributions for both the lenticular and TRAC boom cases. To do so, the resin would also need to be experimentally characterized at more extreme temperatures.

In addition, the application of the multiscale analysis approach with solid, plate/shell and beam models in thermoplastic materials would pave the way to analyze additive manufacturing simulations. Indeed, some preliminary work has been done with the Additive Manufacturing team of Composites Manufacturing & Simulation Center at Purdue University. However, a more systematic comparison between the simulated and experimental results is needed, especially to understand the influence that an uneven distribution of the degree of crystallinity has in the prediction of the final homogenized properties. This approach would consist of integrating the code developed to in-situ simulation of manufacturing processes. This would allow computing the effective properties with nonuniform temperature distributions within the SG using SwiftComp and then them into the manufacturing simulation code.

Finally, an additional future research work area would be the development and integration of a nonlinear MSG-based constitutive model to investigate and capture the effects of viscoelastic-viscoplastic media.

REFERENCES

[1] B. Brenken, E. Barocio, A. Favaloro, V. Kunc, and R. B. Pipes, "Fused filament fabrication of fiber-reinforced polymers: A review," *Additive Manufacturing*, vol. 21, pp. 1–16, May 2018. DOI: 10.1016/j.addma.2018.01.002.

[2] B. Brenken, E. Barocio, A. Favaloro, V. Kunc, and R. B. Pipes, "Development and validation of extrusion deposition additive manufacturing process simulations," *Additive Manufacturing*, vol. 25, pp. 218–226, Jan. 2019. DOI: 10.1016/j.addma.2018.10.041.

[3] Z. Yang, H. Wang, X. Ma, F. Shang, Y. Ma, Z. Shao, and D. Hou, "Flexural creep tests and long-term mechanical behavior of fiber-reinforced polymeric composite tubes," *Composite Structures*, vol. 193, pp. 154–164, Jun. 2018. DOI: 10.1016/j.compstruct.2018.03.083.

[4] A. I. Khan, E. C. Borowski, E. M. Soliman, and M. M. R. Taha, "Examining energy dissipation of deployable aerospace composites using matrix viscoelasticity," *Journal of Aerospace Engineering*, vol. 30, no. 5, p. 04 017 040, Sep. 2017. DOI: 10.1061/(asce)as.1943-5525.0000742.

[5] O. G. Kravchenko, "Prediction of chemical and thermal shrinkage in thermosetting composite," Ph.D. dissertation, School of Aeronautics and Astronautics, Purdue University, Aug. 2015.

[6] L. G. Zhao, N. A. Warrior, and A. C. Long, "A micromechanical study of residual stress and its effect on transverse failure in polymer–matrix composites," *International Journal of Solids and Structures*, vol. 43, no. 18-19, pp. 5449–5467, Sep. 2006. DOI: 10.1016/j.ijsolstr.2005.08.012.

[7] L. Zhao, N. A. Warrior, and A. Long, "A thermo-viscoelastic analysis of process-induced residual stress in fibre-reinforced polymer–matrix composites," *Materials Science and Engineering: A*, vol. 452-453, pp. 483–498, Apr. 2007. DOI: 10.1016/j.msea.2006.10.060.

[8] S. Clifford, N. Jansson, W. Yu, V. Michaud, and J.-A. Manson, "Thermoviscoelastic anisotropic analysis of process induced residual stresses and dimensional stability in real polymer matrix composite components," *Composites Part A: Applied Science and Manufacturing*, vol. 37, no. 4, pp. 538–545, Apr. 2006. DOI: 10.1016/j.compositesa.2005.05.008.

[9] P. Sunderland, W. Yu, and J. A. Månson, "A thermoviscoelastic analysis of process-induced internal stresses in thermoplastic matrix composites," *Polymer Composites*, vol. 22, no. 5, pp. 579–592, Oct. 2001. DOI: 10.1002/pc.10561.

[10] B. Brenken, "Extrusion deposition additive manufacturing of fiber reinforced semi-crytalline polymers," Ph.D. dissertation, School of Aeronautics and Astronautics, Purdue University, 2017.

[11] B. Brenken, A. Favaloro, E. Barocio, V. Kunc, and R. B. Pipes, "Thermoviscoelasticity in extrussion deposition additive manufacturing process simulations," in *Proceedings of the American Society for Composites: Thirty-second Technical Conference*, Purdue University, West Lafayette, IN: ASC, Oct. 2017.

[12] A. Courtois, L. Marcin, M. Benavente, E. Ruiz, and M. Lévesque, "Numerical multiscale homogenization approach for linearly viscoelastic 3D interlock woven composites," *International Journal of Solids and Structures*, vol. 163, pp. 61–74, May 2019. DOI: 10.1016/j.ijsolstr.2018.12.018.

[13] N. Zobeiry, "Viscoelastic constitutive models for evaluation of residual stresses in thermoset composites during cure," Ph.D. dissertation, University of British Columbia, 2003.

[14] O. R. Stohlman and E. Loper, "Thermal deformation of very slender TRAC booms," in *3rd AIAA Spacecraft Structures Conference*, San Diego, California: American Institute of Aeronautics and Astronautics, Jan. 2016. DOI: 10.2514/6.2016-1469.

[15] J. M. Fernandez, "Advanced deployable shell-based composite booms for small satellite structural applications including solar sails," in *4th International Symposium on Solar Sailing 2017*, 2017.

[16] J. M. Fernandez, G. Rose, O. R. Stohlman, C. J. Younger, G. D. Dean, J. E. Warren, J. H. Kang, R. G. Bryant, and K. W. Wilkie, "An advanced composites-based solar sail system for interplanetary small satellite missions," in *2018 AIAA Spacecraft Structures Conference*, Kissimmee, Florida: American Institute of Aeronautics and Astronautics, Jan. 2018. DOI: 10.2514/6.2018-1437.

[17] J. M. Fernandez and T. W. Murphey, "A simple test method for large deformation bending of thin high strain composite flexures," in *2018 AIAA Spacecraft Structures Conference*, Kissimmee, Florida: American Institute of Aeronautics and Astronautics, Jan. 2018. DOI: 10.2514/6.2018-0942.

[18] M. Mobrem and D. Adams, "Lenticular jointed antenna deployment anomaly and resolution onboard the Mars Express Spacecraft," *Journal of Spacecraft and Rockets*, vol. 46, no. 2, pp. 403–410, Mar. 2009. DOI: 10.2514/1.36891.

[19] B. Adamcik, J. Firth, M. Pankow, and J. M. Fernandez, "Impact of storage time and operational temperature on deployable composite booms," in *AIAA SciTech 2020 Forum*, Orlando, Florida: American Institute of Aeronautics and Astronautics, Jan. 2020. DOI: 10.2514/6.2020-1183.

[20] J. R. Blandino, "Analysis of thermal-mechanical interactions of STEM booms," in *2nd AIAA Spacecraft Structures Conference*, Kissimmee, Florida: American Institute of Aeronautics and Astronautics, Jan. 2015. DOI: 10.2514/6.2015-1164.

[21] N. Yamamoto, E. Gdoutos, and C. Daraio, "Engineered thin films with ultra-low thermal expansion coefficient for deployable or deformable space structures," in *54th AIAA/ASME/ASCE/AHS/ASC Structures, Structural Dynamics, and Materials Conference*, Boston, Massachusett: American Institute of Aeronautics and Astronautics, Apr. 2013. DOI: 10.2514/6.2013-1789.

[22] C. Sickinger, L. Herbeck, and E. Breitbach, "Structural engineering on deployable CFRP booms for a solar propelled sailcraft," *Acta Astronautica*, vol. 58, no. 4, pp. 185–196, Feb. 2006. DOI: 10.1016/j.actaastro.2005.09.011.

[23] W. Yu, "Variational asymptotic modeling of composite dimensionally reducible structures," Ph.D. dissertation, Aerospace Engineering, Georgia Institute of Technology, May 2002.

[24] W. Yu, V. V. Volovoi, D. H. Hodges, and X. Hong, "Validation of the variational asymptotic beam sectional analysis," *AIAA Journal*, vol. 40, no. 10, pp. 2105–2113, Oct. 2002.

[25] A. J. Lee and J. M. Fernandez, "Inducing bistability in collapsible tubular mast booms with thin-ply composite shells," *Composite Structures*, vol. 225, p. 111 166, Oct. 2019. DOI: 10.1016/j.compstruct.2019.111166.

[26] J. B. Bai, R. A. Shenoi, and J. J. Xiong, "Thermal analysis of thin-walled deployable composite boom in simulated space environment," *Composite Structures*, vol. 173, pp. 210–218, Aug. 2017. DOI: 10.1016/j.compstruct.2017.04.022.

[27] Z. Hashin, "Viscoelastic behavior of heterogeneous media," *Journal of Applied Mechanics*, vol. 32, no. 3, p. 630, 1965. DOI: 10.1115/1.3627270.

[28] Z. Hashin, "Viscoelastic fiber reinforced materials," *AIAA Journal*, vol. 4, no. 8, pp. 1411–1417, Aug. 1966. DOI: 10.2514/3.3686.

[29] Z. Hashin, "Complex moduli of viscoelastic composites—I. General theory and application to particulate composites," *International Journal of Solids and Structures*, vol. 6, no. 5, pp. 539–552, May 1970. DOI: 10.1016/0020-7683(70)90029-6.

[30] Z. Hashin, "Analysis of composite materials-A survey," *Applied Mechanics Review*, vol. 50, pp. 481–505, 1983.

[31] R. A. Schapery, "A method of viscoelastic stress analysis using elastic solutions," *Journal of the Franklin Institute*, vol. 279, no. 4, pp. 268–289, Apr. 1965. DOI: 10.1016/0016-0032(65)90339-x.

[32] R. A. Schapery, "Stress analysis of viscoelastic composite materials," *Journal of Composite Materials*, vol. 1, no. 3, pp. 228–267, Jul. 1967. DOI: 10.1177/002199836700100302.

[33] R. A. Schapery, "Thermal expansion coefficients of composite materials based on energy principles," *Journal of Composite Materials*, vol. 2, no. 3, pp. 380–404, Jul. 1968. DOI: 10.1177/002199836800200308.

[34] R. M. Christensen, "Viscoelastic properties of heterogeneous media," *Journal of the Mechanics and Physics of Solids*, vol. 17, no. 1, pp. 23–41, Feb. 1969. DOI: 10.1016/0022-5096(69)90011-8.

[35] R. Luciano and E. Barbero, "Analytical expressions for the relaxation moduli of linear viscoelastic composites with periodic microstructure," *Journal of Applied Mechanics*, vol. 62, no. 3, p. 786, 1995. DOI: 10.1115/1.2897015.

[36] P. Upadhyaya and C. S. Upadhyay, "A three-dimensional micromechanical model to predict the viscoelastic behavior of woven composites," *Composite Structures*, vol. 93, no. 11, pp. 2733–2739, Oct. 2011. DOI: 10.1016/j.compstruct.2011.05.031.

[37] R. Hill, "A self-consistent mechanics of composite materials," *Journal of the Mechanics and Physics of Solids*, vol. 13, no. 4, pp. 213–222, Aug. 1965. DOI: 10.1016/0022-5096(65)90010-4.

[38] T. Mori and K. Tanaka, "Average stress in matrix and average elastic energy of materials with misfitting inclusions," *Acta Metallurgica*, vol. 21, no. 5, pp. 571–574, May 1973. DOI: 10.1016/0001-6160(73)90064-3.

[39] S. W. Park and R. A. Schapery, "Methods of interconversion between linear viscoelastic material functions. part i—a numerical method based on prony series," *International Journal of Solids and Structures*, vol. 36, no. 11, pp. 1653–1675, Apr. 1999. DOI: 10.1016/s0020-7683(98)00055-9.

[40] J. Noh and J. Whitcomb, "Efficient techniques for predicting viscoelastic behavior of sublaminates," *Composites Part B: Engineering*, vol. 34, no. 8, pp. 727–736, Dec. 2003. DOI: 10.1016/s1359-8368(03)00082-9.

[41] V. Levin and I. Sevosticmov, "Micromechanical modeling of the effective viscoelastic properties of inhomogeneous materials using fraction-exponential operators," *International Journal of Fracture*, vol. 134, no. 3-4, pp. L37–L44, Aug. 2005. DOI: 10.1007/s10704-005-4103-8.

[42] C. Liu and Y. Shi, "An improved analytical solution for process-induced residual stresses and deformations in flat composite laminates considering thermo-viscoelastic effects," *Materials*, vol. 11, no. 12, p. 2506, Dec. 2018. DOI: 10.3390/ma11122506.

[43] L. C. Brinson and W. S. Lin, "Comparison of micromechanics methods for effective properties of multiphase viscoelastic composites," *Composite Structures*, vol. 41, no. 3-4, pp. 353–367, Mar. 1998. DOI: 10.1016/s0263-8223(98)00019-1.

[44] F. T. Fisher and L. C. Brinson, "Viscoelastic interphases in polymer–matrix composites: Theoretical models and finite-element analysis," *Composites Science and Technology*, vol. 61, no. 5, pp. 731–748, Apr. 2001. DOI: 10.1016/s0266-3538(01)00002-1.

[45] M. Lévesque, K. Derrien, L. Mishnaevski, D. Baptiste, and M. D. Gilchrist, "A micromechanical model for nonlinear viscoelastic particle reinforced polymeric composite materials—undamaged state," *Composites Part A: Applied Science and Manufacturing*, vol. 35, no. 7-8, pp. 905–913, Jul. 2004. DOI: 10.1016/j.compositesa.2004.02.017.

[46] A. H. Muliana and J. S. Kim, "A concurrent micromechanical model for predicting nonlinear viscoelastic responses of composites reinforced with solid spherical particles," *International Journal of Solids and Structures*, vol. 44, no. 21, pp. 6891–6913, Oct. 2007. DOI: 10.1016/j.ijsolstr.2007.03.016.

[47] H. H. Zhang and L. X. Li, "Modeling inclusion problems in viscoelastic materials with the extended finite element method," *Finite Elements in Analysis and Design*, vol. 45, no. 10, pp. 721–729, Aug. 2009. DOI: 10.1016/j.finel.2009.06.006.

[48] A. B. Tran, J. Yvonnet, Q. C. He, C. Toulemonde, and J. Sanahuja, "A simple computational homogenization method for structures made of linear heterogeneous viscoelastic materials," *Computer Methods in Applied Mechanics and Engineering*, vol. 200, no. 45-46, pp. 2956–2970, Oct. 2011. DOI: 10.1016/j.cma.2011.06.012.

[49] A. A. Gusev, "Finite element estimates of viscoelastic stiffness of short glass fiber reinforced composites," *Composite Structures*, vol. 171, pp. 53–62, Jul. 2017. DOI: 10.1016/j.compstruct.2017.03.021.

[50] N. Zobeiry, S. Malek, R. Vaziri, and A. Poursartip, "A differential approach to finite element modelling of isotropic and transversely isotropic viscoelastic materials," *Mechanics of Materials*, vol. 97, pp. 76–91, Jun. 2016. DOI: 10.1016/j.mechmat.2016.02.013.

[51] M. V. Pathan, V. L. Tagarielli, and S. Patsias, "Numerical predictions of the anisotropic viscoelastic response of uni-directional fibre composites," *Composites Part A: Applied Science and Manufacturing*, vol. 93, pp. 18–32, Feb. 2017. DOI: 10.1016/j.compositesa.2016.10.029.

[52] T. Tang and S. D. Felicelli, "Computational evaluation of effective stress relaxation behavior of polymer composites," *International Journal of Engineering Science*, vol. 90, pp. 76–85, May 2015. DOI: 10.1016/j.ijengsci.2015.02.003.

[53] W. Yu and T. Tang, "Variational asymptotic method for unit cell homogenization of periodically heterogeneous materials," *International Journal of Solids and Structures*, vol. 44, pp. 3738–3755, 2007.

[54] A. El-Mourid, R. Ganesan, and M. Lévesque, "Comparison between analytical and numerical predictions for the linearly viscoelastic behavior of textile composites," *Mechanics of Materials*, vol. 58, pp. 69–83, Mar. 2013. DOI: 10.1016/j.mechmat.2012.11.003.

[55] A. Courtois, "3D Interlock composites multi-scale viscoelastic model development, characterization and modeling," Ph.D. dissertation, Mechanical Engineering, Polytechnique Montreal, 2018.

[56] M. Lévesque, K. Derrien, D. Baptiste, and M. D. Gilchrist, "On the development and parameter identification of Schapery-type constitutive theories," *Mechanics of Time-Dependent Materials*, vol. 12, no. 2, pp. 95–127, Mar. 2008. DOI: 10.1007/s11043-008-9052-y.

[57] M. A. Biot, "Theory of stress-strain relations in anisotropic viscoelasticity and relaxation phenomena," *Journal of Applied Physics*, vol. 25, no. 11, pp. 1385–1391, Nov. 1954. DOI: 10.1063/1.1721573.

[58] A. Courtois, M. Hirsekorn, M. Benavente, A. Jaillon, L. Marcin, E. Ruiz, and M. Lévesque, "Viscoelastic behavior of an epoxy resin during cure below the glass transition temperature: Characterization and modeling," *Journal of Composite Materials*, vol. 53, no. 2, pp. 155–171, Jun. 2018. DOI: 10.1177/0021998318781226.

[59] M. Benavente, L. Marcin, A. Courtois, M. Lévesque, and E. Ruiz, "Numerical analysis of viscoelastic process-induced residual distortions during manufacturing and post-curing," *Composites Part A: Applied Science and Manufacturing*, vol. 107, pp. 205–216, Apr. 2018. DOI: 10.1016/j.compositesa.2018.01.005.

[60] M. B. Miana, "Viscoelastic distortion during manufacturing and post-curing of thermoset composites: Chracterization and modeling," Ph.D. dissertation, Mechanical Engineering, Polytechnique Montreal, 2017.

[61] M. Benavente, L. Marcin, A. Courtois, M. Lévesque, and E. Ruiz, "Viscoelastic distortion in asymmetric plates during post curing," *Composites Part A: Applied Science and Manufacturing*, vol. 103, pp. 122–130, Dec. 2017. DOI: 10.1016/j.compositesa.2017.09.017.

[62] A. H. Muliana and R. Haj-Ali, "A multi-scale framework for layered composites with thermo-rheologically complex behaviors," *International Journal of Solids and Structures*, vol. 45, no. 10, pp. 2937–2963, May 2008. DOI: 10.1016/j.ijsolstr.2008.01.015.

[63] S. Sawant and A. Muliana, "A thermo-mechanical viscoelastic analysis of orthotropic materials," *Composite Structures*, vol. 83, no. 1, pp. 61–72, Mar. 2008. DOI: 10.1016/j.compstruct.2007.03.008.

[64] Y. Cai and H. Sun, "Dynamic response of thermo-viscoelasticity of three-dimensionally braided composites," *Journal of Composite Materials*, vol. 48, no. 13, pp. 1575–1583, May 2013. DOI: 10.1177/0021998313488152.

[65] R. S. Spencer and R. F. Boyer, "Thermal expansion and second-order transition effects in high polymers: III. Time effects," *Journal of Applied Physics*, vol. 17, no. 5, pp. 398–404, May 1946. DOI: 10.1063/1.1707730.

[66] M. Mukherjee, M. Bhattacharya, M. K. Sanyal, T. Geue, J. Grenzer, and U. Pietsch, "Reversible negative thermal expansion of polymer films," *Physical Review E*, vol. 66, no. 6, Dec. 2002. DOI: 10.1103/physreve.66.061801.

[67] T. Miyazaki, K. Nishida, and T. Kanaya, "Contraction and reexpansion of polymer thin films," *Physical Review E*, vol. 69, no. 2, Feb. 2004. DOI: 10.1103/physreve.69.022801.

[68] G. Reiter and S. Napolitano, "Possible origin of thickness-dependent deviations from bulk properties of thin polymer films," *Journal of Polymer Science Part B: Polymer Physics*, vol. 48, no. 24, pp. 2544–2547, Sep. 2010. DOI: 10.1002/polb.22134.

[69] R. A. Schapery, "Application of thermodynamics to thermomechanical, fracture, and birefringent phenomena in viscoelastic media," *Journal of Applied Physics*, vol. 35, no. 5, pp. 1451–1465, May 1964. DOI: 10.1063/1.1713649.

[70] M. A. Zocher, S. E. Groves, and D. H. Allen, "A three dimensional finite element formulation for thermoviscoelastic orthotropic media," *International Journal for Numerical Methods in Engineering*, vol. 40, no. 12, pp. 2267–2288, Jun. 1997. DOI: 10.1002/(sici)1097-0207(19970630)40:12{$⟨$}2267::aid-nme156{$⟩$}3.0.co;2-p.

[71] R. Lakes, *Viscoelastic Materials*. Cambridge University Press, Apr. 11, 2009, ISBN: 052188568X.

[72] K. A. Khan and A. H. Muliana, "Effective thermal properties of viscoelastic composites having field-dependent constituent properties," *Acta Mechanica*, vol. 209, no. 1-2, pp. 153–178, Apr. 2009. DOI: 10.1007/s00707-009-0171-6.

[73] H. E. Pettermann and A. DeSimone, "An anisotropic linear thermo-viscoelastic constitutive law," *Mechanics of Time-Dependent Materials*, Sep. 2017. DOI: 10.1007/s11043-017-9364-x.

[74] Y. K. Kim and S. R. White, "Stress relaxation behavior of 3501-6 epoxy resin during cure," *Polymer Engineering & Science*, vol. 36, no. 23, pp. 2852–2862, Dec. 1996. DOI: 10.1002/pen.10686.

[75] Y. K. Kim and S. R. White, "Process-induced stress relaxation analysis of AS4/3501-6 laminate," *Journal of Reinforced Plastics and Composites*, vol. 16, no. 1, pp. 2–16, Jan. 1997. DOI: 10.1177/073168449701600102.

[76] Y. K. Kim and S. R. White, "Viscoelastic analysis of processing-induced residual stresses in thick composite laminates," *Mechanics of Advanced Materials and Structures*, vol. 4, no. 4, pp. 361–387, Oct. 1997. DOI: 10.1080/10759419708945889.

[77] S. R. White and Y. K. Kim, "Process-induced residual stress analysis of AS4/3501-6 composite material," *Mechanics of Advanced Materials and Structures*, vol. 5, no. 2, pp. 153–186, Apr. 1998. DOI: 10.1080/10759419808945897.

[78] A. Ding, S. Li, J. Wang, and L. Zu, "A three-dimensional thermo-viscoelastic analysis of process-induced residual stress in composite laminates," *Composite Structures*, vol. 129, pp. 60–69, Oct. 2015. DOI: 10.1016/j.compstruct.2015.03.034.

[79] A. Ding, S. Li, J. Sun, J. Wang, and L. Zu, "A thermo-viscoelastic model of process-induced residual stresses in composite structures with considering thermal dependence," *Composite Structures*, vol. 136, pp. 34–43, Feb. 2016. DOI: 10.1016/j.compstruct.2015.09.014.

[80] A. Ding, S. Li, J. Sun, J. Wang, and L. Zu, "A comparison of process-induced residual stresses and distortions in composite structures with different constitutive laws," *Journal of Reinforced Plastics and Composites*, vol. 35, no. 10, pp. 807–823, Feb. 2016. DOI: 10.1177/0731684416629764.

[81] Z. Yuan, Y. Wang, G. Yang, A. Tang, Z. Yang, S. Li, Y. Li, and D. Song, "Evolution of curing residual stresses in composite using multi-scale method," *Composites Part B: Engineering*, vol. 155, pp. 49–61, Dec. 2018. DOI: 10.1016/j.compositesb.2018.08.012.

[82] S. L. Simon, G. B. McKenna, and O. Sindt, "Modeling the evolution of the dynamic mechanical properties of a commercial epoxy during cure after gelation," *Journal of Applied Polymer Science*, vol. 76, no. 4, pp. 495–508, Apr. 2000. DOI: 10.1002/(sici)1097-4628(20000425)76:4{$⟨$}495::aid-app7{$⟩$}3.0.co;2-b.

[83] A. T. DiBenedetto, "Prediction of the glass transition temperature of polymers: A model based on the principle of corresponding states," *Journal of Polymer Science Part B: Polymer Physics*, vol. 25, no. 9, pp. 1949–1969, Sep. 1987. DOI: 10.1002/polb.1987.090250914.

[84] D. J. O'Brien, P. T. Mather, and S. R. White, "Viscoelastic properties of an epoxy resin during cure," *Journal of Composite Materials*, vol. 35, no. 10, pp. 883–904, May 2001. DOI: 10.1177/a037323.

[85] T. J. Chapman, J. W. Gillespie, R. B. Pipes, J. A. E. Manson, and J. C. Seferis, "Prediction of process-induced residual stresses in thermoplastic composites," *Journal of Composite Materials*, vol. 24, no. 6, pp. 616–643, Jun. 1990. DOI: 10.1177/002199839002400603.

[86] W. E. Lawrence, J. A. E. Manson, J. C. Seferis, J. W. Gillespie, and R. B. Pipes, "Prediction of residual stress in continuous fiber semicrystalline thermoplastic composites: A kinetic-viscoelastic approach," in *ASC Conference Proceedings, 5th Technical Conference*, 1990.

[87] Y. Xu, P. Zhang, and W. Zhang, "Two-scale micromechanical modeling of the time dependent relaxation modulus of plain weave polymer matrix composites," *Composite Structures*, vol. 123, pp. 35–44, May 2015. DOI: 10.1016/j.compstruct.2014.12.031.

[88] R. M. Haj-Ali and A. H. Muliana, "Numerical finite element formulation of the Schapery non-linear viscoelastic material model," *International Journal for Numerical Methods in Engineering*, vol. 59, no. 1, pp. 25–45, Nov. 2003. DOI: 10.1002/nme.861.

[89] D. H. Pahr and P. K. Zysset, "Influence of boundary conditions on computed apparent elastic properties of cancellous bone," *Biomechanics and Modeling in Mechanobiology*, vol. 7, no. 6, pp. 463–476, Oct. 2007. DOI: 10.1007/s10237-007-0109-7.

[90] D. Pahr and H. J. Böhm, "Assessment of mixed uniform boundary conditions for predicting the mechanical behavior of elastic and inelastic discontinuously reinforced composites," *Computer Modeling and Engineering and Sciences*, vol. 34, no. 2, pp. 117–136, 2008. DOI: 10.3970/cmes.2008.034.117.

[91] K. Kwok and S. Pellegrino, "Viscoelastic effects in tape-springs," in *52nd AIAA/ASME/ASCE/AHS/ASC Structures, Structural Dynamics and Materials Conference*, Denver, Colorado: American Institute of Aeronautics and Astronautics, Apr. 2011. DOI: 10.2514/6.2011-2022.

[92] K. Kwok and S. Pellegrino, "Folding, stowage, and deployment of viscoelastic tape springs," *AIAA Journal*, vol. 51, no. 8, pp. 1908–1918, Aug. 2013. DOI: 10.2514/1.j052269.

[93] K. Kwok, "Shape recovery of viscoelastic beams after stowage," *Mechanics Based Design of Structures and Machines*, vol. 43, no. 1, pp. 95–111, Sep. 2014. DOI: 10.1080/15397734.2014.930668.

[94] K. Kwok and S. Pellegrino, "Micromechanical modeling of deployment and shape recovery of thin-walled viscoelastic composite space structures," in *53rd AIAA/ASME/ASCE/AHS/ASC Structures, Structural Dynamics and Materials Conference*, Honolulu, Hawaii: American Institute of Aeronautics and Astronautics, Apr. 2012. DOI: 10.2514/6.2012-1910.

[95] K. Kwok and S. Pellegrino, "Micromechanics models for viscoelastic plain-weave composite tape springs," *AIAA Journal*, vol. 55, no. 1, pp. 309–321, Jan. 2017. DOI: 10.2514/1.j055041.

[96] A. Gomez-Delrio and K. Kwok, "Stowage and recovery of thin-ply composite deployable structures," in *AIAA SciTech 2020 Forum*, Orlando, Florida: American Institute of Aeronautics and Astronautics, Jan. 2020. DOI: 10.2514/6.2020-0205.

[97] S. Ropers, M. Kardos, and T. A. Osswald, "A thermo-viscoelastic approach for the characterization and modeling of the bending behavior of thermoplastic composites," *Composites Part A: Applied Science and Manufacturing*, vol. 90, pp. 22–32, Nov. 2016. DOI: 10.1016/j.compositesa.2016.06.016.

[98] S. Ropers, U. Sachs, M. Kardos, and T. A. Osswald, "A thermo-viscoelastic approach for the characterization and modeling of the bending behavior of thermoplastic composites – part II," *Composites Part A: Applied Science and Manufacturing*, vol. 96, pp. 67–76, May 2017. DOI: 10.1016/j.compositesa.2017.02.007.

[99] H. Alshahrani and M. Hojjati, "A theoretical model with experimental verification for bending stiffness of thermosetting prepreg during forming process," *Composite Structures*, vol. 166, pp. 136–145, Apr. 2017. DOI: 10.1016/j.compstruct.2017.01.030.

[100] Z. Shou, F. Chen, and H. Yin, "Self-heating of a polymeric particulate composite under mechanical excitations," *Mechanics of Materials*, vol. 117, pp. 116–125, Feb. 2018. DOI: 10.1016/j.mechmat.2017.11.003.

[101] e-Xstream, *Digimat -user's manual*, Sep. 2018.

[102] J. D. Eshelby, "The determination of the elastic field of an ellipsoidal inclusion, and related problems," *Proceedings of the Royal Society of London. Series A. Mathematical and Physical Sciences*, vol. 241, no. 1226, pp. 376–396, Aug. 1957. DOI: 10.1098/rspa.1957.0133.

[103] Moldex3D, *Moldex3D solution Add-on - Viscoelasticity*. [Online]. Available: https://www.moldex3d.com/en/products/software/moldex3d/solution-add-on/viscoelasticity/.

[104] Abaqus, *6.14 documentation*, Dassault Systèmes Simulia Corporation, 2014.

[105] M. T. Abadi, "Micromechanical analysis of stress relaxation response of fiber-reinforced polymers," *Composites Science and Technology*, vol. 69, no. 7-8, pp. 1286–1292, Jun. 2009. DOI: 10.1016/j.compscitech.2009.02.036.

[106] A. Naik, N. Abolfathi, G. Karami, and M. Ziejewski, "Micromechanical viscoelastic characterization of fibrous composites," *Journal of Composite Materials*, vol. 42, no. 12, pp. 1179–1204, Jun. 2008. DOI: 10.1177/0021998308091221.

[107] S. E. Company, *Micromechanics Plugin For Abaqus/CAE. Version 1.15*, Dec. 2017.

[108] W. Yu, "A unified theory for constitutive modeling of composites," *Journal of Mechanics of Materials and Structures*, vol. 11, no. 4, pp. 379–411, 2016.

[109] B. Peng and W. Yu, "A micromechanics theory for homogenization and dehomogenization of aperiodic heterogeneous materials," *Composite Structures*, vol. 199, pp. 53–62, Sep. 2018. DOI: 10.1016/j.compstruct.2018.05.047.

[110] X. Liu, T. Tang, W. Yu, and R. B. Pipes, "Multiscale modeling of viscoelastic behaviors of textile composites," *International Journal of Engineering Science*, vol. 130, pp. 175–186, Sep. 2018. DOI: 10.1016/j.ijengsci.2018.06.003.

[111] E. J. Barbero, *Finite Element Analysis of Composite Materials using Abaqus™*. CRC Press, 2013, ISBN: 9781466516618.

[112] W. Yu, *SwiftComp™ user manual - version 2.1*. [Online]. Available: https://cdmhub.org/resources/scstandard/supportingdocs.

[113] B. Peng, O. Rique, S. Tian, and W. Yu, *Abaqus-SwiftComp GUI*, 2016. [Online]. Available: https://cdmhub.org/resources/1134.

[114] H. F. Brinson, *Polymer Engineering Science and Viscoelasticity*. Springer US, Jan. 24, 2015.

[115] S. P. C. Marques and G. J. Creus, *Computational Viscoelasticity*. Springer Berlin Heidelberg, 2012. DOI: 10.1007/978-3-642-25311-9.

[116] F. Schwarzl and A. J. Staverman, "Time-temperature dependence of linear viscoelastic behavior," *Journal of Applied Physics*, vol. 23, no. 8, pp. 838–843, Aug. 1952. DOI: 10.1063/1.1702316.

[117] P. M. Christensen, *Theory of Viscoelasticity: An Introduction, 2nd Edition.* Academic Press, 1982, ISBN: 978-0-12-174252-2.

[118] A. Pyatigorets, M. Marasteanu, L. Khazanovich, and H. Stolarski, "Application of a matrix operator method to the thermoviscoelastic analysis of composite structures," *Journal of Mechanics of Materials and Structures*, vol. 5, no. 5, pp. 837–854, Dec. 2010. DOI: 10.2140/jomms.2010.5.837.

[119] V. Martynenko and G. Lvov, "Numerical prediction of temperature-dependent anisotropic viscoelastic properties of fiber reinforced composite," *Journal of Reinforced Plastics and Composites*, vol. 36, no. 24, pp. 1790–1801, Aug. 2017. DOI: 10.1177/0731684417727064.

[120] T. Tang and S. D. Felicelli, "Micromechanical investigations of polymer matrix composites with shape memory alloy reinforcement," *International Journal of Engineering Science*, vol. 94, pp. 181–194, Sep. 2015. DOI: 10.1016/j.ijengsci.2015.05.008.

[121] R. A. Schapery, "Viscoelastic behavior and analysis of composite materials," in *Mechanics of Composite Materials*, G. Sendeckyi, Ed., vol. 2, New York: Academic Press, Jan. 1974, pp. 85–169, ISBN: 9781483216683.

[122] O. Rique and W. Yu, "Multiscale modeling of thermoviscoelasticity for composite manufacturing simulation using mechanics of structure," in *AIAA SciTech 2019 Forum*, San Diego, California: American Institute of Aeronautics and Astronautics, Jan. 2019. DOI: 10.2514/6.2019-1203.

[123] R. A. Schapery, "Approximate methods of transform inversion for viscoelastic stress analysis," in *Proc. 4th U.S. Natl. Congr. Appl. Mech.*, ASME, 1962, p. 1075.

[124] C. Teng, W. Yu, and M. Y. Chen, "Variational asymptotic homogenization of temperature -dependent heterogeneous materials under finite temperature changes," *International Journal of Solids and Structures*, vol. 49, pp. 2439–2449, 2012.

[125] Y. Long, O. Rique, J. M. Fernandez, A. C. Bergan, and W. Yu, "Multiscale simulation of deployable composite structures," in *AIAA SciTech 2021 Forum*, Virtual Event, Jan. 2021. DOI: 10.2514/6.2021-0199.

[126] W. Yu, "Simplified formulation of mechanics of structure genome," *AIAA Journal*, pp. 1–9, Feb. 2019. DOI: 10.2514/1.j057500.

[127] W. Yu, "An introduction to micromechanics," in *Composite Materials and Structures in Aerospace Engineering: Applied Mechanics and Materials*, E. Carrera, Ed., vol. 828, Trans Tech Publications Ltd, 2016, pp. 3–24.

[128] C. T. Sun and R. S. Vaidya, "Prediction of composite properties from a representative volume element," *Composites Science and Technology*, vol. 56, pp. 171–179, 1996.

[129] J. Fish, *Practical Multiscaling*. Wiley, 2013.

[130] B. Peng, J. Goodsell, R. B. Pipes, and W. Yu, "Generalized free-edge stress analysis using mechanics of structure genome," *Journal of Applied Mechanics*, vol. 83, no. 10, 2016, Article 101013.

[131] H. M. Sertse, J. Goodsell, A. J. Ritchey, R. B. Pipes, and W. Yu, "Challenge problems for the benchmarking of micromechanics analysis: Level I initial results," *Journal of Composite Materials*, vol. 52, no. 1, pp. 61–80, Apr. 2017. DOI: 10.1177/0021998317702437.

[132] V. L. Berdichevsky, *Variational Principles of Continuum Mechanics*. Springer Berlin, 2009, vol. 1 and 2.

[133] X. Liu, W. Yu, F. Gasco, and J. Goodsell, "A unified approach for thermoelastic constitutive modeling of composite structures," *Composites Part B: Engineering*, vol. 172, pp. 649–659, Sep. 2019. DOI: 10.1016/j.compositesb.2019.05.083.

[134] W. Yu, D. H. Hodges, and J. C. Ho, "Variational asymptotic beam sectional analysis - An updated version," *International Journal of Engineering Science*, vol. 59, pp. 40–64, 2012.

[135] W. Yu and T. Tang, "A variational asymptotic micromechanics model for predicting thermoelastic properties of heterogeneous materials," *International Journal of Solids and Structures*, vol. 44, no. 22-23, pp. 7510–7525, 2007.

[136] O. Rique, X. Liu, W. Yu, and R. B. Pipes, "Constitutive modeling for time- and temperature-dependent behavior of composites," *Composites Part B: Engineering*, vol. 184, p. 107 726, Mar. 2020. DOI: 10.1016/j.compositesb.2019.107726.

[137] H. Lin, L. P. Brown, and A. C. Long, "Modelling and simulating textile structures using TexGen," *Advanced Materials Research*, vol. 331, pp. 44–47, Sep. 2011. DOI: 10.4028/www.scientific.net/amr.331.44.

[138] X. Liu and W. Yu, *TexGen4SC*, Online, Retrieved on December 9, 2019, 2016. [Online]. Available: https://cdmhub.org/resources/texgen4sc.

[139] C. Karch, "Micromechanical analysis of thermal expansion coefficients," *Modeling and Numerical Simulation of Material Science*, vol. 04, no. 03, pp. 104–118, 2014. DOI: 10.4236/mnsms.2014.43012.

[140] X. Liu, K. Rouf, B. Peng, and W. Yu, "Two-step homogenization of textile composites using mechanics of structure genome," *Composite Structures*, vol. 171, pp. 252–262, 2017.

[141] O. Rique, Y. Long, W. Yu, R. B. Pipes, J. M. Fernandez, and A. C. Bergan, "Improved plate and beam models for thermoviscoelastic constitutive modeling of composites," in *American Society for Composites 2020*, Virtual Conference: DEStech Publications, Inc., Sep. 2020. DOI: 10.12783/asc35/34929.

[142] J. M. Fernandez, J. Salazar, M. Y. Hamillage, A. Gomez-Delrio, and K. Kwok, "Large deformation bending relaxation of thin-ply composite laminates," in *22nd International Conference on Composite Materials (ICCM22)*, Melbourne, Australia: RMIT University, Aug. 2019.

[143] J. E. Salazar and J. M. Fernandez, "Experimental characterization of the dimensional stability of deployable composite booms during stowage," in *AIAA SciTech 2021 Forum*, Virtual Event: American Institute of Aeronautics and Astronautics, Jan. 2021. DOI: 10.2514/6.2021-0195.

[144] M. Y. Hamillage, K. Kwok, and J. M. Fernandez, "Micromechanical modeling of high-strain thin-ply composites," in *AIAA SciTech 2019 Forum*, San Diego, California: American Institute of Aeronautics and Astronautics, Jan. 2019. DOI: 10.2514/6.2019-1751.

[145] E. C. Borowski, "Viscoelastic effects in carbon fiber reinforced polymer strain energy deployable composite tape springs," M.S. thesis, University of New Mexico, College Station, TX, Aug. 2017.

[146] O. Rique, S. Tian, J. M. Fernandez, A. C. Bergan, and W. Yu, "Thermoviscoelastic modeling of thin-ply high strain composites by means of multiscale beam models," in *AIAA SciTech 2021 Forum*, Virtual Event, Jan. 2021. DOI: 10.2514/6.2021-0197.

[147] F. Hakkak and S. Khoddam, "On calculation of preliminary design parameters for lenticular booms," *Proceedings of the Institution of Mechanical Engineers, Part G: Journal of Aerospace Engineering*, vol. 221, no. 3, pp. 377–384, Mar. 2007. DOI: 10.1243/09544100jaero138.

[148] O. R. Stohlman, "Coupled radiative thermal and nonlinear stress analysis for thermal deformation in large space structures," in *2018 AIAA Spacecraft Structures Conference*, Kissimmee, Florida: American Institute of Aeronautics and Astronautics, Jan. 2018. DOI: 10.2514/6.2018-0448.

[149] R. J. Crowson and R. G. Arridge, "Linear viscoelastic properties of epoxy resin polymers in dilatation and shear in the glass transition region. 1. Time-temperature superposition of creep data," *Polymer*, vol. 20, no. 6, pp. 737–746, Jun. 1979. DOI: 10.1016/0032-3861(79)90249-0.

[150] M. Sadeghinia, K. M. B. Jansen, and L. J. Ernst, "Characterization and modeling the thermo-mechanical cure-dependent properties of epoxy molding compound," *International Journal of Adhesion and Adhesives*, vol. 32, pp. 82–88, Jan. 2012. DOI: 10.1016/j.ijadhadh.2011.10.007.

[151] M. Hojjati, A. Johnston, S. V. Hoa, and J. Denault, "Viscoelastic behavior of cytec FM73 adhesive during cure," *Journal of Applied Polymer Science*, vol. 91, no. 4, pp. 2548–2557, 2003. DOI: 10.1002/app.13416.

[152] M. L. Williams, R. F. Landel, and J. D. Ferry, "The temperature dependence of relaxation mechanisms in amorphous polymers and other glass-forming liquids," *Journal of the American Chemical Society*, vol. 77, no. 14, pp. 3701–3707, Jul. 1955. DOI: 10.1021/ja01619a008.

[153] T. O. Williams, "A two-dimensional, higher-oder, elasticity-based micromechanics model," *International Journal of Solids and Structures*, vol. 42, pp. 1009–1038, 2005.

[154] L. A. Carlsson, D. F. Adams, and R. B. Pipes, *Experimental Characterization of Advanced Composite Materials*. CRC Press, Mar. 2014. DOI: 10.1201/b16618.

[155] P. Hubert, A. Johnston, A. P. A, and K. Nelson, "Cure kinetics and viscosity models for Hexcel 8552 epoxy resin," in *46th international SAMPE symposium*, Long Beach, California: CRC Press, May 2001.

[156] C. N. Velisaris and J. C. Seferis, "Crystallization kinetics of polyetheretherketone PEEK matrices," *Polymer Engineering and Science*, vol. 26, no. 22, pp. 1574–1581, Dec. 1986. DOI: 10.1002/pen.760262208.

[157] M. C. Li, J. J. Wu, A. C. Loos, and J. Morton, "A plane-strain finite element model for process-induced residual stresses in a graphite/PEEK composite," *Journal of Composite Materials*, vol. 31, no. 3, pp. 212–243, Feb. 1997. DOI: 10.1177/002199839703100301.

[158] C. N. Velisaris and J. C. Seferis, "Heat transfer effects on the processing-structure relationships of polyetheretherketone (PEEK) based composites," *Polymer Engineering and Science*, vol. 28, no. 9, pp. 583–591, May 1988. DOI: 10.1002/pen.760280907.

[159] M. Avrami, "Kinetics of phase change. I General theory," *The Journal of Chemical Physics*, vol. 7, no. 12, pp. 1103–1112, Dec. 1939. DOI: 10.1063/1.1750380.

[160] O. Rique, J. E. Goodsell, W. Yu, and R. B. Pipes, "Three-dimensional thermoelastic properties of general composite laminates," *Journal of Composite Materials*, vol. 52, no. 13, pp. 1799–1808, Oct. 2017. DOI: 10.1177/0021998317734037.

[161] G. Andrews, A. Black, J. Graham, and O. Rique, "Preliminary design of a rotating detonation engine for launch vehicle applications," in *2018 AIAA Aerospace Sciences Meeting*, Kissimmee, Florida: American Institute of Aeronautics and Astronautics, Jan. 2018. DOI: 10.2514/6.2018-1671.

[162] O. Rique, E. Barocio, and W. Yu, "Experimental and numerical determination of the thermal conductivity tensor for composites manufacturing simulation," in *American Society for Composites 2017*, West Lafayette, Indiana: DEStech Publications, Inc., Nov. 2017. DOI: 10.12783/asc2017/15217.

[163] O. Rique, Y. Long, J. Goodsell, W. Yu, and R. B. Pipes, "Composite de-tooling simulation using an improved plate and shell theory based on mechanics of structure genome," in *American Society for Composites 2016*, Williamsburg, Virginia: DEStech Publications, Inc., Oct. 2016.

[164] M. Knauf, E. Barocio, J. Miller, M. Prall, O. Rique, D. Sommer, and O. Wingfie, "Uniting composite manufacturing theory and application: Practical manufacturing methods in a team-based curriculum," in *American Society for Composites 2016*, Williamsburg, Virginia: DEStech Publications, Inc., Oct. 2016.

A. MATERIAL PROPERTY DATA

This appendix first presents a brief compendium of the formulation required to describe the behavior of thermoset and thermoplastic composites. Then, it also contains the relevant constitutive material data for the different material systems used in the numerical studies of this dissertation. Most of the data have been gathered from the literature. PMT-F7 toughened epoxy resin data were provided by NASA LaRC [143].

A.1 Thermoset and Thermoplastic Composites

This section provides additional constitutive relations for thermoset and thermoplastic composites to complement the formulation for linear thermoviscoelasticity. Since most of these formulae are obtained from data reduction of phenomenological processes experimentally measured, slight variations from a thermorheologically simple media to another one may be expected.

A.1.1 Thermoset Composites

In thermoset composites the resin transforms from a viscous liquid before the gel point to a viscoelastic solid with increasing viscosity through the formation of polymer networks [55]. The temperature around which the polymer transforms from a brittle glassy state to a viscous rubbery state is denoted as the glass transition temperature T_g. The material properties around T_g significantly evolve as the resin mechanical properties decrease and the stress relaxation becomes predominant. Consequently, the stress relaxation becomes important in thermoset composites when the temperatures are close to the glass transition temperature and the resin is not completely polymerized. The glass transition temperature is also function of the DOC, as it increases monotonically with the DOC. The DOC can be related with the cure dependent glass transition temperature $T_g(X)$ by means of the DiBenedetto [83] equation as

$$\frac{T_g(X) - T_{g0}}{T_{g\infty} - T_{g0}} = \frac{C_{DB} X}{1 - (1 - C_{DB})X} \tag{A.1}$$

where C_{DB} stands for a material parameter computed from experimental data, X is the DOC, and $T_{g\infty}$ and T_{g0} are the glass transition temperatures of the fully cured (i.e. $X = 1$) and uncured thermoset resin (i.e. $X = 0$), respectively.

The evolution of the shift factor a_T with the temperature varies as a function of T_g in case of thermoset composites ([149],[150]). For temperatures below and above T_g, the Arrhenius [151] and the Williams-Landel-Ferry (WLF) [152] equations apply respectively as

$$\begin{cases} \log a_T = \frac{E_a}{\ln 10 R}\left(\frac{1}{T} - \frac{1}{T_0}\right) & T < T_g(X) \\ \log a_T = \frac{-C_1(T-T_0)}{C_2+(T-T_0)} & T \geq T_g(X) \end{cases} \tag{A.2}$$

where E_a represents the activation energy expressed with unit J/mol, R stands for the universal gas constant equal to 8.314 J/K/mol, C_1 and C_2 are material constants adjusted from experimental data, and T_0 stands for reference temperature. E_a can also vary with the DOC depending on the thermoset resin [12]. If T_g is used as T_0, $C_1 = 17.44$ and $C_2 = 51.6$ can be used ([114], [153]). If T_g is used as the reference temperature, when the temperature is equal to the glass transition temperature (i.e. $T = T_g$), $a_T = 1$. In general, it is expected to have an increase in the relaxation rate for increased temperatures or for small DOC values [55]. The CTE of the thermoset resin also exhibits a discontinuity at T_g and thus, its value is different if temperatures below or above T_g are considered [114].

The DOC of the thermoset resin can be modeled by means of phenomenological rate expressions with distinct grade of complexity. These semi-empirical expressions are reduced from experimental data [154] and vary depending on the thermoset material considered. The simplest classical model to describe the cure kinetics for manufacturing simulation is the n-model order [155], which reads as

$$\frac{dX}{dt} = A \exp\left(\frac{-E_a}{RT}\right)(1-X)^n \tag{A.3}$$

where n is a material parameter that needs to be determined from experimental data also known as first exponential constant, and A is the frequency factor. The complexity of the cure kinetics model can be increased if an autocatalytic model, which is also known as n-m

model [155], is considered. The autocatalytic model for purely autocatalytic behavior reads as

$$\frac{dX}{dt} = A \exp\left(\frac{-E_a}{RT}\right) X^m (1-X)^n \tag{A.4}$$

where m is a material parameter also determined from the experimental data, known as the second exponential constant. If the diffusion of the reactants is considered, a diffusion-controlled term can be added to the autocatalytic model of Eq. (A.3) as [155]

$$\frac{dX}{dt} = \frac{A \exp\left(\frac{-E_a}{RT}\right) X^m (1-X)^n}{1 + \exp\left(C_0[X - (X_{C0} + X_{CT})T]\right)} \tag{A.5}$$

where C_0 is the diffusion constant, and X_{C0} and X_{CT} are the material constants that account for the critical DOC at $T = 0$ K, and the increase in critical DOC with temperature T, respectively.

It is noted that all the modeling approaches here presented consider the DOC and temperature as independent field variables so TTSP can be applied ([12], [114]).

A.1.2 Thermoplastic Composites

In thermoplastic composites made of semi-crystalline polymers, thermorheologically simple behavior can be assumed if only the phase transition around T_g is present. To achieve these conditions, fully crystallized material samples of a semi-crystalline material can be characterized up to the melting point [10]. During the manufacturing process of thermoplastic composites the material transitions from a viscous fluid to a viscoelastic solid. In this period, the constituent properties of the material have thermoviscoelastic behavior and are governed by the crystallization process. In a semi-crystalline thermoplastic material, crystallization happens during the cold-down between the crystallization and glass-transition temperatures [85]. At the molten stage and before crystallization, the thermoplastic material has negligible stiffness. However, during the cool down process the composite material shrinks and internal stresses are developed while the material increases its stiffness. Similarly to the case of thermoset composites, the process of crystallization generates crystallization

strains that lead to part deformations and additional residual stresses. The CTEs of the semi-crystalline polymer also exhibit temperature dependency and vary their value depending on T_g. In general, the value of the CTEs is higher above T_g [114] because the amount of free polymer grows above T_g. In case of the crystallization shrinkage, it is driven by amount of densification of the matrix material and DOC. However, compared to thermoset composites, T_g of a thermoplastic is fixed as it is defined by the molecular weight and architecture of the polymer.

Analogously to the thermoset composites, the Arrhenius [151] and the WLF [152] equations can be used to describe the shift factor of the thermoplastic polymer below and above T_g as [114]

$$\begin{cases} \log a_T = \frac{E_a}{\ln 10 R}\left(\frac{1}{T} - \frac{1}{T_0}\right) & T < T_g \\ \log a_T = \frac{-C_1(T-T_0)}{C_2+(T-T_0)} & T \geq T_g \end{cases} \tag{A.6}$$

where the two constants C_1 and C_2 are experimentally fit to the values obtained for $\log a_T$ for each material. It is also noted that for thermoplastic composites T_g does not vary as a function of DOC.

There are different crystallization kinetics models depending on the thermoplastic material considered. For instance, the Velisaris and Seferis [156] crystallization kinetics model is broadly used to describe the behavior of polyetheretherketone (PEEK) thermoplastic matrices ([85], [86], [157], [11]). The complete expression for this model reads as

$$\frac{X_{vc}}{X_{vc}^{\infty}} = w_1 F_{vc1} + w_2 F_{vc2} \tag{A.7}$$

where X_{vc} represents the volume fraction of crystallinity, X_{vc}^{∞} is the equilibrium volume fraction of crystallinity, F_{vc1} is the time integral expression describing crystal nucleation, F_{vc2} is the time integral expression describing the growth for processes, and w_1 and w_2 are the weight factors [86]. F_{vc1} and F_{vc2} are given by [158]

$$F_{vci} = 1 - \exp\left[- C_{i,1} \int_0^t T \exp\left(\frac{-C_{i2}}{T - T_g + 51.6} - \frac{-C_{i3}}{T(T_{m,i} - T)^2}\right) n_i \tau^{n_1 - 1} d\tau \right] \tag{A.8}$$
$$i = 1, 2$$

where $T_{m,i}$ are the crystal melt temperatures for dual mechanisms, n_i are the Avrami exponents for dual mechanisms [159], and $C_{i,1}$, $C_{i,2}$, and $C_{i,2}$ are model constants [85]. The weight factors are constrained as

$$w_1 + w_2 = 1 \tag{A.9}$$

It is noted that this model assumes that the crystallization temperatures are independent of the cooling rate.

A.2 T300/PMT-F4 Thermoset Composite

T300/PMT-F4 thermoset composite material properties are used for this study [95]. The T300 fiber is modeled as transversely isotropic with constituent properties given in Table A.1.

Table A.1. Constituent properties of T300 fiber characterized as transversely isotropic [95].

E_{1f} (MPa)	E_{2f} (MPa)	G_{12f} (MPa)	ν_{12f}	ν_{23f}	α_{11f} (μ/°C)	α_{22f} (μ/°C)
233,000.0	15,000.0	8,963.0	0.200	0.330	-0.540	10.080

The PMT-F4 epoxy matrix is modeled as a thermorheologically simple isotropic material with time and temperature dependency. The time dependent Young's modulus of the matrix is approximated by Prony series that include the temperature effect as

$$E_m = E_\infty + \sum_{s=1}^{n} E_s \exp\left(-\frac{\xi}{\lambda_s}\right) \tag{A.10}$$

where E_∞ is the long-term modulus, E_s stand for the Prony series coefficients of the resin, λ_s are the discrete stress relaxation times, and ξ is the reduced time as a function of the temperature given by Eq. (2.2). The Prony series coefficients are given in Table A.2. A constant Poisson's ratio of $\nu_m = 0.33$ [110] and CTE of $\alpha_m = 60\ \mu/°C$ are assumed. It is noted that E_∞, ν_m, and α_m are used to normalize the values of the effective properties. In addition, whereas the Poisson's ratios and the CTEs are shown with three digits after the decimal point, one digit after the decimal point is used for the rest of material properties.

Table A.2. Prony series coefficients and relaxation times for PMT-F4 [95].

s	∞	1	2	3	4	5	6	7
λ_s (s)	-	10^3	10^5	10^6	10^7	10^8	10^9	10^{10}
E_s (MPa)	1,000.0	224.1	450.8	406.1	392.7	810.4	203.7	1,486.0

The shift factor a_T for PMT-F4 epoxy resin, which depends on the temperature, is defined by a WLF equation as

$$\log a_T = -\frac{28.3816(T - T_0)}{93.291 + (T - T_0)} \tag{A.11}$$

where the temperature T is expressed in °C and $T_0 = 40$°C [95]. The evolution of the normalized E_m for different temperatures is shown in Figure A.1. At $T = 100$°C, the resin modulus is relaxed as it is equal to E_∞ and keeps constant as the time passes. For $T = 20$°C, the resin modulus decreases with increased time, but this decrease cannot be observed clearly in Figure A.1 as it is equal to 0.58% for the period plotted.

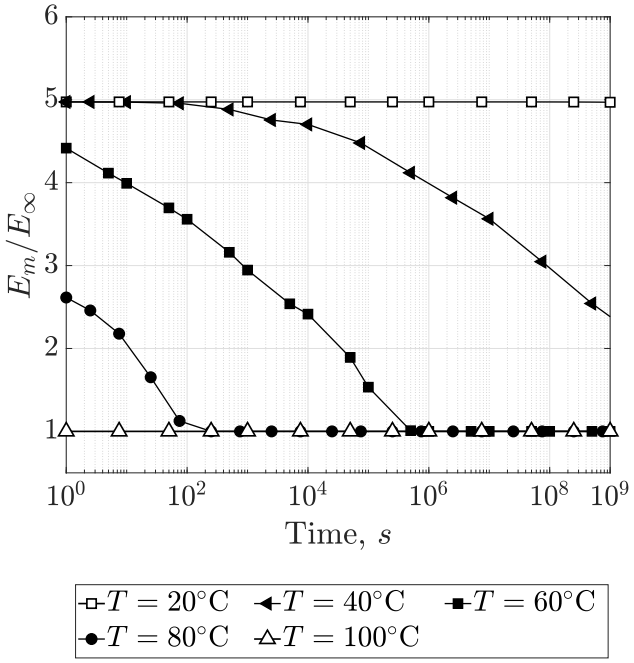

Figure A.1. Evolution of normalized PMT-F4 resin modulus for different temperatures.

A.3 Time-dependent Versus Prony Series Coefficients for M30S/PMT-F7 Plain Wave Composite

During this PhD dissertation work, the PMT-F7 toughened epoxy resin data experimentally characterized by NASA LaRC were used. These modulus relaxation data were gathered during a tensile stress relaxation test and given as a time-dependent property and were later made available for the general public by Salazar et al. [143]. However, for the purpose of the present work, Prony series coefficients were fit and summarized in Table A.3. A reference temperature of $T_0 = 40°$ C was selected to shift these experimental data, as it represents the maximum boom stowage temperature expected for the NASA solar sail application ([15], [16]). At this temperature, the material will achieve the highest expected relaxation during the mission and thus, the results will be representative of the worst-case deployment scenario. The Figure A.2 shows the experimental data of the time-dependent Young's modulus of PMT-F7 provided by NASA LaRC against the one available in the literature ([144], [145]). It can be observed that the NASA LaRC resin relaxes faster than the one available in the literature ([144], [145]). The fit Prony series coefficients for the NASA LaRC material are summarized in Table A.3 and the fit results are compared against the actual data in Figure A.2.

Table A.3. Prony series coefficients fit for PMT-F7 experimental data provided by NASA LaRC at $T_0 = 40°$C.

s	λ_s (s)	E_r (MPa)
∞		1546.0
1	3.70E+01	324.7
2	1.00E+02	236.3
3	5.00E+02	7.1
4	1.00E+03	7.1
5	5.00E+03	201.2
6	1.00E+04	81.5
7	5.00E+04	89.5
8	1.00E+05	223.9
9	5.00E+05	19.5
10	1.00E+06	109.3
11	5.00E+06	60.0

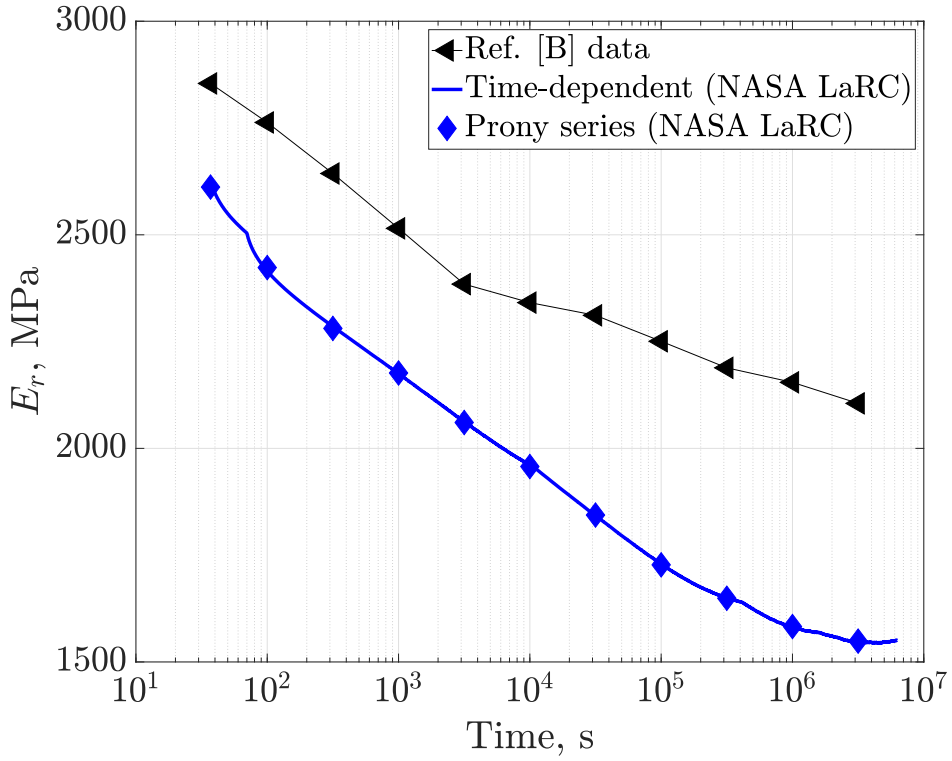

Figure A.2. Evolution of the Young's modulus of the PMT-F7 resin at $T_0 = 40°$ C. Note that Ref. [B] represents Ref. [145].

The constituent materials can be input into SwiftComp™ [112] either using time-dependent material properties, such as the ones directly measured in the experiments, or by means of Prony series coefficients. To prove that both approaches lead to the same set of effective properties, a yarn was modeled with a 2D SG as an hexagonal square pack with a fiber volume fraction of 0.62 [144]. The M30S fiber was modeled as transversely isotropic material and data from Ref. [144] were used. Then, two different viscoelastic homogenization analyses were run in SwiftComp™ [112] representing the PMT-F7 toughened resin data from Ref. [145] as time-dependent property and by means of Prony series coefficients. For completeness, the same homogenization was run but considering PMT-F7 toughened resin data from NASA LaRC. For all the three cases, a Poisson's ratio of 0.36 was used for the resin and isotropic behavior was assumed. The interphase between the fiber and the matrix was not modeled.

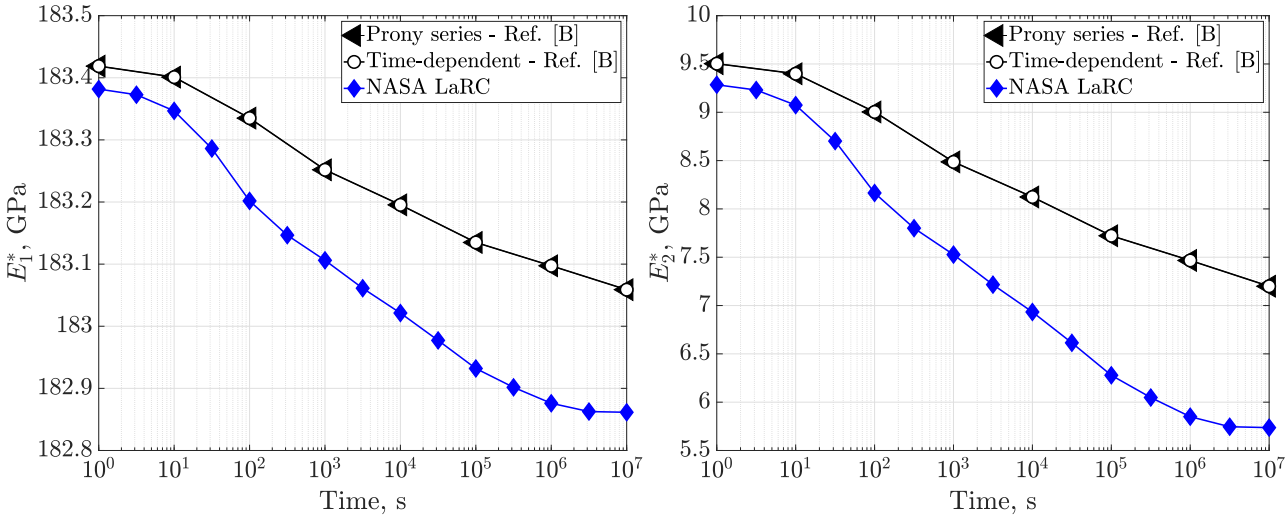

Figure A.3. Evolution of the effective Young's modulus for the yarn. It is noted that $E_2^* = E_3^*$ and that Ref. [B] represents Ref. [145].

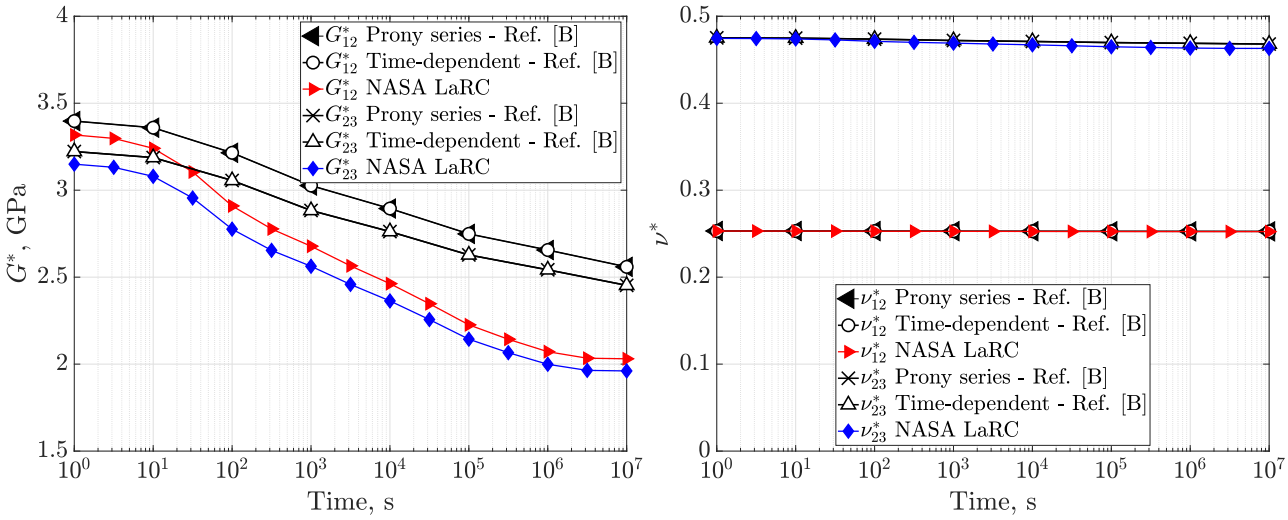

Figure A.4. Evolution of the effective shear moduli (Left) and Poisson's ratios (Right) modulus for the yarn. It is noted that $G_{12}^* = G_{13}^*$ and $\nu_{12}^* = \nu_{13}^*$ and that Ref. [B] represents Ref. [145].

The evolutions of the effective engineering constants of the yarn are shown in Figures A.3 and A.4. It can be observed that expressing the resin either as time-dependent input or by means of Prony series coefficients lead to the same effective properties. Therefore, SwiftComp^{TM} [112] can handle the directly measured experimental time-dependent data without losing accuracy. It also eliminates extra efforts in fitting these data into Prony series coefficients. In addition, as expected, the effective properties computed from the NASA LaRC resin relaxes faster than those computed from data in Ref. [145]. This was more evident for the matrix dominated properties such as the Young's modulus in the transverse direction and shear moduli with 25.5% and 26% of difference at $t = 10^7$ s, respectively. Both resin types lead to the same effective Poisson's ratios, which did not relax with increased time for this particular microstructure.

The parameters for the PMT-F7 toughened epoxy resin shift function were manually fit from experimental data provided by NASA LaRC for this study. To do so, the resin relaxation behavior at 30°C, 40°C, 50°C, 60°C and 80°C were used in the calculations. The 70°C relaxation data were discarded because they exhibited an unexpected behavior for this type of resin. It is noted that these data were later partially published by Salazar and Fernandez [143]. The data were plotted for each of the temperature values. The horizontal axis represented the common logarithm of time in seconds, and the vertical axis represented the relaxed value of the resin. Since 40°C data were considered as reference temperature T_0, shift factor of $a_T = 1$ was used for all the data at 40°C. In other words, $\log t = 0$ corresponds to T_0 and for this particular case at T_0, $\log t = \log \xi$ since $a_T = 1$. Then, following the TTSP, the 30°C, 50°C, 60°C and 80°C curves were shifted horizontally until they lied on top of the 40°C curve. The amount needed to shift in the horizontal axis was considered as the shift function value in common logarithmic scale for each temperature. These values were later converted into the real scale and input into a Matlab script to fit into the WLF equation. The script used a nonlinear least-squares curve-fitting function with the Levenberg-Marquardt algorithm to compute the coefficients for the WLF equation.

Since $T > T_g$, the objective was to find the parameters C_1 and C_2 of Eq. (A.2). Finally, the expression for WLF equation was found to be equal to

$$\log a_T = -\frac{3.6868(T - T_0)}{13.5513 + (T - T_0)} \tag{A.12}$$

where the temperature was expressed in °C and $T_0 = 40$ °C.

B. ADDITIONAL FORMULATION FOR THE DIRECT INTEGRATION METHOD

This appendix details intermediate steps of the derivation of the MSG-based solid model with the direct integration method. The aim of this appendix is to provide additional details so that the derivation can be reproduced. It is noted that the formulation here presented was adapted from Zocher et al. [70].

1. Computation of $M_{ijkl}\Delta\varepsilon(\xi_{n+1})$. Substituting the first expression of Eq. (3.58) and the approximation given by Eq. (3.59) into the first term on the right hand side of Eq. (3.55), we have that

$$
\begin{aligned}
&\int_{\xi_n}^{\xi_{n+1}} C_{ijkl}\left(T_0, \xi_{n+1}(t)-\xi(\tau)\right)\dot{\varepsilon}_{kl}(\tau)d\tau \\
&= \int_{\xi_n}^{\xi_{n+1}} \left[C_{ijkl,\infty} + \sum_{s_1=1}^{m_1} C_{ijkl,s_1}\mathrm{e}^{\left(-\frac{\xi_{n+1}(t)-\xi(\tau)}{\lambda_{s_1}}\right)}\right]\frac{\partial\left(\varepsilon_{ij_n} + R_{\varepsilon_{ij_{n+1}}}(\xi-\xi_n)H(\xi-\xi_n)\right)}{\partial\xi(\tau)}d\xi(\tau) \\
&= \int_{\xi_n}^{\xi_{n+1}} C_{ijkl,\infty}R_{\varepsilon_{ij_{n+1}}}\Big((\xi-\xi_n)\delta(\xi-\xi_n) + H(\xi-\xi_n)\Big)d\xi(\tau) \\
&+ \int_{\xi_n}^{\xi_{n+1}} R_{\varepsilon_{ij_{n+1}}}\Big((\xi-\xi_n)\delta(\xi-\xi_n) + H(\xi-\xi_n)\Big)\left[\sum_{s_1=1}^{m_1} C_{ijkl,s_1}\mathrm{e}^{\left(-\frac{\xi_{n+1}(t)-\xi(\tau)}{\lambda_{s_1}}\right)}\right]d\xi(\tau) \\
&= C_{ijkl,\infty}R_{\varepsilon_{ij_{n+1}}}\Delta\xi_{n+1} + \left[\sum_{s=1}^{m_1}\frac{\lambda_{s_1}}{\xi_{n+1}}C_{ijkl,s_1}\left(1-\mathrm{e}^{\left(-\frac{\Delta\xi_{n+1}}{\lambda_{s_1}}\right)}\right)\right]R_{\varepsilon_{ij_{n+1}}}\Delta\xi_{n+1} \\
&= \left[C_{ijkl,\infty} + \frac{1}{\Delta\xi_{n+1}}\sum_{s_1=1}^{m_1}\lambda_{s_1}C_{ijkl,s_1}\left(1-\mathrm{e}^{\frac{-\Delta\xi_{n+1}}{\lambda_{s_1}}}\right)\right]\Delta\varepsilon_{n+1} \;\equiv\; M_{ijkl}\Delta\varepsilon_{n+1}
\end{aligned}
\tag{B.1}
$$

where it is noted that

$$
\int_{\xi_n}^{\xi_{n+1}} H(\xi-\xi_n)d\xi(\tau) = (\xi-\xi_n)H(\xi-\xi_n) = \Delta\xi_{n+1} \quad \text{if } \xi(\tau) > \xi_n \tag{B.2}
$$

and

$$
\int_{\xi_n}^{\xi_{n+1}} (\xi-\xi_n)\delta(\xi-\xi_n)d\xi(\tau) = 0 \quad \text{if } \xi(\tau) > \xi_n \tag{B.3}
$$

2. Computation of $\eta_{ij}\Delta\theta(\xi_{n+1})$. Similarly to the case of the $M_{ijkl}\Delta\varepsilon_{n+1}$, we need to substitute the second expression of Eq. (3.58) and the approximation given by Eq. (3.59) into the second term on the right hand side of Eq. (3.55). Then, we have that

$$
\begin{aligned}
&\int_{\xi_n}^{\xi_{n+1}} \beta_{ij}\left(T_0, \xi_{n+1}(t) - \xi(\tau)\right)\dot{\theta}(\tau)d\tau \\
&= \int_{\xi_n}^{\xi_{n+1}} \left[\beta_{ij,\infty} + \sum_{s_2=1}^{m_2} \beta_{ij,s_2} \mathrm{e}^{\left(-\frac{\xi_{n+1}(t)-\xi(\tau)}{\lambda_s}\right)}\right] \frac{\partial(\theta_n + R_{\theta_{n+1}}(\xi-\xi_n)H(\xi-\xi_n))}{\partial\xi(\tau)} d\xi(\tau) \\
&= \int_{\xi_n}^{\xi_{n+1}} \beta_{ij,\infty} R_{\theta_{n+1}}\Big((\xi-\xi_n)\delta(\xi-\xi_n) + H(\xi-\xi_n)\Big)d\xi(\tau) \\
&+ \int_{\xi_n}^{\xi_{n+1}} R_{\theta_{n+1}}\Big((\xi-\xi_n)\delta(\xi-\xi_n) + H(\xi-\xi_n)\Big)\left[\sum_{s_2=1}^{m_2} \beta_{ij,s_2} \mathrm{e}^{\left(-\frac{\xi_{n+1}(t)-\xi(\tau)}{\lambda_{s_2}}\right)}\right] d\xi(\tau) \\
&= \beta_{ij,\infty} R_{\theta_{n+1}} \Delta\xi_{n+1} + \left[\sum_{s_2=1}^{m_2} \frac{\lambda_{s_2}}{\xi_{n+1}} \beta_{ij,s_2}\left(1 - \mathrm{e}^{\left(-\frac{\Delta\xi_{n+1}}{\lambda_{s_2}}\right)}\right)\right] R_{\theta_{n+1}}\Delta\xi_{n+1} \\
&= \left[\beta_{ij,\infty} + \frac{1}{\Delta\xi_{n+1}} \sum_{s_2=1}^{m_2} \lambda_{s_2}\beta_{ij,s_2}\left(1 - \mathrm{e}^{\frac{-\Delta\xi_{n+1}}{\lambda_{s_2}}}\right)\right]\Delta\theta_{n+1} \;\equiv\; \eta_{ij}\Delta\theta_{n+1}
\end{aligned}
\tag{B.4}
$$

where Eqs. (B.2) - (B.3) have been applied in the derivation.

3. Computation of Ω_{ij} - Viscoelastic part. To compute the value of Ω_{ij}, we substitute Eqs. (3.52, 3.57, 3.58) into the first term of the right hand-side of Eq. (3.56) as

$$
\begin{aligned}
&\int_0^{\xi_n} \Delta C_{ijkl}\dot{\varepsilon}_{kl}(\tau)d\tau = \int_0^{\xi_n} \left[C_{ijkl,\infty} + \sum_{s_1=1}^{m_1} C_{ijkl,s_1} \mathrm{e}^{\left(-\frac{\xi_{n+1}(t)-\xi(\tau)}{\lambda_{s_1}}\right)}\right. \\
&\left. - C_{ijkl,\infty} + \sum_{s_1=1}^{m_1} C_{ijkl,s_1} \mathrm{e}^{\left(-\frac{\xi_n(t)-\xi(\tau)}{\lambda_{s_1}}\right)}\right]\dot{\varepsilon}_{kl}(\tau)d\tau \\
&= \int_0^{\xi_n} \left[\sum_{s_1=1}^{m_1} C_{ijkl,s_1} \mathrm{e}^{\left(-\frac{\xi_n(t)+\Delta\xi_{n+1}-\xi(\tau)}{\lambda_{s_1}}\right)} - \sum_{s_1=1}^{m_1} C_{ijkl,s_1} \mathrm{e}^{\left(-\frac{\xi_n(t)-\xi(\tau)}{\lambda_{s_1}}\right)}\right]\dot{\varepsilon}_{kl}(\tau)d\tau \\
&= -\sum_{s_1=1}^{m_1} \left[\left(1 - \mathrm{e}^{\left(\frac{-\Delta\xi_{n+1}}{\lambda_{s_1}}\right)}\right)\int_0^{\xi_n} C_{ijkl,s_1} \mathrm{e}^{\left(-\frac{\xi_n(t)-\xi(\tau)}{\lambda_{s_1}}\right)}\dot{\varepsilon}_{kl}(\tau)d\tau\right] \\
&= -\sum_{s_1=1}^{m_1} \left(1 - \mathrm{e}^{\left(\frac{-\Delta\xi_{n+1}}{\lambda_{s_1}}\right)}\right) D_{ij,s_1}(\xi_n)
\end{aligned}
\tag{B.5}
$$

To solve the integral part of Eq. (B.5) represented by the term $D_{ij,s_1}(\xi_n)$, we need to approximate the partial derivatives following Eq. (3.59) as

$$\dot{\varepsilon}_{kl}(\tau) = \frac{\partial \varepsilon_{kl}(\tau)}{\partial \xi(\tau)} \approx R_{\varepsilon_{kl_n}} \equiv \frac{\Delta \varepsilon_{kl}}{\Delta \xi_n} \qquad (\xi_n - \Delta_n \xi \leq \xi(\tau) \leq \xi_n) \tag{B.6}$$

where $\Delta\varepsilon_{kl}$ and $\Delta\xi_n$ and hence, $R_{\varepsilon_{kl_n}}$ are determined from the previous step. It is noted that from Eq. (3.52), $\xi_n - \Delta_n = \xi_{n-1}$. Then, the integral part of Eq. (B.5) can be further developed as

$$\begin{aligned}
D_{ij,s_1}(\xi_n) &= \int_0^{\xi_n} C_{ijkl,s_1} \mathrm{e}^{\left(-\frac{\xi_n(t)-\xi(\tau)}{\lambda_{s_1}}\right)} \dot{\varepsilon}_{kl}(\tau) d\tau \\
&= \int_{\xi_{n-1}}^{\xi_n} C_{ijkl,s_1} \mathrm{e}^{\left(-\frac{\xi_n(t)-\xi(\tau)}{\lambda_{s_1}}\right)} \dot{\varepsilon}_{kl}(\tau) d\tau + \int_0^{\xi_{n-1}} C_{ijkl,s_1} \mathrm{e}^{\left(-\frac{\xi_n(t)-\xi(\tau)}{\lambda_{s_1}}\right)} \dot{\varepsilon}_{kl}(\tau) d\tau \\
&= \int_{\xi_{n-1}}^{\xi_n} C_{ijkl,s_1} \mathrm{e}^{\left(-\frac{\xi_n(t)-\xi(\tau)}{\lambda_{s_1}}\right)} R_{\varepsilon_{kl_n}} d\tau + \int_0^{\xi_{n-1}} C_{ijkl,s_1} \mathrm{e}^{\left(-\frac{\xi_n(t)+\Delta\xi_n-\Delta\xi_n-\xi(\tau)}{\lambda_{s_1}}\right)} \dot{\varepsilon}_{kl}(\tau) d\tau \\
&= \lambda_{s_1} C_{ijkl,s_1} R_{\varepsilon_{kl_n}} \left(1 - \mathrm{e}^{\frac{-\Delta\xi_n}{\lambda_{s_1}}}\right) + \mathrm{e}^{\frac{-\Delta\xi_n}{\lambda_{s_1}}} \int_0^{\xi_{n-1}} C_{ijkl,s_1} \mathrm{e}^{\left(-\frac{\xi_{n-1}(t)-\xi(\tau)}{\lambda_{s_1}}\right)} \dot{\varepsilon}_{kl}(\tau) d\tau \\
&= \lambda_{s_1} C_{ijkl,s_1} R_{\varepsilon_{kl_n}} \left(1 - \mathrm{e}^{\frac{-\Delta\xi_n}{\lambda_{s_1}}}\right) + \mathrm{e}^{\frac{-\Delta\xi_n}{\lambda_{s_1}}} D_{ij,s_1}(\xi_{n-1})
\end{aligned} \tag{B.7}$$

4. Computation of Ω_{ij} - Thermoviscoelastic part. To compute the value of Ω_{ij}, we substitute Eqs. (3.52, 3.57, 3.58) into the second term of the right hand-side of Eq. (3.56) as

$$\begin{aligned}
\int_0^{\xi_n} \Delta\beta_{ij} \dot{\theta}(\tau) d\tau &= \int_0^{\xi_n} \left[\beta_{ij,\infty} + \sum_{s_2=1}^{m_2} \beta_{ij,s_2} \mathrm{e}^{\left(-\frac{\xi_{n+1}(t)-\xi(\tau)}{\lambda_{s_2}}\right)} \right. \\
&\left. - \beta_{ij,\infty} + \sum_{s_2=1}^{m_2} \beta_{ij,s_2} \mathrm{e}^{\left(-\frac{\xi_n(t)-\xi(\tau)}{\lambda_{s_2}}\right)} \right] \dot{\theta}(\tau) d\tau \\
&= \int_0^{\xi_n} \left[\sum_{s_2=1}^{m_2} \beta_{ij,s_2} \mathrm{e}^{\left(-\frac{\xi_n(t)+\Delta\xi_{n+1}-\xi(\tau)}{\lambda_{s_2}}\right)} - \sum_{s_2=1}^{m_2} \beta_{ij,s_2} \mathrm{e}^{\left(-\frac{\xi_n(t)-\xi(\tau)}{\lambda_{s_2}}\right)} \right] \dot{\theta}(\tau) d\tau \\
&= -\sum_{s_2=1}^{m_2} \left[\left(1 - \mathrm{e}^{\left(\frac{-\Delta\xi_{n+1}}{\lambda_{s_2}}\right)}\right) \int_0^{\xi_n} \beta_{ij,s_2} \mathrm{e}^{\left(-\frac{\xi_n(t)-\xi(\tau)}{\lambda_{s_2}}\right)} \dot{\theta}(\tau) d\tau \right] \\
&= -\sum_{s_2=1}^{m_2} \left(1 - \mathrm{e}^{\left(\frac{-\Delta\xi_{n+1}}{\lambda_{s_2}}\right)}\right) B_{ij,s_2}(\xi_n)
\end{aligned} \tag{B.8}$$

To solve the integral part of Eq. (B.8) represented by the term $B_{ij,s_2}(\xi_n)$, we need to approximate the partial derivatives following Eq. (3.59) as

$$\dot{\theta}(\tau) = \frac{\partial \theta(\tau)}{\partial \xi(\tau)} \approx R_{\theta_n} \equiv \frac{\Delta\theta}{\Delta\xi_n} \qquad (\xi_n - \Delta\xi \leq \xi(\tau) \leq \xi_n) \tag{B.9}$$

where $\Delta\varepsilon_{kl}$ and $\Delta\xi_n$ and hence, R_{θ_n} are determined from the previous step. Then, the integral part of Eq. (B.8) can be further developed as

$$\begin{aligned}
B_{ij,s_2}(\xi_n) &= \int_0^{\xi_n} \beta_{ij,s_2} \mathrm{e}^{\left(-\frac{\xi_n(t)-\xi(\tau)}{\lambda_{s_2}}\right)} \dot{\theta}(\tau) d\tau \\
&= \int_{\xi_{n-1}}^{\xi_n} \beta_{ij,s_2} \mathrm{e}^{\left(-\frac{\xi_n(t)-\xi(\tau)}{\lambda_{s_1}}\right)} \dot{\theta}(\tau) d\tau + \int_0^{\xi_{n-1}} \beta_{ij,s_2} \mathrm{e}^{\left(-\frac{\xi_n(t)-\xi(\tau)}{\lambda_{s_2}}\right)} \dot{\theta}(\tau) d\tau \\
&= \int_{\xi_{n-1}}^{\xi_n} \beta_{ij,s_2} \mathrm{e}^{\left(-\frac{\xi_n(t)-\xi(\tau)}{\lambda_{s_2}}\right)} R_{\theta_n} d\tau + \int_0^{\xi_{n-1}} \beta_{ij,s_2} \mathrm{e}^{\left(-\frac{\xi_n(t)+\Delta\xi_n-\Delta\xi_n-\xi(\tau)}{\lambda_{s_2}}\right)} \dot{\theta}(\tau) d\tau \\
&= \lambda_{s_2} \beta_{ij,s_2} R_{\theta_n} \left(1 - \mathrm{e}^{\frac{-\Delta\xi_n}{\lambda_{s_2}}}\right) + \mathrm{e}^{\frac{-\Delta\xi_n}{\lambda_{s_2}}} \int_0^{\xi_{n-1}} \beta_{ij,s_2} \mathrm{e}^{\left(-\frac{\xi_{n-1}(t)-\xi(\tau)}{\lambda_{s_2}}\right)} \dot{\theta}(\tau) d\tau \\
&= \lambda_{s_2} \beta_{ij,s_2} R_{\theta_n} \left(1 - \mathrm{e}^{\frac{-\Delta\xi_n}{\lambda_{s_2}}}\right) + \mathrm{e}^{\frac{-\Delta\xi_n}{\lambda_{s_2}}} B_{ij,s_2}(\xi_{n-1})
\end{aligned} \tag{B.10}$$

C. SOFTWARE DEVELOPMENT

Abaqus SwiftComp GUI

SwiftComp^{TM} [112] can be used as as a plugin for other commercial codes or a standalone code. To facilitate the use of SwiftComp^{TM} [112], a simple graphic user interface (GUI) with a toolbar integrating the functions of SwiftComp^{TM} [112] was developed for Abaqus CAE in 2016. This GUI was named as Abaqus SwiftComp GUI [113].

Since the viscoelastic and thermoviscoelastic homogenization capabilities developed in this dissertation were added to SwiftComp^{TM} [112], the Abaqus SwiftComp GUI [113] was accordingly updated to be able to consider viscoelastic and thermoviscoelastic constituent properties. To do so, the capability to define time-dependent constituent properties was added (see Figure C.1). It should be noted that the default material library of Abaqus CAE [104] only considers isotropic viscoelastic properties defined by means of Prony series coefficients. However, the current development of Abaqus SwiftComp GUI [113] enabled the definition of viscoelastic or thermoviscoelastic material properties not only for isotropic but also for any kind of material anisotropy such orthotropic defined either by stiffness matrix or engineering constants, and general anisotropic (see Figure C.2). Furthermore, the capability to input the time-dependent material properties, such as the ones directly measured in the experiments, was also supported. For this latter purpose, the constituent properties were defined in a text file (see Figure C.2 right).

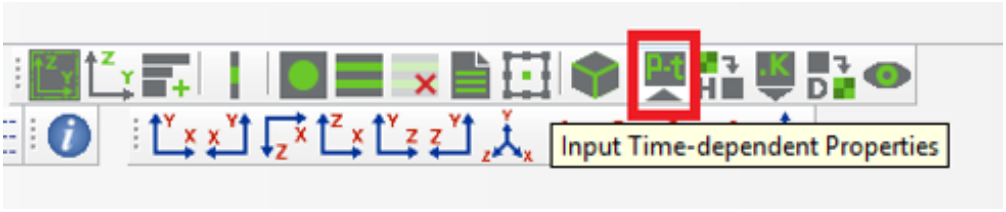

Figure C.1. Abaqus SwiftComp GUI toolbox with time-dependent material input function activated.

Finally, when the homogenization step was carried out (see Figure C.3), the viscoelastic and thermoviscoelastic analyses were added. For both analyses, the user needs to define the initial time, final time and time increment in decades as shown in Figure C.4.

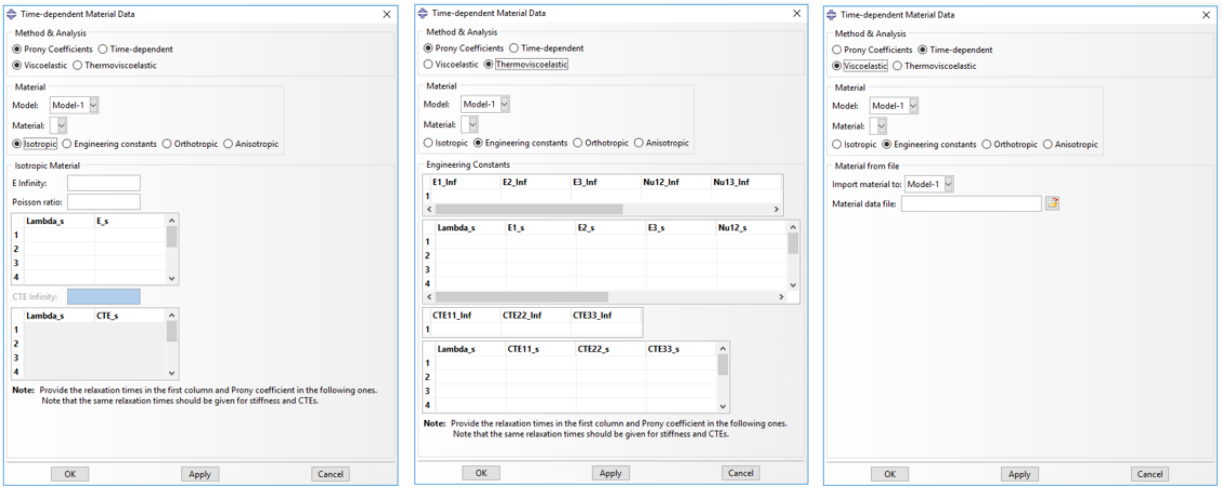

Figure C.2. Abaqus SwiftComp GUI thermoviscoelastic material input types: viscoelastic defined by Prony series coefficients (left), thermoviscoelastic defined by Prony series coefficients (middle) and time-dependent input from a text file (right).

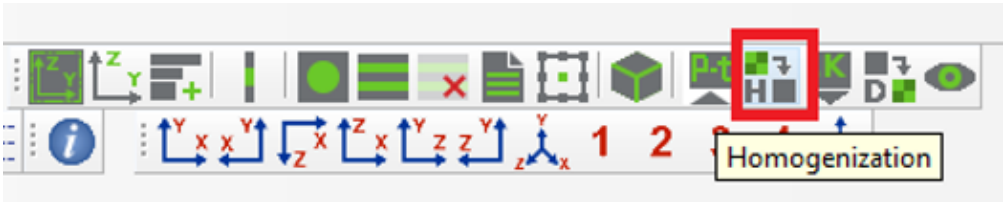

Figure C.3. Abaqus SwiftComp GUI toolbox with homogenization function activated.

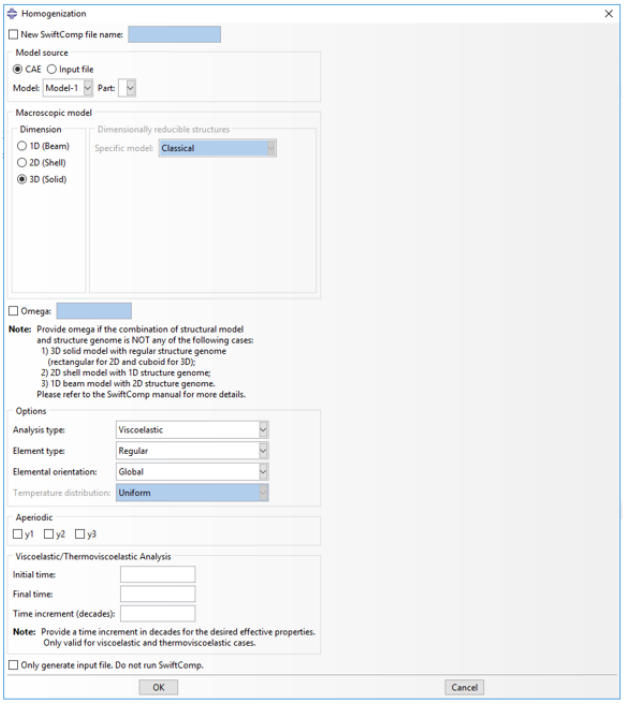

Figure C.4. Abaqus SwiftComp GUI thermoviscoelastic or viscoelastic homogenization step.

VITA

Orzuri was born and raised in the province of Biscay, Basque Country, Spain. She holds a Bachelor's and Master's Degree in Aeronautical Engineering by the Polytechnic University of Catalonia (Barcelona-Tech). She also holds a Master's Degree in Mechanical Manufacturing and Automation by Beihang University in Beijing, China. During her studies at Beihang, she did an internship focused on the structural analysis of wind turbines at Goldwind Science & Technology, Co. In August 2015, she started her graduate studies at Purdue University advised by Dr. Wenbin Yu and co-advised by Dr. R. Byron Pipes. She researched on the constitutive modeling of linear thermoviscoelasticity of composite materials at the Composites Manufacturing and Simulation Center in West Lafayette, Indiana. She completed her Doctor of Philosophy in Aeronautics and Astronautics Engineering at Purdue University majoring in Structures and Materials in May 2021.

Orzuri is native Basque and Spanish speaker, fluent in Catalan and English, and also studied German, French, and Mandarin Chinese. She is married to Dr. Arnau Pons, who also obtained his Doctor of Philosophy in Aeronautics and Astronautics Engineering from Purdue University. In her spare time, she enjoys outdoor walks and treks in the nature.

Awards

- AIAA Materials Technical Committee Innovation Scholars at SciTech 2021 Award.
- Finalist selected by Dassault Systèmes for the Dr. David M. Aber Scholarship Competition (2019 COExperience Annual Experience & TecniFair).
- AIAA Diversity Scholarship to attend 2019 AIAA SciTech Forum. Scholarship sponsored by Aurora Flight Sciences.
- Scholarship from Stanford University to attend Women in Aerospace Symposium 2018. Hosted by MIT, CU Boulder and Stanford University at Stanford University in May 2018.

Publications

Journal Papers

1. O. Rique, J. M. Fernandez, A. C. Bergan and W. Yu. Multiscale thermoviscoelastic composite beam cross-sectional analysis using mechanics of structure genome. Preprint prepared for *Composites Part B: Engineering*. Currently under review by NASA LaRC.

2. Y. Long, O. Rique, W. Yu, J. M. Fernandez and A. C. Bergan. Simulation of column bending test using an anisotropic viscoelastic shell model. Preprint prepared for *Composites Science and Technology*. Currently under review by NASA LaRC.

3. O. Rique, X. Liu, W. Yu, and R. B. Pipes. Constitutive modeling for time- and temperature-dependent behavior of composites. *Composites Part B: Engineering*, 184:107726, March 2020. Ref. [136]

4. O. Rique, J. E. Goodsell, W. Yu, and R B. Pipes. Three-dimensional thermoelastic properties of general composite laminates. *Journal of Composite Materials*, 52(13):1799-1808, October 2017. Ref. [160]

Conference Papers

1. O. Rique, S. Tian, J. M. Fernandez, A. C. Bergan and W. Yu. Thermoviscoelastic modeling of thin-ply high strain composites by means of multiscale beam models. In *AIAA SciTech 2021 Forum*. American Institute of Aeronautics and Astronautics, Virtual Event, January 2021. Ref. [146]

2. Y. Long, O. Rique, J. M. Fernandez, A. C. Bergan and W. Yu. Multiscale simulation of deployable composite structures. In *AIAA SciTech 2021 Forum*. American Institute of Aeronautics and Astronautics, Virtual Event, January 2021. Ref. [125]

3. O. Rique, Y. Long, W. Yu, R. B. Pipes, J. M. Fernandez, and A. C. Bergan. Improved plate and beam models for thermoviscoelastic constitutive modeling of composites. In *American Society for Composites 2020*. DEStech Publications, Inc., Virtual Conference, September 2020. Ref. [141]

4. O. Rique and W. Yu. Multiscale modeling of thermoviscoelasticity for composite manufacturing simulation using mechanics of structure genome. In *AIAA SciTech 2019 Forum*. American Institute of Aeronautics and Astronautics, San Diego, California, January 2019. Ref. [122]

5. G. Andrews, A. Black, J. Graham and O. Rique. Preliminary design of a rotation detonation engine for launch vehicle applications. In *AIAA SciTech 2018 Forum*. American Institute of Aeronautics and Astronautics, Kissimmee, Florida, January 2018. Ref. [161]

6. O. Rique, E. Barocio, and W. Yu. Experimental and numerical determination of the thermal conductivity tensor for composites manufacturing simulation. In *American Society for Composites 2017*. DEStech Publications, Inc., West Lafayette, Indiana, November 2017. Ref. [162]

7. O. Rique, Y. Long, J. Goodsell, W. Yu, and R. B. Pipes. Composite de-tooling simulation using an improved plate and shell theory based on mechanics of structure genome. In *American Society for Composites 2016*. DEStech Publications, Inc., Williamsburg, Virginia, October 2016. Ref. [163]

8. K. Knauf, E. Barocio, O. Rique, et al. Uniting Composites Manufacturing Theory and Application: Practical Manufacturing Methods in a Team-Based Curriculum. In *American Society for Composites 2016*. DEStech Publications, Inc., Williamsburg, Virginia, October 2016. Ref. [164]